THE DEFORMATION BEHAVIOUR OF A Mg-8Al-0.5Zn ALLOY

by

JAYANT JAIN

A THESIS SUBMITTED IN PARTIAL FULFILLMENT OF THE

REQUIREMENTS FOR THE DEGREE OF

DOCTOR OF PHILOSOPHY

in

The Faculty of Graduate Studies

(MATERIALS ENGINEERING)

THE UNIVERSITY OF BRITISH COLUMBIA

(Vancouver)

November 2010

Abstract

In this work, the deformation behaviour of an Mg-8Al-0.5Zn (AZ80) alloy having a fixed initial grain size of ~ 32 μm was studied by varying the initial texture, temperature, stress state and microstructure. The work focused on investigating the influence of these variables on the mechanical properties, work hardening characteristics, texture evolution and deformation mechanisms of the alloy. The initial materials with different starting textures (i.e. strongly and weakly textured) and microstructures (i.e. solution-treated and aged) were obtained through a series of thermo-mechanical treatments including cold rolling, annealing and ageing. The uniaxial compression and tension deformation experiments were carried out on strongly and weakly textured solution-treated and aged samples at 77K and 293K. Neutron diffraction, slip trace analysis, high and low resolution EBSD were used to characterize the texture evolution and deformation mechanisms of the alloy. In addition, a visco-plastic self consistent (VPSC) model was used to predict the influence of initial texture and temperature on the deformation behaviour.

The results show that temperature and loading direction with respect to initial texture has a pronounced effect on yield strength and work hardening. It is found that there is a substantial difference between the nature of twinning, slip system activity and texture development as a function of deformation temperature. It is shown that the VPSC model is effective in predicting the deformation response of alloy when it is dominated by slip. The same model however proved to be inadequate for twinning dominated deformation. The results illustrate that precipitates are capable of changing the balance of deformation mechanisms and texture development of the alloy. They were found to be extremely

effective in reducing the well known tension compression yield asymmetry exhibited by magnesium and its alloys.

Table of Contents

List of Tables

List of Figures

Acknowledgements

It is my pleasure to express my profound gratitude to my supervisors, Dr. Warren Poole and Dr. Chad Sinclair, for their support, guidance and encouragement. In particular, I would like to thank them for helping me to grown as a researcher. Sincere thanks are also due to Dr. Michael Gharghouri for helping me in neutron texture measurements at Chalk River. I also thank Dr. Carlos Tomé at Los Alamos National Laboratory for kindly providing me the VPSC package. I would like to express my thanks to Dr. Jianxin Zou for helping me with the electron microscopy work. I extend my heartiest thanks to all staff members (Rudy Cardeno, Mary Fletcher, Ross Mcleod, David Torok, Carl Ng, Debbie Burgess, Mary Jansepar, Fiona Webster, Michelle Tierney) at Department of Materials Engineering at UBC for assistance on my research work. My special thanks to Dr. Mehran Maalekian, Dr. Thomas Garcin, Hamid Azizi-Alizamini, Leo Colley. David Marechal, Guillaume Lefebvre, Guillaume Badinier, Reza Roumina, Babak Raeisinia, Phil Tomlinson, Dr. Fateh Fazeli, Amir Hossein Nobari , Elizabeth Sterling, Sina Shahandeh, Michael Gaudet, Morteza Toloui, Nidal Alshwawreh, QiangDu and all other friends at UBC for their support.

Finally, this thesis is dedicated to the memory of my father. I would also like to thank my mother and sisters for their support throughout my education. I would like to give my special thanks to my wife Garima whose patience, love and encouragement have enabled me to complete this work.

CHAPTER 1 - Introduction

Magnesium is the eighth most abundant element in the earth's crust. It has a hexagonal crystal structure with a c/a ratio of 1.624 and is approximately 37% lighter by volume than aluminum and 78% lighter than iron. Its light weight makes it a potential candidate for automotive and aerospace applications. The significance of weight reduction in structural applications can be realised by comparing the material index (a material design parameter) for bending of beams. The best materials for a light, stiff beam (under specified stiffness, length and square section shape) are those with the largest values of M_b (where M_b is the material index for a beam given as $M_b = E^{1/2}/\rho$, E is the elastic modulus and ρ is the density of the material). The M_b of magnesium is approximately 51% higher than for steel and 17% higher than for aluminum.

The use of magnesium as a structural material has a long history. During World War I, the world production of magnesium was ~3000 tons/year although it was reduced to ~400 tons/year soon after the war. The production picked up again during World War II, but then again dropped immediately after the war. In the 50's and 60's, significant efforts were made to develop magnesium technology. Interestingly, in the decades that followed there was relatively little research on this light metal. Recently, there has been a renewed interest in developing magnesium and its alloys for the transportation and electronic industries, mostly driven by the increasing importance of fuel economy and the need to reduce weight.

Despite a long history and attractive properties, the current applications of magnesium and its alloys are limited. This is often related to their limited room

temperature ductility, highly anisotropic and asymmetric plastic behaviour (i.e. difference between tensile and compressive behaviour), poor crash performance and poor corrosion resistance. The recent demands for light weight structural materials have increased the interest towards improving the performance of existing magnesium alloys and developing new ones. However, one of the factors that limit their application is a lack of knowledge of their deformation behaviour.

The fundamental understanding of yielding and work hardening response for hexagonal metals is much more complex than it is for face-centered cubic (FCC) and body-centered cubic (BCC) metals. This is because, unlike face-centered and body-centered lattices, the hexagonal lattice does not provide enough number of geometrically equivalent slip systems to satisfy the von Mises[1] criterion for polycrystal deformation. To accomplish this, more than one crystallographic slip mode and/or twin mode must be activated.

In general, magnesium exhibits deformation on several crystallographic slip and twin systems. The activation stresses for these are widely different. Because of this, the plastic properties of magnesium are very anisotropic and asymmetric. Further, the relative roles of individual slip and twin modes strongly depend on temperature, loading conditions, alloying, crystallographic texture, and microstructure. Currently, there is a lack of systematic studies where these factors have been examined over a wide range of conditions. Knowledge of the active deformation mechanisms and the variation in their relative contribution as a function of these variables is required for accurately predicting the plastic response and texture evolution of magnesium and its alloys. This is particularly

[1] According to the von Mises criterion, five independent slip systems are needed to accommodate an arbitrary homogenous plastic deformation.

important for the development of reliable material models for use in forming and crash performance. In addition, one can also think of manipulating the mechanical behaviour by controlling the activity of different deformation mechanisms.

The present research work is focussed on understanding the influence of initial texture, stress state, temperature and microstructure on the deformation behaviour of an Mg-8Al-0.5Zn (AZ80) alloy. This alloy is an excellent model alloy as the crystallographic texture and precipitate state can be readily modified. The alloy is also of commercial interest as a casting alloy and potentially as a wrought alloy. This thesis is organised as follows. First, a review of the relevant literature is provided in chapter 2. The scope and objectives of the present research are outlined in chapter 3. Chapter 4 contains a description of experimental and modelling methodologies employed in this study. In chapter 5, the experimental results obtained on strong and weak textured material deformed at 77K and 293K are presented and discussed. To further elucidate the effects of initial texture and temperature on deformation characteristics of the alloy, the viscoplastic self-consistent (VPSC) model has been used as described in chapter 6. The experimental results obtained on aged material are presented and discussed in chapter 7. Finally, chapter 8 contains a summary of experimental and modelling observations, conclusions obtained from this study and suggestions for future work.

CHAPTER 2 - Literature Review

2.1 Introduction

This literature review begins with a brief introduction to the crystallography of hexagonal close packed (HCP) crystals. After that, a general overview of the deformation mechanisms available to HCP metals will be presented. Following this, the characteristics of the slip and twinning modes of magnesium will be described. The current understanding of work hardening in HCP metals, particularly in magnesium, and the hardening effects related to twinning will be reviewed next.

In the present study, the influence of initial texture, low-temperature and microstructure (i.e. aged condition) on deformation behaviour of AZ80 magnesium alloy has been studied. Consequently, it is useful to review the available literature in this area. In this work, the deformation characteristics of magnesium alloy AZ80 are studied using a viscoplastic self-consistent (VPSC) model. Therefore, a brief overview of polycrystal plastic deformation models including VPSC will also be presented.

2.2 The crystallography of HCP metals

A comprehensive review of crystallography in HCP materials has been carried out by Partridge [1]. The primitive hexagonal unit cell (Figure 2.1a) has axes $a_1 = a_2 \neq c$ and corresponding angles $\alpha = \beta = 90°$, $\gamma = 120°$. The symmetry of the hexagonal lattice can be illustrated by the hexagonal prism which can be constructed from three primitive hexagonal unit cells, such as shown in Figure 2.1. In the close-packed hexagonal structure the atoms are stacked in a sequence of ABABAB…, as demonstrated in Figure 2.1b. An

ideal close packing of spherical atoms in this sequence generates a structure that is characterised in terms of lattice dimensions with a c/a ratio of 1.632. Some of the important HCP metals are listed in Table 2.1. None of these metals in their pure form has an ideal c/a ratio, but magnesium and cobalt have a c/a ratio within 1% of the ideal.

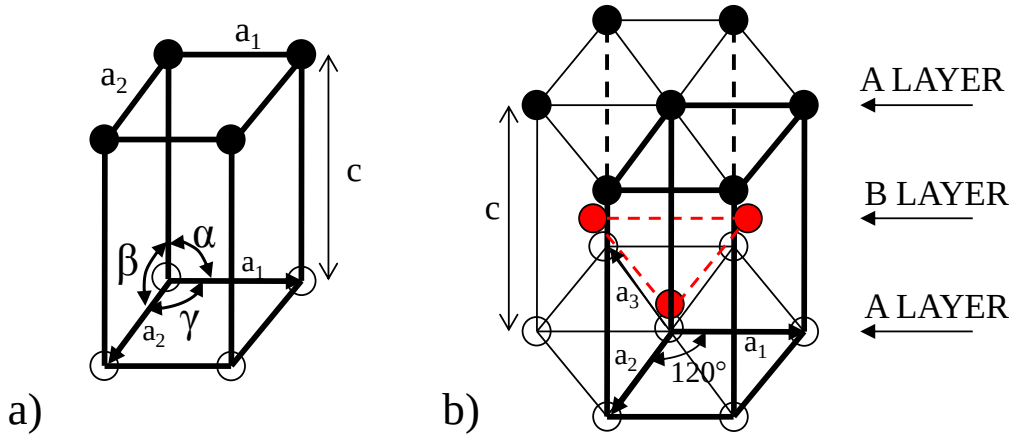

Figure 2.1: a) The primitive hexagonal unit cell illustrating the axes $a_1 = a_2 \neq c$ and corresponding angles $\alpha = \beta = 90°$, $\gamma = 120°$and **b)** the hexagonal close-packed structure. The thick solid lines in b) delineate the primitive hexagonal unit cell.

Table 2.1: Properties of common hexagonal close-packed metals at 300K [2]

Metal	*Be*	*Ti*	*Zr*	*Mg*	*Co*	*Zn*	*Cd*
c/a ratio	1.568	1.587	1.593	1.623	1.628	1.856	1.886
Preferred slip plane	basal (0001)	prism $\{10\bar{1}0\}$	prism $\{10\bar{1}0\}$	basal (0001)	basal (0001)	basal (0001)	basal (0001)

The important crystallographic planes and directions in the hexagonal lattice are illustrated in Figure 2.2. In order to avoid confusion, a four index Miller-Bravais notation has been used throughout the review to identify the crystallographic planes and directions. The important crystallographic formulae for hexagonal lattice are summarised in Appendix A1.

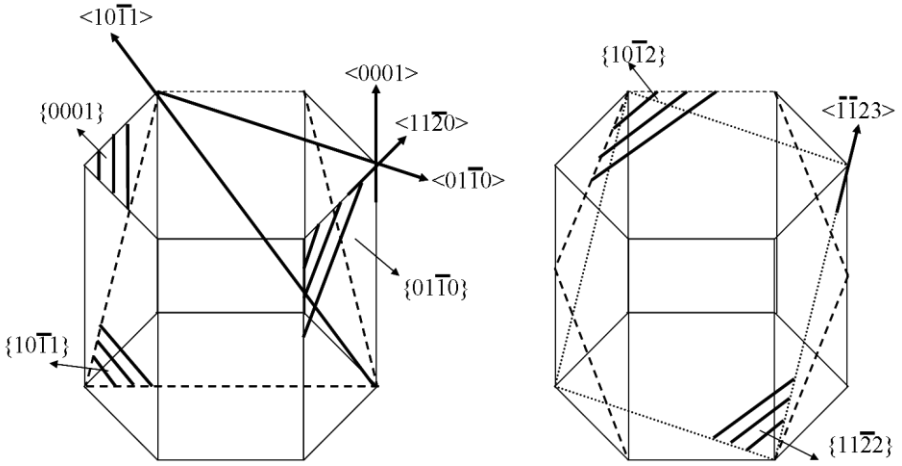

Figure 2.2: Schematic diagram illustrating the important planes and directions in the hexagonal system.

2.3 Deformation modes of HCP metals

According to von Mises [3], five independent slip systems[2] are needed to accommodate an arbitrary homogenous plastic deformation. In FCC metals, the twelve $\{111\}<1\bar{1}0>$ slip systems provide five independent systems and satisfy this condition. However, the situation in HCP metals is much more complex owing to the following

[2] An independent slip system produces a shape change that cannot be obtained by combination of other systems.

reasons. First, the deformation of HCP metals typically involves both slip and twinning, each slip and twinning system having different critical resolved shear stresses. Second, different families of slip systems and twin systems become activated depending on texture, sense of loading, temperature and grain size.

2.3.1 Dislocations in HCP metals

Slip is one of the most important deformation mechanisms in crystalline solids [2]. It involves the motion of dislocations on a specific crystallographic plane along a specific crystallographic direction. Often, slip planes are the close packed planes and slip directions in the slip planes are the close packed directions. The magnitude and the direction of shear displacement on a particular plane is given by the Burgers vector [2]. Figure 2.3 shows the

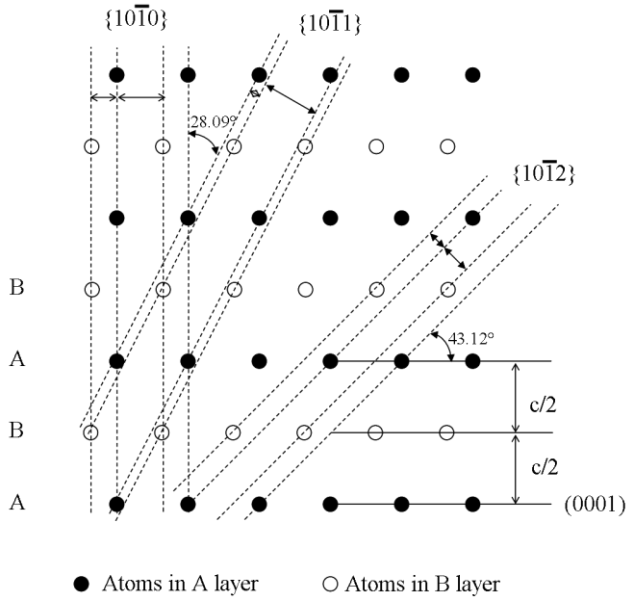

Figure 2.3: Schematic diagram illustrating the interplanar spacings of $(0001), (10\bar{1}2), (10\bar{1}1)$ and $(10\bar{1}0)$ planes in magnesium. Note that the arrows indicate the interplanar spacing, while the dashed lines highlight the non-basal planes.

interplanar spacings of the basal (i.e. (0001)) and non-basal planes (e.g. $\{10\bar{1}0\}, \{10\bar{1}1\}$) in magnesium. The intrinsic lattice resistance to slip is expected to be smaller for planes having the largest interplanar spacings and containing the shortest lattice translation vectors. In magnesium, the (0001) plane exhibits the largest interplanar spacing (i.e. c/2 as indicated in Figure 2.3), it is therefore slip on this plane that is considered to be the easiest among all slip planes. On the other hand, the non-basal planes are more closely spaced and thus slip on these planes is expected to be more difficult.

Similar to the Thompson tetrahedron for face-centred-cubic metals, the bi-pyramid construction for HCP crystals can be used to describe the Burgers vectors of dislocations (Figure 2.4). The important dislocations and their Burgers vectors are summarised in Table 2.2. Notice that among the perfect dislocations listed, only the glide directions with the three $1/3<11\bar{2}0>$ dislocations are coplanar, lying on the close-packed plane (basal plane), and are associated with the shortest Burgers vector. Slip by the $1/3<11\bar{2}0>$ (0001) systems

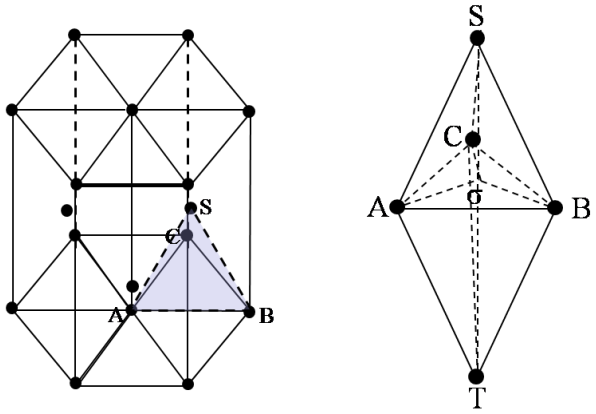

Figure 2.4: Bi-pyramid construction in HCP lattice to describe the Burgers vectors. See Table 2.2 for more description.

Table 2.2: Dislocations in hexagonal close-packed structures [2]. The notation matches that in the bi-pyramid construction of Figure 2.4

Type	*AB* *(perfect)*	*TS* *(perfect)*	*SA/TB* *(perfect)*	*Aσ* *(partial)*	*σS* *(partial)*	*AS* *(partial)*
b	$1/3<11\bar{2}0>$	[0001]	$1/3<11\bar{2}3>$	$1/3<\bar{1}100>$	1/2[0001]	$1/6<\bar{2}203>$
b	a	c	$(c^2+a^2)^{1/2}$	$a/\sqrt{3}$	c/2	$(a^2/3+c^2/4)$
b^2	a^2	$8/3a^2$	$11/3a^2$	$1/3a^2$	$2/3a^2$	a^2
Total No. of dislocations	6	2	12	6	4	12
Possible glide plane	(0001), $\{10\bar{1}0\}$, $\{10\bar{1}1\}$	$\{10\bar{1}0\}$	$\{11\bar{2}2\}$	$\{10\bar{1}n\}$	-	-

in metals such as beryllium, magnesium, cadmium and zinc is similar to $1/2<1\bar{1}0>\{111\}$ slip in FCC metals, in that the critical resolved shear stress (CRSS) is low [2].

Dislocations of <a> type Burgers vectors may dissociate in the basal plane into two low energy Shockley partials dislocations of the type Aσ and σB (Table 2.2, Figure 2.5) separated by an intrinsic stacking fault[3], the reaction is:

$$AB \rightarrow A\sigma + \sigma B \tag{2.1}$$

Or

$$\frac{1}{3}[11\bar{2}0] \rightarrow \frac{1}{3}[10\bar{1}0] + \frac{1}{3}[01\bar{1}0] \tag{2.2}$$

[3] It is the local region in the crystal where the regular atomic sequence has been interrupted.

The stacking fault energy (γ) on the basal plane of magnesium is ≈ 30 mJm^{-2} [1]. This is lower than the stacking fault energy of cubic metals such as pure aluminium (≈ 166 mJm^{-2}) and copper (≈ 78 mJm^{-2}) but it is similar to silver (≈ 25 mJm^{-2}). Nevertheless, the dissociated AB dislocations on the basal plane can cross-slip to any $\{10\bar{1}n\}$ type plane via the constriction of screw segments [1, 2]. In magnesium, there are reports [4-8] that suggest the cross-slip of <a> type dislocations occurs from the basal plane to the prism plane and vice versa. The complete process of cross-slip is illustrated schematically in Figure 2.6. One difference between cross-slip in the HCP and FCC cases is that after cross-slip the glide resistance is different in HCP. For example, in Figure 2.6, prism slip is more difficult than basal slip.

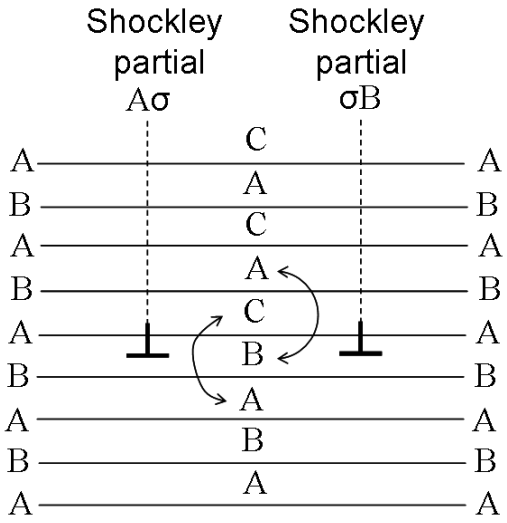

Figure 2.5: Dissociation of a perfect dislocation with Burgers vector AB (Figure 2.4) into two Shockley partial dislocations separated by a stacking fault. Double arrows indicate the two errors in the two-fold stacking sequence of the basal planes.

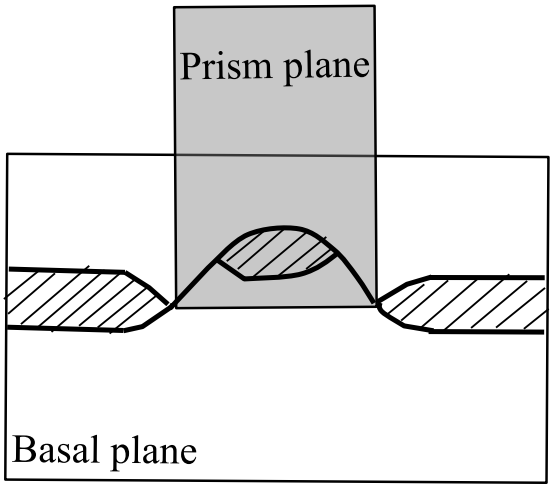

Figure 2.6: Schematic of re-dissociation of a constricted dislocation in the prism plane of magnesium after cross-slip from the basal plane.

2.3.2 Crystallography of twinning in HCP metals

Twinning is another common mechanism of plastic deformation in HCP materials, particularly when straining is carried out at low temperatures or at high speeds. A deformation twin is a region of a crystal that has undergone a homogenous shape deformation in such a way that the resulting structure is identical with that of parent, but oriented differently. Several comprehensive review articles have been published on deformation twinning [1, 9-13]. Figure 2.7 illustrates the change in shape of a sphere of material, the top half having undergone a twinning shear. In this event, there are two material planes that remain undistorted namely, the K_1 (first undistorted plane) and K_2 (second undistorted but rotated plane) planes as indicated in Figure 2.7. The crystallographic shear direction η_1 lies in the first undistorted plane. The second characteristic direction, η_2, lies in K_2 and is perpendicular to the intersection of K_1 and K_2. The magnitude of the twinning shear (S) is given by:

$$S = 2\cot(2\phi) \tag{2.3}$$

where 2ϕ is the angle between K_1 and K_2.

The theoretical tensile strain due to transformation of a single crystal into a twin is [14]:

$$\varepsilon_t = \sqrt{1 + 2S\sin(\phi)\cos(\lambda) + S^2\sin^2\phi} - 1 \tag{2.4}$$

Where ε_t is the tensile strain due to twinning, λ is the angle between the tensile stress axis and the twinning shear direction and ϕ is the angle between the twinning plane normal and the tensile axis. Table 2.3 summarizes the twinning elements, corresponding shears and maximum tensile strains (calculated from (2.4)) that may result from a particular type of twin in most common HCP metals. It can be noticed that the $\{10\bar{1}2\}<10\bar{1}\,\bar{1}>$ twinning system is seen in almost all HCP metals. Further, it should be mentioned that the direction and the magnitude of twinning shear in HCP metals depend on c/a ratios [12]. For instance,

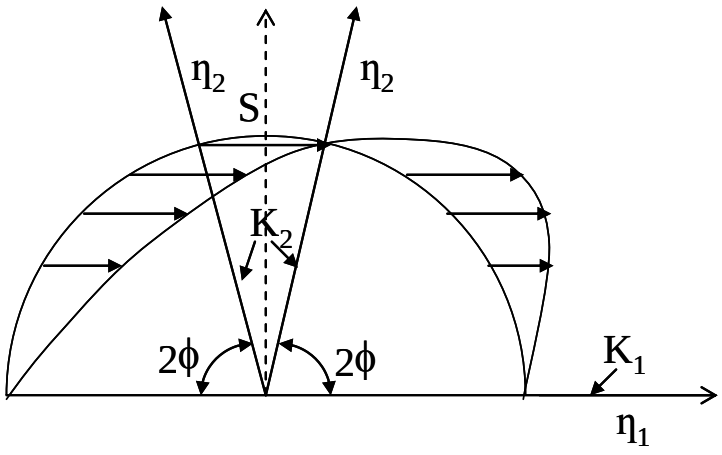

Figure 2.7: Shows the conversion of a sphere into an ellipsoid by the twinning shear η_1 and illustrated the various important twinning elements.

Table 2.3: Twinning elements and maximum tensile strain resulting from various twinning modes in HCP metals [15]

Metal	K_1	η_1	K_2	η_2	*Twinning Shear, S**	*Maximum tensile strain in single crystal*
Mg	$\{10\bar{1}2\}$	$<10\bar{1}\bar{1}>$	$\{\bar{1}012\}$	$<10\bar{1}1>$	+0.131	0.065
Mg	$\{10\bar{1}1\}$	$<10\bar{1}2>$	$\{10\bar{1}\bar{3}\}$	$<30\bar{3}2>$	-0.14	0.07
Ti	$\{10\bar{1}2\}$	$<10\bar{1}\bar{1}>$	$\{\bar{1}012\}$	$<10\bar{1}1>$	+0.18	0.09
Ti	$\{11\bar{2}2\}$	$<11\bar{2}3>$	$(11\bar{2}\bar{4})$	$<22\bar{4}3>$	-0.22	0.11
Be	$\{10\bar{1}2\}$	$<10\bar{1}\bar{1}>$	$\{\bar{1}012\}$	$<10\bar{1}1>$	+0.19	0.095
Zn	$\{10\bar{1}2\}$	$<10\bar{1}\bar{1}>$	$\{\bar{1}012\}$	$<10\bar{1}1>$	-0.14	0.07
Cd	$\{10\bar{1}2\}$	$<10\bar{1}\bar{1}>$	$\{\bar{1}012\}$	$<10\bar{1}1>$	-0.17	0.085
Zr	$\{11\bar{2}1\}$	$<11\bar{2}6>$	(0001)	$<11\bar{2}0>$	+0.63	0.35
Zr	$\{10\bar{1}2\}$	$<10\bar{1}\bar{1}>$	$\{\bar{1}012\}$	$<10\bar{1}1>$	+0.17	0.085
Zr	$\{11\bar{2}2\}$	$<11\bar{2}3>$	$(11\bar{2}\bar{4})$	$<22\bar{4}3>$	-0.23	0.12

* A positive shear causes elongation parallel to the <c> axis

* A negative shear causes contraction along the <c> axis

when c/a $<\sqrt{3}$, the twinning shear direction for $(10\bar{1}2)$ twin lies along $<10\bar{1}\bar{1}>$, but along $<\bar{1}011>$ when c/a $>\sqrt{3}$. Similarly, the dependence of twinning shear (γ) on the c/a ratio due to twinning on the $\{10\bar{1}2\}\ <10\bar{1}\bar{1}>$ twin system is given by [11]:

$$\gamma = \frac{(c/a)^2 - 3}{(c/a)\sqrt{3}} \tag{2.5}$$

2.3.3 Characteristics of twinning in HCP metals

It is generally thought that the process of nucleation of a twin and its subsequent growth can be treated separately. In the literature, two approaches have been considered for the nucleation of twin embryos, homogenous (when a local stress concentration reaches a critical value) [16] and heterogeneous (at a defect site in crystal lattice such as a dislocation) nucleation [17-19]. The heterogeneous nucleation of twins at defects such as grain boundaries are generally considered to be the most common [17-20]. Once nucleated, the lengthening and widening of twins has been described in terms of various dislocation glide-based mechanisms [17, 21-25]. Recent atomistic studies [26-29] on $(\bar{1}012)$ twinning in hexagonal close packed crystals provide further insight in to the atomic-scale processes responsible for twin nucleation and growth.

There are certain microstructural variables such as grain orientation, grain size, grain boundary misorientation and precipitation that can significantly affect the phenomenon of twin nucleation and growth [30-34]. The research group at Los Alamos [33] has been systematically characterizing the deformation twins using large EBSD data sets collected from more than 40 scans of 400 × 600 μm in size to draw correlations between microstructural features and the nucleation and growth of $\{10\bar{1}2\}$ twins in magnesium. The reported results indicate that the twin variant observed is not always the one with the highest Schmid factor[4]. Among the total twins investigated, 47% and 27% of twins had the first highest and the second highest Schmid factor, respectively, and they all were wide. On the other hand, the third and the fourth highest Schmid factor twins (0.125 <

[4] The Schmid factor is given by $\cos\phi\cos\lambda$, where ϕ and λ are the angle of stress axis with the slip plane normal and the slip direction, respectively.

Schmid factor < 0.375) constituted 16% and 8% of the total twins and appeared comparatively thinner. It was also reported that the tendency of twin nucleation leading to adjoining twin pairs increases with the decrease in grain boundary misorientation angle.

Like slip, twinning occurs by the passage of dislocations. However, the twinning dislocations shear material only in one sense and only on their twin planes. In general, deformation twins are known to form at the speed of sound such that their formation in some cases creates audible sound (e.g. “cry of tin”) and in some cases causes the stress-strain curve to be serrated [11, 12]. The reason for the rapid growth is that the stress required to nucleate a twin is presumed to be significantly greater than the stress needed for growth of the twin. As a result, once nucleated, the twin will be driven at high speed by the local over-stress and will continue to propagate until the stress is relaxed or the twin meets an obstacle.

Deformation twins are generally lenticular in shape, meaning that the boundaries between the twinned and untwined regions do not coincide exactly with the twinning plane (K_1). Their central plane is, however, approximately parallel to K_1. The shape of the deformation twins is related to the overall energy change as the twin forms [12]. There are two main contributions to this overall energy change: one is the creation of a new surface involving surface energy and the other is the change in strain energy that results when one portion of material sheared while other does not. The final shape is therefore a result of the balance between the two opposing terms [12].

The relationship between twinning and texture is important in HCP metals. For instance, in Figure 2.8 a stress normal to the basal plane produces equal shear stress

components on all six $\{10\bar{1}2\}$ twinning planes. However, a compressive or tensile stress parallel to (0001) and along $[10\bar{1}0]$, for example, places a larger stress on two planes than on the other four (Figure 2.8). In short, a tensile or compressive stress normal to the basal plane is not equivalent, with regard to the activation of twinning modes, to a compressive or tensile stress applied parallel to the basal plane. Most recently, Park and colleagues [35] have shown this using Schmid analysis.

2.3.4 Summary

In this section, the important characteristics of slip and twin modes has been reviewed in HCP metals. Twinning in particular can contribute significantly to the deformation of these metals. However, it has limited strain accommodation capability and dependence for activation on the sense of applied stress.

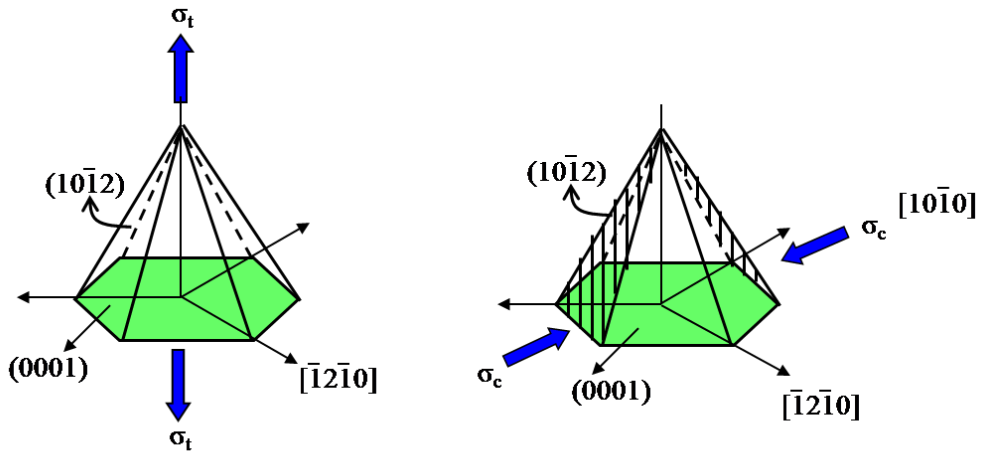

Figure 2.8: Schematic illustrating that a tensile stress normal to the basal plane in a HCP metal is not equivalent in its effect on activating twinning modes to a compressive stress parallel to the basal plane.

2.4 Deformation of magnesium

2.4.1 Slip modes in magnesium

Slip in HCP magnesium has been observed on the following planes: (0001) basal [36, 37], $\{10\bar{1}0\}$ prismatic [38], $\{10\bar{1}1\}$ 1st order pyramidal [39, 40] and $\{11\bar{2}2\}$ 2nd order pyramidal [41-43] (schematically drawn in Figure 2.9). The typical characteristics of each slip mode are listed in Table 2.4. The combination of basal and prism slip (or 1st order pyramidal alone) provides only four independent modes. Moreover, slip in the $<11\bar{2}0>$ direction does not produce strain parallel to the <c> axis. The strain along the <c> axis can be accommodated either by <c+a> slip on the 2nd order pyramidal plane ($\{11\bar{2}2\}$) or by twinning. The 2nd order pyramidal <c+a> slip alone can provide the necessary five independent modes. However, several single crystal studies [38-43] on pure magnesium have reported that the CRSS to activate non-basal slip is significantly higher than that of basal slip, being roughly two orders of magnitude higher than basal slip at ambient-temperature (see Table 2.4).

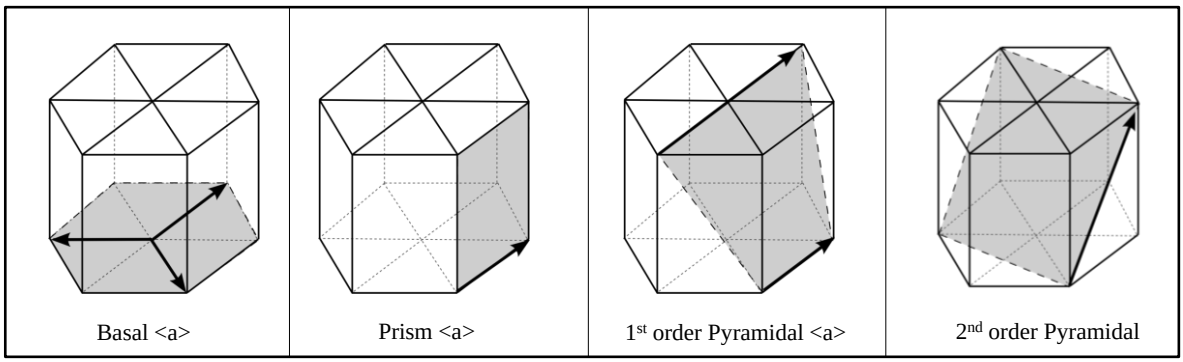

Figure 2.9: Illustrates the basal and non-basal slip systems (both <a> and <c+a> type) in HCP magnesium. The Burgers vector of the dislocation is given by the solid arrow.

Table 2.4: Characteristics of slip modes in magnesium single crystals

Mode	*Plane*	*Direction*	*Crystallographic elements (slip systems)*	*CRSS in MPa at ambient-temperature*	*Number of independent modes*
Basal	(0001)	$<11\bar{2}0>$	(0001) $<11\bar{2}0>$	0.49[36, 37]	2
Prismatic	$\{10\bar{1}0\}$	$<11\bar{2}0>$	$\{10\bar{1}0\}$ $<11\bar{2}0>$	44[1, 38]	2
Pyramidal 1st order	$\{1\bar{1}01\}$	$<11\bar{2}0>$	$\{1\bar{1}01\}$ $<11\bar{2}0>$	-	4
Pyramidal 2nd order <c+a>	$\{11\bar{2}2\}$	$<11\bar{2}\bar{3}>$	$\{11\bar{2}2\}$ $<11\bar{2}\bar{3}>$	10[41], 40[42], 2.3[43]	5

The early work of Hauser and co-workers [44] and more recent work of Keshavarz and Barnett [45] using slip trace analysis has confirmed the importance of non-basal slip at low temperatures. Recent dislocation observations [8, 43, 46, 47] using transmission electron microscopy (TEM) provide further support for non-basal slip. Moreover, in polycrystalline magnesium alloys, it has been argued by Koike and co-workers [46, 47] that the constraints imposed by neighbouring grains helps in reducing the required ratio of CRSS for non-basal to basal slip from approximately 90 to between 2 and 8, thereby making it easier for non-basal slip to occur. A number of researchers [48-50] have also emphasised that the inclusion of non-basal slip (both prismatic <a> type and pyramidal <c+a> type) is essential to simulate the mechanical response of magnesium alloys at ambient temperature.

2.4.2 Twin modes in magnesium

It is well known that active twin types are dependent on the direction of internal twinning stress with respect to the HCP <c> axis of a given grain [1]. For instance, in magnesium, $\{10\bar{1}2\}$ twins are expected when a grain is in tension along the <c> axis, while $\{10\bar{1}1\}$ and $\{10\bar{1}3\}$ twins are expected when a grain is in compression along the <c> axis [1, 51, 52]. Twinning on the $\{10\bar{1}2\}$ plane leads to extension along the <c> axis ("extension twin"), with the basal plane in the twin being reoriented through 85.2° around the $<1\bar{2}10>$ axis as indicated in Figure 2.10a. Comparatively, the effect of $\{10\bar{1}1\}$ twinning is contraction parallel to the <c> axis ("contraction twin"), with the basal plane being reoriented through 57° around the $<1\bar{2}10>$ axis as depicted in Figure 2.10b.

There has been debate in the literature whether twinning can be understood by a CRSS criterion such as Schmid's law or not. Such an approach has been applied to model the deformation behaviour of materials exhibiting twinning [53, 54]. Some reports [35, 55, 56] support the applicability of the CRSS criteria while, others do not [33, 57, 58]. In case of models that apply a CRSS criterion, the CRSS for $\{10\bar{1}2\}$ extension twinning is considered to be 2-3 MPa [59]. Conversely, the CRSS is taken to be 114 MPa for $\{10\bar{1}1\}$ contraction twinning [60].

It has been reported by several authors [47, 61, 62] that extension twins have a different appearance compared to contraction twins. The $\{10\bar{1}2\}$ twins are typically thicker and depart frequently from a common lenticular shape. On the other hand, the $\{10\bar{1}1\}$ contraction twins are typically thin.

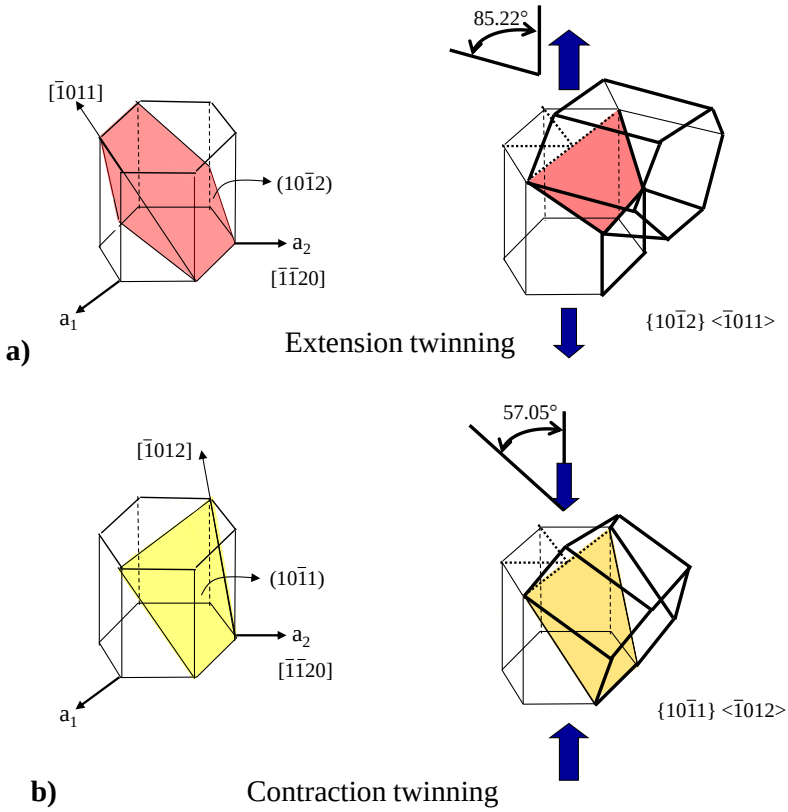

Figure 2.10: Shows schematically the re-orientation of the <c> axis which results from **a)** $\{10\bar{1}2\}$ extension and **b)** $\{10\bar{1}1\}$ contraction twinning in magnesium.

In addition to primary twinning, re-twinning inside a primary twin (double twinning) can also provide an additional mechanism of plasticity. The double twins of $\{10\bar{1}1\}$-$\{10\bar{1}2\}$ and $\{10\bar{1}3\}$-$\{10\bar{1}2\}$ types, typically characterized respectively by 37.5° and 22.3° boundary misorientation around a $<1\bar{2}10>$ axis, have been observed in single crystals [63-65] of certain orientations, and in polycrystals [62, 66]. Most recently, Martin and colleagues [67] have identified all the possible variant specific twin-matrix orientation relationships for these double twins. In the aforementioned double twins, the sequence involved twinning first on either $\{10\bar{1}1\}$ or $\{10\bar{1}3\}$ plane followed by re-twinning on

$\{10\bar{1}2\}$ planes. The reorientation of the basal plane from the primary $\{10\bar{1}1\}$ twinning and from the secondary $\{10\bar{1}2\}$ twinning was illustrated by Hartt and Reed-Hill [65] and more recently by Barnett and co-workers [68]. Hartt and Reed-Hill's schematic diagram is shown in Figure 2.11. It has been suggested by various researchers [64-66, 68] that these double twins are of considerable significance as they could induce localised softening due to the favourable alignment of basal poles (approximately 37° to the loading axis) for basal dislocation slip in the double twinned volume. Eventually, this could also lead to fracture in the material.

In addition, detwinning may occur in magnesium alloys during unloading or strain path changes. Detwinning is a contraction of a twinned region, a process that does not require nucleation [69]. During detwinning, the existing twins can disappear or become narrower under reverse loading or unloading. There are several recent investigations [70-72] in magnesium alloys that have emphasised the importance of detwinning.

2.4.3 Summary

The literature reviewed in this section indicates that basal slip has the lowest CRSS of all slip modes in magnesium. Comparatively, slip on prismatic and pyramidal slip systems is more difficult owing to higher CRSS values. Twinning on $\{10\bar{1}2\}$ and $\{10\bar{1}1\}$ planes provides strain parallel to the <c> axis, the former supplies the extension along the <c> axis while, the latter provides the compression along the <c> axis. Double twinning of type $\{10\bar{1}1\}-\{10\bar{1}2\}$ and detwinning of $\{10\bar{1}2\}$ twins under reverse loading are also commonly reported in magnesium.

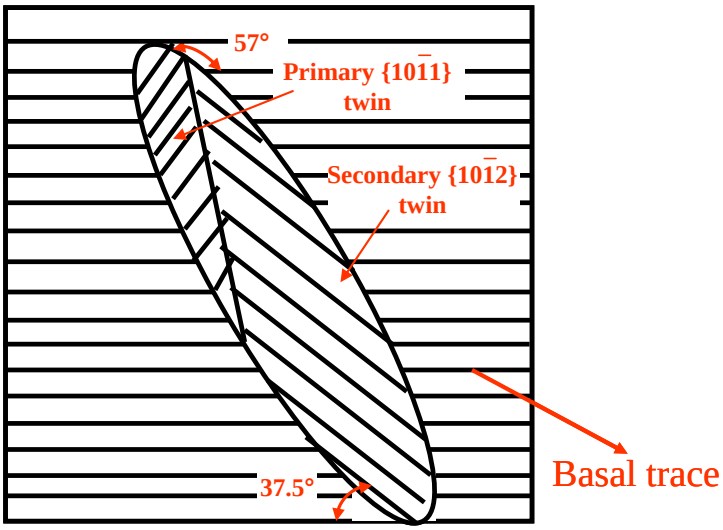

Figure 2.11: Schematic of a $\{10\bar{1}1\}$-$\{10\bar{1}2\}$ double twin based on Hartt and Reed-Hill's [65] analysis of a replica taken from a single crystal. The crosshatched lines correspond to basal plane traces and the image zone axis is a $<1\bar{2}10>$.

2.5 Work hardening in HCP crystals

2.5.1 A general overview on work hardening

The work hardening of hexagonal close packed materials is much more complex than it is for cubic metals [73, 74]. For instance, as compared to cubic metals, the hexagonal lattice does not provide a sufficient number of crystallographically equivalent slip systems to satisfy the von Mises criteria [3] for polycrystal deformation. In order to achieve at least five geometrically independent systems, more than one crystallographic slip mode must be activated and the CRSS value of the difficult slip modes in magnesium (e.g. prism slip, pyramidal slip) varies considerably (see Table 2.4). Moreover, the situation

becomes increasingly complicated when twinning enters as an additional mode of deformation (see section 2.5.2 for more details).

The behaviour of an unconstrained hexagonal single crystal may resemble that of a FCC crystal [75]. However, the difference between FCC and HCP polycrystals is very strong due to the constraints between the neighbouring grains. Here the hard modes must also be activated, and these dominate the macroscopic behaviour [73]. It has been reported by a number of researchers [61, 76, 77] that the work hardening rates exhibited by magnesium and its alloys are very high (e.g. the hardening rate (θ) normalised by the shear modulus (μ) ~ 0.2-0.3), i.e. much higher than one would expect in FCC or BCC metals [73, 74] where the maximum hardening rate in single phase materials would be θ/μ ~ 0.05-0.1.

Agnew and co-workers [78] have measured the internal strains in magnesium alloys using in situ neutron diffraction. They found that magnesium exhibits a prolonged elastic plastic transition, similar to composite materials, up to as high as 10% macroscopic strain. They have reported continuous rapid accumulation of elastic lattice strains even at the highest applied stresses. According to Agnew et al. [78] the strain hardening rate would then be determined through load sharing between the elastic, hard oriented, and the plastic, soft oriented grains.

Work hardening behaviour has also been found to depend on alloying additions. For example, Cáceres and Rovera [79] have studied the solid solution effects on Mg-Al alloys with Al contents ranging from 1 to 8 wt%. Their results suggest that the more concentrated alloys exhibit higher hardening rates. They attributed this to an increased

contribution from forest hardening to the strength of materials with the concentration of solute.

Originally, Cáceres and Blake [80] and later Cáceres et al. [81] studied the work hardening behaviour of randomly oriented and strongly textured polycrystals of pure magnesium deformed in tension or compression at room temperature. They indicated that the overall behaviour of pure magnesium closely resembles that of FCC polycrystals. Strain hardening by the accumulation of forest dislocations was considered to be the chief hardening mechanism. There is a need for caution with this interpretation owing to the much more complex interaction of deformation modes in HCP metals compared to cubic metals.

2.5.2 Hardening effects related to twinning

To understand the plastic deformation and work hardening behaviour of magnesium, the role of deformation twinning should be carefully considered. Twinning activity, in particular, has three main effects: i**)** a geometric effect in which crystallographic re-orientation resulting from twinning could either place the twinned crystal in a "hard" orientation or in a "soft" orientation, ii**)** a Hall-Petch[5] type effect in which twinning introduces additional barriers to dislocation motion inside and around twins, and iii**)** a Basinski effect in which twinning transforms the glissile dislocations into sessile dislocations. For a reliable constitutive description of plastic deformation of HCP metals it is essential to consider these three factors.

[5] The Hall-Petch (H-P) relation is the relationship between yield stress σ_y and the average grain size *d* of material, $\sigma_y = \sigma_i + kd^{-1/2}$ where, σ_i is the lattice friction stress and k is a H-P constant.

2.5.2.1 The geometric effect

A number of authors [61, 76, 82, 99] have emphasised the importance of crystallographic re-orientation due to twinning in determining the work hardening characteristics of magnesium alloys. It has been widely reported [61, 76, 82, 99] that the in-plane compression of magnesium sheets exhibit a distinct stress strain response, marked by very high hardening rates, as illustrated by the "S" shape curve in Figure 2.12. The explanation offered to this type of stress strain curve is that $\{10\bar{1}2\}$ twinning starts quite early in the deformation leading to a regime of low hardening up to the point where twinning becomes exhausted (~ up to 5-6% strain). Once most twinning finishes, the stress rises rapidly. The high hardening rate arises from the fact that the $\{10\bar{1}2\}$ twinning reorients the original grain by ~85°. Consequently, the twinned portion of the grain is in a hard orientation for subsequent slip and/or twinning.

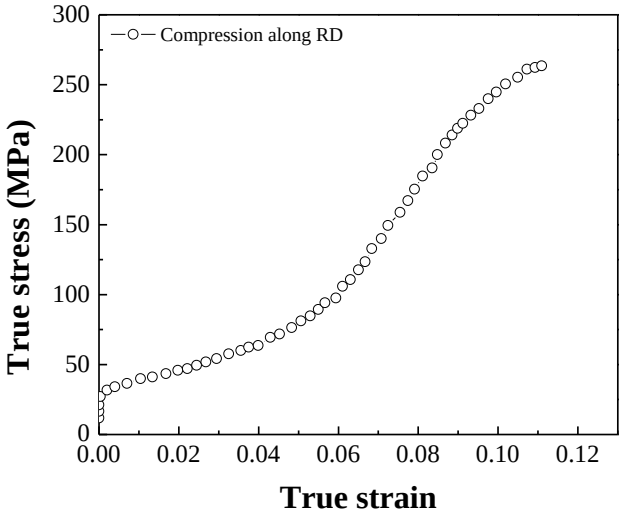

Figure 2.12: True stress vs. true strain curve for sample subjected to plane-strain compression with <c> axis extension, adapted from reference [99].

2.5.2.2 The Hall-Petch type effect

Salem et al. [83] have studied the strain hardening response of HCP α-titanium in compression. The results suggest an increase in the strain hardening rate after an initial drop at small strain. This was attributed to deformation twinning. Deformation twins appear to reduce the effective slip distance and increase the strain hardening rate via a Hall-Petch type mechanism [84].

The effectiveness of twin boundaries in blocking slip dislocations depends on slip-twin interaction. Yoo [85, 86] has analyzed the possible slip-twin interaction in HCP metals from crystallographic and energetic points of view and concluded that the $\{10\bar{1}2\}$ twins in magnesium are repulsive twins (acting as a barrier to dislocation glide) while, the $\{10\bar{1}1\}$ twins are attractive twins. The repulsive interaction between basal or prismatic dislocations and $\{10\bar{1}2\}$ twins would develop local stress concentration due to a dislocation pileup at the interface. Recently, Koike et al. [46] have explained the observed recovered regions in the microstructure of a 16 % - elongated AZ31 sample based on slip–twin interaction. The $\{10\bar{1}1\}$ twins in the deformed matrix were found to absorb dislocations by dissociating them and forming interface ledges (consistent with Yoo [85, 86]). According to Koike et al. [46], the $\{10\bar{1}1\}$ twins in magnesium alloys can contribute to dynamic recovery at ambient temperature.

2.5.2.3 The Basinski effect

Crystallographic reorientation due to twinning can transform originally glissile dislocations into sessile dislocations. Consequently, the material within the twinned domain would be harder than the untwinned regions. This effect is also known as the “Basinski

effect" as it was first proposed by Basinski et al. [87]. A maximum of 20% increase in yield stress via this mechanism have been reported in Hadfield steels [88] and titanium [89]. In the past, several researchers [61, 90, 91] have invoked this mechanism in magnesium but with little experimental proof. It should be noticed that $\{10\bar{1}2\}$ twinning in magnesium nearly flips the basal plane into the prismatic plane and vice versa, implying that basal dislocations will lie close to hard prism planes whereas prism dislocations will lie nearly on soft basal planes. Nonetheless, there is a need for careful examination to probe the significance of this mechanism for magnesium alloys.

2.5.3 Summary

In general, the work hardening response of HCP polycrystals is a result of the complex nature of slip and twinning behavior and their strong dependence to external (temperature, strain rate) and internal parameters (alloying, microstructure and texture). Twinning in particular can have significant effect on the hardening behaviour of these metals.

2.6 Influence of orientation on deformation behaviour of magnesium alloys

2.6.1 Single crystals

Plastic deformation of HCP materials such as magnesium is strongly affected by the relationship between the loading axis and the crystallographic orientation. The early work of Schmid and Boas [92] showed, particularly for HCP metals, that the tensile yield stress varied greatly with orientation. For example, the tensile yield stress can be written as

the ratio of resolved shear stress (τ) and Schmid factor ($\cos\phi\cos\lambda$, where ϕ and λ are the angle of stress axis with the slip plane normal and the slip direction, respectively) i.e. $\sigma = \tau/\cos\phi\cos\lambda$, also known as Schmid's law. It is implicit in the relationship that the applied tensile stress will vary between wide limits for different crystals at the same stage of deformation [93]. An illustration of the significant variation in tensile yield stress as a function of inclination of the <c> axis for different slip systems and the $\{10\bar{1}2\}$ twinning system is given in Figure 2.13. This figure is recreated from the work of Barnett and co-workers [94]. The curves were plotted by assuming the CRSS ratios for basal to prismatic slip, basal to pyramidal <c+a> slip and basal to extension twinning as 1:2, 1:15 and 1:0.7, respectively. Notice that with the change in the orientation of the crystal the relative importance of each mode can vary substantially.

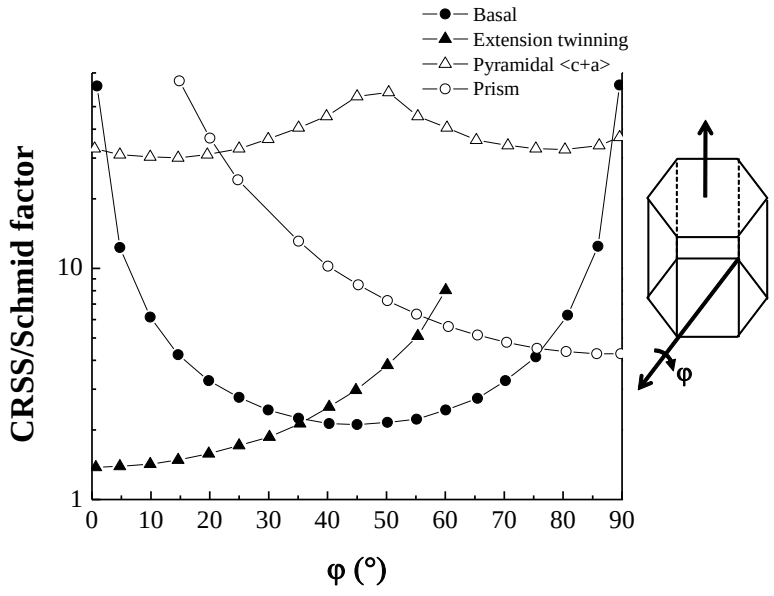

Figure 2.13: Schmid factor normalised CRSS values plotted as a function of the inclination of c axis to the imposed stress (for tension), adapted from reference [94].

The plastic properties of magnesium single crystals have been studied in detail [52, 63-65, 95, 96] during the 1950's and 60's with extensive application of slip trace analysis and constrained deformation experiments. The main conclusion of these studies was that magnesium possesses two easy deformation modes at room temperature: slip on the (0001) basal plane along $<1\bar{2}10>$ close packed directions and twinning on $\{10\bar{1}2\}$ planes. Moreover, the stress-strain response is influenced by the orientation of the crystal relative to the loading axis prior to deformation. As can be seen from work of Kelly and Hosford [96]. They studied the deformation behaviour of pure magnesium single crystals in plane strain deformation experiment by varying the crystal orientations as shown in Figure 2.14.

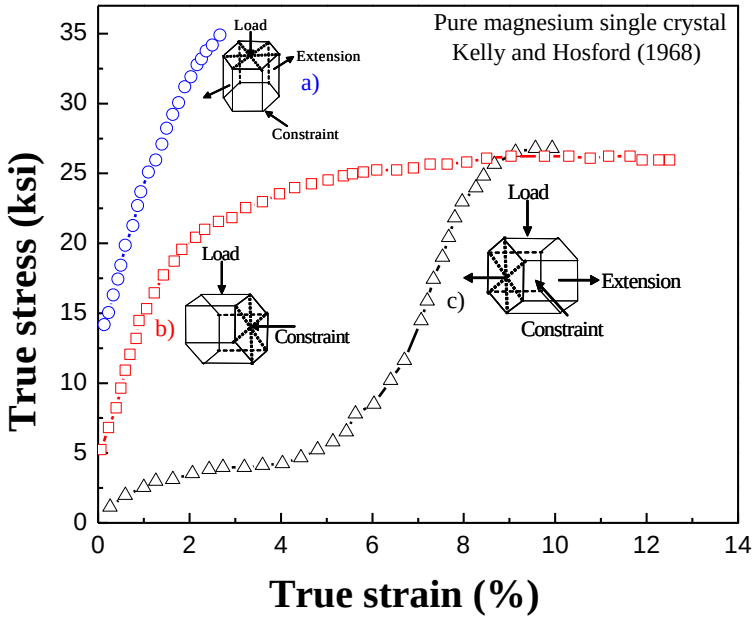

Figure 2.14: True stress vs. true strain response of pure magnesium single crystals loaded in orientation most favourably oriented for **a)** <c+a> slip **b)** prismatic slip and **c)** $\{10\bar{1}2\}$ extension twinning. The inset drawing illustrates the orientation of loading axis and constrained direction in the hexagonal crystal. The figure is adapted from reference [96].

2.6.2 Polycrystal

In general, wrought polycrystalline aggregates show strong crystallographic texture (preferred orientation) which results in a strong anisotropy in mechanical behaviour. Sheet magnesium alloys possess “basal texture” where the basal plane is predominately aligned parallel to the rolling plane ($\pm 20°$ tilt towards rolling direction) [97]. Such texture is known to influence several aspects of the material, in particular the yielding and work hardening characteristics. Kelly and Hosford [98] studied the deformation behaviour of strongly textured polycrystalline magnesium in plane strain compression, similar to their single crystal study on pure magnesium. They found that the stress strain curves are similar in their general form of asymmetry to those obtained on single crystals (see Figure 2.14) and can be interpreted in terms of deformation modes observed in single crystals.

The early work of Kelly and Hosford [98] also showed the yield loci for textured pure magnesium sheet as shown in Figure 2.15. It is interesting to notice the shape and size of yield loci at different strain levels. The strength in compression is lower than in tension and it was attributed to the easy activation of $\{10\bar{1}2\}$ twinning in compression but not in tension. The yield loci at 5% strain shows asymmetry similar to that of the locus at 1% strain, while the yield locus at 10% strain, exhibits comparable strength in all the quadrants. This is consistent with completion of twinning at about 6% strain. For an accurate description of yield loci of magnesium, it is imperative to take into account some key sources of anisotropy: slip and/or twinning activity and texture development during deformation.

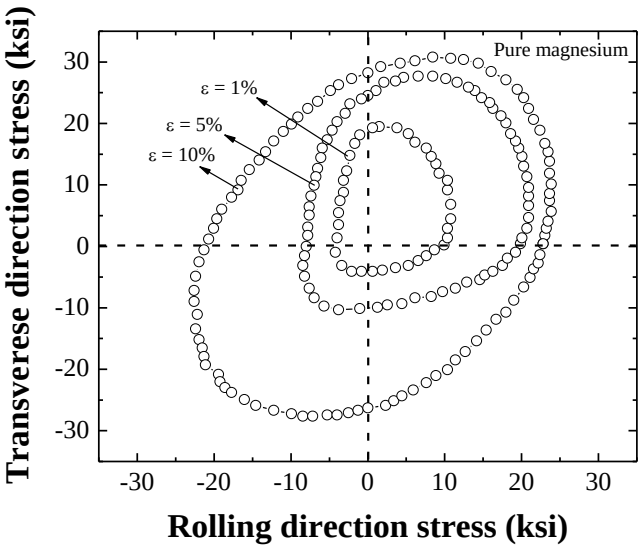

Figure 2.15: Yield loci for textured pure magnesium at 1%, 5% and 10% strain. The plotted loci are fit to limited data of uniaxial tension, uniaxial compression and plane strain compression experiments. The figure is adapted from reference [98].

Barnett et al. [99] have repeated Kelly and Hosford's [98] deformation experiments in selected orientations. Their results were consistent with those of Kelly and Hosford [98]. Similar studies have been carried out by various other researchers [100, 101] on pure magnesium and AZ31 magnesium alloys at high temperature.

Agnew et al. [8] did a systematic study on the plastic anisotropy in wrought magnesium alloy AZ31 by conducting tensile tests on variously oriented samples (e.g. parallel to rolling direction, 45° to rolling direction) at a range of temperatures (room-temperature – 250 °C) and strain rates (10^{-5}- 0.1 s^{-1}). Their results suggest that the strong in plane anisotropy at low temperatures can be attributed to the initial crystallographic texture and greater than anticipated non-basal prismatic slip of $<11\bar{2}0>$ type Burgers vectors.

2.6.3 Summary

The work reviewed in this section highlights that the relative contribution of various deformation mechanisms (slip and twin modes) depends strongly on the specific loading condition and the initial texture. Indeed, this is a key source of asymmetric behaviour and anisotropy exhibited by magnesium single crystals and polycrystals in different loading conditions. It is essential to consider the role of crystallographic texture in determining the yielding and hardening response of magnesium alloy.

2.7 Effects of low homologous temperature on the deformation response of magnesium alloys

In this review, the term low-temperature is used to correspond to deformation at homologous temperatures[6] of $\leq 0.33T_m$ (where T_m is the melting temperature). Over the last decade or so, there have been numerous experimental and modelling studies [89, 102-110] focusing on investigating the low-temperature mechanical behaviour of HCP metals. While many studies have centered on Zr, Be, Hf and Ti, few studies have systematically examined the effects of low-temperature on the mechanical response of magnesium alloys.

Figure 2.16 shows the temperature dependence of CRSS values for various slip systems in pure magnesium determined from single crystal experiments taken from the literature [36, 37, 43, 111]. It can be seen that basal slip is only slightly temperature dependant whereas there is strong temperature dependence for the non-basal activity. For instance, prismatic <a> slip and pyramidal <c+a> slip are two times and three times more

[6] Homologous temperature expresses the temperature of a material as a fraction of its melting point using the Kelvin scale.

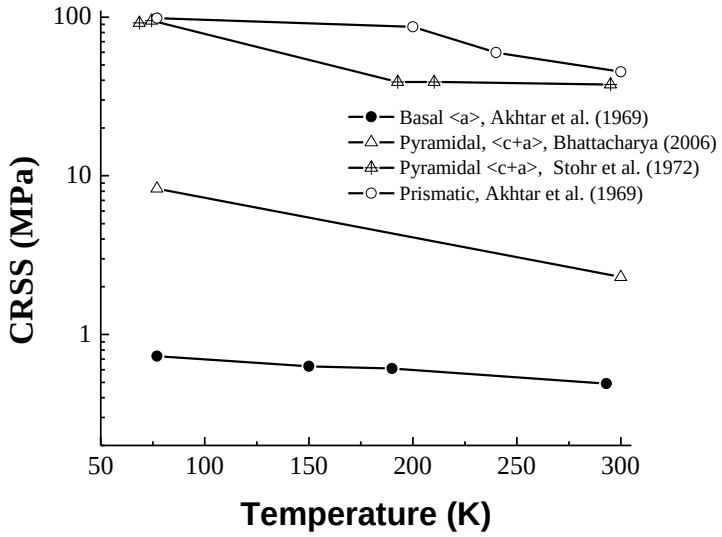

Figure 2.16: The temperature dependence of CRSS for various slip systems in pure magnesium.

difficult, respectively at 77K than at 293K. It should also be noticed that there is apparent discrepancy in single crystal data for <c+a> slip. The values reported by Bhattacharya [43] are approximately 10-15 times lower than the values reported by Stohr et al. [111]. The noted discrepancy was primarily ascribed to the quality of the single crystals. According to Bhattacharya [43], their lower CRSS values can be related to better single crystal quality. This suggests that alloying may play an important role in determining the CRSS.

The earliest work in polycrystalline magnesium was performed by Hauser et al. [112]. They investigated the deformation mechanisms in extruded pure Mg sheets under uniaxial tension at 78-298K. The samples had a basal texture parallel to the sheet plane. The results indicated that basal (<11 $\bar{2}$ 0> type) and prismatic (<11 $\bar{2}$ 0> type) slip occurred frequently at and below room temperature at stress concentration sites such as grain

boundaries. The ease of prismatic slip was attributed to the localized inhomogeneous stress caused by constraints imposed on a grain by its neighbours [112].

Hauser and colleagues [112] also qualitatively studied the incidence of $\{10\bar{1}2\}$ extension twinning in magnesium at 78K, 195K, 273K and 298K. They reported that the number of twins was not altered by lowering the test temperature. This conclusion is somewhat surprising as they had loaded the specimens in tension normal to the <c> axes which is unfavourable for $\{10\bar{1}2\}$ twinning.

Ando and colleagues [113] studied the deformation behaviour of magnesium single crystals in tension along a $<11\bar{2}0>$ direction at low temperature. Their results suggest that the crystal deformed primarily by 2nd order pyramidal <c+a> slip in the temperature range of 77K-293K.

More recently, Bhattacharya [43] has studied the tensile behaviour of polycrystalline pure magnesium in the temperature range of 4.2-300K. The main conclusion of his study was that magnesium exhibits anomalous yield stress and flow stress behaviour at low temperatures. Both the yield stress and the flow stress were found to be lower at 4.2K than at 77K. This behaviour was ascribed to the temperature dependence of <c+a> slip activity. According to Bhattacharya [43], the glide due to <c+a> slip is more favourable at 4.2K than at 77K because at higher temperature thermal activation dissociates the <c+a> dislocation into a glissile, <a> type dislocation on the basal plane, and a sessile, <c> type of dislocation on the prism plane. The glide of such dissociated dislocation becomes difficult due to sessile nature of the component <c> dislocation.

2.7.1 Summary

In HCP metals, the relative importance of various slip and twin modes can vary substantially with the change in test temperature and potentially alloy additions. In relation to this many detailed experimental and simulation studies are available on metals like Zr, Be, however, little is explored for magnesium alloys. Based on the limited single crystals and polycrystal studies on magnesium, it is realised that the significance of slip and twin modes can vary at low temperatures.

2.8 Precipitation and its influence on the deformation behaviour of magnesium alloys

2.8.1 Precipitation in Mg-Al alloys

Figure 2.17 shows the Mg rich portion of the Mg-Al binary equilibrium phase diagram. The maximum equilibrium solid solubility of aluminum in magnesium is 11.5 wt% at the eutectic temperature of 432°C, which decreases with decreasing temperature (e.g. at 200°C equilibrium concentration - 2.9 wt% Al). When the aluminum content exceeds the solubility limit in magnesium, the incoherent equilibrium β-$Mg_{17}Al_{12}$ precipitates (BCC structure) forms. Compared with the phases present in binary Mg-Al alloys, no new phases occur in ternary Mg-Al-Zn alloys if the Al:Zn ratio $\geq$ 3:1 [115, 116]. The β phase ($Mg_{17}Al_{12}$) has been thoroughly studied [115-121] and two distinct, competitive modes of precipitation have been identified.

The nucleation and growth of isolated precipitates in the parent HCP matrix is referred to as continuous precipitation. Continuous precipitates are of lath shape on the

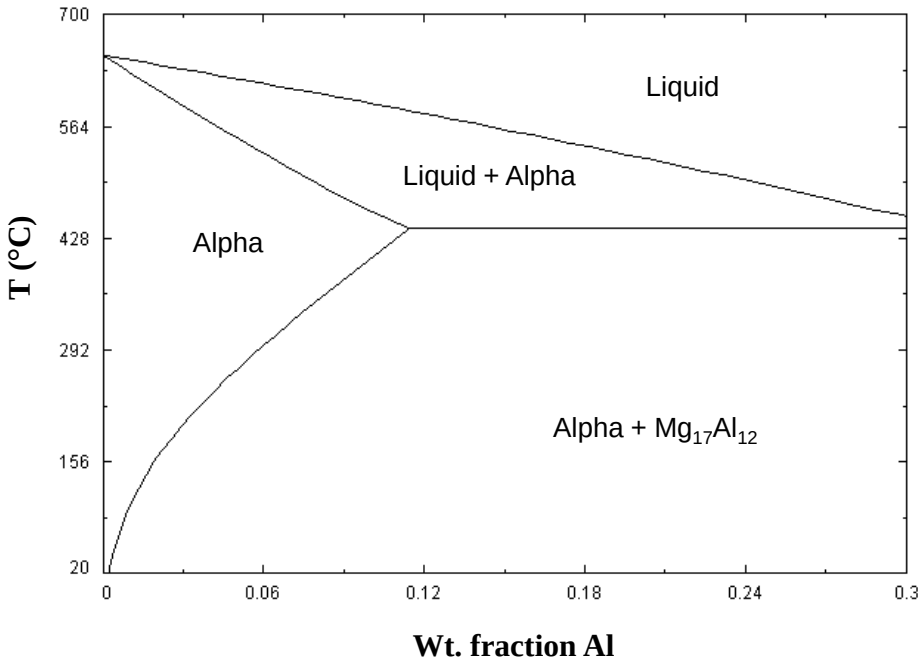

Figure 2.17: Magnesium rich portion of Mg-Al binary equilibrium phase diagram [114].

basal plane of magnesium solid solution matrix. The precipitate morphology and orientation relationship with the matrix has been studied by various researchers [115-123]. Table 2.5 briefly summarizes the shape, size and orientation of continuous precipitates in the Mg-Al-Zn system. It should be noted that the majority of these precipitates are relatively large as the length of precipitates is approximately 1-2 μm (compared, e.g. to the strengthening precipitates in aluminum alloys). The inter-particle spacing are also large, at approximately 0.2-2 μm [115-123].

Unlike continuous precipitation, discontinuous precipitates appear as alternating lamellae of solute depleted HCP phases and precipitate phases ($Mg_{17}Al_{12}$) that form behind an advancing high angle grain boundary. Table 2.5 briefly compares the morphology and orientation relationship of discontinuous precipitates to continuous precipitates.

Table 2.5: Illustrates the details of common precipitate type in the Mg-Al-Zn system. L, W and T correspond to length, width and thickness of precipitates, respectively

Precipitate type	*Orientation relationship**	*Shape*	*Size (μm)*	*Comments*
Continuous	$(0001)_m \parallel (110)_p$ $[11\bar{2}0]_m \parallel [111]_p$	Lath shape, (rare) spherical	L = 1-2 W = 0.2-0.3 T = 0.01-0.02	Formed by volume diffusion and dominates at most temperatures
Discontinuous	Crystallographic relationship with matrix is less stringent	Single seam, double seam, lamellar aggregates	-	Formed by grain boundary diffusion

* The subscript m and p correspond to matrix and particle, respectively.

2.8.2 Influence of precipitation on slip and twinning behaviour

2.8.2.1 Deformation of single crystals

In 1963, Byrne [124] studied the plastic deformation of Mg-1.24Mn alloy single crystals. The aging treatment in this alloy generates precipitate ribbons of α-Mn type normal to the basal plane. The alloy single crystals were tested in both the solution treated and the aged condition. In the solution treated condition, an increase in CRSS of five times that of pure magnesium has been reported and primarily ascribed to the clustering of the solute atoms given the 42% difference in atomic radii between Mg and Mn. On the other hand, the CRSS value increased by a factor of two going from the solution treated state to the aged condition. This increase was attributed to the solid solution in equilibrium with the

precipitates. It was also reported that the α-Mn precipitates are incapable of inhibiting twinning.

In the late 1960's, Chun and Byrne [125] studied the precipitate strengthening mechanisms in Mg-5.1wt% Zn alloy single crystals favourably oriented for basal slip. They found that the crystals in the quenched and aged state exhibit CRSS values of approximately 10 times and 40 times that of pure magnesium, respectively. In another study from the same group [126], Mg-5.1wt% Zn single crystal was tested in an orientation favourable for twinning such that the tensile axis was placed along the [0001] direction. They found that controlled precipitation can be extremely effective in inhibiting the twinning and increasing the strain to failure.

2.8.2.2 Deformation of polycrystals

There are a limited number of studies that examine deformation mechanisms in the presence of precipitates. In 1970, Eckelmeyer and Hertzberg [127] reported that low asymmetry in the tension-compression behaviour can be achieved in wrought Mg-9wt% Y alloy and that this can be attributed to a reduction in the $\{10\bar{1}2\}$ twinning activity.

Clark [128] has studied age hardening mechanisms in a Mg-5wt%Zn alloy using transmission electron microscopy (TEM). He suggested that basal slip and $\{10\bar{1}2\}$ twinning are the principal modes of deformation in aged Mg-Zn alloys. Moreover, the slip dislocations were found to be bowed between MgZn′ rods (the precipitate rods were aligned normal to the basal plane) while, twinning tends to shear the hardening precipitate, resulting in a re-orientation of MgZn′ rods. Most recently, Stanford and Barnett [129] have studied the deformation behaviour of a binary Mg-Zn alloy using a combination of

experimental and modelling (VPSC) techniques. Their observations in TEM suggest that the precipitates are not sheared by the twinning activity in contradiction with the earlier observations by Clark [128]. They reported that the presence of particles would tend to increase the number density of twins, reduce the twin size and decrease the total twin volume fraction. In addition, their VPSC modelling results inferred that the prismatic planes are hardened more by precipitation than the basal slip.

To the author's knowledge, there are only two studies in high aluminum bearing AZ series magnesium alloy that examine the effect of precipitates on deformation behaviour. The seminal work by Clark [117] represents an early attempt at studying the deformation mechanism in polycrystalline Mg-9wt%Al alloy by subjecting samples to uniaxial compression. The solution treated material undergoes deformation by basal slip and $\{10\bar{1}2\}$ twinning, whereas precipitate-containing material shows non-basal prismatic slip ($<11\bar{2}0>$ type) along with basal slip. The enhanced non-basal slip and suppression of dominant $\{10\bar{1}2\}$-twinning was attributed to the presence of precipitates. However, the exact mechanism by which precipitates suppress twin formation and enhance non-basal slip was not clear. Nevertheless, suppression of dominant $\{10\bar{1}2\}$-twinning and increase in activity of non-basal slip by precipitation rather than by a matrix orientation effect is interesting.

More recently, Gharghouri and co-workers [130] examined the nature of interaction between the precipitates and the twins in aged binary Mg-7.7at%Al alloy using TEM. They found that the nature of interaction depends on the relative thickness of the

twin and the precipitate ($Mg_{17}Al_{12}$). Twins were found to engulf the precipitates, impinge upon precipitates and bypass the precipitates without shearing the precipitates.

2.8.3 Influence of precipitation on work hardening behaviour

The process of strain hardening arising from the presence of undeformable particles is briefly considered here. Plastic deformation of a material containing hard non deformable particles produces internal stresses that must be exceeded before further deformation can occur [131-134]. The difference in elastic and plastic properties of the phases produces elastic and plastic incompatibilities, which in turn produce internal stresses [135-137]. Brown and Clarke [133, 134] have calculated this mean back stress for a number of particle geometries (e.g. ribbons, discs, fibres) using Eshelby's inclusion method. They showed the mean back stress in the matrix due to particles is given by:

$$\sigma_P = 4\phi\gamma\mu f\varepsilon \tag{2.6}$$

where $\phi = \dfrac{\mu_P}{(\mu_P - \gamma(\mu_P - \mu))}$, γ is an accommodation factor (for disc-shaped particles $\gamma = 1/(2(1-\nu))$, where ν is the Poisson's ratio), μ_P and μ are the shear modulus of the particle and matrix, respectively, f is the volume fraction of particles and ε is the unrelaxed plastic strain. It should be noted that the back stress term linearly increases with the applied strain provided there is no plastic relaxation.

Gharghouri and colleagues [55] have applied this approach to understanding the hardening response of a binary Mg-7.7at%Al alloy. In order to recognize the role of second phase $Mg_{17}Al_{12}$ during deformation of the alloy, they measured the mechanical properties

of a single crystal of β phase $Mg_{17}Al_{12}$. The reported elastic modulus and yield strength was approximately 80 GPa and 1 GPa respectively, which is significantly different from the parent HCP matrix (modulus for magnesium 45 GPa). They showed in the absence of plastic relaxation (i.e. at low strains) around particles, the above expression can reasonably predict the hardening response of the alloy. In addition, Cáceres and co-workers [138] successfully applied equation (2.6) to estimate the maximum stress due to particles in their sand cast and high pressure die cast Mg-9Al-1Zn (AZ91) magnesium alloy.

2.8.4 Summary

It is clear from the work reviewed above that precipitation can have a significant effect on deformation response of magnesium alloys. Some types of precipitation can considerably change the slip and twinning characteristics of the alloy. Moreover, the work hardening response can also vary substantially due to precipitates. In the aged magnesium alloys, the interaction of precipitates with slip and twinning is complex and relatively poorly understood.

2.9 Modelling the polycrystal plastic deformation behaviour of HCP metals

There are many reasons why it is desirable to develop robust models for prediction of deformation and texture: i) the cost of experiments compared to simulations are very high, ii) one can generate wealth of additional information, iii) underlying mechanisms and physics can be better understood and iv) one can test various hypotheses.

2.9.1 Polycrystal plastic deformation models

The prediction of polycrystal plastic deformation behaviour from the response of their single crystal constitutes has been the subject of interest for almost eight decades now (since Sachs 1928 [139] and Taylor 1938 [140]). The biggest challenge to this is to mathematically solve a problem that includes interaction among the grains. To tackle such situation, models based on the averaging/homogenization methods in which the overall quantities are represented as some proper average of their local counterparts have been developed [139-144].

Within an HCP polycrystal, the individual grains split up into groups of hard and soft grains. The partition of plastic strain can thus be quite different between these groups. The well known Taylor model [140, 141] under such situations may not be adequate as it assumes the local grain level strains are identical to the overall macroscopic one. The crystal plasticity finite element (CPFEM) [145-147] and self-consistent viscoplastic models [148-151] have been developed to handle these cases. In CPFEM models, local heterogeneity can be taken into account by discretizing the grains into many elements. A disadvantage of this approach is that it requires long computation times to deal with even a relatively small number of grains.

Another approach is viscoplastic self-consistent (VPSC) models in which each grain is assumed to be an ellipsoidal inclusion embedded in an infinite homogenous effective medium (HEM) whose properties coincide with the average properties of the polycrystal, as shown in Figure 2.18. The local grain level constitutive response is coupled to the aggregate behaviour using the self-consistent algorithm based on Eshelby's inclusion formalism [152]. After each straining step the self-consistent criteria ensures that the

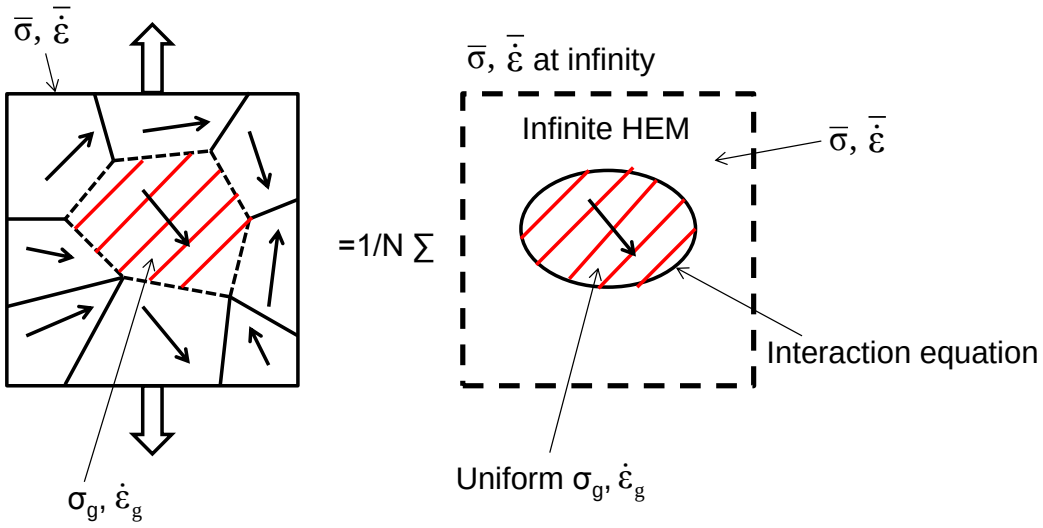

Figure 2.18: Schematic representation of the calculation scheme of the VPSC model where each grain (ellipsoidal inclusion) is embedded within a medium with average properties. The arrows within the grain indicate the orientation of the grains. σ_g and $\dot{\varepsilon}_g$ are the grain stress and strain rate, while $\bar{\sigma}$ and $\bar{\dot{\varepsilon}}$ are polycrystal stress and strain rate values.

averages of all grain level stresses and strain rates equal to those imposed macroscopically i.e. it satisfies both strain compatibility and stress equilibrium in the average sense. The local grain deformation in VPSC depends on grain orientation, grain shape and grain interaction with the surrounding (each grain sees the average neighborhood in the 1-site model). The details of the entire formulation can be found elsewhere [149-151]. The single crystal constitutive equation, the interaction equation, the hardening and twinning model are described in Appendix A2.

2.9.2 Twinning models

It is important to briefly review here the main approaches that are commonly used to model the twinning behaviour. Two types of model are common: the type a), also known

as Kalidindi's model [153, 154], in which grains are divided into twinned and non-twinned regions (increases the number of grains in the simulations) and the type b), also known as predominant twin reorientation (PTR) scheme, in which grains are allowed to be completely reoriented when a certain criterion is met (number of grains remains constant) [151]. In the present study, the model of type (b) has been used in the Los Alamos VPSC model [149] to account for twinning. Within the PTR scheme, a grain is allowed to be completely reoriented based on the most active twin system present in that grain. The details of model are presented in Appendix A2.4.

2.9.3 VPSC studies on magnesium alloys

In 2001, Agnew and co-workers [48] made their first attempt to implement a VPSC code for analysing the mechanical behaviour of pure magnesium and its solid solution alloys containing Li or Y additions. They have demonstrated the utility of VPSC models in interpreting the differences in the mechanical behaviour of different alloys. The results showed that the plane strain compression textures of the alloys exhibit an increased tendency for the basal poles to rotate away from the normal direction towards the rolling direction and this was primarily attributed to enhanced activity of the non basal <c+a> slip mode. They have also reported that the alloys had improved ductility in compression compared to pure magnesium owing to the enhanced non basal <c+a> slip activity.

Recently, Jain and Agnew [82] have employed the VPSC model to study the mechanical behaviour of AZ31B magnesium alloy sheet material tested in uniaxial compression along three sample directions (rolling, transverse and normal direction) over the temperature range of 22-250°C. The key conclusions from their study are: i) in-plane compression results in profuse $\{10\bar{1}2\}$ twinning, which was shown to result in very low R-

value (given by ratio of width strain to thickness strain), ii) the basal slip and $\{10\bar{1}2\}$ extension twinning are athermal deformation mechanisms, iii) $\{10\bar{1}2\}$ twinning is responsible for hardening of material due to rapid texture evolution and due to twin boundaries acting as barrier to dislocation motion, iv) the twin barrier effect reduces with increasing temperature and v) the enhanced ductility at moderate temperatures (100-200°C) was attributed to thermally activated prismatic <a> and pyramidal <c+a> slip mechanisms. There are several other similar studies available on AZ31 magnesium alloy [8, 155].

2.9.4 Summary

Polycrystal plastic deformation models allow us to link the aggregate response with the grain-level behaviour. In this regard, the model based on the viscoplastic self-consistent formulation is attractive as it accounts for the heterogeneous deformation of polycrystals which is of particular interest for the non-cubic metals and alloys. The work reviewed above clearly highlights the potential of VPSC simulations in interpreting the mechanical behaviour of magnesium alloys. One can predict the texture evolution, individual mode activities and mechanical properties using a VPSC model. As indicated earlier, VPSC have been successfully employed for analysing the mechanical behaviour of AZ31 magnesium alloy. However, to the author's knowledge, there has been no such previous attempt made on AZ80 magnesium alloy.

CHAPTER 3 - Scope and Objectives

This study is focussed on the AZ80 (Mg-8Al-0.5Zn) magnesium alloy having a fixed starting average grain size (i.e. ~ 32μm). In this work, deformation behaviour of an AZ80 alloy is studied by varying: i) the crystallographic texture (i.e. strong and weak texture), ii) the temperature (i.e. 77K and 293K), iii) the stress state (i.e. tension/compression) and iv) the microstructure (i.e. solution-treated vs. aged).

The broad objective of this work is to examine the influence of initial texture, temperature, stress state and precipitates on deformation behaviour of the AZ80 magnesium alloy. This study aims at systematic characterization of the influence of these variables on the yield strength, work hardening behaviour, texture evolution and associated deformation mechanisms of the alloy. The following objectives are sought in this work:

i) Examination of the effects of low homologous temperature on deformation behaviour of strong and weak textured AZ80 alloy. In particular, the work focuses on analysing the effects of temperature on the mechanical properties, work hardening characteristics, texture evolution, slip activity and twinning behaviour of the alloy.

ii) To evaluate the VPSC model for deformation of the AZ80 magnesium alloy. The VPSC model is employed to examine the effects of initial texture, stress state and temperature on deformation mechanisms and texture evolution of the alloy. Moreover, the present study will seek a physically based approach for setting the adjustable parameters in the model.

iii) To examine the influence of precipitation on the mechanical behaviour and texture development of the AZ80 alloy. This study aims to investigate the effects of precipitates on the microstructural evolution, slip activity and twinning behaviour of the alloy.

CHAPTER 4 – Materials and Methodologies

4.1 Introduction

This chapter is concerned with the experimental methods involved in this study and the basic overall design of the experimental and modelling work. Figure 4.1 shows a schematic representation of the variables involved in the present study i.e. crystallographic texture, microstructure (precipitate state), test temperature and the loading path. The experimental work involved a number of important tasks including i) the production of materials with different starting textures and ii) the generation of different microstructures i.e. a supersaturated solid solution (solution-treated) and a homogeneous distribution of precipitates (aged). To accomplish these, suitable processing conditions (e.g. heat treatment condition, rolling condition etc.) have been determined. In addition, for examining the effect of low homologous temperature on deformation behaviour of AZ80 alloy, deformation tests were carried out at room temperature and with samples submerged in liquid-nitrogen.

The organization of this chapter is as follows. Section 4.2 provides details on the starting material. Section 4.3 describes the various characterization tools and the related sample preparation techniques used. The processing of the alloy with different starting textures and microstructures is summarised in section 4.4. The matrix of mechanical testing is described in section 4.5. Section 4.6 includes the description of various methods used for characterizing the deformation modes in the present study. The methodology involved in the VPSC simulations is described in section 4.7.

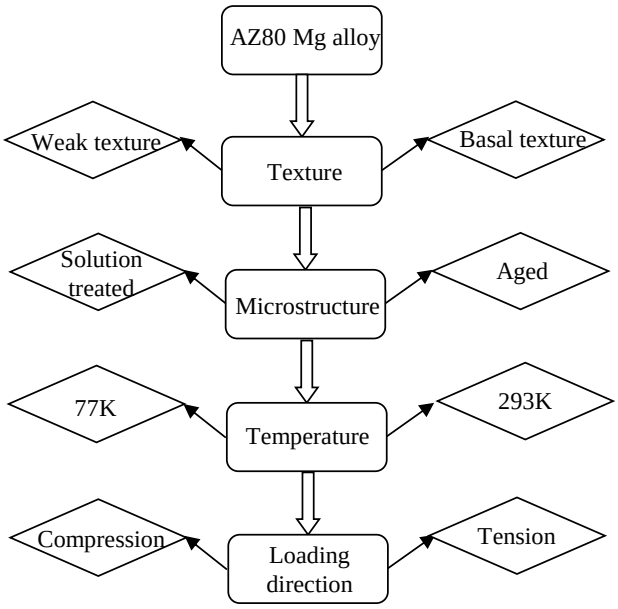

Figure 4.1: Schematic representation of the variables involved in deformation study.

4.2 Initial material details

The direct chill cast AZ80 magnesium alloy used in this study was supplied by Timminco Inc., Canada. The size of the as-cast billet was about 220 mm in height and 300 mm in diameter. Table 4.1 shows the chemical composition of the as-received alloy. For reference, the chemical composition of the AZ80 alloy is shown on a section of the quaternary phase diagram in Figure 4.2. At temperatures below approximately 355°C, the β-$Mg_{17}Al_{12}$ precipitates from the parent HCP alpha phase, in addition to the insoluble Al_8Mn_5 phase which precipitates during solidification.

Table 4.1: Nominal chemical composition of the commercial AZ80 magnesium alloy

Element	*Al*	*Zn*	*Mn*	*Mg*
wt %	8	0.5	0.2	Bal.

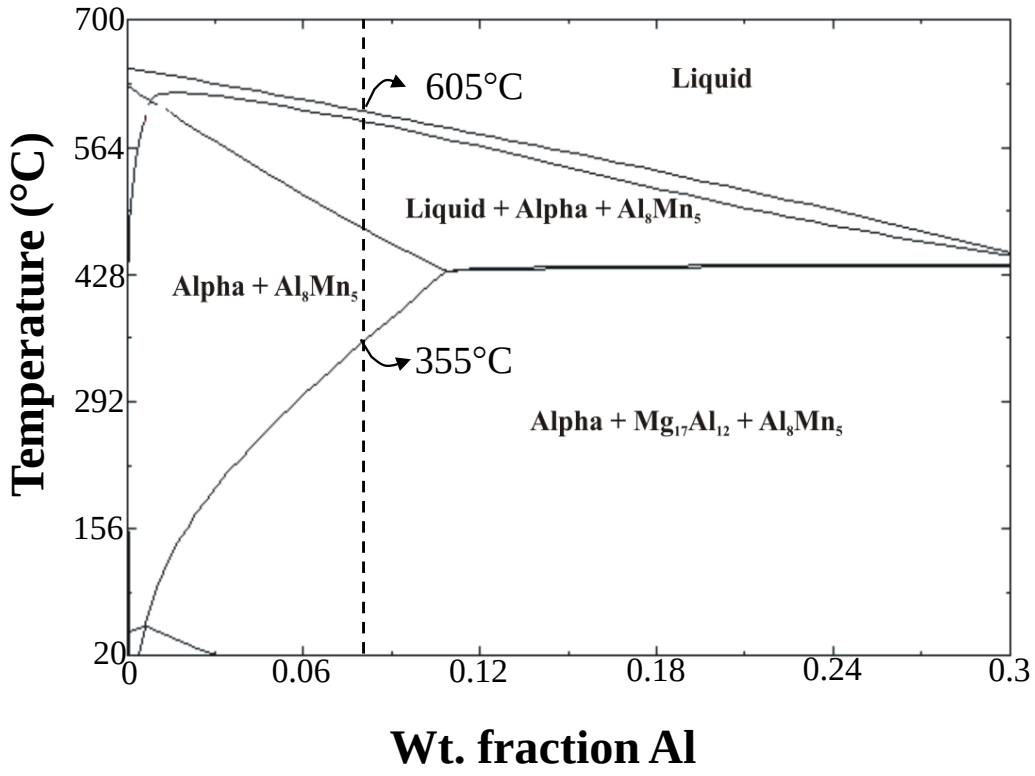

Figure 4.2: Mg-rich end of the Mg-Al-Zn-Mn phase diagram. The quaternary isopleth is plotted at 0.5 wt% Zn and 0.2 wt% Mn. The dashed line indicates the bulk Al content of the AZ80 alloy [114].

4.3 Material characterization: sample preparation and tools

4.3.1 Metallography

Sample preparation for optical microscopy, scanning electron microscopy (SEM), and electron backscatter diffraction (EBSD) was as follows: Mechanical grinding (600/800/1200/2400 grade SiC) was performed and followed by diamond suspension polishing using 6μm and 1μm compound. After diamond polishing, samples were chemically polished in 10% Nital (90 ml of ethyl alcohol and 10ml of nitric acid) solution for 30-60 s at room-temperature.

For optical metallography, the chemically polished surface was etched in an acetic-picral solution (4.2 g picric acid, 10 ml acetic acid, 10 ml water, 70 ml ethanol) to reveal the grain structure. The sample was immersed in the solution until its surface turned light orange (~ 30 s) and was then rinsed with ethanol and dried in a blast of air. For revealing the precipitates, chemically polished samples were also deep etched in 10% hydrofluoric acid solution in ethanol for 1-2 s.

For EBSD observations, an additional step of electrolytic polishing is required. The electro-polishing was carried out in a separate cell consisting of an anode, a cathode (stainless steel) and an electrolyte (20% nitric acid in 80% absolute ethanol), maintained at -20°C. A voltage of 20-30V was used. The electrolyte was constantly stirred with a magnetic stirrer to avoid the formation of bubbles on the surface of the sample. After electro-polishing, samples were quickly rinsed with ethanol and dried under a blast of air.

4.3.2 Microstructure and texture characterization

4.3.2.1 Optical-Nomarski microscopy

A Nikon EPIPHOT 300 optical microscope was used to characterize the initial microstructure and to study the surface slip traces. Grain size measurements by optical microscopy were based on ASTM E 112 [156] and were obtained from the measurement of 500-1000 grains. For revealing the slip lines unambiguously, a Nomarski lens was specifically attached to an optical microscope. A detailed procedure of slip trace analysis is described later section in 4.6.1.

4.3.2.2 Scanning electron microscopy (SEM)

The microstructure of as-cast, solution-treated and aged samples was studied using a Hitachi S-570 scanning electron microscope (SEM) operating at 20 keV. The homogenization of the as-cast structure and dissolution of β-$Mg_{17}Al_{12}$ phase during solution treatment was studied by SEM using secondary electron (SE) images. For revealing the distribution of precipitates in an aged sample SE images were also utilised.

4.3.2.3 Electron back scattered diffraction (EBSD) analysis

In the present study, two EBSD systems were used to characterize the microstructures in deformed and undeformed states. One system was mounted on a tungsten filament SEM giving a spatial resolution on the order of 1 μm while the second was mounted on a FEG SEM giving a spatial resolution of ~50 nm.

The low resolution EBSD system was used to determine the orientation of the grains, to measure the twin area fraction and to compute the microtexture. The measurements were carried out on a Hitachi S-570 SEM equipped with a electron back scattered detector. The operating conditions were as follows: accelerating voltage 20 keV, sample tilt 70°, working distance 23 mm, step size 1-2 μm. To obtain the information on texture, a large step size (~ 4-5 μm) was used in an attempt to increase grain statistics. The indexing rate of the measured EBSD maps was typically around 80%. A medium level (five neighbouring points) of zero solution extrapolation has been applied to the data to remove non-indexed points.

Selected high resolution EBSD maps were also measured to examine the formation of twins. EBSD measurements were made using a JEOL 6500F field emission gun scanning electron microscope operated at 15 keV equipped with HKL Channel 5

software at a step size of about 80-320 nm. The indexing rate of the EBSD maps was typically 85% and they were cleaned in the same manner as mentioned above. Two types of maps were plotted: an inverse pole figure map and a band contrast map. In the inverse pole figure map the compression direction is plotted in the crystal reference frame. The band contrast map is based on the Kikuchi pattern quality. For plotting, an available grey scale which typically varies from 0-255 has been used. In this the minimum pattern quality was shaded as black, while increasing brightness indicates increasing pattern quality. The presence of grain boundaries and defects on the surface such as slip lines, deteriorate the pattern quality and are therefore revealed in the band contrast map.

4.3.2.4 Neutron diffraction texture measurements

Neutron diffraction has been employed to characterize the texture and estimate the twin volume fraction in deformed samples (procedure outlined in section 4.6.3). Texture measurements were made on the E3 spectrometer at the Canadian Neutron Beam Centre at Chalk River Laboratories, Canada. Figure 4.3 shows a schematic drawing of the neutron texture measurement unit. The incident neutron beam of wavelength 2.2 Å was obtained from the {311} reflection of a germanium monochromating crystal. The cross section of the beam was 25.4 mm × 25.4 mm. The sample orientation was controlled by Eulerian cradle which was programmed to scan χ from 0-90° and η from 0-360° by increments of 5°, as indicated in Figure 4.3. Four pole figures, $\{0001\}, \{10\bar{1}0\}, \{10\bar{1}1\}$ and $\{10\bar{1}2\}$, were measured in each case. Approximately, 7×10^7 grains were involved in the neutron analysis. The measurement of each sample took approximately 10 hr (including background determination). The neutron data were analysed and subsequently plotted using the Chalk River texture package.

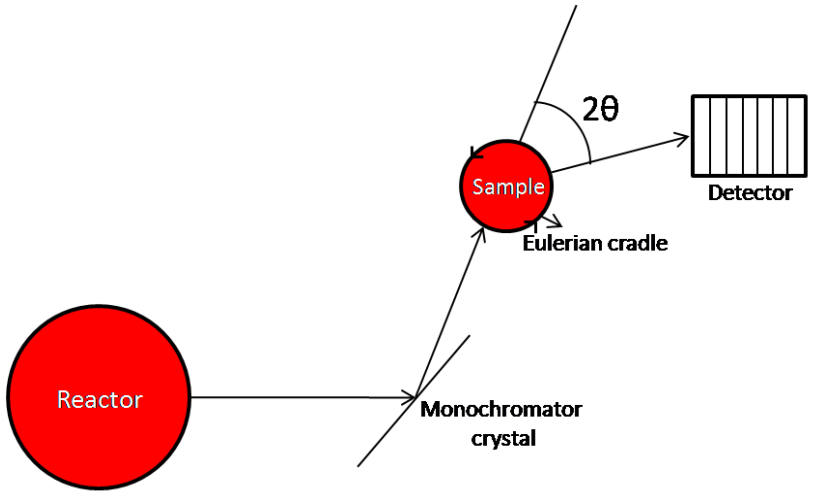

Figure 4.3: Schematic representation of neutron diffraction unit used for texture measurements.

4.4 Processing of initial material

Figure 4.4 shows an SEM of the as-cast AZ80 alloy. The β phase $Mg_{17}Al_{12}$ is distributed throughout the matrix, primarily along grain boundaries, i.e. the former interdendritic region during solidification. The as-received material was then subsequently treated in several steps as illustrated in the schematic diagram shown in Figure 4.5, while the details of the processing are described in the next three sections.

4.4.1 Preparation of weakly textured solution treated samples

The as-received alloy was given a homogenization and solution treatment with the purpose of eliminating the as-cast segregation and dissolving the β-$Mg_{17}Al_{12}$ phase. A temperature of 415°C was selected based upon the Mg-Al-Zn-Mn equilibrium phase diagram (Figure 4.2). This is well above the equilibrium solvus temperature of the AZ80 alloy, which is roughly around 355°C, and below the liquidus of 480°C. To study

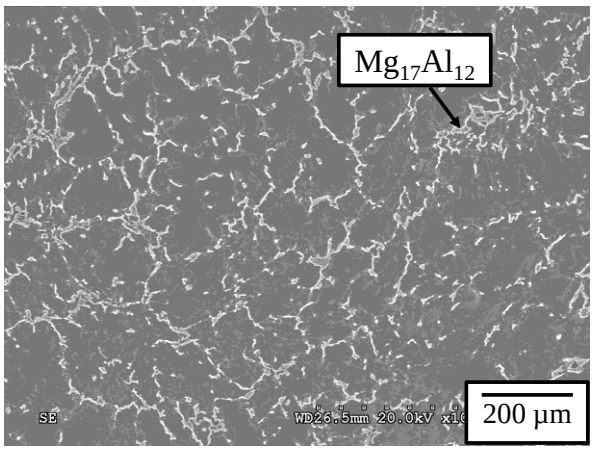

Figure 4.4: Secondary electron micrograph (SEM) micrograph of the as-received material.

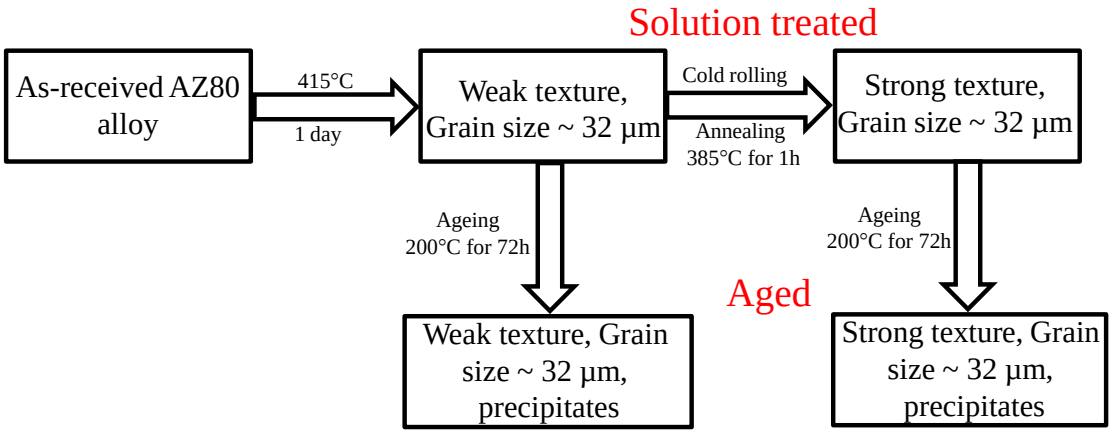

Figure 4.5: Schematic drawing illustrating the key steps involved in the processing of the as-received material.

dissolution of the β phase and homogenization, samples were solution treated for various times (i.e. ½, 1, 2, 4 and 7 days) at 415°C and then quenched into cold water. All the heat treatments were carried out under flowing argon to reduce oxidation. Figure 4.6a and 4.6b show that there was a complete dissolution of the β phase after 1 day or 7 days. However, a

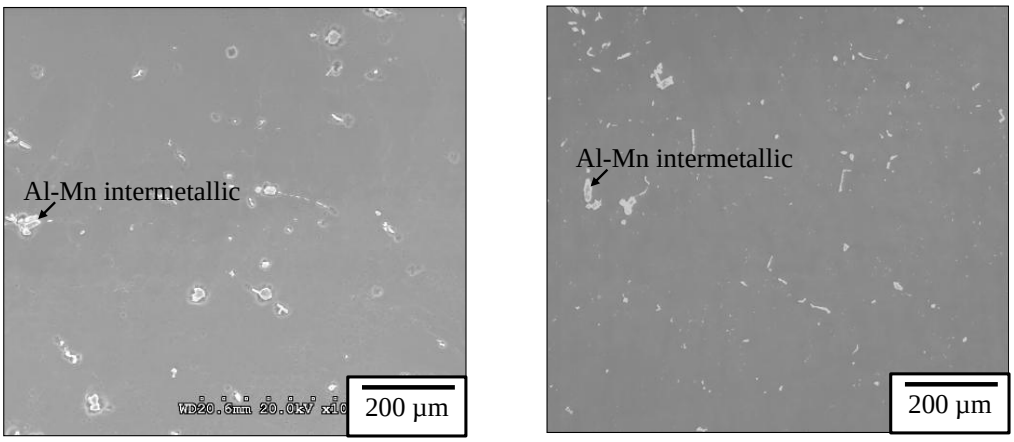

(a) (b)

Figure 4.6: SEM micrographs of samples solution treated at 415°C for **a)** 1 day and **b)** 7 days.

number of insoluble Mn rich Al-Mn intermetallics (confirmed by energy-dispersive X-ray (EDX) analysis) were observed. These are presumed to be the Al_8Mn_5 phase (see the phase diagram in Figure 4.2). There is little difference between a 1 day and 7 day heat-treatment and it was therefore concluded that the solution treatment at 415°C for 1 day was sufficient to dissolve the β phase. It should also be mentioned that this heat treatment condition was previously applied by other researchers [157] to a similar alloy.

Figure 4.7a shows an etched optical micrograph of solution-treated AZ80 alloy. The initial grain size was 32 µm, as measured by optical microscopy using ASTM E112 [156]. This was found to be consistent with the measurement from EBSD maps. Figure 4.7b and 4.7c, respectively show the {0001} basal and $\{10\bar{1}0\}$ prismatic pole figures (measured from neutron diffraction) of the as-received material. Although the {0001} pole figure shows some preferred alignment of basal poles perpendicular to the casting direction

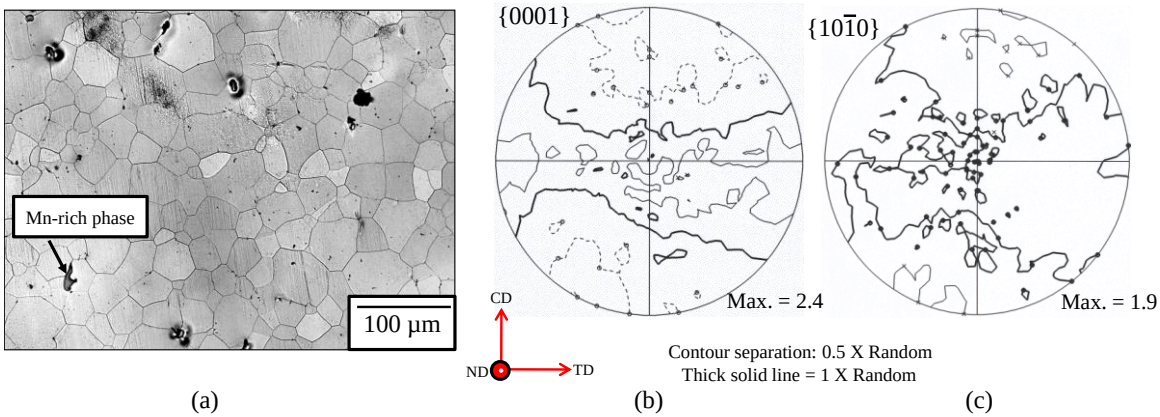

Figure 4.7: a) An optical micrograph showing the grain structure of solution-treated (415°C for 24h) AZ80 alloy. **b)** and **c)** show the {0001} and {10$\bar{1}$0} (stereographic) pole figures, measured from neutron diffraction, representing the texture of the same material. The pole figures are contoured in multiples of random distribution (m.r.d.) with the thick solid black line corresponding to 1 m.r.d.. The contour levels above and below 1 m.r.d. are given by solid and dotted lines, respectively, in 0.5 m.r.d. steps. The CD, TD and ND correspond to casting direction, transverse direction and normal direction of the sample, respectively.

(CD), the overall texture of this material is weak (maximum intensity of 2.4 m.r.d.). This condition is referred to as weak-textured solution-treated in the subsequent discussions.

4.4.2 Preparation of strong textured solution treated samples

The samples in the supersaturated solid solution state (described in section 4.4.1) were also cold-rolled and annealed with the aim of producing a microstructure consisting of grains of similar average size (i.e. 32 µm) but with a strong recrystallized texture. To accomplish this, solution-treated samples of 120mm x 65mm x 14mm, were cold rolled on a laboratory rolling mill (roll diameter: 154 mm) and then annealed isothermally at 385°C

(i.e. above the solvus temperature of the alloy) in the time range 180s -1h. Cold rolling involved a total reduction of 20-22% which was accomplished in 4-5 passes. All annealing experiments were conducted in salt baths consisting of sodium nitrate/potassium nitrate salt mixture. A stainless steel bag (0.085 mm thick) was used to hold the samples in the salt bath with the purpose of preventing corrosion of the samples. The material had a fully recrystallised microstructure after annealing at 385°C for 180 s and 385°C for 1 h. The grain size measured from optical micrographs was determined to be 20 μm for 180 s annealed sample and 32 μm for the 1 h annealed sample as shown in Figure 4.8.

Figure 4.8b and 4.8c shows the {0001} and $\{10\bar{1}0\}$ pole figures (measured via EBSD), respectively, representing the texture of the same material. The texture after cold rolling and annealing can be characterized as a typical 'basal texture' (with maximum

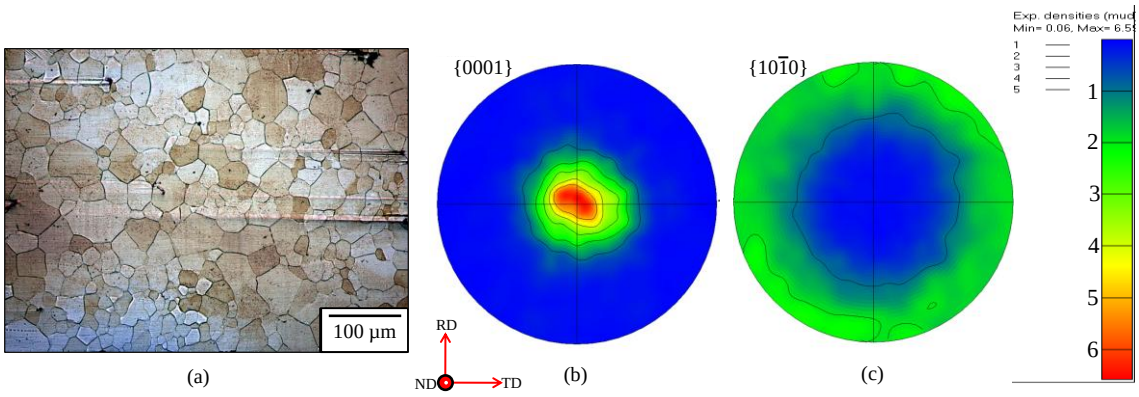

Figure 4.8: a) An optical micrograph showing the grain structure of cold rolled (20-22%) and annealed (385°C for 1 h.) sample, **b)** and **c)**, respectively show the EBSD measured {0001} and $\{10\bar{1}0\}$ pole figures (stereographic), representing the texture of the same material. The RD, TD and ND correspond to rolling direction, transverse direction and normal direction of the sample, respectively. The intensity colour scale is given in m.r.d..

intensity of 6.5 m.r.d.) exhibiting preferred alignment of basal poles around the normal direction. This texture is typical of results from other commercial AZ series magnesium alloys such as AZ31 [8]. In the following discussion, this condition is referred to as strong textured solution-treated material.

4.4.3 Preparation of weak and strong textured aged samples

The ageing curve of the alloy was measured at 200°C and 250°C with a series of hardness measurements at different ageing times. Vickers micro-hardness measurements were conducted on polished samples using a load of 300 g. The observed hardness readings are the averages of ten readings taken at random locations throughout the sample. Figure 4.9 shows the change in hardness as a function of time for ageing. Note that the solution treated hardness was measured to be 55 HV. The increase in hardness is attributed to the precipitation of the β phase. The peak hardness is a function of ageing temperature with a higher peak hardness observed at 200°C compared to 250°C. The difference in hardness is considered to be due to the difference in volume fraction of precipitates at the two temperatures considered (see the phase diagram in Figure 4.2).

To examine the effect of precipitates, solution-treated samples of the weak and strong textured material (~ 32 μm grain size) were age-hardened at 200°C for 72 h (peak aged condition) in an argon atmosphere. Figure 4.10a and 4.10b illustrate the secondary electron micrographs of a sample aged at 200°C for 72 h. at lower and higher magnification. A very high volume fraction (~9-10% vol. of β-$Mg_{17}Al_{12}$ as determined from equilibrium phase diagram) of precipitates exists for this ageing condition. It can also be observed that the precipitation has occurred in both intergranular and intragranular regions. The majority of these precipitates appear to be large (several μm in dimensions)

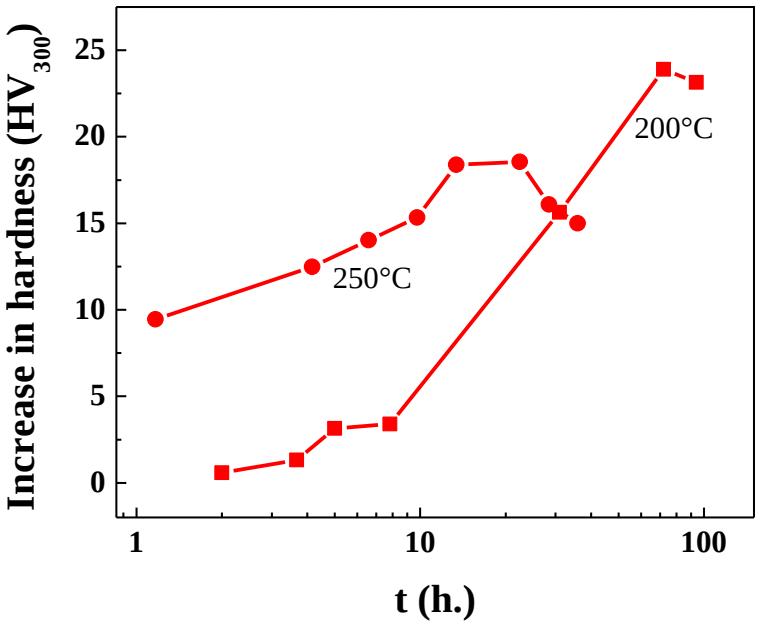

Figure 4.9: Ageing curve of AZ80 alloy at 200°C and 250°C. Note that the solution treated hardness was measured to be 55 HV.

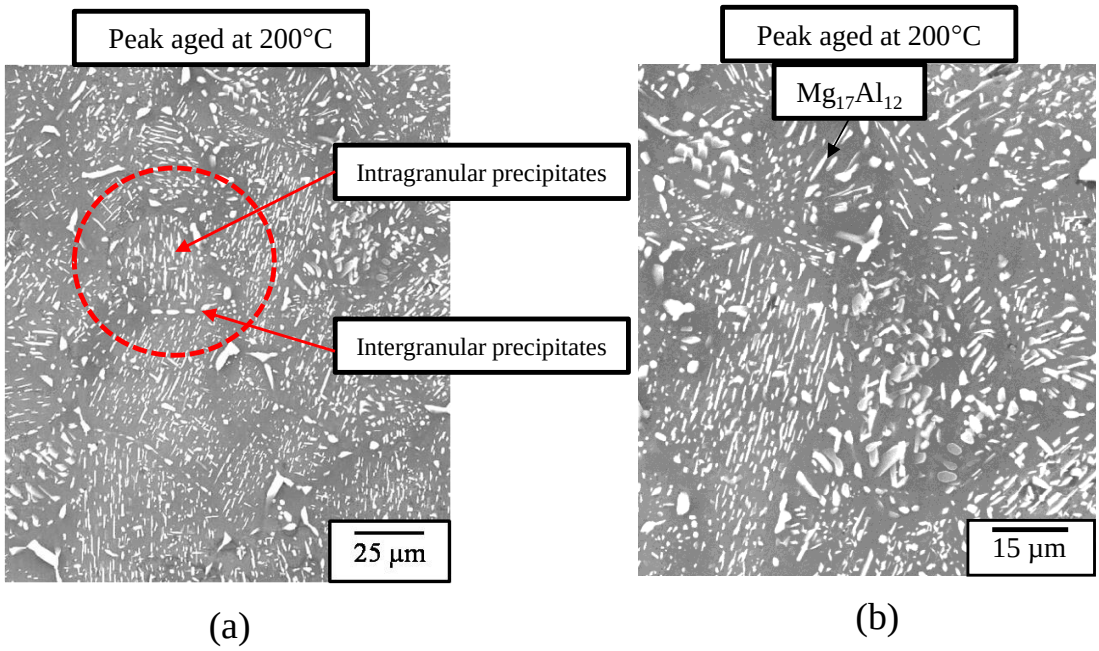

Figure 4.10: **a)** Secondary electron micrograph of AZ80 alloy solution treated and aged at 200°C for 72 h (peak aged condition) and **b)** higher magnification image of (a).

which is consistent with the literature reviewed in chapter 2, section 2.8.1). Moreover, the average grain size was not observed to change during the ageing treatment.

4.5 Mechanical properties testing

4.5.1 Mechanical test matrix

After the preparation of the samples, the material was tested under several conditions. Table 4.2 provides a list of conditions utilized for testing the material. As indicated, the alloy was tested in both supersaturated solid solution condition and in the

Table 4.2: List of mechanical tests employed in the current study. Notice that G.S. corresponds to the grain size, while the reference frames (e.g. RD, TD and ND) are described previously in Figure 4.7 and 4.8

Material state		*Type of tests*	*77K*	*293K*
Weak textured material	Solution treated (G.S. ~ 32 μm)	Compression parallel to ND	✓	✓
		Tension parallel to ND	×	✓
	Aged (G. S. ~ 32μm)	Compression parallel to ND	✓	✓
		Tension parallel to ND	×	✓
Strong textured material	Solution treated (G. S. ~ 32μm)	Compression parallel to ND	✓	✓
		Compression parallel to RD	✓	✓
		Tension parallel to RD	✓	✓
	Aged (G. S. ~ 32μm)	Compression parallel to ND	×	×
		Compression parallel to RD	×	✓
		Tension parallel to RD	×	✓

✓ designates tested condition, while × indicates condition that was not tested.

aged condition with starting textures either weak or strong. Further, the loading condition at the macroscale was specifically chosen to activate a particular slip and/or twinning mode as will be discussed later. In addition, for examining the effect of low homologous temperature, the alloy was tested at 77K and 293K.

Testing on the strongly textured sheet material was conducted in three different orientations i.e. compression parallel to ND, tension parallel to RD and compression parallel to RD which will be referred as through thickness compression (TTC), in-plane tension (IPT) and in-plane compression (IPC), respectively.

4.5.2 Compression testing

Compression samples were machined from the as-cast and rolled plate of AZ80 (Mg-8Al-0.5Zn) magnesium alloy. Compression tests were carried out on weak textured material with compression axis oriented normal to the casting direction (Figure 4.11a) i.e. along the ND direction, strong textured material with compression axis oriented along both the normal direction (Figure 4.11b) and the rolling direction (Figure 4.11c). The schematic drawing illustrating the sample geometry for different tests is shown in Figure 4.11. Cube-shaped samples were chosen as they facilitate polishing of the surface prior to compression for sequential EBSD and slip trace analysis which will be described later.

Compression tests were carried out on an Instron 50 kN capacity screw driven mechanical test machine. For tests at 77K, the compression platens were immersed in a Styrofoam container, which was filled with liquid nitrogen. During the experiments, Teflon tape (0.05 mm thick) coated with molybdenum disulphide was used as a lubricant between specimen and test fixture and a displacement rate of 2.1×10^{-2} mm.s^{-1} was maintained. The

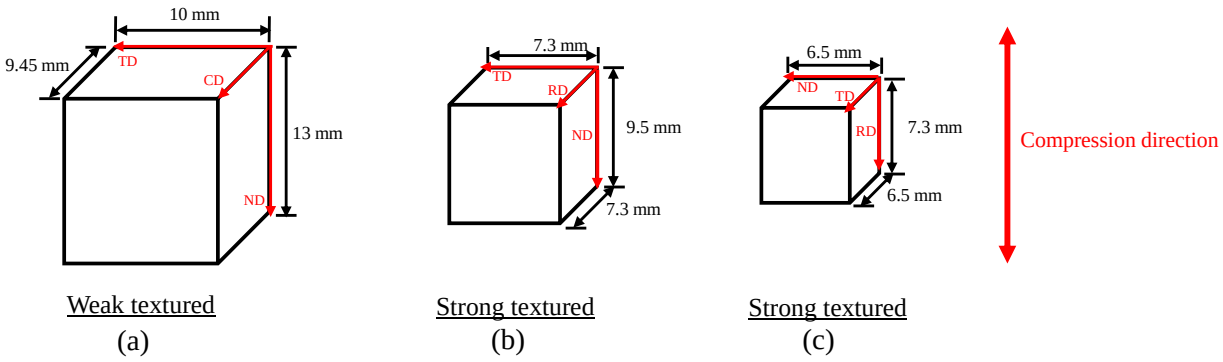

Weak textured
(a)

Strong textured
(b)

Strong textured
(c)

Figure 4.11: Schematic drawing illustrating the compression sample geometry for a sample having **a)** weak texture **b)** strong texture with compression direction parallel to ND and **c)** strong texture with compression direction parallel to RD.

coated side of the lubricant was placed on the top surface of the sample. As it was not possible to attach an extensometer to the sample during testing the displacement of the crosshead was monitored. The resulting load-displacement data was converted to true stress and true strain after correction for the compliance of the test machine. To obtain the machine compliance, the loading system was assumed to behave like a linear elastic spring (based on ASTM standard [158]). The measured displacement was subtracted from the machine displacement to obtain the sample displacement. Negligible barrelling was observed after testing, confirming the uniformity of deformation in compression. The yield strength was determined by applying the 0.2% offset, while the work hardening data was obtained using the Microsoft Excel function 'slope (y, x)' (y and x correspond to true stress and true strain, respectively). This function calculates the slope of a regression line through the selected data points. In the present case, the slope was calculated on a moving averaging based on five data points. To ensure reproducibility, each test was repeated at least three times.

In this study, compression tests were conducted in two different ways. Samples were either continuously compressed to failure or compression was conducted up to various intermediate strain levels (e.g. 0.02, 0.05, 0.08 etc.) after which observations were made on the bulk texture and microstructure evolution.

4.5.3 Tensile testing

Flat sheet tensile specimens were machined from an as-cast and rolled sheet of AZ80 magnesium alloy. The dimensions of the tensile samples are shown in Figure 4.12. Note that samples were either pulled normal to the casting direction i.e. along the normal direction (ND) or along the rolling direction (RD).

A 5 kN capacity screw driven Instron test machine was used to perform the tensile test. The tests were done at constant displacement rate, corresponding to a nominal strain rate between 0.9×10^{-3} and 1×10^{-3} s^{-1}. The elongation of the sample was assessed through an extensometer (gauge length 25.4 mm) attached on to the sample cross section. For tests at 77K, the entire testing rig including extensometer was immersed in a container filled with liquid nitrogen. The low temperature tests commenced when significant boiling of the

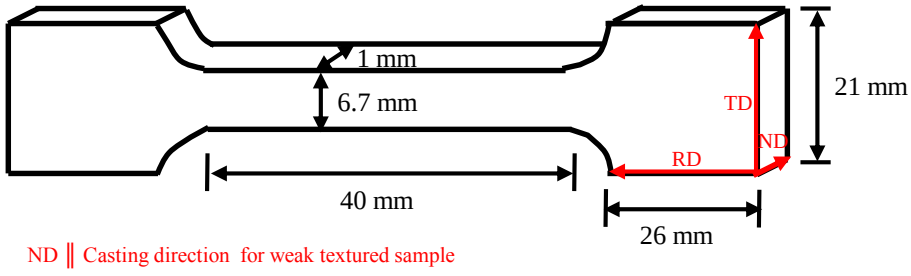

Figure 4.12: Schematic drawing illustrating the tensile sample geometry.

liquid nitrogen had stopped. The true stress-true strain data were calculated from the recorded load displacement data in the usual manner. The yield strength and work-hardening rate were determined in the same manner as described in section 4.5.2.

4.6 Characterization of deformation modes

4.6.1 Slip trace analysis

In this study, slip trace analysis was used for identifying the most likely slip plane. For trace analysis one of the faces of cube shaped specimens was metallographically prepared and electrolytically polished (in the same manner as described in section 4.3.1) immediately after solution treatment. Then a local area was marked using fiducial hardness indents. In some cases, the electropolished samples were also aged under flowing argon and quenched in cold water. This preserves the surface prior to deformation experiments. The crystallographic orientation of grains in the local area was then determined using the Channel 5 HKL EBSD system attached to a Hitachi S-570 scanning electron microscope (see section 4.3.2.2 for more details on EBSD). After a strain of 0.05, the same area was observed again in an optical Nomarski microscope to characterize slip lines on the surface. A schematic drawing illustrating the slip step emanating from the polished sample surface is shown in Figure 4.13.

The following steps were performed to determine the crystallographic plane/direction best matching the observed trace:

i) Measurement of the crystallographic orientation of the grain(s) using EBSD. The coordinate system of the sample is defined from this measurement.

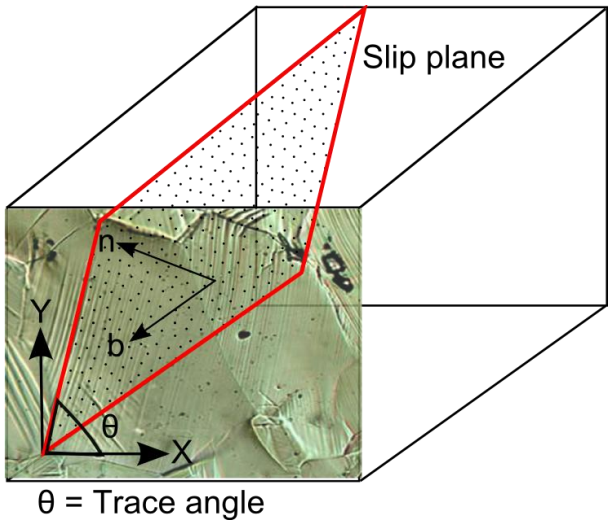

Figure 4.13: A schematic drawing illustrating the slip step on the polished surface. X and Y define the sample co-ordinate system.

ii) Acquisition of an optical image of the deformed sample surface using an optical microscope equipped with a Nomarski prism. Care was exercised to ensure the optical image was taken with the same reference axes as the EBSD measurement.

iii) Draw a line manually to select a trace and measure its inclination angle with respect to the sample reference frame.

iv) Calculate the observation plane normal from the EBSD data.

v) For each slip system, the cross product of slip plane normal and surface normal was calculated to give all possible slip plane traces.

vi) Calculation of direction cosine of slip plane trace with the X-direction of the sample reference axes (see Figure 4.13).

vii) Comparison of observed and calculated trace angles (θ) obtained by considering all the slip systems listed in Table 4.3.

It should be noted that the present analysis considered all the expected slip systems and included all possible variations for a set of slip systems (Table 4.3).

During the trace analysis, the angle of intersection of the slip plane with the free surface (see angle θ in Figure 4.13) was compared with the experimentally determined value. For the first selection, the closest fit was considered as the relevant slip system. These fits were typically within 1-2 degrees. However, it was observed that in a number of cases, the second best fit was only slightly worse than the best fit. In these cases, it was considered that the identification was therefore within the error of measurements and thus ambiguous. Only in cases where the difference between the first and second best fit was greater than 3 degrees, was the fit considered unambiguous. These are the results that were reported in the results section.

Table 4.3: List of all considered slip systems for calculating trace angles

Slip mode	*Slip plane*	*Slip direction*	*Slip system*	*Possible variants of slip system*
Basal <a>	(0001)	$<11\bar{2}0>$	$(0001)<11\bar{2}0>$	3
Prism <a>	$\{10\bar{1}0\}$	$<11\bar{2}0>$	$\{10\bar{1}0\}<11\bar{2}0>$	6
Pyramidal <a>	$\{10\bar{1}1\}$	$<11\bar{2}0>$	$\{10\bar{1}1\}<11\bar{2}0>$	6
Pyramidal <c+a>	$\{11\bar{2}2\}$	$<11\bar{2}3>$	$\{11\bar{2}2\}<11\bar{2}3>$	6

In most instances it was possible to distinguish slip lines from twins in the optical micrographs by the fact that slip traces appear as thin lines, whereas twins typically appear as being lenticular. For cases where it was difficult to distinguish between whether a feature was a twin or a slip trace then such ambiguous features were not considered for the analysis. In the present study, slip trace analysis was utilised for characterizing the slip lines of the weak textured alloy (in both solution-treated and aged conditions) deformed to strain of 0.05 at 77K and 293K.

4.6.2 Sequential EBSD mapping

In an individual grain, the orientation change resulting from slip and twinning activity can be followed using a sequential mapping in EBSD. In this approach, prior to testing, one of the faces on the compression sample was metallographically prepared as described in section 4.3.1 and a local area was identified by hardness indents. The orientation of grains in this area was determined using EBSD. After a certain compressive strain, this local area was again re-examined in the EBSD system to track the orientation change resulting from slip and twinning. Without knowing the initial orientation of the grains it is difficult to unambiguously identify the twins simply based on the boundary misorientation characteristics, especially in the cases where twins depart frequently from a lenticular shape. Thus, a sequential approach of probing the same area in EBSD at different strain levels (e.g. 0.02, 0.05) was utilised for determining the twin area fraction as a function of strain.

4.6.3 Neutron texture analysis

It is known that as both slip and twinning contribute to texture evolution, the large re-orientation associated with twinning results in a very significant and rapid texture

evolution. This distinct characteristic of twinning can be utilised in estimating twinning fractions from experimentally measured {0001} pole figures. The evolution of twinned volume fraction can be measured by recording the change in intensity from the undeformed state to the deformed state within a certain orientation space. A detailed procedure to do so is described in the Appendix A3. In the present study, the neutron data were used to evaluate the twinning kinetics of solution-treated and aged samples deformed at 77K and 293K.

4.7 VPSC methodology

In this study, the Los Alamos VPSC model (version 6) [149] has been employed to simulate the plastic deformation of the AZ80 magnesium alloy. Figure 4.14 shows a schematic diagram illustrating the steps involved in the VPSC simulations. The first task was to generate the appropriate input texture file (Figure 4.14). Simulations of strong textured material were performed using a texture file containing 1079 orientations of equal weights (obtained from EBSD) which is representative of the measured initial texture of material given in Figure 4.8. Alternatively, for the weak textured material, a discretized texture file of 10,500 orientations was used. These orientations were obtained by discretization of the orientation distribution function **(**ODF) that had been obtained from measured neutron diffraction data. The discretization was performed using "ODFVF3" [159], which is part of the Los Alamos texture analysis package.

Simulations were performed for both uniaxial compression and tension boundary conditions using incremental straining steps of approximately 0.005. For the calculations, the input boundary conditions (i.e. velocity gradient components ($\overline{\dot{D}}_{ij}$) and stress

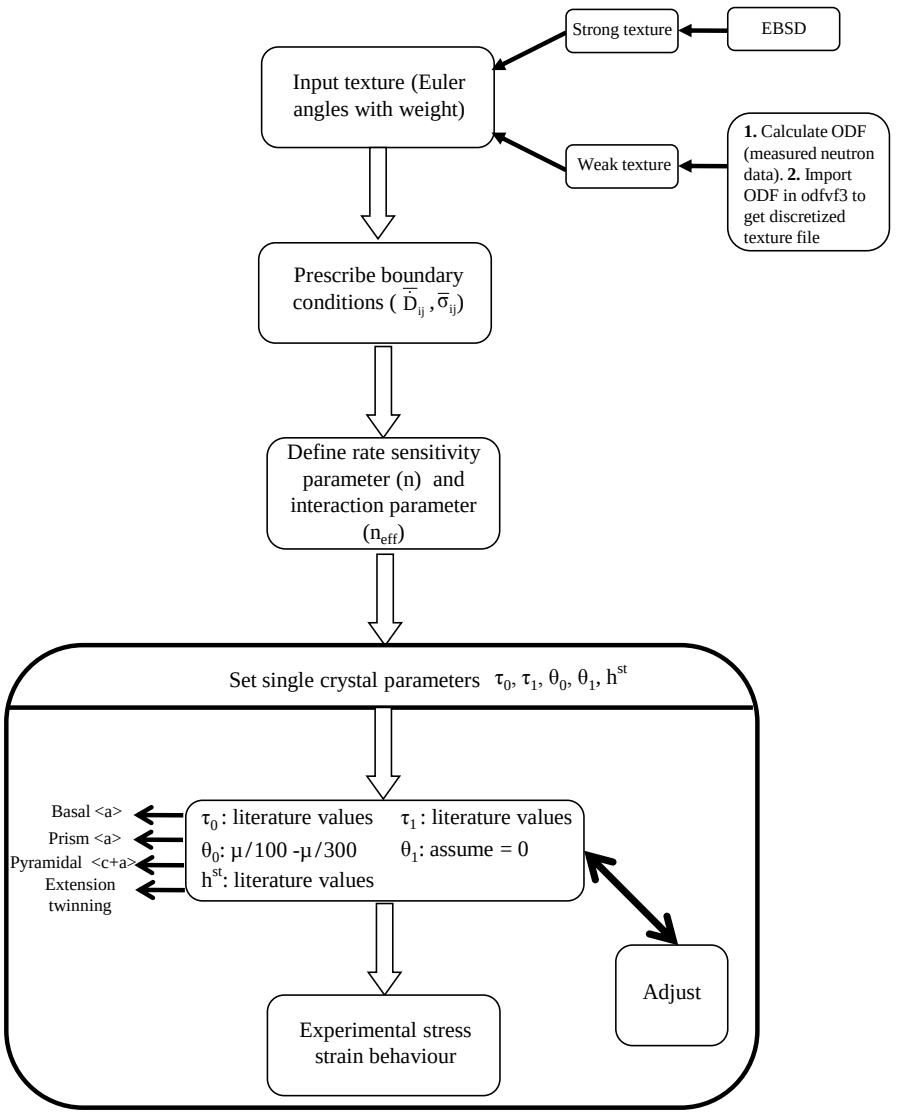

Figure 4.14: A schematic drawing illustrating the steps involved in the VPSC simulations.

components ($\bar{\sigma}_{ij}$)) are as follows:

$$\dot{\bar{D}}_{ij} = \begin{pmatrix} * & 1 & 1 \\ 1 & * & 1 \\ 1 & 1 & 1 \end{pmatrix}, \bar{\sigma}_{ij} = \begin{pmatrix} 1 & * & * \\ * & 1 & * \\ * & * & * \end{pmatrix} \quad (4.1)$$

Where the asterisk indicates that the corresponding value is not prescribed. Equation 4.1 indicates that the strain rate was imposed along the macroscopic straining direction (in this case $\dot{\varepsilon}_{33}$) while its transverse components ($\dot{\varepsilon}_{22}$ and $\dot{\varepsilon}_{11}$) were set as unknowns. In this way the R-value (ratio of width strain to thickness strain) of the material is not prescribed from the outset.

After each deformation step, the shape and crystallographic orientation of grains are updated (according to the procedure outlined in [160-162]), while local (grain-level) and global deviatoric stress and strain rate tensors are calculated (as described in Appendix A2). During calculations, an exponent of n = 20 was used (see equation A2.1 in Appendix A2) to describe the rate dependence of slip and twinning systems. The local response is coupled with the aggregate using an interaction equation (see equation A2.6) derived from the Eshelby's [152] inclusion formalism. During this an interaction parameter (n_{eff}) which dictates the interaction strength between grain to its neighbours is assigned to be n_{eff} =10 (i.e. intermediate between Taylor ($n_{eff} \rightarrow 0$) upper bound and Sachs ($n_{eff} \rightarrow \infty$) lower bound approach). This is a typical value used by many authors for calculating the response of HCP materials [54, 82].

During calculations four deformation modes were considered to be active per grain i.e. basal <a>, prismatic <a>, pyramidal <c+a> and $\{10\bar{1}2\}$ extension twinning (Figure 4.14). The shape change produced by the pyramidal <a> slip systems can be achieved through the combination of basal <a> and prismatic <a> slip systems, therefore the pyramidal <a> slip system is not included in the current simulations with an aim to keep the fitting parameters minimum. One might also argue about the possible inclusion of

contraction and double twinning considering the experimental evidence for their existence [62, 63, 66]. It will be clear from the experimental results presented in chapter 5, section 5.2 that these twin modes are relatively less important in the overall shear accommodation owing to the fact that they exist with volume fractions much lower than $\{10\bar{1}2\}$ extension twins.

The VPSC model for hexagonal materials has a large number of possible parameters that can be varied in order to obtain good agreement with experiment. In this work, it has been attempted to reduce the number of adjustable parameters using physical arguments. One way of doing this is through the reduction in total slip/twin modes as described in the previous paragraph. A detailed description of how the remaining adjustable single crystal parameters were set (Figure 4.14) is provided in section 6.2, however a brief outline of the approach can be given here. Starting from literature data, the values of the single crystal parameters were set and a simulation was performed. The results were compared quantitatively between the predicted and experimental stress-strain curves. Also a qualitative comparison between the slip and twin mode activity observed experimentally and due to simulations was made. Based on knowledge of the texture, loading condition and experimental results (e.g. slip trace analysis) the single crystal parameters for the most active deformation systems was adjusted. This procedure was iterated until a good agreement was obtained between experiment and simulation.

Simulating the response of material with different starting textures (strong and weak) in different deformation paths (i.e. TTC, IPT and IPC), while ensuring a single set of self-consistent single crystal parameters provides a strong test for the model.

CHAPTER 5 - The Deformation of AZ80 at Low Temperatures

5.1 Introduction

This chapter is concerned with a study of the effect of i) temperature and ii) initial texture on the mechanical response of the solution-treated AZ80 magnesium alloy. Both strong and weak, initial textures were examined. First the experimental results obtained on strong textured material will be presented in section 5.2. The advantage of examining the strong textured magnesium first is that by changing the test direction with respect to the texture one can favour certain deformation modes [98, 163]. Specifically: i) compression parallel to ND (TTC) favours pyramidal <c+a> slip (Figure 5.1a), ii) tension parallel to RD (IPT) favours prismatic slip (Figure 5.1b) and iii) compression parallel to RD (IPC) favours extension twins (Figure 5.1c). On the other hand, the weakly textured material operates all the deformation modes making interpretation more complex as will be presented in section 5.3. The results section includes mechanical tests, neutron diffraction, Nomarski microscopy, high and low resolution EBSD characterization. These results will be discussed in detail to provide a self-consistent view of the material behaviour.

5.2 Strong textured material

Figure 5.2 shows the inverse pole figure map of the strong textured, solution-treated AZ80 alloy prior to deformation. The average initial grain size was determined to be 32 μm using ASTM E 112 [156]. The maps in Figure 5.2a and 5.2b illustrate the orientation of loading axis prior to TTC and IPT or IPC, respectively. As can be seen during TTC, the majority of grains have their <c> axes close to being parallel to the

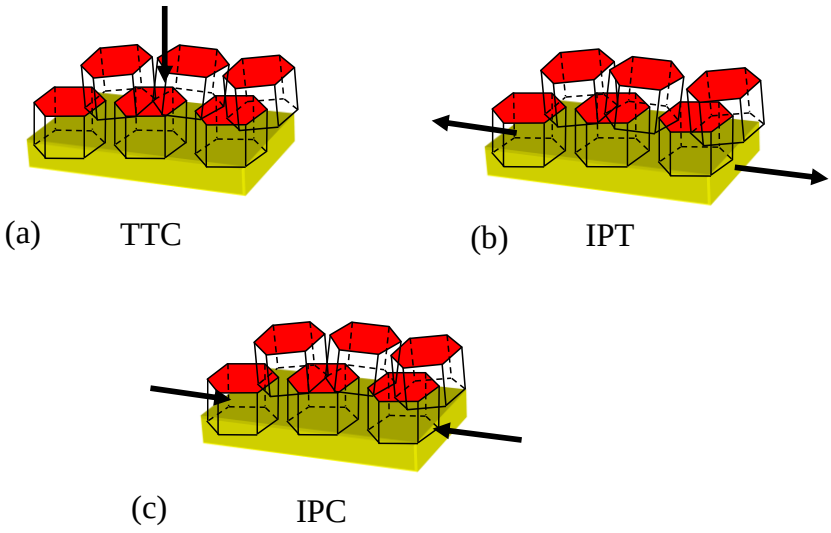

Figure 5.1: Schematic drawings illustrating the orientation and the sense of loading axis with respect to HCP <c> axes for **a)** through-thickness compression (TTC) **b)** in-plane tension (IPT) and **c)** in-plane compression (IPC).

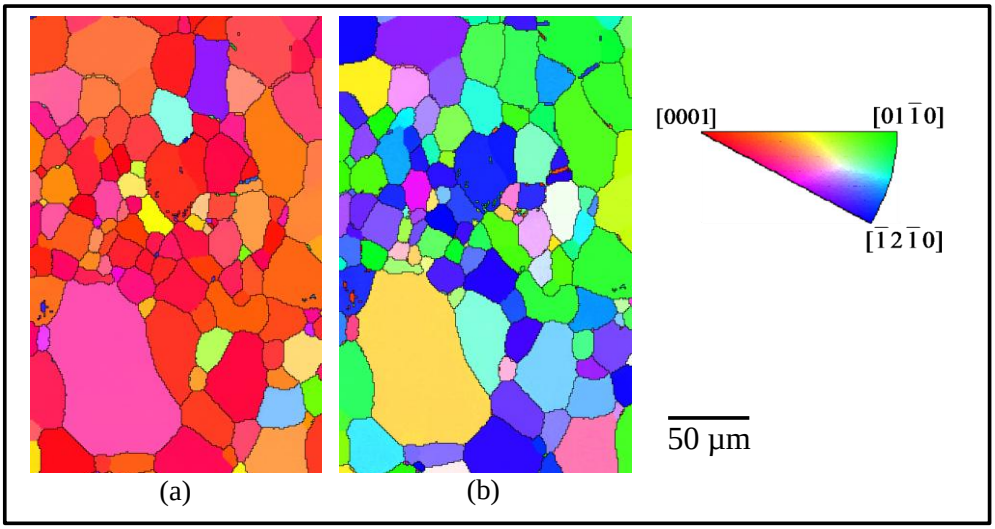

Figure 5.2: Loading axis inverse pole figure (IPF) maps of a recrystallised sample (referred to here as strong textured case) for **a)** TTC and **b)** IPT or IPC case. The colouring in the IPF map indicates the orientation of loading axis with respect to the HCP reference frame.

compression axis, while during IPT or IPC the <c> axes lie approximately perpendicular to the loading axis.

5.2.1 Experimental results

5.2.1.1 Macroscopic stress-strain behaviour

5.2.1.1.1 Through-thickness compression (TTC)

Figure 5.3a shows the true stress-true strain response of strong textured solution-treated samples compressed in the through-thickness (TT) direction at 77K (blue curve) and 293K (red curve). The maximum compressive strain that could be applied was limited by a sudden catastrophic failure of the sample. Significant differences in the stress strain responses can be noticed for the two test temperatures. Table 5.1 provides a summary of the 0.2% yield stress and the failure stress for the samples tested at 77K and 293K. The samples deformed at 77K exhibit approximately 1.5 times higher yield stress and nearly 2 times higher failure stress than the samples deformed at 293K. In addition, the samples deformed at 77K reveal what appears to be a rather extended elastic-plastic transition (Figure 5.3a). This can be attributed to the micro-yielding of grains in soft orientations (due to <c>-axis spread in the initial texture). Several authors [78, 164, 165] have reported a similar pseudo-elastic response in magnesium alloys and ascribed it to the local activation of basal slip.

It is significant to point out that the fracture stresses observed are extremely high, particularly at 77K. To interpret this in a more quantitative manner, it is assumed that the

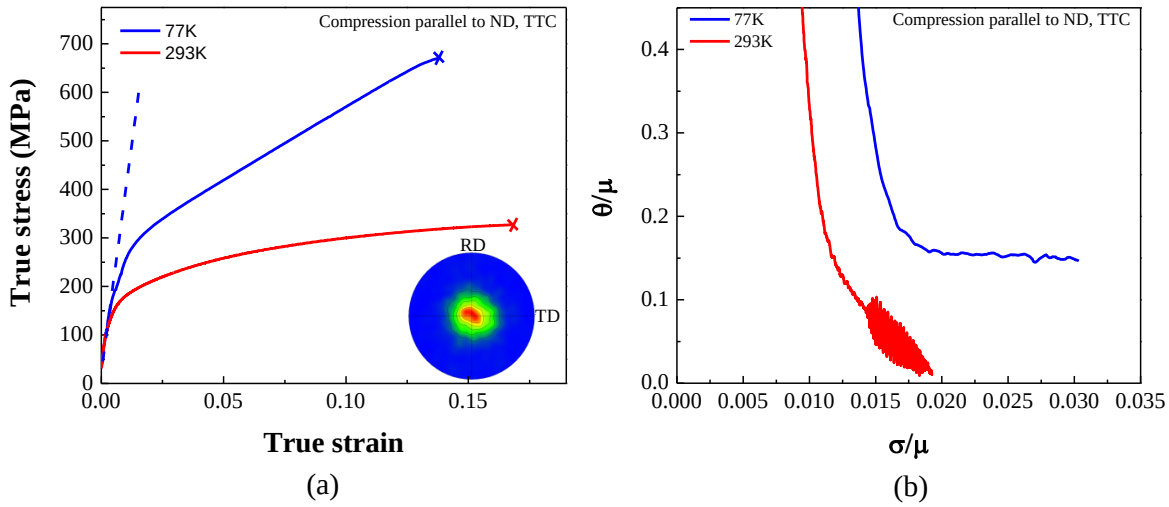

Figure 5.3: a) True stress-strain curves and **b)** normalised work hardening rate (θ/μ) vs. normalised stress (σ/μ) plots for strong textured solution-treated AZ80 alloy compressed along ND direction (referred here as TTC) at 77K (blue curve) and 293K (red curve). The {0001} pole figure (inset) illustrates the texture prior to compression. The broken line (blue colour) is added to guide the linear elastic portion of the stress strain curve, while × indicates the fracture of the sample.

Table 5.1: Value of 0.2% offset yield stress and maximum failure stress for samples deformed in compression and tension at 77K and 293K. Each reported value is an average of three measurements. The variation between these three measurements was within ± 5%

Testing condition			*0.2% offset yield strength (MPa)*	*Maximum stress to failure (MPa)*
Strong textured	Through-thickness compression (TTC)	77K	225	670
		293K	160	326
	In-plane tension (IPT)	77K	224	322
		293K	164	318
	In-plane compression (IPC)	77K	110	922
		293K	93	362

maximum resolved shear stress is the compressive stress divided by two then it gives a maximum shear stress of 335 MPa at 77K. This is approximately within a factor of two compared to the theoretical shear strength of $\mu/20$ (where μ is the shear modulus $\approx$ 17 GPa) or approximately 850 MPa. The theoretical shear stress could easily be reached at a local level if one considers stress concentrations around Mn second phase particles or at other inhomogeneities in the microstructure.

The work hardening behaviour can be quantitatively analysed by numerically differentiating the stress strain data. Figure 5.3b compares the hardening rate normalized by the temperature dependent shear modulus as a function of the true stress for the two testing conditions. The hardening rates exhibited by the sample tested at 77K (blue curve) are extremely high compared with the sample tested at 293K (red curve). Shortly after yield, the work hardening rate is constant with stress for the sample deformed at 77K while it steadily decreases with stress for the sample deformed at 293K. Furthermore, at 77K, the hardening curve is smooth while at room-temperature, oscillations are observed for normalised stresses of ≥ 0.014, which corresponds to $\geq 5\%$ strain. Indeed, Corby and co-workers [166] have observed similar serrations in the flow behaviour of solution-treated AZ91 (Mg-9Al-1Zn) magnesium alloy at room-temperature. They attributed this to the interaction between the moving dislocations and Al solute atoms.

5.2.1.1.2 In-plane tension (IPT)

The tensile stress-strain response of samples loaded in the RD-TD plane (referred to as in-plane tension or IPT) at 77K (blue curve) and 293K (red curve) are shown in Figure 5.4a. For the sample deformed at 77K, the yield stress is approximately 1.7 times

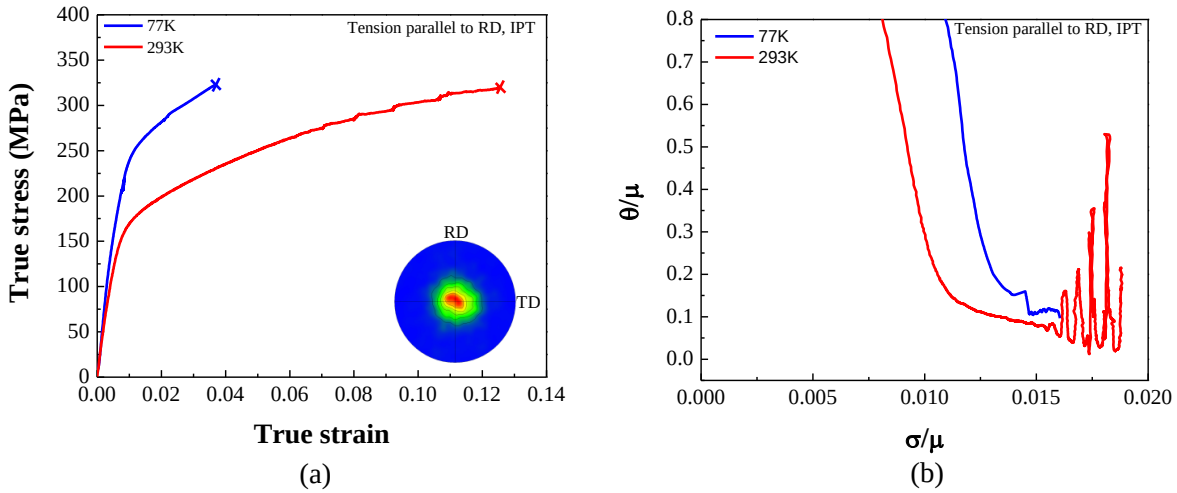

Figure 5.4: a) True stress-strain curves and **b)** normalised work hardening rate (θ/μ) vs. normalised stress (σ/μ) plots for strong textured solution-treated AZ80 alloy tensioned along RD (referred here as IPT) at 77K (blue curve) and 293K (red curve). The {0001} pole figure (inset) illustrates the texture prior to compression, while the symbol × indicates the fracture of the sample.

greater than at 293K, while the fracture stress is almost independent of test temperature (see Table 5.1). The other significant difference between the two conditions was the uniform elongation, which is considerably lower at 77K than at 293K (i.e. 3% vs. 12%). It is also worth noting that samples tested at 293K exhibit serrated flow that can be seen shortly after a true strain of approximately 5-6% (similar to the TTC case presented above). The serrations appear larger here but this is probably a reflection of the difference in testing methodology for compression and tension tests, i.e. for compression tests the use of an extensometer mounted on the sample is not possible.

The variation of θ/μ versus σ/μ for the samples deformed at 77K and 293K are presented in Figure 5.4b. In general, the work hardening plots exhibit an initial transient

region of rapid decrease in work hardening rate followed by a region of gradual decrease. For the RT case, it can also be observed that the work hardening curve which was smooth at lower macroscopic stresses shows oscillations at larger stresses (i.e. after $\sigma/\mu \sim 0.015$).

5.2.1.1.3 ***In-plane compression (IPC)***

Figure 5.5a shows the true stress-strain response of samples compressed parallel to the rolling direction (i.e. in-plane compression, IPC) at 77K (blue curve) and 293K (red curve). In general, the flow curves exhibit a well defined elastic-plastic transition followed by a low hardening plateau which is considered to be associated with $\{10\bar{1}2\}$ twinning [99]. After a true strain of ≈ 5-6%, an inflection is reached in the curve where the

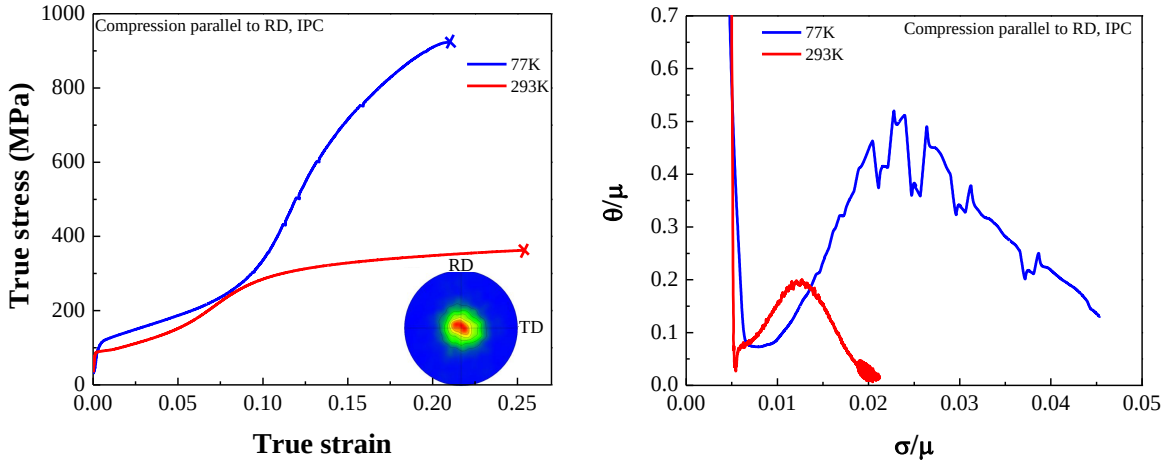

Figure 5.5: a) True stress-strain curves and **b)** normalised work hardening rate (θ/μ) vs. normalised stress (σ/μ) plots for strong textured solution-treated AZ80 alloy compressed along RD direction (referred as IPC) at 77K (blue curve) and 293K (red curve). The {0001} pole figure (inset) illustrates the texture prior to compression, while the symbol × indicates the fracture of the sample.

hardening rate starts to increase with increasing strain. Eventually, the curve reaches a point where the hardening rate attains a maximum. Thereafter it starts to decrease again. More specifically, the yield stress at 77K is only slightly higher than at 293K, however, the fracture stress is very large at 77K compared with that at 293K (see Table 5.1). Also, the curve at 77K shows several points with load drops.

Figure 5.5b shows the normalised work hardening rate (θ/μ) plotted against the normalised true stress (σ/μ). For deformation at 77K and 293K, after the initial decrease associated with elastic-plastic transition, the hardening rate dramatically increases, reaches a maximum and then decreases. The value of maximum hardening rate attained at 77K is almost double to that of at 293K (e.g. $(\theta/\mu)_{77K} \sim 0.45$ while, $(\theta/\mu)_{293K} \sim 0.22$).

5.2.1.2 EBSD observations on strong textured material

The representative EBSD maps of selected deformation conditions are presented in this section. The intent of these maps is to underline the key deformation mechanisms responsible for strain accommodation under specific loading condition.

5.2.1.2.1 Through-thickness compression (TTC)

Figure 5.6 provides a comparison of deformed microstructures obtained for the samples compressed to 0.08 strain in ND direction (i.e. TTC) at 77K and 293K. The results of the EBSD measurements are presented in the form of band contrast maps (Figure 5.6a and 5.6b) and inverse pole figure (IPF) maps (Figure 5.6c and 5.6d). The active twin types in these maps were identified using the boundary misorientation axis-angle relationship. Several types of boundaries were identified, including extension twins, contraction twins and contraction-extension twins.

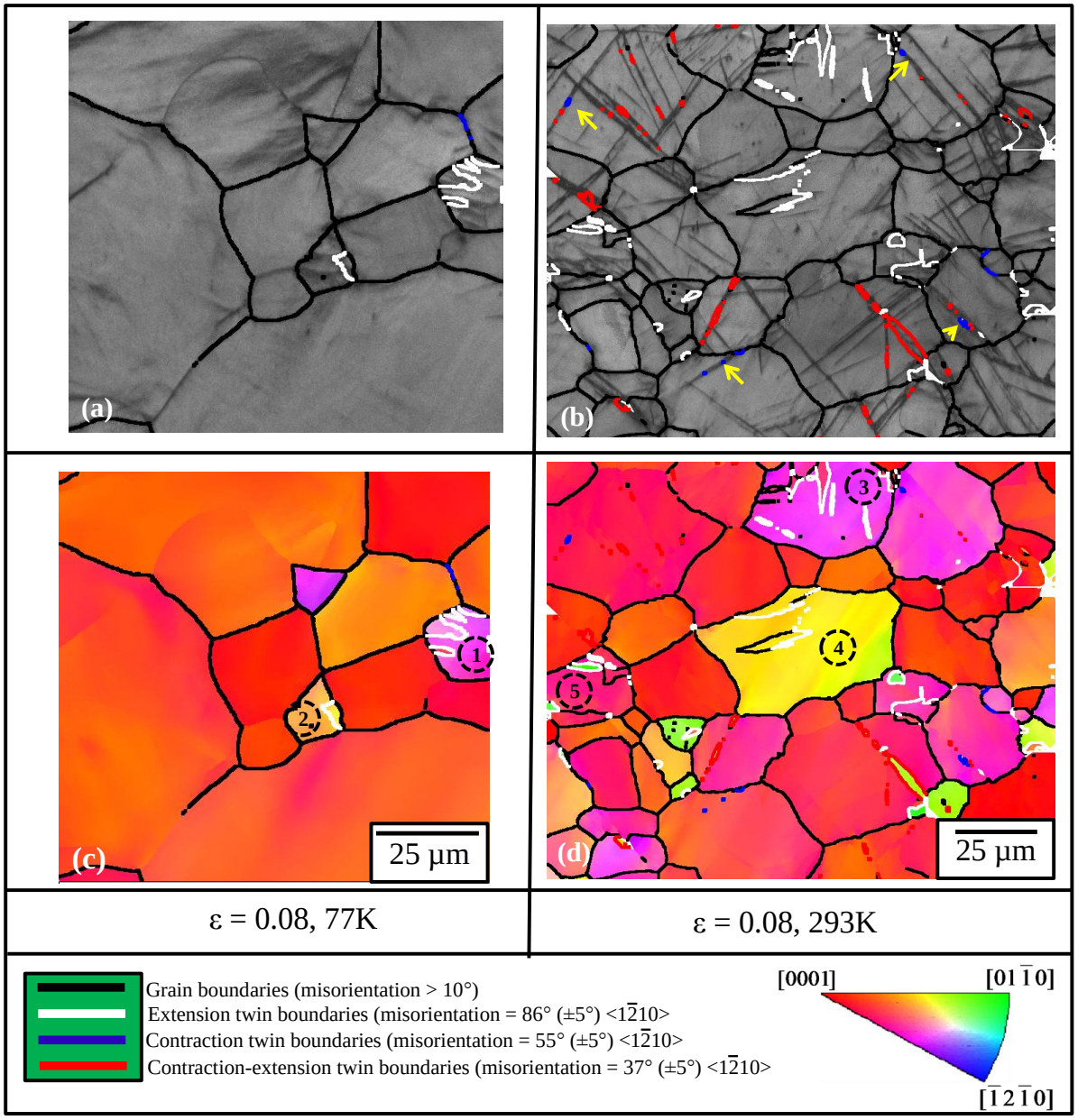

Figure 5.6: a) and **b)** show the pattern quality EBSD maps for the samples compressed in TT direction to a strain of ~ 0.08 at 77K and 293K, respectively while, **c)** and **d)** illustrate the corresponding compression axis inverse pole figure (IPF) maps. The numbered grains highlight the grains that exhibit extension twinning. The colouring in the IPF map indicates the orientation of the compression axis with respect to the HCP reference frame (bottom right of the maps). The arrows in b) indicate the presence of contraction twins.

At a strain of 0.08, $\{10\bar{1}2\}$ extension twins are observed in a few grains (see the grains labelled as 1-5 in Figure 5.6c and 5.6d) with c-axis oriented roughly at 45° to the compression axis (notice the colouring of the grains that exhibit extension twinning) at both temperatures. For the RT sample, there are grains with their c-axis oriented close to the compression axis that contain $\{10\bar{1}1\}$ contraction twins (see the arrowed twins highlighted with blue colour boundaries in Figure 5.6b) and $\{10\bar{1}1\}-\{10\bar{1}2\}$ contraction-extension double twins (red colour boundaries). Additionally, one can also discover many unidentified fine features that are present in the band contrast map of this particular condition (see Figure 5.6b). It may be that these features correspond to very fine deformation twins. In comparison the map from the sample deformed at 77K does not reveal the fine features in the band contrast maps and there is no evidence of presence of contraction twins or contraction-extension double twins at 77K. However, these results are based upon the limited number of grains that were analysed.

5.2.1.2.2 In-plane compression (IPC)

The EBSD band contrast map of a sample compressed parallel to the rolling direction (IPC) to a true strain of 0.05 at 293K is shown in Figure 5.7a, while the corresponding compression axis IPF map is presented in Figure 5.7b. For this condition maps were only measured for samples deformed at 293K. At a strain of 0.05, a significant fraction of material has been re-oriented with their c axis close to the compression axis (see the colour of grains before and after compression in Figure 5.2b and Figure 5.7b, respectively). A careful analysis of these maps reveal several distinct characteristics: i) the main active twin system is $\{10\bar{1}2\}$ confirmed by boundary misorientation analysis (notice

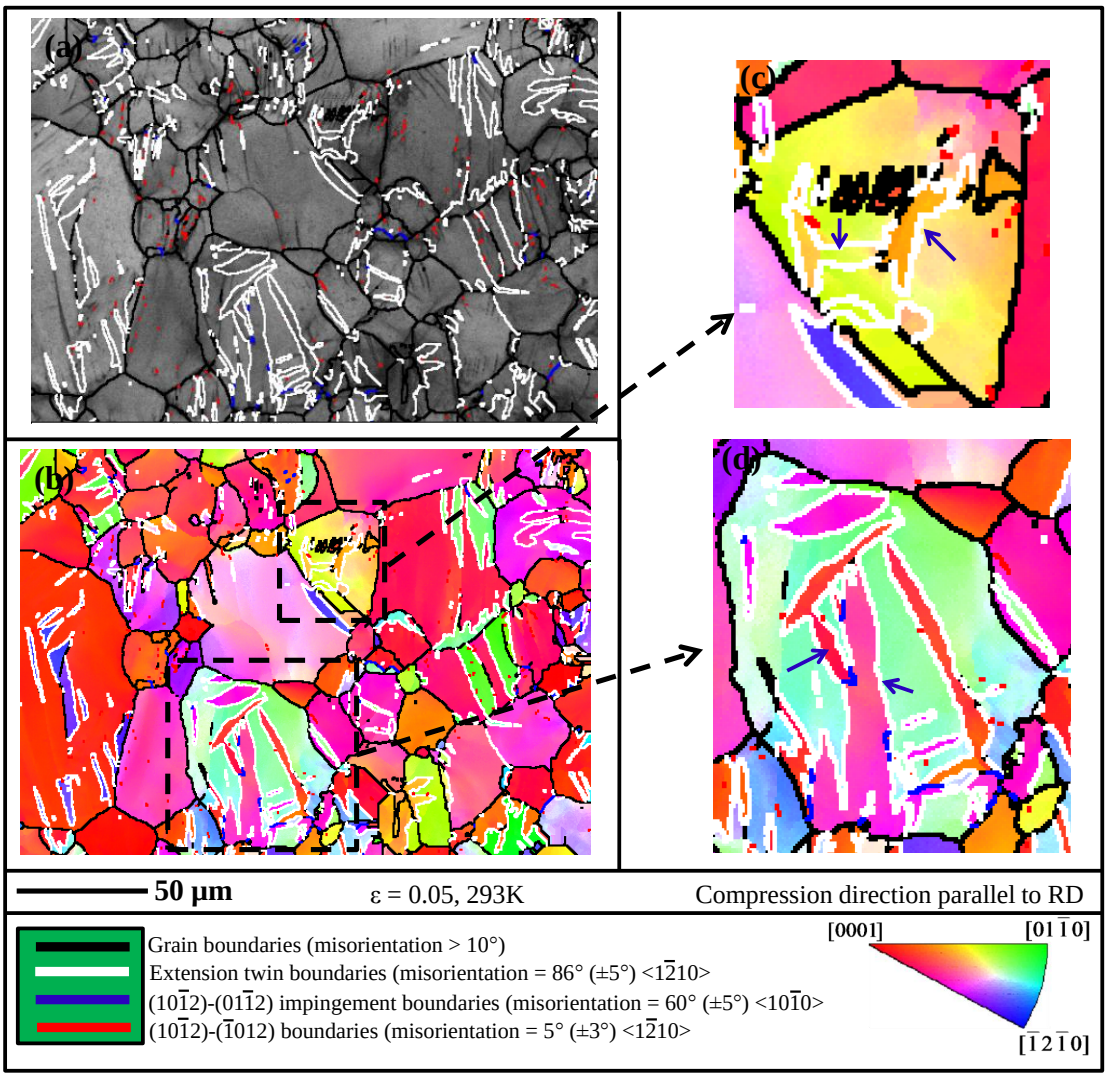

Figure 5.7: a) EBSD pattern quality map and **b)** the compression axis IPF map of solution-treated sample compressed along RD direction (i.e. IPC) to a true strain of 0.05 at 293K, while **c)** and **d)** are the expanded views of the grains shown in b). The colouring in the IPF map indicates the orientation of compression axis with respect to the HCP reference frame. The arrows indicate the different variants of extension twins in a specific grain.

the white colour boundaries in Figure 5.7), ii) the majority of twins appear as thick bands as opposed to thin bands observed in TTC sample, iii) qualitative observation of the IPC map reveals a considerably greater concentration of twins as compared to the TTC map, iv)

many grains contain more than one active twin variant (see the arrowed twins in Figure 5.7c and 5.7d), v) these different twin variants impinge on each other and result in boundaries having a misorientation of 5° $<1\bar{2}10>$ (see the red colour boundaries in Figure 5.7) and 60° $<10\bar{1}0>$ (see the blue colour boundaries in Figure 5.7d). A detailed explanation on the formation twin-twin impingement boundaries has recently been given by Nave and Barnett [99]. In brief, when a grain twins on both the $(10\bar{1}2)$ and $(\bar{1}012)$ (or equivalent pairs of) planes, impingement of these twins results in a boundary of misorientation 5° $<1\bar{2}10>$. Similarly, the impingement of $(10\bar{1}2)-(0\bar{1}12)$ twins results in a boundary of 60° misorientation about $<10\bar{1}0>$.

5.2.2 Discussion

The discussion of the results on strong textured materials is divided into two sections. In the first section, the effect of loading direction on the yield and work hardening characteristics of the alloy is addressed. In the second section, the effect of temperature on the mechanical properties of the alloy is discussed.

5.2.2.1 Effect of loading direction

The loading direction has a pronounced effect on the yield strength and the work hardening characteristics of the AZ80 magnesium alloy (Figure 5.8). For instance, the TTC sample exhibits a yield strength that is approximately 2 times higher than the yield strength for the IPC sample at 77K and a nearly 1.7 times higher at RT as can be seen in Figure 5.8. During IPC, most grains are oriented such that their c-axes are nearly perpendicular to the macroscopic compression direction. In such a situation, one would anticipate the deformation to be accommodated by extension twinning and prismatic slip. However,

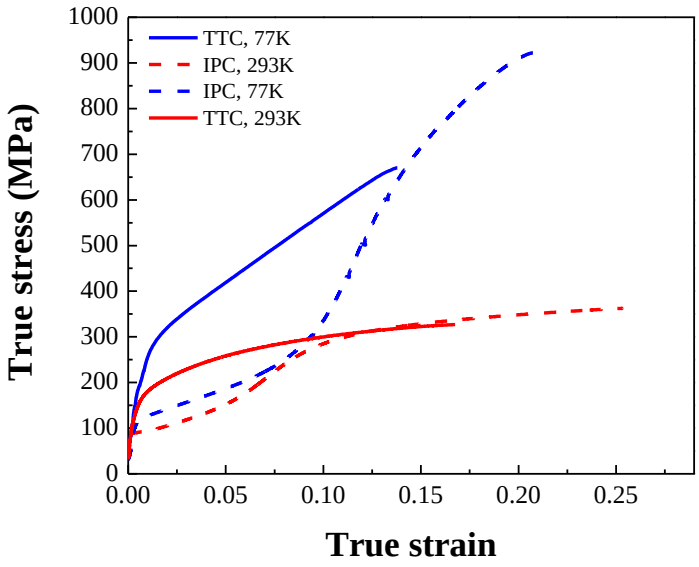

Figure 5.8: Effect of loading direction on true stress strain response of strong textured AZ80 alloy at 77K (blue colour) and 293K (red colour).

compared to prismatic slip, $\{10\bar{1}2\}$ twinning is easy to activate (has a much lower CRSS value (see ref. [38, 59]). Thus, it is expected that deformation will be dominated by $\{10\bar{1}2\}$ twinning. On the other hand, during TTC, the grains are oriented with their <c>-axes near to the compression axis. Therefore, the resolved shear stress on the basal and prismatic slip systems is nearly zero, and deformation must occur by the difficult <c+a> slip and/or twinning on $\{10\bar{1}1\}$ and $\{10\bar{1}1\}-\{10\bar{1}2\}$ planes. However, these systems are significantly stronger (have much higher CRSS value) compared to $\{10\bar{1}2\}$ twinning and {0001} basal slip (see ref. [38, 41, 42, 59, 60]). This explains the fact that the TTC compression samples exhibit much higher yield strength than the IPC samples.

Overall, the work hardening rates of all samples in the plastic regime are very high (θ/μ ~ 0.15-0.3), i.e. much higher than one would expect in FCC or BCC metals [74]

where the maximum hardening rate in single phase materials would be $\theta/\mu \sim 0.05\text{-}0.1$. As seen in Figure 5.9, the work hardening characteristics of the TTC samples differ significantly from the IPC samples. At 293K, the work hardening rate of the IPC samples following yield dramatically increases, reaching a maximum, before decreasing again. Comparatively, the work hardening rate of TTC sample decreases with increasing flow stress. In the past, several authors [61, 99, 107, 110, 167] have reported a similar increase in hardening rates for many HCP metals (e.g. Zr, Ti, Mg etc.) loaded under similar conditions. They commonly ascribed this to the twinning activity. However, the general description of the hardening curve for magnesium is different from other HCP metals. For example, in Zr, an increase in hardening rate is indicative of onset of twinning while, the point of maximum hardening dictates the saturation of twinning [107, 110]. Comparatively, in magnesium a considerable fraction had reportedly been twinned prior to the onset of the rapid rise in the hardening rate (e.g. for pure magnesium at 3% strain around 42% of material had twinned [33]). Over the years, several factors have been considered to explain the high hardening rates: i) the geometric effect [76, 99, 100], ii) the Hall-Petch effect [82], iii) the Basinski effect [90, 91]. Nonetheless, complete quantitative explanation on this is still missing.

5.2.2.2 Effect of temperature

Nearly, a factor of 1.4 drop in yield strength is observed in the TTC samples with increasing temperature from 77K to 293K (Figure 5.10). During TTC, pyramidal <c+a> slip and contraction twinning are considered to be the important deformation mechanisms. Basal slip can also be active in grains that are oriented slightly away from the compression axis. Based on the EBSD observations, only the 293K-TTC samples showed the presence

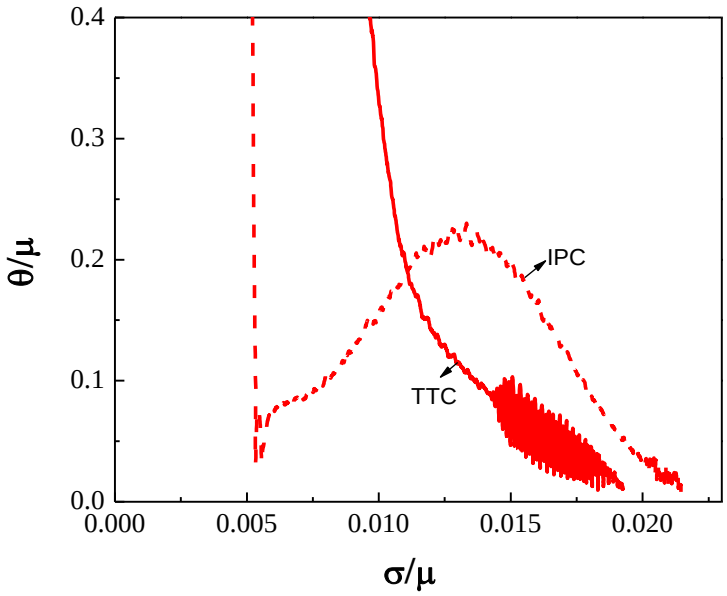

Figure 5.9: Normalised work hardening rate (θ/μ) vs. normalised stress (σ/μ) plots for strong textured solution-treated AZ80 alloy in IPC (dashed line) and TTC (solid line) at 293K.

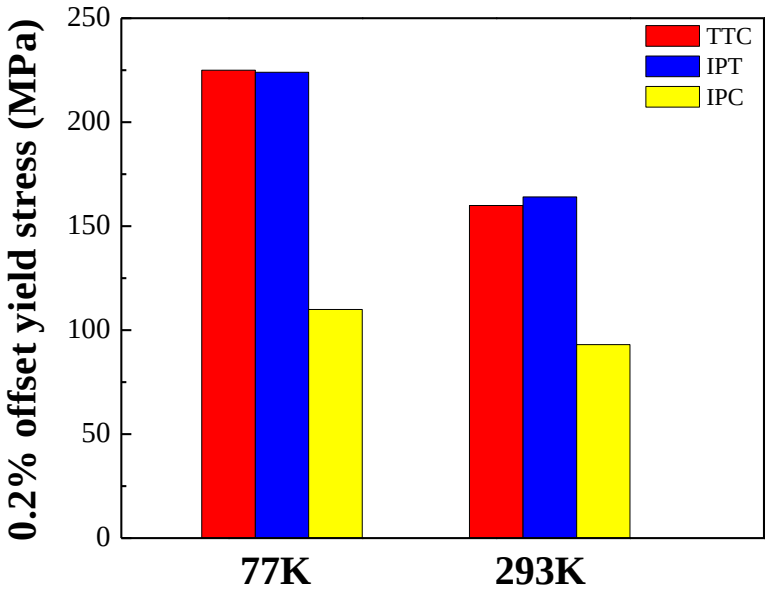

Figure 5.10: 0.2% offset yield stress for samples deformed in TTC (red bars), IPT (blue bars) and IPC (yellow bars) at 77K and 293K.

of contraction twins and contraction-extension double twins, while both 293K-TTC and 77K-TTC samples illustrated the presence of extension twins in the grains that are oriented nearly 45° away from the compression axis. The latter observation can relate to easy activation of $\{10\bar{1}2\}$ extension twinning even in the grains less suitably oriented for twinning (Schmid factor < 0.35). Recently, Beyerlein and co-workers [33] have reported similar observations in pure magnesium. According to them, the crystallographic orientation is not the only factor that determines twinning. Factors that can affect the local grain boundary stress state such as neighbour grain orientations also need to be accounted for in magnesium.

In the present analysis, the <c>-axis contraction twins and double twins ($\{10\bar{1}1\}-\{10\bar{1}2\}$) appeared as fine bands consistent with the previous reports [47, 62]. Because of the size of these twins it is expected that the volume fraction of material associated with them would be low. Based on this, one may also speculate that the overall contribution from these twins to strain accommodation and texture evolution will be less significant. These twins can play a significant role, however in the process of damage initiation as suggested by other researchers [65, 66, 68]. The results also indicate a drop in the importance of contraction twinning with lowering temperature to 77K. This conflicts with conventional wisdom which emphasises the increase in twinning contribution with decreasing temperature. Nonetheless, if one considers a previously reported statement that the twin activation stress is temperature independent [169] then the drop in yield stress with increasing temperature would reflect the temperature-dependant decrease in CRSS for 2nd order pyramidal <c+a> slip.

A yield stress drop of nearly a factor of 1.65 is observed in IPT with increasing temperature from 77K to 293K (Figure 5.10). During IPT, deformation is expected to be dominated by prism <a> slip [8, 47, 170-172]. One cannot neglect, however the possibility of basal slip, particularly in grains with their c-axes oriented slightly away from the ND direction of the sheet. Recent investigations [8, 47] on sheet AZ31 magnesium alloy loaded in IPT illustrate the importance of prismatic slip. The drop in yield stress with increasing temperature can reflect the drop in the CRSS value of prismatic slip with increasing temperature.

Unlike the TTC and IPT case, a small drop in yield strength is observed for IPC sample with increasing temperature from 77K to 293K as can be seen in Figure 5.10. Based on the initial loading condition, $\{10\bar{1}2\}$ extension twinning is expected to be the dominant deformation mechanism at both temperatures. The EBSD observations further confirm the presence of copious amounts of $\{10\bar{1}2\}$ extension twinning under IPC (Figure 5.7). The near insensitivity of yield stress with temperature seems consistent with the literature which suggests that the twin activation stress is nearly temperature independent [169].

As can be seen from Figure 5.11, reducing the testing temperature to 77K markedly affects the work hardening characteristics of TTC and IPC samples. For TTC, after initial yield, the hardening curve at 77K exhibits a nearly constant hardening region over a substantial range of strain. This resembles stage II work hardening in cubic crystals (where athermal dislocation storage dominates) [73]. This can be attributed to the lack of dynamic recovery at 77K. The stacking fault energy calculations of Legrand [4] suggest that the cross-slip of basal dislocations to prism planes and vice-versa is favourable in

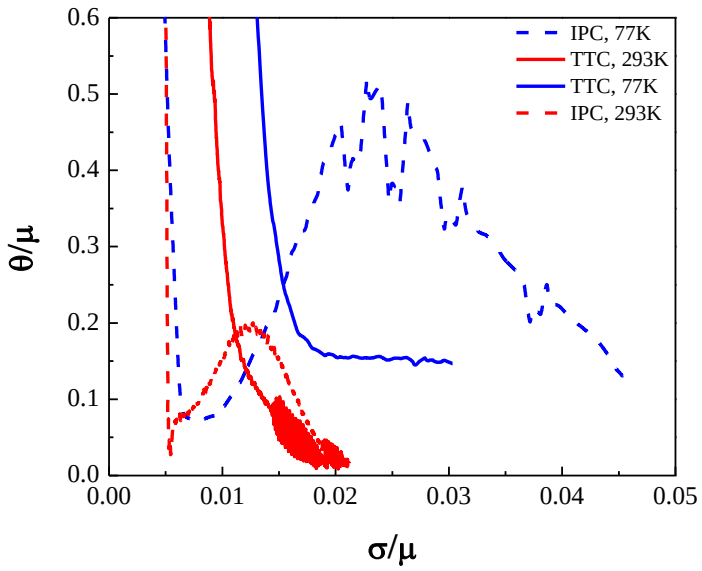

Figure 5.11: Normalised work hardening rate (θ/μ) vs. normalised stress (σ/μ) plots for samples tested in IPC (dashed lines) and TTC (solid lines) at 77K (blue colour) and 293K (red colour).

magnesium. Several authors [5, 7, 8] have confirmed this experimentally. Based on this, at 293K, barriers to dislocation motion can be overcome by cross-slip. Cross-slip, however, becomes more difficult at 77K. This results in lower rates of dynamic recovery and therefore a high hardening rate. One might also argue for the importance of cross-slip of pyramidal <c+a> slip which is presumably very difficult at 77K due to its large Burgers vector. There is, unfortunately, no direct experimental evidence to supports this.

The general shape of the hardening curve of 77K-IPC sample is very similar to 293K-IPC samples except the highest hardening rate achieved by 77K-IPC sample is twice as high as that in the 293K-IPC sample (Figure 5.11). While a detailed understanding of this effect is lacking at present, one might speculate that it is related to the temperature dependence of i) the rate of mechanical twinning ii) rate of dynamic recovery.

5.2.3 Summary

The mechanical behaviour of strong textured solution-treated AZ80 alloy at low-homologous temperatures has been investigated. The testing of strong textured material in variety of loading conditions (i.e. TTC, IPT and IPC) allowed us to preferentially probe the various deformation mechanisms operative in magnesium.

The yield and work hardening characteristic of the strong textured alloy varies greatly with the loading direction. The observed differences in the stress strain behaviour can be rationalised based on the specific slip and/or twin system activated. Moreover, the temperature has a pronounced effect on the mechanical properties of the alloy. This can be understood based on the change in relative strength of particular slip modes and/or twin modes with temperature.

5.3 Weak textured material

Understanding the mechanical behaviour of weak textured material is much more challenging than the strong textured material. This is mainly due to the fact that deformation in such materials is accomplished by a mix of several slip modes and twin modes. The resulting behaviour is therefore strongly influenced by their complex interactions. In this section, a description of the mechanical behaviour of weak textured AZ80 alloy loaded in compression at 77K and 293K is provided. In particular, deformation mechanisms are quantitatively analysed and their role in deformation response at different temperatures is discussed.

Figure 5.12 shows the loading axis IPF map of solution-treated AZ80 alloy prior to compression. The initial material has an equiaxed grain structure with an average grain

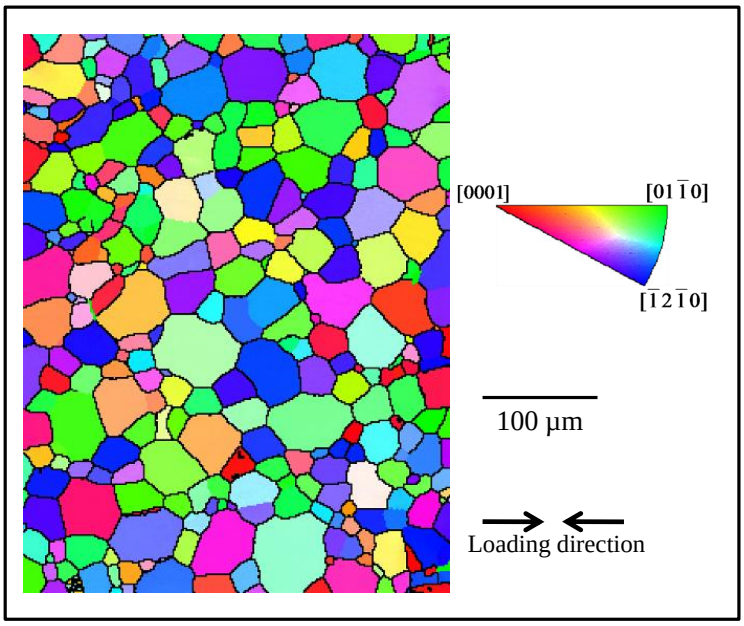

Figure 5.12: Loading axis inverse pole figure (IPF) map of solution-treated AZ80 sample (referred here as weak textured material) illustrating the grain orientations and their structure prior to compression.

size of 32 µm i.e. the same grain size as the strongly textured material. As it can be noticed from Figure 5.12, the initial texture is nearly random with respect to compression direction (see the colour of the grains). The overall texture in this case can be described as weak texture (confirmed from neutron measured pole figure shown in Figure 5.14a).

5.3.1 Experimental results

5.3.1.1 Macroscopic stress-strain behaviour

Figure 5.13a shows the true stress true strain response of weak textured samples deformed in uniaxial compression at 77K and 293K. The 0.2% yield stress and the failure stress for the two test temperatures are summarized in Table 5.2. As one might expect, the

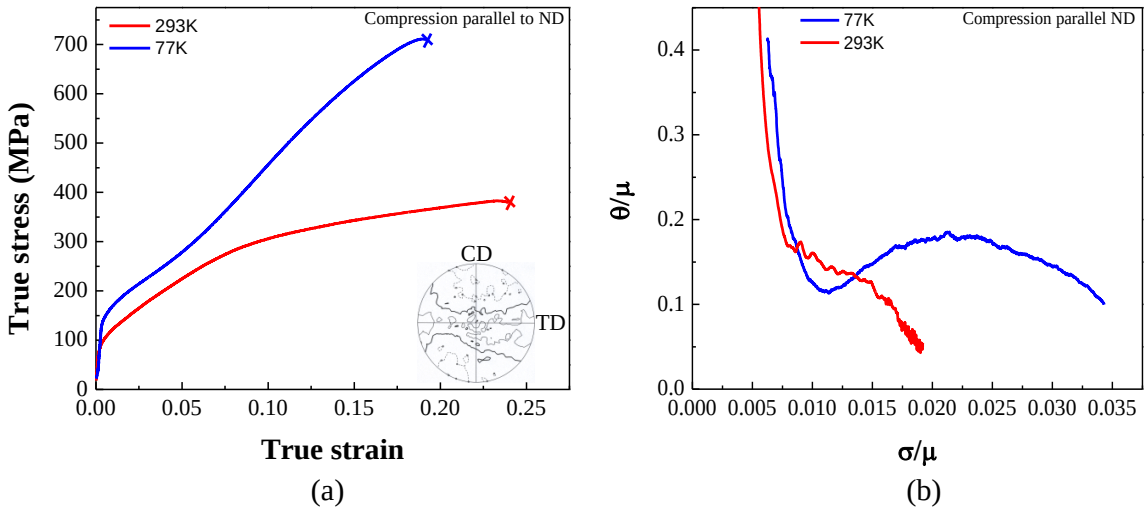

Figure 5.13: a) True stress-strain curves and **b)** normalised work hardening rate (θ/μ) vs. normalised stress (σ/μ) plots for weak textured solution-treated AZ80 tested at 77K (blue curve) and 293K (red curve). The {0001} pole figure (inset) illustrates the texture prior to compression, where the CD and TD correspond to casting direction and transverse direction of the sample, respectively. Note that the symbol × indicates the fracture of the sample and the compression direction is at the center of the pole figure.

Table 5.2: Value of 0.2% yield strength and maximum stress to failure for weak textured samples compressed at 77K and 293K. Each reported value is an average of three measurements. The variation between these three measurements was within ± 3%

Testing condition			*0.2% offset yield strength (MPa)*	*Maximum stress to failure (MPa)*
Weak textured	Compression parallel to ND	77K	145	711
		293K	95	382

sample tested at 77K exhibits a higher yield strength and maximum stress at failure compared to the sample tested at 293K.

The corresponding normalised work hardening plots obtained from compression tests are presented in Figure 5.13b. At room-temperature, the hardening rate continuously decreases as the flow stress increases. At 77K, after an initial decrease, the hardening rate dramatically increases, reaches a maximum (i.e. $\theta / \mu \sim 0.175$). This is usually regarded as an indicator of significant deformation twinning during loading.

5.3.1.2 Bulk texture evolution

Neutron diffraction has been employed to systematically characterize the texture evolution in the weak textured alloy. The representative $\{0001\}$ and $\{10\bar{1}0\}$ pole figures of solution treated samples deformed in uniaxial compression at 77K and 293K are shown in Figure 5.14. The initial texture (labelled as $\varepsilon = 0$) and the texture after a true strain of 0.05 and 0.18 (i.e. just before fracture) for 77K deformed samples are shown in Figure 5.14a, 5.14b and 5.14c, respectively. Similarly, the textures after true strains of 0.05, 0.18 and 0.23 (i.e. measured from broken sample) for 293K deformed samples are presented in Figure 5.14d, 5.14e and 5.14f, respectively.

After $\approx 5\%$ strain, the alloy exhibits a typical "basal" texture, having its <c> axis aligned close to the compression axis and the tendency of $<10\bar{1}0>$ direction to align normal to the compression axis (Figure 5.14b and 5.14d). Further straining only serves to strengthen this texture as can be seen in Figure 5.14c, 5.14e and 5.14f (e.g. the maximum intensity of basal poles increases from 5.7 multiples of random distribution (m.r.d.) to 6.9 m.r.d. with increasing strain from 0.05 to 0.18 at 77K).

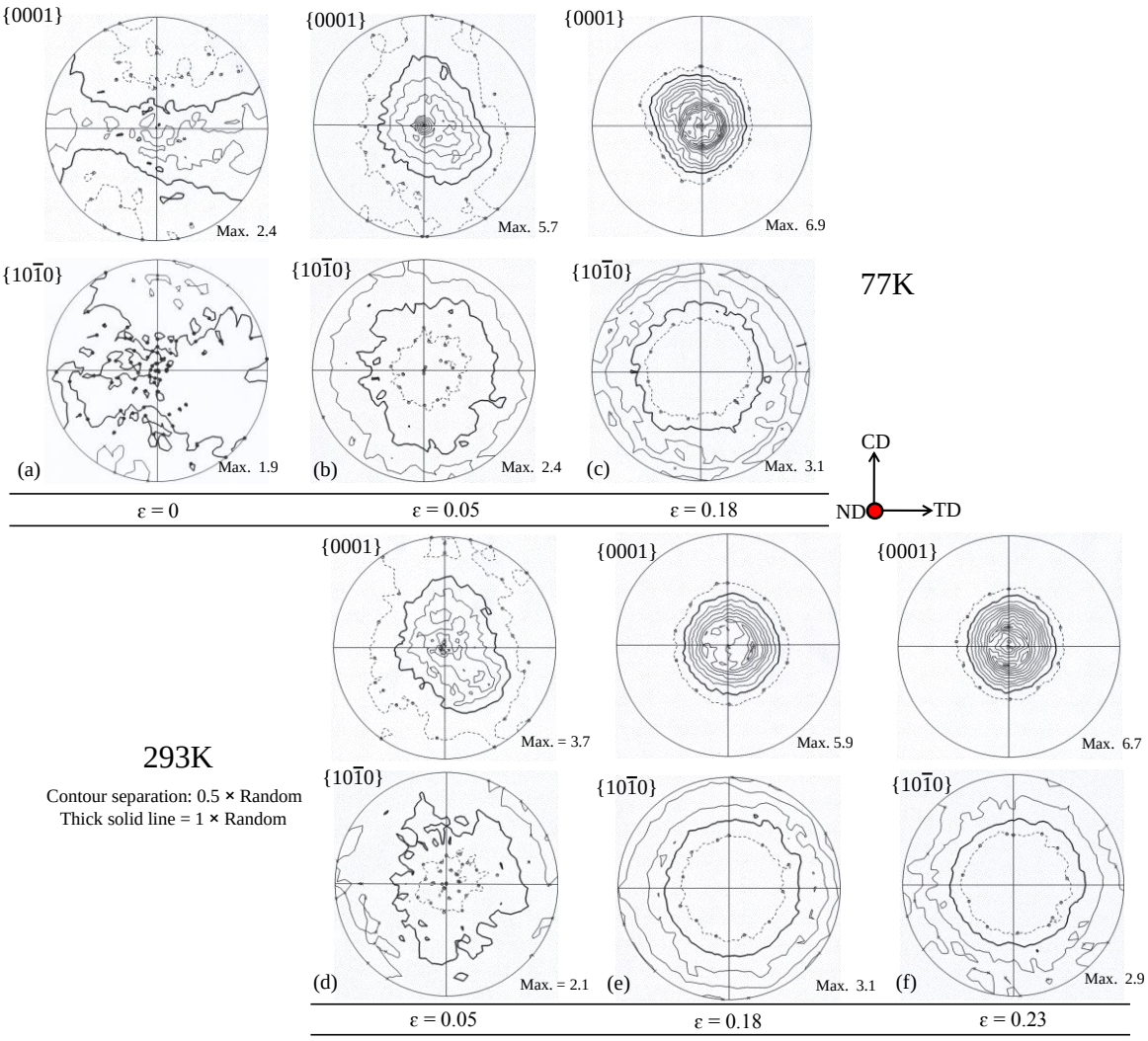

Figure 5.14: {0001} and {10$\bar{1}$0} pole figures (stereographic) representing the texture of the solution-treated sample **a)** before compression **b)** and **c)** after compressive strains of 0.10 and 0.18, respectively, at 77K while, **d)**, **e)** and **f)** after compressive strains of 0.10, 0.18 and 0.23, respectively at 293K. The CD, TD and ND correspond to casting direction, transverse direction and normal direction of the sample, respectively. Note that the compression direction is normal to the center of the pole figure (i.e. along ND direction).

Comparing the strength of the textures from samples deformed at 293K and 77K one observes similar results when compared at equal strain. This can be seen more quantitatively by evaluating the volume fraction of grains having their <0001> oriented within 40° of the compression axis (Figure 5.15). As can be seen in Figure 5.15, the <0001> texture strength increases with increasing strain for both temperatures. Moreover, except for 2% strain, the texture strength at all strain levels is only slightly higher at 77K than at 293K.

The experimentally measured {0001} pole figures were further evaluated in a more quantitative manner by estimating the extension twin volume fractions. The detailed procedure used is outlined in the Appendix A3. Figure 5.16 shows the evolution of the

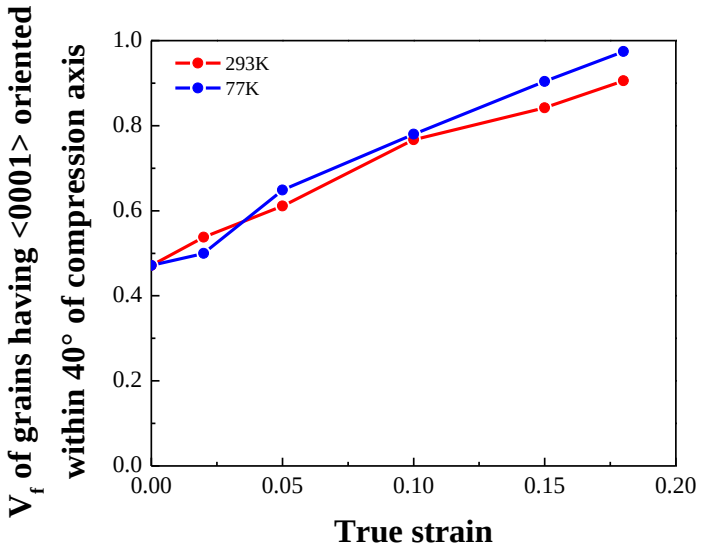

Figure 5.15: Volume fraction of grains having c-axes oriented within 40° of compression axis calculated for 77K (blue line with closed circles) and 293K (red line with closed circles) deformed samples.

$\{10\bar{1}2\}$ twin volume fraction versus strain for the 77K (blue curve) and 293K (red curve) deformed samples. The twinning fraction increases with increasing strain for both temperatures being similar regardless of temperature.

It is further interesting to compare these twinning fractions with the experimental stress strain curves (Figure 5.17). As mentioned earlier the stress strain curve at 77K has an inflection roughly at point B, which was initially thought to be twinning related. However, the comparison of twinning fractions at the two temperatures does not seem to support this at least in a simple manner. As the twinning fractions look very similar at 77K and 293K.

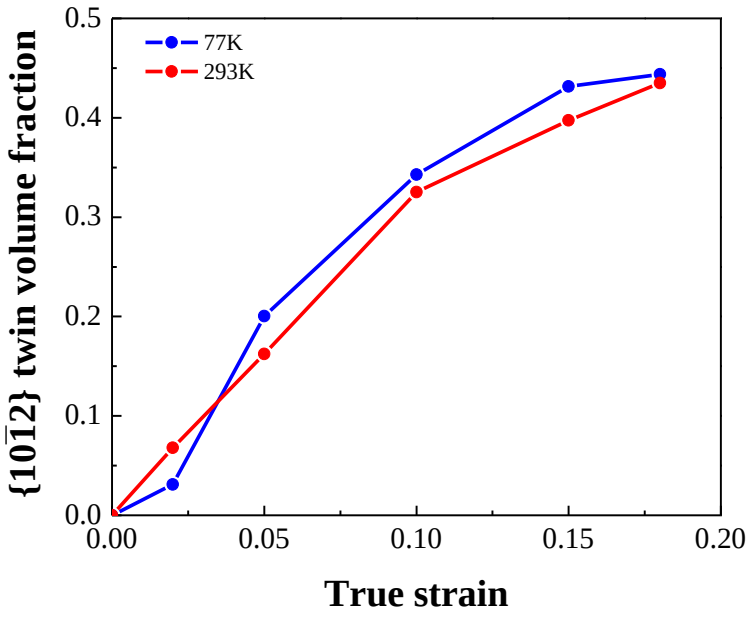

Figure 5.16: $\{10\bar{1}2\}$ twin volume fractions (%) as a function of true strain for solution treated samples deformed in uni-axial compression at 77K (blue line with closed circles) and 293K (red line with closed circles).

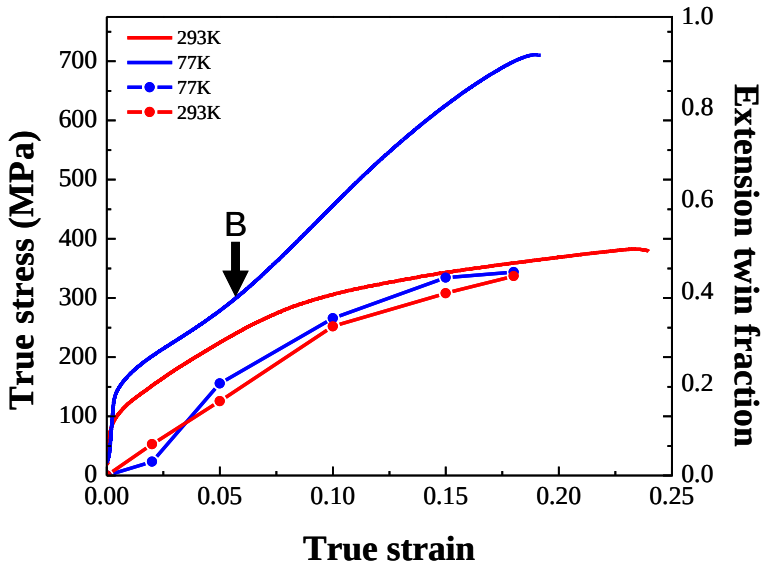

Figure 5.17: True stress-strain curve and the corresponding evolution of extension twin volume fractions for the samples deformed at 77K and 293K. The "B" marks the inflection in the stress strain response.

5.3.1.3 Microstructural observations on weak textured material

5.3.1.3.1 Nomarski-optical microscopy

As was described in chapter 4, section 4.6.1, slip trace analysis was performed to identify the slip mode corresponding to the observed slip traces. In this section, results obtained from samples deformed to a strain of 0.05 at 77K and 293K are presented. An example of an optical micrograph using Nomarski contrast is shown in Figure 5.18 for a sample that was deformed to a strain of 0.05 at 293K. One can clearly see the slip lines on the surface and a number of examples where the slip line could be unambiguously determined are shown. The trace analysis reveals that the slip lines result from both basal and non-basal (<a> and <c+a> type) slip (see grains in Figure 5.18a, 5.18b, 5.18c and

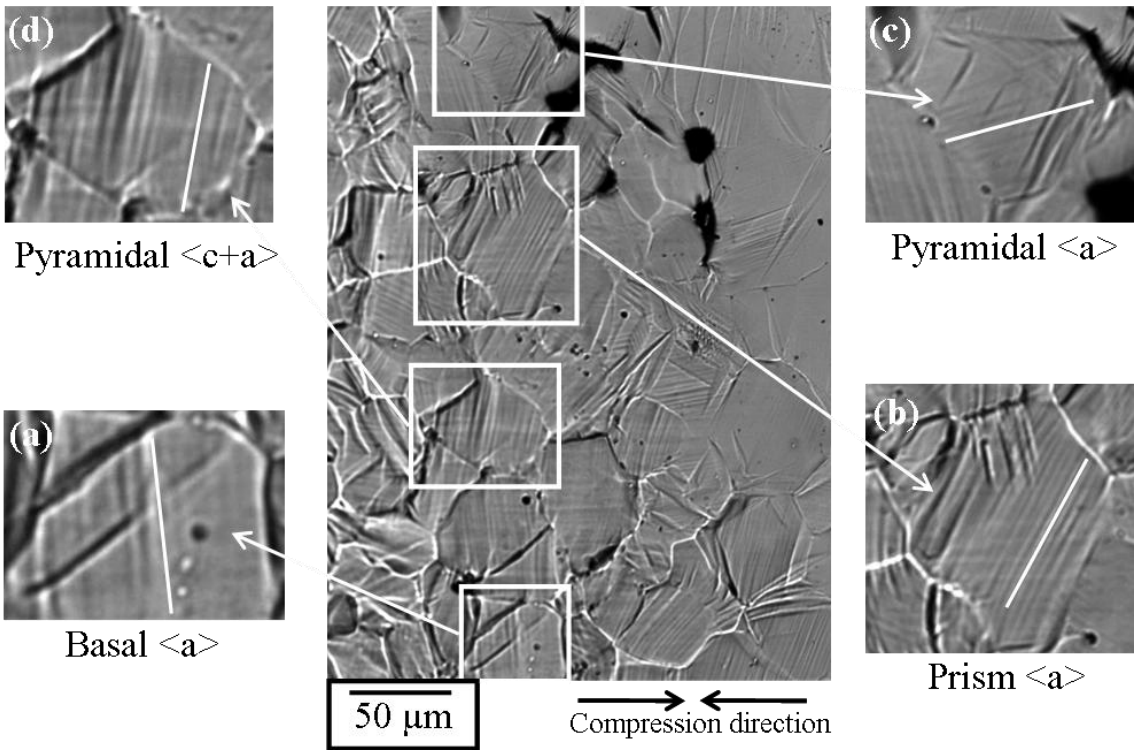

Figure 5.18: Slip markings on a sample surface deformed to 0.05 strain at 293K for **a)** basal <a> type **b)** prismatic <a> type **c)** pyramidal <a> type **d)** 2nd order pyramidal <c+a> type. The marked white colour line is a guide to slip trace.

5.18d). Table 5.3 provides a summary of observed traces from ≈ 100 grains for the samples deformed to a strain of 0.05 at 77K and 293K. It can be seen that an increase in temperature (i.e. from 77K to 293K) results in an increase of activity of 2nd order pyramidal <c+a> and a decrease in the activity of prismatic <a> slip.

Once the slip system associated with a given slip trace was identified, it was then possible to calculate the resolved shear stress acting on this slip system from the relationship between the loading direction and the crystallographic orientation of the grain

Table 5.3: Comparison of observed traces for the samples deformed to strain of 0.05 at 77K and 293K

Condition	*No. of grains observed*	*% Basal*	*% Prismatic*	*% Pyramidal*	*% 2nd order Pyramidal <c+a>*
77K	99	13	27	31	29
293K	100	11	17	28	44

using Schmid's law. In the following, the Schmid factor for the direction that gives the maximum value is reported. Figure 5.19 is a histogram that shows the number distribution of grains with a given Schmid factor. Data is shown for the analysis from compression tests at 77K and 293K, shown in blue and red, respectively. Figure 5.19a, 5.19b, 5.19c and 5.19d show results for basal, prismatic, pyramidal and 2nd order pyramidal slip traces, respectively. As can be seen from this figure, slip occurs on systems with high values for the Schmid factor. In fact, for non-basal slip lines, no cases were found where the Schmid factor was below 0.4. In addition to confirming, the prevalence for slip on systems with a high resolved shear stress, it also provides a confidence check on the trace analysis.

5.3.1.3.2 Low resolution EBSD observations

In addition to identification of slip system activity, the sequential EBSD patterns can be used to provide information on deformation twinning. In this case, the analysis can only be done on samples after unloading. Some evidence exists in the literature [70-72] that detwinning can occur during unloading. As it was not possible to consider this effect in the current work, the results presented here represent a lower bound to the amount of

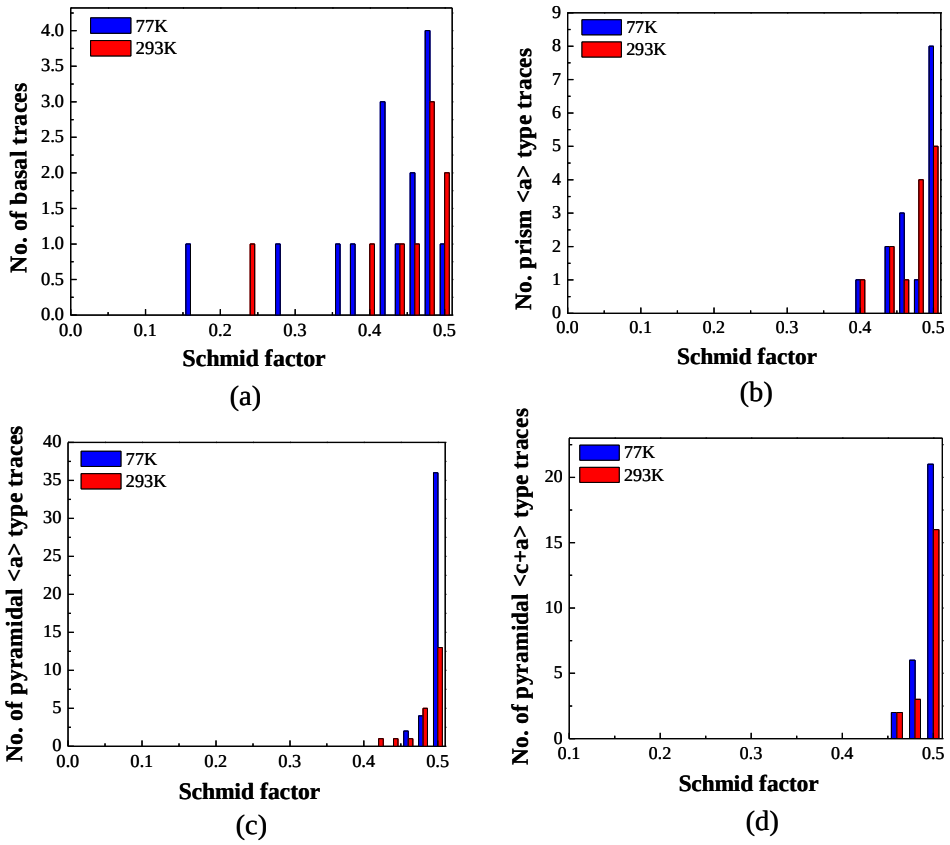

Figure 5.19: A histogram plotted between number of observed slip traces and Schmid factor for **a)** basal <a> type **b)** prism <a> type **c)** pyramidal <a> type and **d)** pyramidal <c+a> type. The black and red bars indicate to the traces observed correspondingly at 77K and 293K.

deformation twinning. Figure 5.20a and 5.20b compare the IPF map of the same area before and after 0.05 strain in uniaxial compression at 293K. The majority of active twin types at this strain level are found to be of $\{10\bar{1}2\}$ type based on boundary misorientation axis-angle relationship (see the marked white colour boundaries in Figure 5.20b, 5.20c and 5.20d). A number of other observations can be made from this figure. For instance, many twinned and untwinned grains show a significant level of internal misorientation (see the colour change in IPF triangle). This is presumably related to the heterogeneity of slip

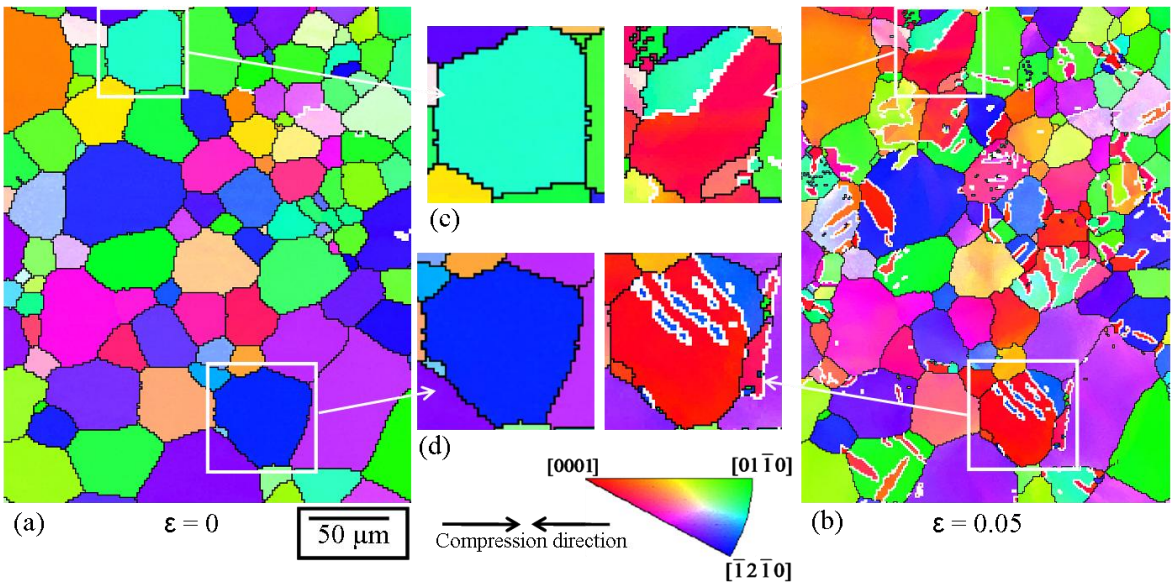

Figure 5.20: Inverse pole figure map of **a)** initial microstructure before deformation **b)** after a true strain of 0.05 in uni-axial compression at 293K. The colour code of inverse pole figure map is provided in the middle of the Figure. The black boundaries are grain boundaries (misorientation angle > 10°). The white boundaries are $\{10\bar{1}2\}$ twin boundaries based on misorientation axis-angle relationship ($86° < 11\bar{2}0 >$, ±5°). **c)** and **d)** shows the local change in orientation of crystal with increasing strain for the grains delineated by a white box in a and b.

activity and local lattice rotations. Figure 5.20c and 5.20d show an expanded view of a small number of grains before and after deformation. It can be observed that in this case the twins grow to sizes comparable to the original grain size. It is also interesting to notice the way the twins consume the parent grain (Figure 5.20d). Small portions of matrix between twins remain as untwinned. This complex morphology can be generated via nucleation of more than one identical twin variant.

The above approach (sequential EBSD) has also been employed for twin statistics analysis. Using this method one can unambiguously distinguish between the parent (pre-

twinning orientation) and twin orientations. Table 5.4 provides a summary of twin area fractions calculated from sequential maps of 77K and 293K deformed samples at 0.02 and 0.05 strain levels. For each condition, four maps of 0.5mm×0.4mm (~800 grains) were analyzed and then the average twin area fraction was reported. An error associated with the estimation was given by a standard deviation (Table 5.4). The results indicate subtle differences in the twinning fractions at the observed strain levels for the two test temperatures. Nevertheless, they are consistent with the notion that twinning fraction increases with increasing strain and lower deformation temperature. The above presented results were also compared with the results from analysis of neutron diffraction as shown in Figure 5.21. This comparison reveals that the EBSD estimation is only slightly lower than the neutron assessment, except for the sample strained to $\varepsilon = 0.02$ at 77K (Figure 5.21a). The exact reason for this result is not clear. However, the former can be understood by the consideration that fine scale twins in this sample could be easily missed in the EBSD maps. Since the EBSD spatial resolution was ~ 1 μm. This therefore gives a lower bound estimation of twin fraction.

Table 5.4: Comparison of twinned area fractions for the samples deformed at 77K and 293K. The area fraction was determined via sequential EBSD

Condition		*Strain*	*Twin area fraction (%)*	*Standard deviation*
Weak textured material (compression parallel to ND)	77K	0.02	6	2.2
		0.05	17.8	3
	293K	0.02	5.5	1
		0.05	12.3	2.2

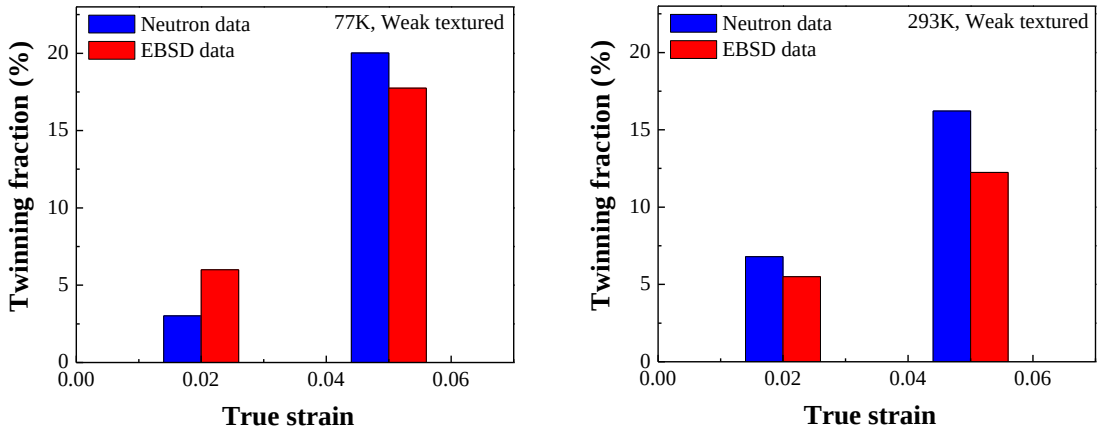

Figure 5.21: Comparison of twinning fractions estimated from sequential EBSD mapping and neutron diffraction data for **a)** 77K and **b)** 293K deformed samples.

5.3.1.3.3 High Resolution EBSD observations

In this section, results on the microstructural characterization of deformed specimens using high resolution EBSD are presented. As noted above, fine microstructural features, such as twins, could be easily missed in the low resolution EBSD maps.

An illustration of deformed microstructures of weak textured material compressed to a true strain of 0.08 at 77K and 293K is presented in Figure 5.22. As earlier, the EBSD data are plotted in the form of band contrast maps (Figure 5.22a and 5.22b) and IPF maps (Figure 5.22c and 5.22d). Several types of boundaries (high angle, extension twin, extension twin impingement) are plotted in these maps. The boundary misorientation axis-angle pair analysis on these maps reveals several $\{10\bar{1}2\}$ type twins (white boundaries) and various twin impingement boundaries resulting from impingement of $(10\bar{1}2)-(\bar{1}012)$ type (red boundary) and $(10\bar{1}2)-(0\bar{1}12)$ type (blue boundary) twins. To illustrate this further, some examples are specifically shown in Figure 5.22e, 5.22f and 5.22g. One can

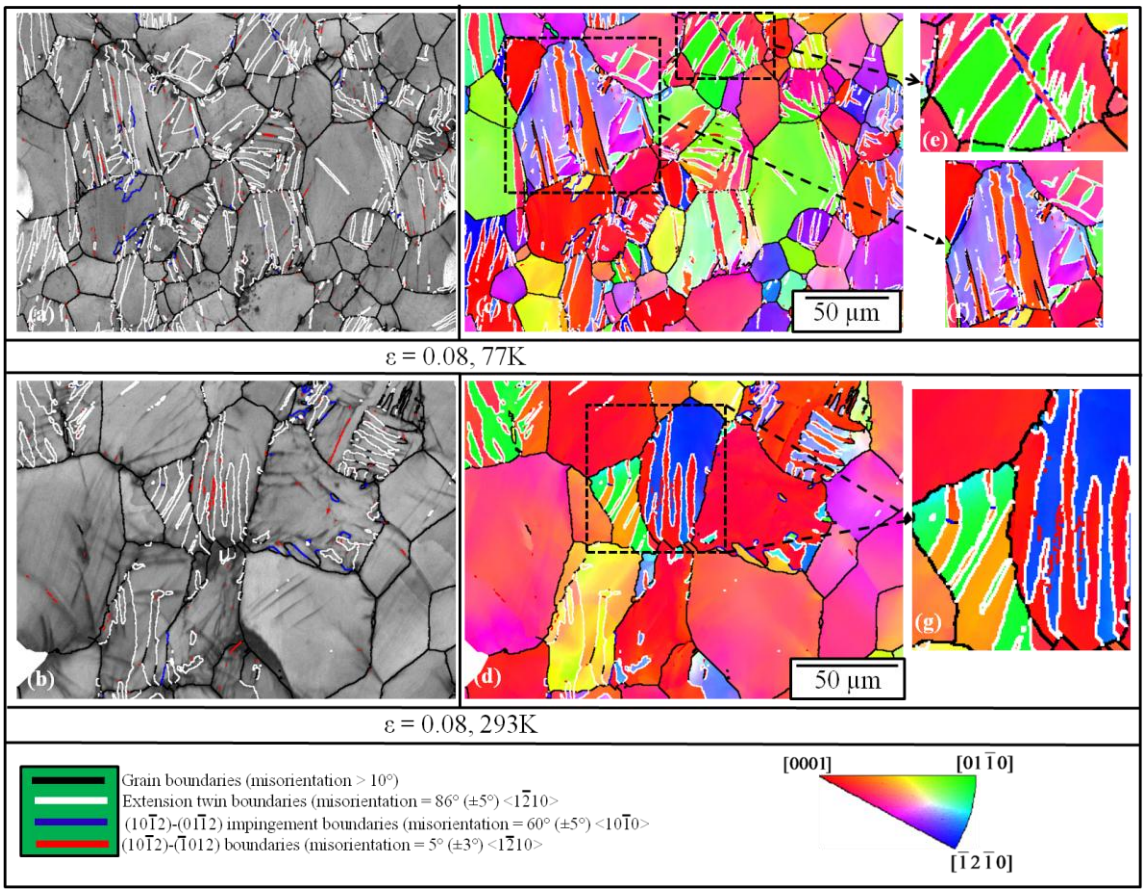

Figure 5.22: a) and **b)** respectively, show the pattern quality EBSD maps for samples deformed to a true strain of 0.08 at 293K and 77K while, **c)** and **d)** respectively, show the compression axis inverse pole figure maps for the samples deformed to a true strain of 0.08 at 293K and 77K. **e)**, **f)** and **g)** show the examples where different variants of extension twins impinge on each other for the grains delineated by a black box in c and d. The colour code of the map is provided at the bottom right of the maps.

notice grains frequently contain more than one active twin variant at both temperatures. No evidence of either contraction twinning ($\{10\bar{1}1\}$) nor double contraction-extension twinning ($\{10\bar{1}1\}-\{10\bar{1}2\}$) could be found in these samples as expected from the starting texture relative to the imposed deformation.

At a strain of 0.08, both deformed microstructures consist of heavily twinned grains. Although, the twinning fractions are not significantly different, the grains show a much more complex nature of extension twinning at 77K than at 293K (discussed in more detail in section 5.3.2.3.2). An interesting observation related to this is the presence of double extension twins in the samples deformed at 77K. This involves twinning first on a $\{10\bar{1}2\}$ plane of the matrix and then re-twinning on the $\{10\bar{1}2\}$ plane of primary twin. In approximately 10% of extension twins (10 observations in 110 primary extension twins), such complex morphologies were observed within extension twins. A more detailed analysis on the formation of such double twins using EBSD and TEM techniques is presented in the Appendix A4 (and has also been published recently [173]). Nonetheless, this is to be contrasted with observations at room temperature where no such double twinning has been observed.

5.3.2 Discussion

5.3.2.1 Macroscopic stress strain behaviour

It can be noticed from Figure 5.23 that the macroscopic yield stress of the weak textured alloy is comparable to that of the IPC case. It is, however significantly lower than the TTC and IPT cases. This can be rationalised based on the easy activation of basal slip and extension twinning compared to non-basal slip during straining of weak textured and IPC samples.

Unlike the TTC and IPT cases for the strong textured material, the macroscopic stress strain response of the weak textured alloy at 77K and 293K are very similar up to a strain of approximately 5%, only the flow stress level is slightly higher at 77K than 293K

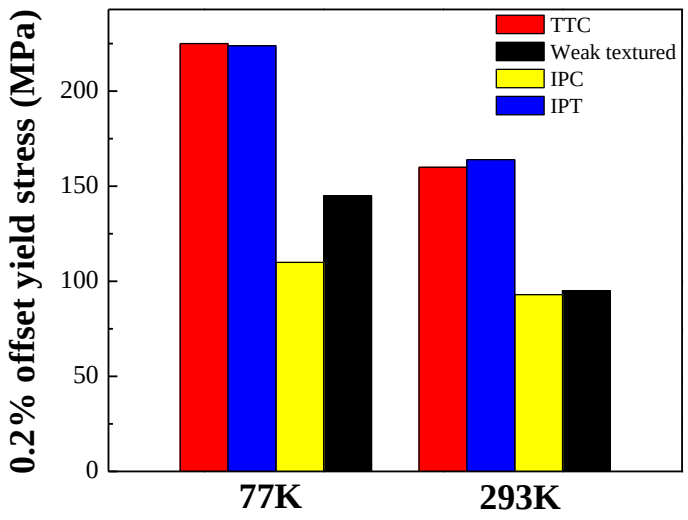

Figure 5.23: Comparison of 0.2% offset yield stresses for strong and weak textured samples deformed at 77K and 293K.

(Figure 5.24). This can be attributed to a weak temperature dependence of basal slip and $\{10\bar{1}2\}$ extension twinning [38, 59]. After $\approx$5% strain, the 77K curve exhibits a sudden increase in the hardening rate while, the 293K curve continues to harden at a decreasing rate. One may describe this by considering several factors: i) the texture hardening, ii) the temperature effect on the rate of dynamic recovery and iii) the Hall-Petch effect.

The texture development during deformation can cause additional hardening. According to Kocks [174], the contribution of texture to strain hardening can be given by:

$$d\sigma/d\varepsilon \equiv \theta = \bar{\tau}\, d\overline{M}/d\varepsilon + \overline{M}\, d\bar{\tau}/d\varepsilon \qquad (5.1)$$

Here, θ is the strain hardening rate, M is the Taylor factor, τ and ε are the stress and strain, respectively, the over bars indicate the averages over the polycrystal. The first term

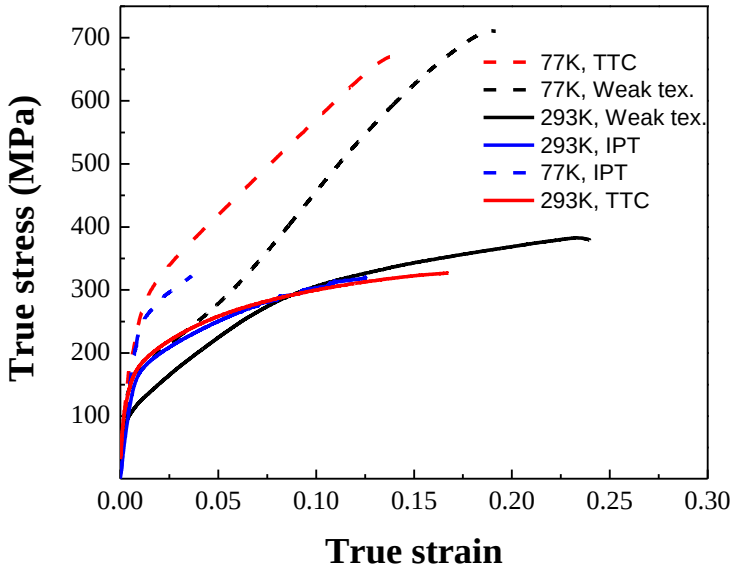

Figure 5.24: True stress strain curves for strong textured samples tested in TTC and IPT loadings and for weak textured sample compressed along ND direction at 77K and 293K.

of Equation 5.1 represents the texture effect while, the second term reflects the hardening due to a change in dislocation structure.

At ≈5-6% strain, a significant fraction of material has already been reoriented such that the c-axes of many grains reside close to the compression axis (see Figure 5.14 and 5.15). In such a situation, the subsequent deformation response would then closely resemble that of the TTC deformed samples, where deformation is dominated by difficult <c+a> slip and $\{10\bar{1}1\}$ contraction twinning. To elucidate this further, stress strain curves of strong textured material in TTC and weak textured material after subtracting the initial 5% compressive strain are plotted together in Figure 5.25. As expected, the responses look very similar for the two conditions. The small differences between the curves can be attributed to differences in the textures and how the texture development occurred i.e. the

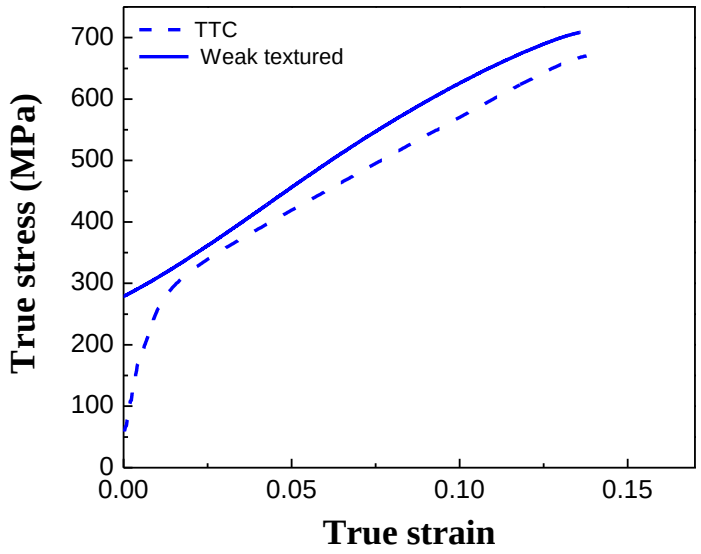

Figure 5.25: True stress strain response of strong textured alloy in TTC (dashed line) and weak textured alloy (solid line) subjected to uniaxial compression at 77K. Note that the curve of weak textured alloy is plotted after subtracting an initial 5% strain.

difference between starting with the basal texture vs. twin and slip to get the basal texture.

The subsequent loading of the weak textured sample (i.e. after 5% strain) yields a strengthening of the basal texture (e.g. maximum intensity increases from 5.7 m.r.d. to 6.9 m.r.d. with increasing strain from 0.05 to 0.18 for 77K case). Such a texture change primarily arises from the contribution of basal <a> slip and pyramidal <c+a> slip. However, one cannot also deny the possible role of extension and contraction twinning. Several authors [8, 99] have shown a similar increase in texture strength under similar conditions. Most recently, Cáceres and Lukác [175] have calculated the Taylor factors in textured and random polycrystals of magnesium. For textured polycrystal the Taylor factor was estimated to be between 2.1-2.5, increasing to about 4.5 for randomly textured polycrystals. It should be mentioned that the Taylor factor calculation was based on the

assumption of equal strain hardening in all the active slip systems. Nonetheless, it reflects the potential effect of texture development on strain hardening.

Since 2nd order pyramidal <c+a> slip is expected to play a key role in <c>-axis deformation, it is essential to examine its role more closely. The formation of <c+a> dislocation requires cross slip first of an <a> dislocation from the basal plane to prism plane then <c+a> dislocations from prism plane to $\{11\bar{2}2\}$ plane. At low temperatures, the activation of <c+a> dislocations requires higher stress because there is not enough resolved stress to activate cross slip (as discussed in section 5.2.2.2). In addition, Obara and co-workers [41] have pointed out that the work hardening rate of this slip system is very high especially below 200°C. They ascribed this to the exhaustion of highly mobile screw dislocations (due to locking at forest dislocations) during deformation. Considering all these, it is anticipated that the hardening of the <c+a> slip system will play an important role in the description of the hardening curve at 77K.

Additionally, a twin boundary could act as a barrier to the motion of glide dislocations and therefore it can be expected to harden the material in a manner similar to Hall-Petch effect. Several experimental and modelling studies [82, 162, 167, 176] have realised the importance of this factor. Some reports [177] have suggested that the twin barrier effect is less significant in magnesium as compared to other HCP metals. This is related to the fact that in many occasions twins in magnesium grow to sizes equivalent of parent grain. The present results are consistent with that (see section 5.3.1.3.2). Moreover, the analysis implies that the amount of twinning at both temperatures is quite similar. Thus, only slight differences might arise from the difference in twin morphologies at two temperatures.

5.3.2.2 Texture evolution

The study of texture evolution can be used to infer information about the active slip and twin modes. It is well known that basal slip and extension twinning are responsible for the development of a strong basal texture during straining of magnesium alloys. Further, the 2nd order pyramidal <c+a> slip and contraction twinning tend to develop a splitting in the basal texture such that the peak basal pole intensity is rotated towards RD [48, 178].

The experimental texture evolution towards a strong basal texture is consistent with the activity of basal slip and extension twinning occurring from the earliest stages of deformation. At higher strains, the texture shows a tendency for the <0001> basal peak to split, this can be considered as an indicator of pyramidal <c+a> slip [48]. Further, with lowering temperature only a slight difference in strength of the basal texture has been observed at each stage of deformation (Figure 5.26). This is probably due to similar twin contents at 77K and 293K (Figure 5.26).

Nonetheless, one noticeable difference observed between the textures measured at 77K and 293K is in the splitting of basal poles. As can be seen in Figure 5.27, the texture at 77K exhibits six peaks each separated by ~ 60° (see the numbered peaks). This is in contrast with the two peaks observed at 293K where each is separated by ~ 180° (notice the numbered peaks in Figure 5.27b). In addition, one should also notice that the texture peaks observed at 77K are roughly 10° closer toward compression axis than at 293K (i.e. at $\chi = 15^{\circ}$ vs. $\chi = 25^{\circ}$). The exact mechanism responsible for this behaviour is not clear.

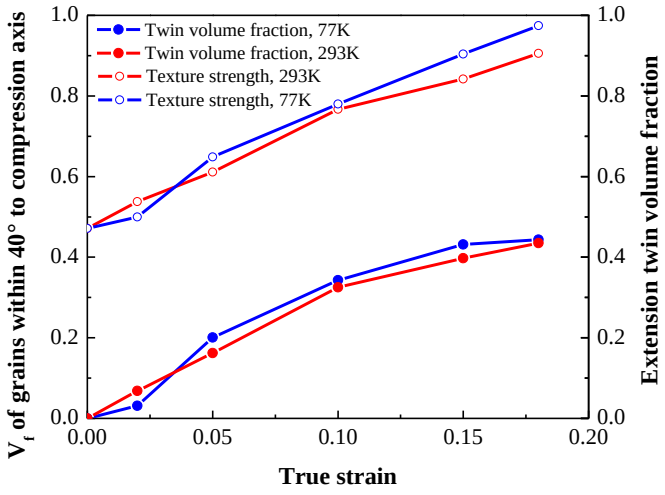

Figure 5.26: Volume fraction of grains within 40° to compression axis and extension twin volume fractions both are plotted against true strain for samples deformed at 77K and 293K.

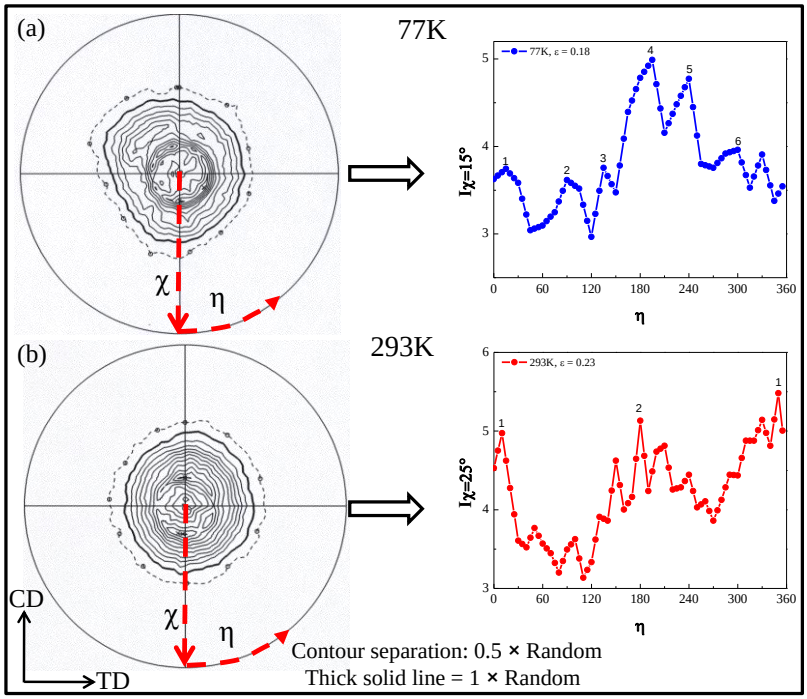

Figure 5.27: Show the {0001} pole figures (stereographic) and their corresponding line scans plots for samples compressed to a strain of **a)** 0.18 at 77K and **b)** 0.23 at 293K. Note that η is the azimuthal angle (0-360 degrees) and χ is the tilt angle (0-90 degrees). The compression direction is at the center of the pole figure, while the CD and TD correspond to casting direction and transverse direction of the sample, respectively.

5.3.2.3 Deformation mechanisms

5.3.2.3.1 Slip modes

The trace analysis gives us an idea about the important slip systems being active under specific loading condition. The results indicate that all the major slip systems are active at 77K and 293K. Notice that the current experimental evidence contradicts previous single crystal studies which suggest that the non-basal slip is extremely difficult to activate at low temperatures. There are, however, several other reports that support the observation of non-basal slip systems at room-temperature and below. For instance, the early work of Hauser et al. [179] on polycrystalline pure magnesium provides evidence of prismatic <a> type slip active at 77K. They attributed this to the grain boundary effects. Recent work of Koike and co-workers [7, 47] provides additional support to this argument. Furthermore, the work of Ando and Tonda [180] on magnesium single crystals shows that the second order pyramidal (<c+a> type) slip is active in the temperature range of 77K-293K. Most recently, Keshavraz and Barnett [181] have identified basal and non-basal slip traces at room temperature in an AZ31 magnesium alloy. It can also be argued that the presence of alloying additions (Al and Zn) in AZ80 alloy may promote the non-basal slip in comparison with pure magnesium. The potential effect of solute additions on slip system activities is discussed in chapter 7, section 7.3.3.1.

One must be careful regarding the conclusions that can be drawn from the analysis given above due to a number of factors. First, slip lines will appear on the surface only for cases where many dislocations that have a significant component of their Burgers vector perpendicular to the free surface escape from the crystal, i.e. if the Burgers vector was parallel or nearly parallel to the free surface, no slip line would be observed. Second, in

most cases only one predominant set of slip lines is observed in a single grain in contradiction to the requirement of multiple slip systems for general deformation, i.e. even if one relaxes the von Mises condition at least 2-3 slip systems are necessary for general shape changes [174]. This suggests that the slip lines thus represent only partial information on the nature of deformation in the grain. However, the identification of a particular slip system in a given grain does indicate that this slip system is making a contribution to the deformation of that grain.

Considering all of the above comments, one can make some preliminary comments regarding the relative activities of various slip systems at 77K and 293K. The comparison indicates that the percentage of grains exhibiting 2nd order pyramidal <c+a> slip increases with increasing temperature from 77K to 293K (Figure 5.28). This is obvious due to ease of slip at higher temperature. However, it is not clear why the importance of prismatic <a> slip decreases with increasing temperature (Figure 5.28).

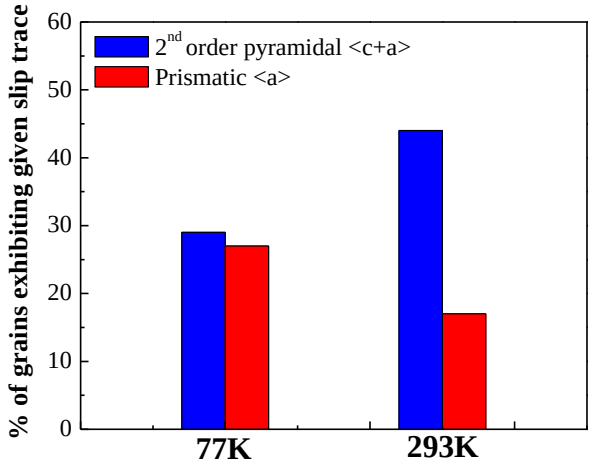

Figure 5.28: A comparison of grains exhibiting 2nd order pyramidal <c+a> (blue bars) and prismatic <a> (red bars) slip traces at 77K and 293K (from $\approx$100 grains) for samples deformed to 0.05 strain.

5.3.2.3.2 Twin modes

In this work, deformation twinning is characterized systematically using various techniques such as neutron diffraction, low resolution EBSD and high resolution EBSD. Each technique has its own advantages and limitations. For instance, sequential EBSD can be extremely effective in characterizing the twinned microstructures by tracking the individual twin formation. Using this approach, an unambiguous estimation of twinning fractions can be obtained. However, the technique is limited in terms of overall grain statistics and the evaluations at large strains. In recent years, several authors [33, 182, 183] have utilised the EBSD technique for analysing twinned microstructures. Various characteristics of twinning (e.g. morphology, Schmid factor, neighbour misorientation analysis) have been used in these studies. However, the biggest challenge associated with all of these is to unambiguously distinguish the parent orientations from the twinned orientations.

Another approach that has been successfully employed to characterize deformation twinning in HCP metals is neutron diffraction [162, 184, 185]. The technique can be very effective if the operative twin modes are known a priori and the operative modes result in a distinct change in texture such as the $\{10\bar{1}2\}$ twinning mode in magnesium which results in a nearly 85° change in crystal orientation. However, such an analysis is limited to a situation where no overlapping of primary and secondary twinning modes occurs.

The EBSD analysis suggests that the $\{10\bar{1}2\}$ extension twinning plays a dominant role in deformation response of weak textured AZ80 alloy during uniaxial compression at

77K and 293K. Alternatively, there was no evidence of $\{10\bar{1}1\}$ contraction twinning. These results are consistent with previous reports [59] implying that the CRSS to activate $\{10\bar{1}2\}$ twinning is significantly lower than $\{10\bar{1}1\}$ contraction twinning.

At low strain levels, the EBSD measured twin fractions were found to be in reasonable agreement with those obtained from neutron data. In an effort to gain further insight into the effect of temperature on twinning kinetics, neutron diffraction has been utilised. A comparison of twinning fractions obtained for 77K and 293K deformed samples suggests that the differences between the twinning fractions at the two temperatures are small (see Figure 5.26). This observation of a weak temperature dependence of twin fraction is interesting as it is in contradiction with the idea the twinning activity at low temperature should increase due to the difficulty of non-basal slip and cross-slip at low temperature. It might be that the observed differences are less due to the initial texture of the material which favours less twinning when compared to strong textured material loaded under IPC. Nonetheless, to further confirm this effect the strong textured case favourable for $\{10\bar{1}2\}$ extension twinning should be closely examined.

In this work, several complex morphologies associated with $\{10\bar{1}2\}$ twinning have been observed, particularly at 77K using high-resolution EBSD maps. For instance, a double twinning sequence involving double extension $\{10\bar{1}2\}-\{10\bar{1}2\}$ twinning has been observed in samples compressed at 77K (see Appendix A4 for more details). No evidence of this double twinning sequence could be found at room temperature where non-basal slip is expected to be significantly easier. Some more examples of complex twinning behaviour at low-temperature are shown in Figure 5.29. The grain at the top left of the figure displays

many extension twins emanating from the grain boundary (Figure 5.29a). Also shown in the figure is an example where twins appeared in a near zigzag pattern (Figure 5.29b). The latter observation is very similar to the one observed during martensitic transformations where such features are formed in order to compensate the strain of the surrounding austenite [186]. Nonetheless, the local conditions responsible for such behaviour need to be further analysed. Such complex twin morphologies provide significant challenges for modelling the plastic deformation behaviour.

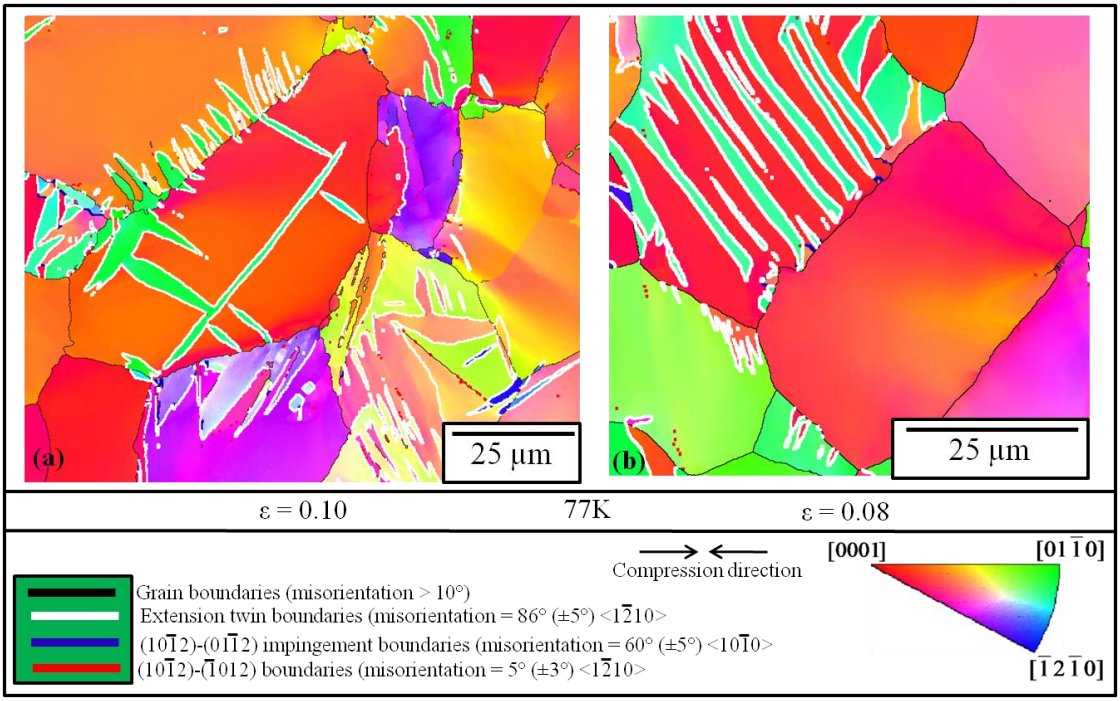

Figure 5.29: Examples of complex twinning behaviour observed for 77K deformed samples at strain of **a)** 0.10 and **b)** 0.08. The compression axis is plotted in the IPF map. The colour code of the same is provided at the bottom right of the map.

5.3.3 Summary

In this work, the effect of temperature on the mechanical behaviour of weakly textured solution-treated AZ80 alloy has been investigated. To the author's knowledge this is a first systematic attempt of examining the effect of low temperature on deformation response of the AZ80 magnesium alloy. In the present study, the influence of temperature on the mechanical properties, work hardening characteristics, texture evolution and deformation mechanisms has been evaluated. In addition, deformation response of weakly textured material has been analysed using results of strong textured material.

The temperature had a pronounced effect on the work hardening characteristics of the alloy. The high hardening rates observed at 77K can be attributed to the texture hardening and the temperature effect on the rate of dynamic recovery. The hardening effect arising from a dynamic Hall-Petch effect appears to be of less significance. In the present study, the effects of temperature on deformation mechanisms and resulting texture development have been quantitatively analysed. Though the temperature had a weak effect on the basal texture strength, it significantly affects the characteristics of the final basal texture. Two approaches (neutron diffraction and sequential EBSD mapping) have been used to quantitatively analyse the twinning fractions in deformed samples. The results from both were consistent.

The important findings of this work can be summarised as follows: i) the $\{10\bar{1}2\}$ twinning fractions were found to be weakly temperature dependant, ii) the contribution of pyramidal <c+a> slip was found to be increased with increasing temperature, iii) in contrast, the importance of prismatic <a> slip was found to be decreased with increasing

temperature, iv) microstructural analysis revealed the complex nature of $\{10\bar{1}2\}$ twinning e.g. grains frequently contain more than one active twin variant per grain at both temperatures, in many cases, twins were found to consume significant portion of the parent grain and v) a new double twinning sequence consistent with double extension ($\{10\bar{1}2\}$-$\{10\bar{1}2\}$) twinning has been observed at 77K.

The experimental study has provided an understanding of the deformation response of strong and weak textured material at low temperatures. This will play an important role in modelling the polycrystal plastic deformation behaviour. The experimental results obtained from this chapter will further be analysed using the VPSC model in the next chapter.

CHAPTER 6 - VPSC Simulations to Interpret the Deformation of AZ80

6.1 Introduction

In the previous chapter, experimental results for the mechanical behaviour of strong and weak textured, solution-treated AZ80 alloy deformed at 77K and 293K were analysed. In this chapter, the Los Alamos viscoplastic self-consistent (VPSC) model of Lebensohn and Tomé [149] is used to further understand these results and gain more insight into deformation mechanisms of the alloy. The VPSC formulation has been successfully used for predicting the deformation and textures of various metals [150, 187] and geological materials [188]. The methodology involved in the simulations was presented earlier in chapter 4, section 4.7. This chapter begins with the task of establishing the various model parameters (section 6.2). The model predictions and analysis for strong textured and weak textured materials will be presented in section 6.3. Within this section, the model predictions are compared with the variety of available experimental information such as stress strain response, mode activity, texture and twinning fraction. Section 6.4 contains discussion on the model parameters, assumptions and description of twin system hardening. A summary of the results is provided in section 6.5.

6.2 Establishment of model fitting parameters

In this section, the task of establishing the model fit parameters for deformation at 293K and 77K is addressed. First, it is important to recall the list of various adjustable parameters in the model. The local grain level constitutive response is described by:

$$\dot{\varepsilon}_{ij} = \dot{\gamma}_0 \sum_S m_{ij}^S \left(\frac{\tau_r}{\tau_c}\right)^n \tag{6.1}$$

Where $\dot{\varepsilon}_{ij}$ is the grain strain rate, $\dot{\gamma}_0$ is a reference strain rate (1 s^{-1}), m_{ij}^S is the Schmid tensor of the slip and twin system, which is given by normal, n_i^S, and Burgers vector, b_i^S, of the system as, $m_{ij}^S = \frac{1}{2}(n_i^S b_j^S + n_j^S b_i^S)$, τ_r is the resolved shear stress on the system, τ_c is the threshold stress of the system, n is the inverse of rate sensitivity (n = 20). A simple Voce-type hardening law is used to describe the hardening of slip and twin systems. Accordingly, the evolution of the threshold stress (τ_c) as a function of accumulated shear strain (Γ_c) in each grain is given by:

$$\tau_c = \tau_0 + (\tau_1 + \theta_1 \Gamma_c) \times [1 - \exp(-\theta_0 \Gamma_c / \tau_1)] \tag{6.2}$$

where τ_0 is the initial CRSS value and τ_1 is the back extrapolated stress value, θ_0 and θ_1 are the initial and large hardening rates, respectively (Figure 6.1). Consequently, for each deformation mode, there are four primary fitting parameters τ_0, τ_1, θ_0 and θ_1, giving 16 total fitting parameters for the 4 modes considered here (i.e. basal, prismatic, 2nd order pyramidal and extension twinning). The model also accounts for latent hardening via the matrix "h^{st}" (describes the hardening effect upon the s^{th} mode due to activity of the t^{th} mode). In the present case "h^{st}" is a 4 × 4 matrix of adjustable parameters. In principle, the total number of fitting parameters is large, however, some physically-based assumptions can allow us to reduce the total number of fitting parameters. Since, the strain levels examined in the present case are relatively low it is reasonable to assume the stage IV

hardening parameter, θ_1, is zero for all deformation systems. Furthermore, the latent hardening coefficient describing the coupling between twinning and slip or other twin modes (i.e. h^{TT}) is the only parameter that was adjusted. All other components of h^{st} are assumed to be equal to 1. This physically reflects the assumption that the barrier effect posed by twin boundaries on subsequent slip and twinning activity can be stronger than that due to slip system interactions.

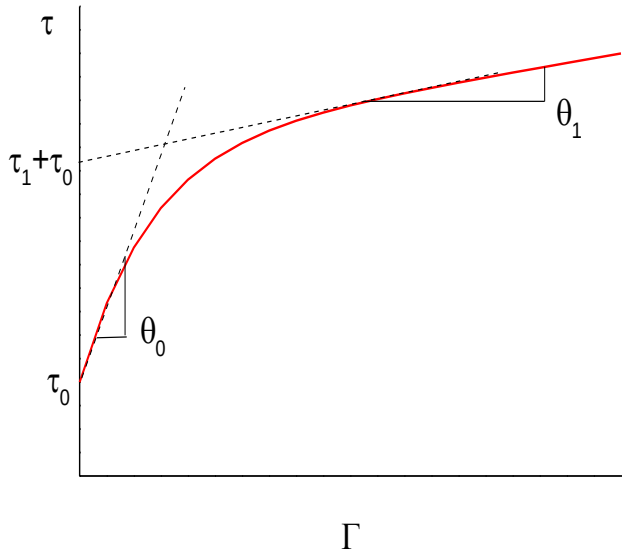

Figure 6.1: Schematically illustrating the parameters of Voce equation 6.2.

6.2.1 Fitting VPSC parameters to the AZ80 alloy deformed at room-temperature

In order to establish the initial CRSS values and the hardening parameters for the AZ80 alloy, the case of AZ31 (Mg-3Al-1Zn) alloy where the experimental data is taken from the literature has been utilised. Agnew and co-workers [78] have reported the stress

strain response of AZ31 alloy sheet, having a similar starting texture to the material studied here, with a grain size of roughly 50 μm (similar to the present case of 32 μm), tested in through-thickness compression (TTC) and in-plane tension (IPT) directions. In the following, their experimental curves and their recently published [82] VPSC fitting parameters will be utilised as a guide to determine parameters. It was decided to use physical arguments to fix θ_0, the temperature independent stage II hardening coefficient, for all the slip systems. In doing so the values of τ_1 had to be adjusted from those reported in [82]. The typical values of θ_0 for pure metals with close-packed structures lies in the range of μ/100-μ/300[7] (where μ is the shear modulus) [73]. This gives values close to 100-200 MPa for magnesium (μ is approximately 17 GPa for magnesium). In fact, a recent study [43] on pure magnesium single crystals confirms that similar values are obtained for crystals tested in orientations favourable for basal <a> slip and 2nd order pyramidal <c+a> slip. For the present simulations, the latent hardening parameters were kept the same as in ref. [82] i.e. no latent hardening for slip-slip interaction and h^{TT} of 4 for twin related interactions. The present analysis indicates that a high value for the latter is essential to match the post-twin-dominated hardening rates of the IPC case.

For a given strain path, the most likely deformation systems are known a priori. For instance, during IPT, one would expect the prism and basal <a> slip to be the dominant deformation mechanisms. Thus, the parameters from these modes were adjusted to match the experimental stress strain curves. Similarly, the parameters of other deformation systems were deduced. Table 6.1 lists the final parameters determined for the AZ31 alloy.

[7] This is for cases of multiple slip systems. The one difference for HCP deformation is that the dislocations on different slip systems may have different Burgers vectors and CRSS values.

Table 6.1: Best-fit VPSC parameters of AZ31 and AZ80 magnesium alloy. The stress values are normalised by the CRSS value for basal slip, 29 MPa for AZ31 and 39 MPa for AZ80. The initial hardening rate values are normalised by $\mu/200$ for both AZ31 and AZ80. The asterisks denote normalised values

Test alloy (293K)	*Mode*	τ_0^*	τ_1^*	θ_0^*	θ_1	h^{TT}
AZ31 and AZ80	Basal	1	1.9	1	0	4
	Prismatic	3.9	5	1.8	0	4
	Pyramidal <c+a>	6	0.5	1.5	0	4
	Extension twin	1.1	0	0	0	4

Notice that the tabulated stress values are normalised with the CRSS for basal slip, which is 29 MPa, while the initial hardening rate values are normalised with μ/200. For the input texture, the EBSD measured texture file obtained from recrystallised sample of AZ80 alloy containing 1079 discrete orientations (of equal weights) has been used (Figure 6.2). This texture is similar to the one reported by Agnew et al. [78] for the AZ31 alloy i.e. a maximum basal pole intensity of 4 m.r.d. vs. 5 m.r.d. for AZ31 alloy. Using these parameters (Table 6.1) and the starting texture given in Figure 6.2, a good prediction of TTC and IPT cases can be achieved, as shown in Figure 6.3a and 6.3b, respectively. It should be noticed that these are cases which are slip dominated, having very little twinning.

Compared to AZ31, the AZ80 alloy represents a case where the alloy contains a much higher Al content (i.e. 8 wt% Al vs. 3 wt %) in solid solution. The addition of Al

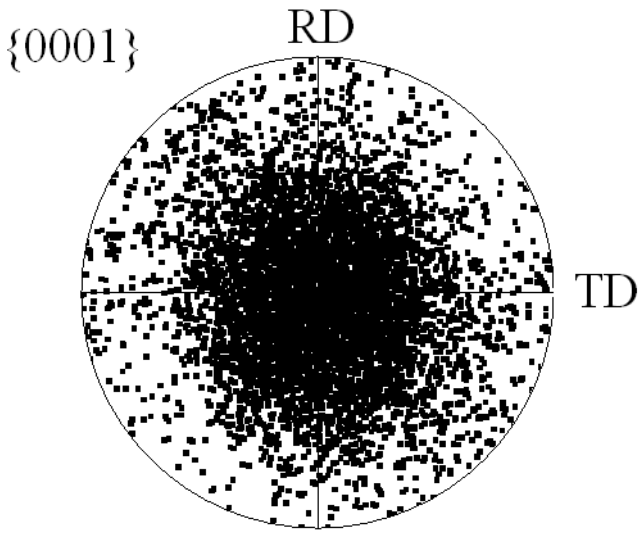

Figure 6.2: The {0001} EBSD measured pole figure obtained from rolled and recrystallised sample of AZ80 alloy showing 1079 discrete orientations. Each point on the pole figure represents a single grain orientation. The RD and TD correspond to the sample rolling and transverse directions, respectively.

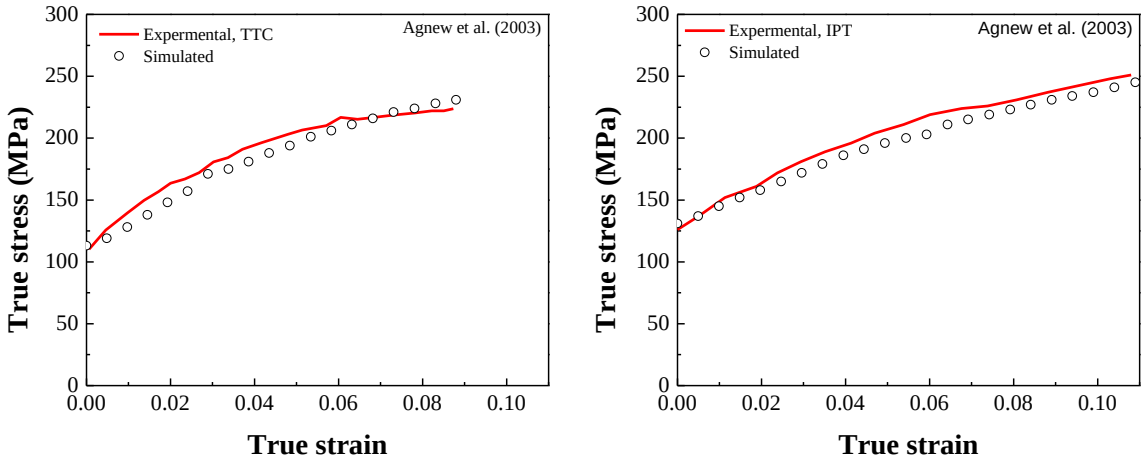

Figure 6.3: Experimental (–-) and predicted (o) plastic response for AZ31 alloy **a)** compression along sheet ND direction and **b)** tension along sheet RD direction. The plotted experimental curves were obtained from ref. [78].

increases the CRSS value for basal slip [37, 38]. The effect of Al on non-basal slip is, however, unclear. For instance, it was reported by Akhtar and Teghtsoonian [37, 38] that Al softens the prismatic plane at low solute levels. On the other hand, there was a suggestion that Al hardens slip on the prismatic plane at high solute contents [189-191]. The recent study of Hutchinson and Barnett [190] suggests that for high solute levels the effect on CRSS ratio of prismatic to basal slip saturates i.e. the CRSS ratio remains the same. This view has been adopted in the current work. Moreover, since there was no information available on the influence of solute on the <c+a> slip system and extension twinning, it was decided to use the same CRSS ratios for all deformation mechanisms of the AZ80 alloy as those used for the AZ31 alloy. Thus the only adjustable parameter is the CRSS for basal slip. In the case of AZ80, it was found that τ_{CRSS}^{Basal} = 39 MPa compared to 29 MPa for AZ31 (Table 6.1).

The final parameters determined to fit experimental data on the AZ80 are listed in Table 6.1. Similar to AZ31, a reasonable prediction of TTC and IPT cases can be obtained for the AZ80 alloy (Figure 6.4a and 6.4b). It is interesting to point out that the addition of Al is predicted not to change the relative strength of individual mechanisms compared to AZ31 alloy. In other word, the CRSS ratios remain the same. Furthermore, it can be seen from Table 6.1 that the θ_0 values and the latent hardening parameters are similar for both AZ31 and AZ80 alloys.

6.2.2 Fitting VPSC parameters to the AZ80 alloy deformed at 77K

After obtaining the parameters for room-temperature deformation, the next task was to determine the values of the adjustable parameters for deformation at 77K. To

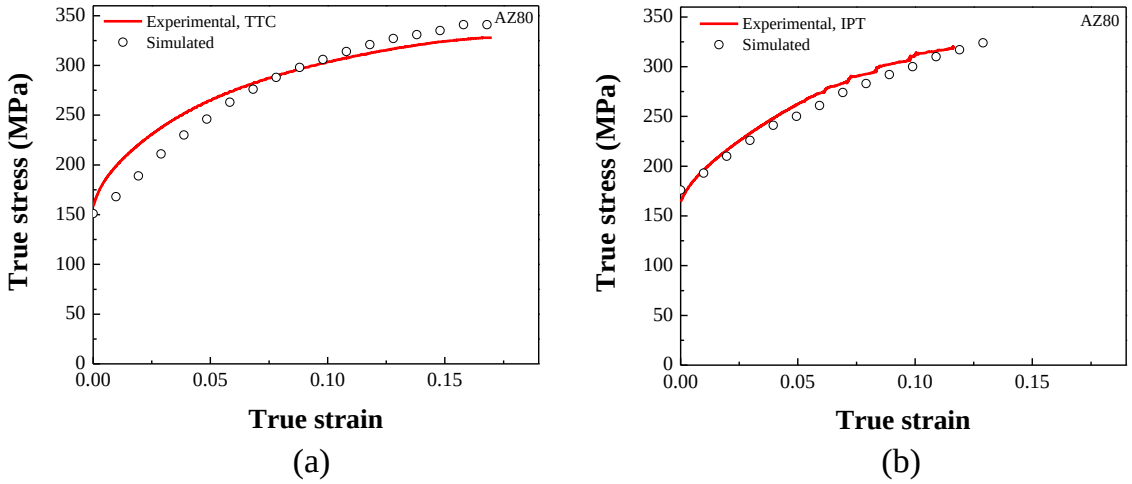

Figure 6.4: Experimental (–-) and predicted (o) plastic response for AZ80 alloy **a)** compression along sheet ND direction (TTC) and **b)** tension along sheet RD direction (IPT).

accomplish this, the Voce hardening parameters from Table 6.1 were adjusted in such a manner that: i) the <a> slip (basal and prismatic) is assumed to be weakly temperature dependant [37, 38], ii) the non-basal <c+a> slip is strongly temperature dependant [43, 111], iii) the twinning is nearly athermal in nature [169] and iv) the initial hardening (θ_0) rate is temperature independent (only corrected for temperature dependence of the shear modulus) [74]. Table 6.2 gives the best fit values of the adjustable parameters for the alloy deformed at 77K. Note that the tabulated stress values are normalised with the CRSS for basal slip, which is 68 MPa, while the initial hardening rate values are normalised with $\mu/200$. It should also be noted that the latent hardening parameters from twinning (h^{TT}) have been assumed to be temperature independent.

Table 6.2: Parameters for VPSC constitutive model of AZ80 alloy deformed at 77K. The stress values are normalised by the CRSS value of basal slip (68 MPa), while the initial hardening rate values are normalised by $\mu/200$ (where μ at 77K is $\approx$ 20 GPa for magnesium). The asterisks denote normalised values

Test alloy (77K)	*Mode*	τ_0^*	τ_1^*	θ_0^*	θ_1	h^{TT}
AZ80	Basal	1	1.5	1	0	4
	Prismatic	3	3	1.8	0	4
	Pyramidal <c+a>	7.4	1.5	1.5	0	4
	Extension twin	0.6	0	0	0	4

6.3 Modelling predictions and analysis

6.3.1 Mechanical behaviour of strong textured material

In this section, the simulation results for strong textured solution-treated AZ80 alloy tested along different deformation paths (TTC, IPT and IPC) at 77K and 293K are presented. The initial texture presented in Figure 6.2 and the parameters listed in Table 6.1 and Table 6.2 are utilised to predict the response of this material.

6.3.1.1 Through thickness compression (TTC)

In this case, simple observation of loading with respect to texture would suggest basal slip and 2nd order pyramidal <c+a> slip. This can be seen further via the Schmid analysis that was carried on the starting texture (Figure 6.5a). It can be seen (Figure 6.5b)

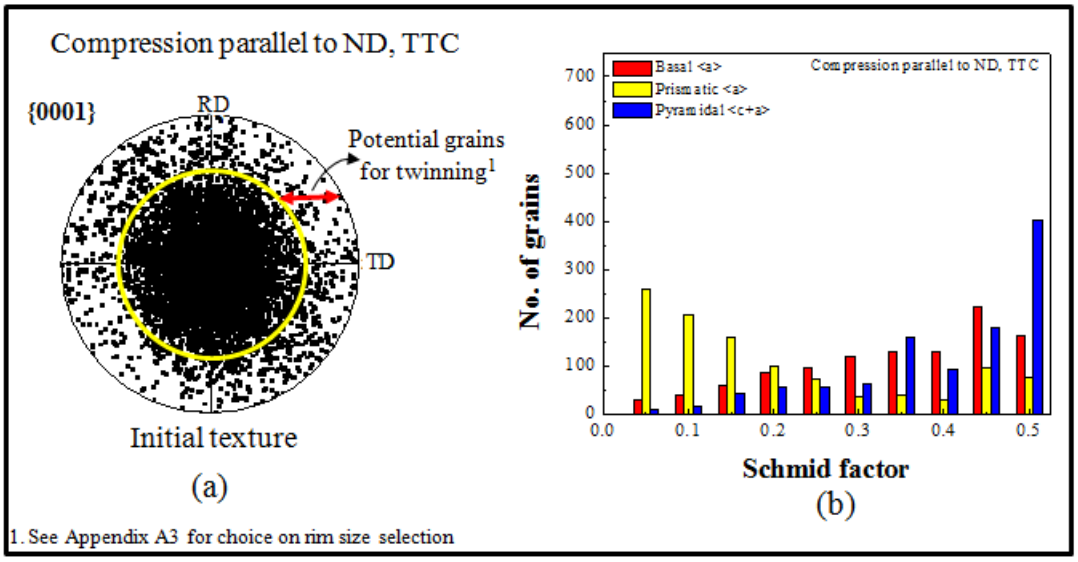

Figure 6.5: a) The {0001} pole figure illustrating the texture prior to TTC simulations and **b)** a histogram generated from Schmid analyses on this data is plotted for basal <a> (red bars), prismatic <a> (yellow bars) and 2nd order pyramidal <c+a> (blue bars) slip.

that a significant fraction of all grains are well oriented for basal <a> slip (e.g. 35% of total grains have a Schmid factor for basal slip > 0.4) and pyramidal <c+a> slip (e.g. 54% of total grains have a Schmid factor > 0.4). In this situation, one would not expect prismatic <a> slip since its CRSS is higher than basal slip and its Schmid factor is low (Figure 6.5b).

Figure 6.6a presents the predicted and experimental stress strain response for the samples compressed in the ND direction (i.e. TTC) at 77K and 293K. Notice that the figure contains only the plastic part of the stress strain curve. The solid lines and open circles represent the experimental curves and model predictions, respectively. The VPSC predictions are in reasonable agreement with experiments. The corresponding predicted relative slip and twin system activities are shown in Figure 6.6b and 6.6c, respectively. The

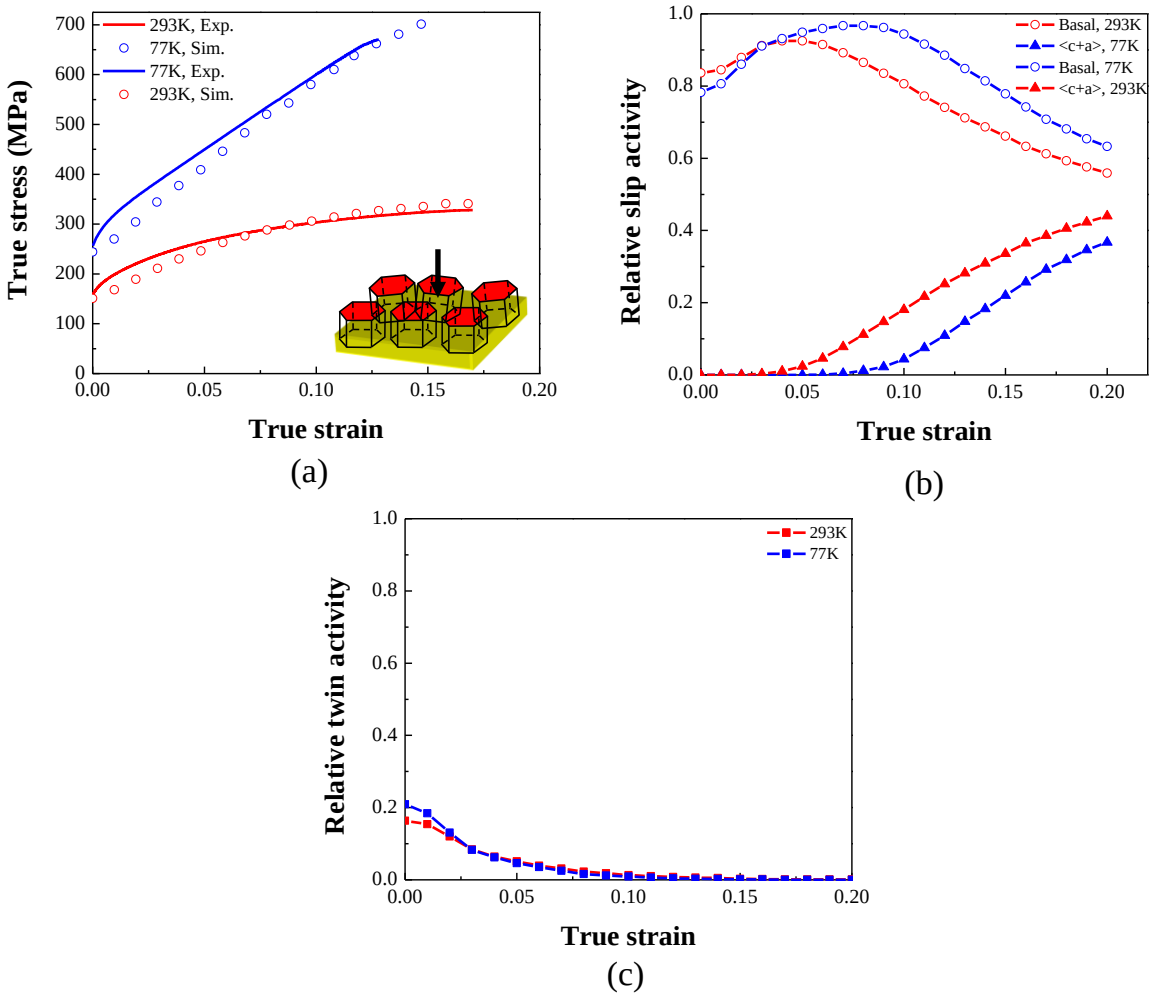

Figure 6.6: a) Experimental (–-) and predicted (o) stress strain response (only the plastic portion) for strong textured solution-treated AZ80 alloy compressed along TT direction at 77K (blue colour) and 293K (red colour) **b)** and **c)** respectively, show the predicted relative slip and twin system activities of each mode during straining. The inset drawing in a) illustrates the orientation and sense of loading axis with respect to the HCP <c> axis.

relative activity of a particular mode corresponds to the incremental fraction of shear strain contributed by that mode. Notice that the prism <a> slip is omitted from the plot because of its negligible contribution for this loading condition.

As expected, up to ≈5% strain, deformation is dominated by basal slip with little extension twinning (Figure 6.6b and 6.6c). The initial dominance of basal <a> slip over pyramidal <c+a> slip can be ascribed to its low CRSS value. The activation of twinning can be ascribed to the presence of grains in the outer rim of the basal texture (as highlighted in Figure 6.5a). Combination of basal slip and extension twinning tends to generate a sharper basal texture as seen in the {0001} pole figure after a TTC strain of 0.10 (Figure 6.7a). A Schmid analysis has been carried out on this texture (Figure 6.7b). The results suggest that a significant fraction of all grains are now well oriented for pyramidal <c+a> slip (e.g. 80% of total grains have a Schmid factor > 0.4). Comparatively, a small fraction of grains are well oriented for basal <a> slip (e.g. 18% of all grains have a Schmid factor for basal slip > 0.4). Consequently, one might expect the decline in basal <a> slip

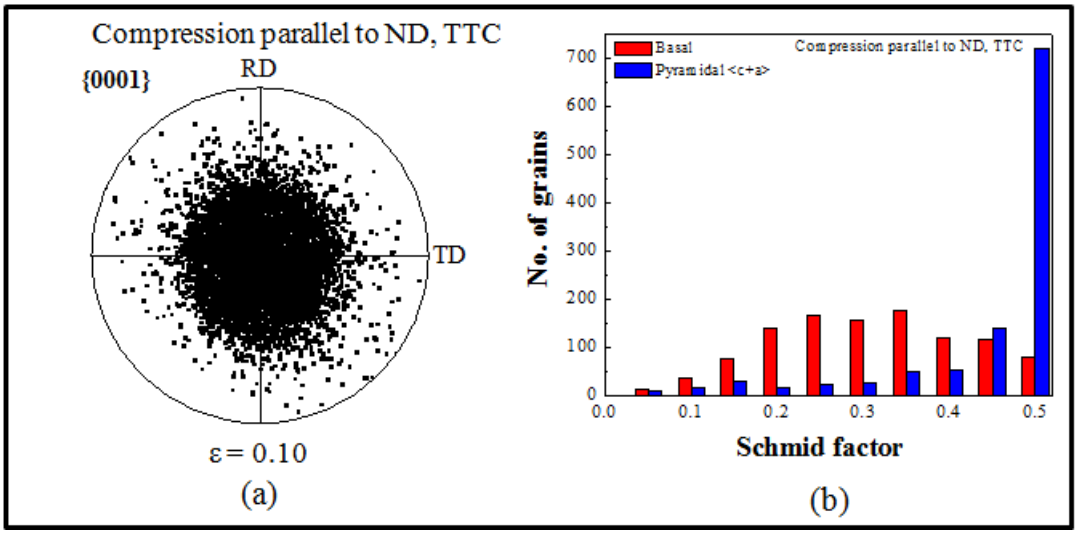

Figure 6.7: a) The {0001} pole figure illustrating the texture after the TTC to a strain of 0.10 and **b)** a histogram generated from Schmid analyses on this data is plotted for basal <a> (red bars) and 2nd order pyramidal <c+a> (blue bars) slip.

and increase in pyramidal <c+a> slip, both being consistent with the present results (Figure 6.6b). In addition, one noticeable difference observed between the two temperatures is in the activity of pyramidal <c+a> slip which is delayed by ~ 2-3% strain at 77K than at 293K (Figure 6.6b). This is interpreted as being to the difficulty of slip at low temperatures.

The prediction of extension twinning during TTC is also consistent with the EBSD observations (see chapter 5, section 5.2.1.2.1). The presence of extension twinning was ascribed to the spread of the c-axes in the initial texture (Figure 6.5a). As indicated earlier contraction and double twinning were not included in these simulations. Considering these factors, it is expected that the contribution of pyramidal <c+a> slip must reflect the total strain accommodated by all the <c>-axis compression deformation mechanisms which is apparently higher at 293K than at 77K (Figure 6.6b). This is in qualitative agreement with the experimental findings that operation of contraction twinning and contraction-extension double twinning decreases with decreasing temperature below room-temperature (chapter 5, section 5.2.1.2.1).

With VPSC, one can also predict the material's R-values, a measure of plastic anisotropy. The R-value is given by the ratio of width strain (ε_w) to thickness strain (ε_t). For TTC, IPT and IPC, the R values can be given as $\varepsilon_{RD}/\varepsilon_{TD}$, $\varepsilon_{TD}/\varepsilon_{ND}$ and $\varepsilon_{TD}/\varepsilon_{ND}$, respectively. Some preliminary comparisons of the model predicted R-values with the experimentally determined values seem to be in good agreement as compared in Table 6.3.

6.3.1.2 In-plane tension (IPT)

Similar to TTC, a simple consideration of loading with respect to texture for IPT would imply basal <a> and prismatic <a> slip (Figure 6.8). This can be seen more clearly

Table 6.3: Comparison of measured and predicted R-values (at fracture) for AZ80 alloy tested in TTC, IPT and IPC at 293K

Test condition	*Measured R-value*	*Predicted R-value*
TTC	1.4	1.4
IPT	1.2	1.1
IPC	1.4	1.6

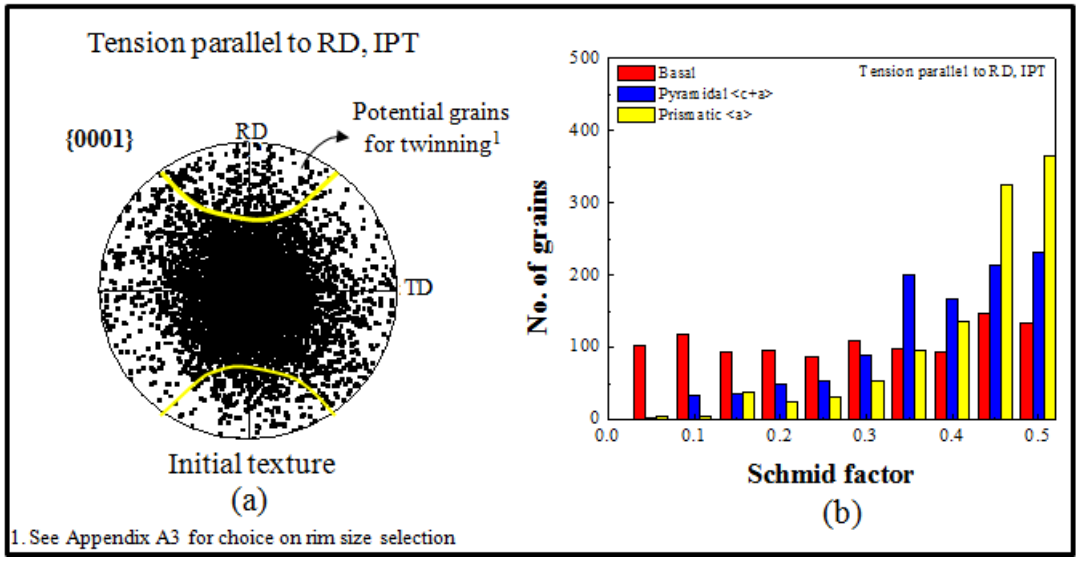

Figure 6.8: a) The {0001} pole figure illustrating the texture prior to IPT simulations and **b)** a histogram generated from the Schmid analyses on this textured for basal <a> (red bars), prismatic <a> (yellow bars) and 2nd order pyramidal <c+a> (blue bars) slip modes.

from the results of Schmid factor calculations presented in Figure 6.8b. Initially, a significant number of grains have a high Schmid factor for basal <a> slip (e.g. 26% of total grains have a Schmid factor > 0.4) and for prismatic <a> slip (e.g. 64% of total grains have a Schmid factor > 0.4). Thus one would expect the operation of basal <a> slip and

prismatic <a> slip during IPT. On the other hand, it is expected that pyramidal <c+a> slip will contribute little due to its high CRSS value.

The experimental and VPSC predictions of stress strain response for the samples deformed in tension parallel to the RD direction (i.e. IPT) of the sheet are shown in Figure 6.9a. Similar to the results described above, the solid lines and open circles represent the experimental and model predictions, respectively. The corresponding slip and twin system activities are presented in Figure 6.9b and 6.9c, respectively. At both temperatures, the model reasonably predicts the yielding and work hardening response of the alloy.

For the sample loaded at 293K, the deformation is mainly accommodated by basal slip and prismatic slip with a small contribution from extension twinning (low strains) and 2^{nd} order pyramidal <c+a> slip (high strains). In contrast, when loaded at 77K, the deformation is largely accommodated by basal and prismatic slip. A small contribution from extension twinning exists, while pyramidal <c+a> slip is completely suppressed. It is interesting to point out that the model prediction of the increase in importance of prismatic <a> slip with lowering temperature is in qualitative agreement with the slip trace analysis results obtained from weak textured material (chapter 5, Table 5.3).

The slip system activities presented in Figure 6.9b displays interesting trends. For example, at $\approx$ 10% strain, the basal activity declines to about 47% from its initial value of 83%, while the prismatic activity rapidly increases to about 50% from its initial value of 4.7%. These marked changes in the slip system activities can be ascribed to grain reorientation. For instance, the texture at 10% strain exhibits a stronger basal texture than the initial texture. This change arises from basal <a> and prismatic <a> slip, as well as

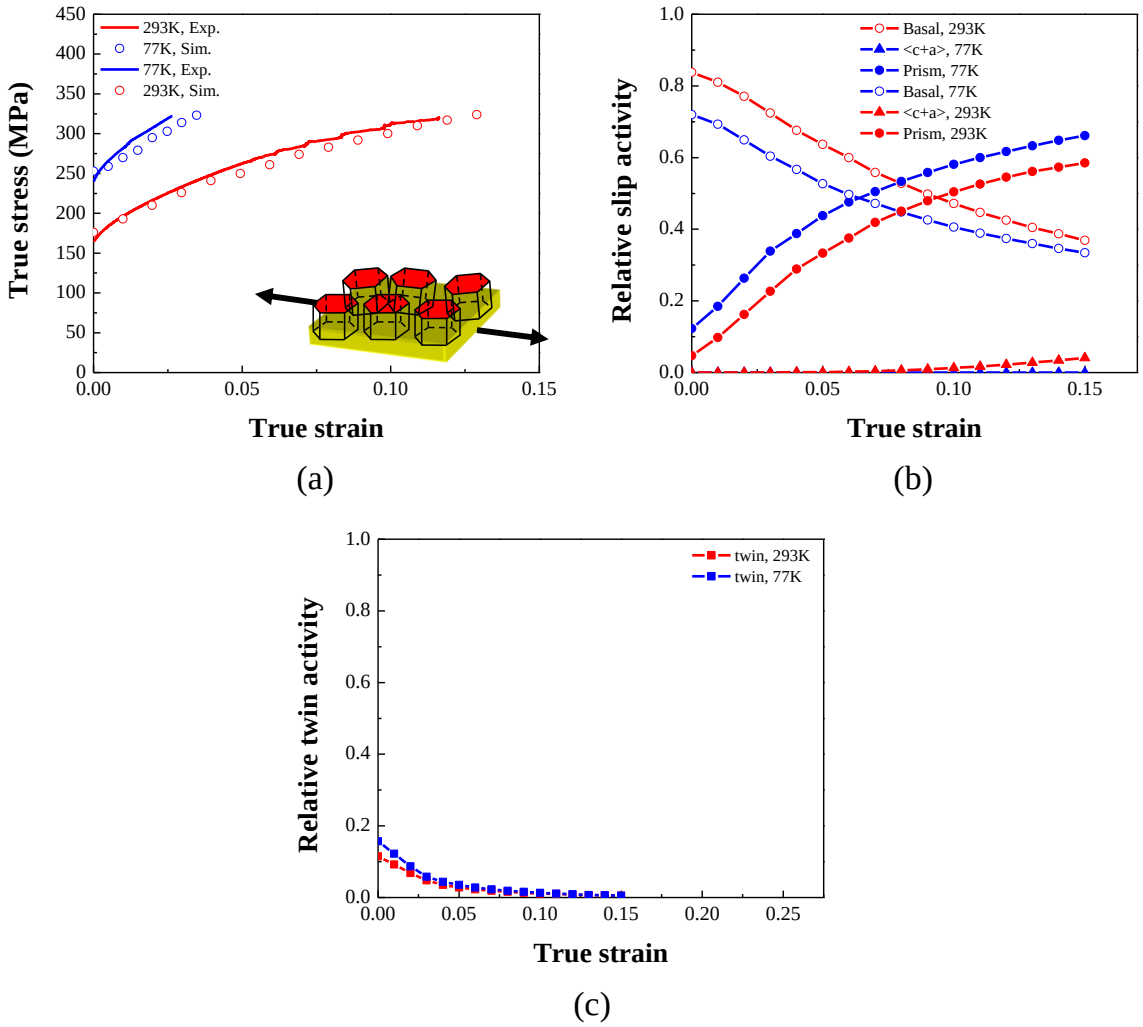

Figure 6.9: a) Experimental (–) and predicted (o) stress strain response (only the plastic portion is plotted) for strong textured solution-treated AZ80 alloy during tensile straining along IP direction at 77K (blue colour) and 293K (red colour) **b)** and **c)** respectively, show the predicted slip and twin system activities of each mode. The inset drawing in a) illustrates the orientation and sense of loading axis with respect to the HCP <c> axis.

extension twinning (Figure 6.10a). This texture change lowers the Schmid factor for basal <a> slip, while it increases the Schmid factor for prismatic <a> slip (Figure 6.10b). At 10% strain only 14% of grains have a Schmid factor > 0.4 for basal slip as compared to 76% of grains with Schmid factor > 0.4 for prismatic slip.

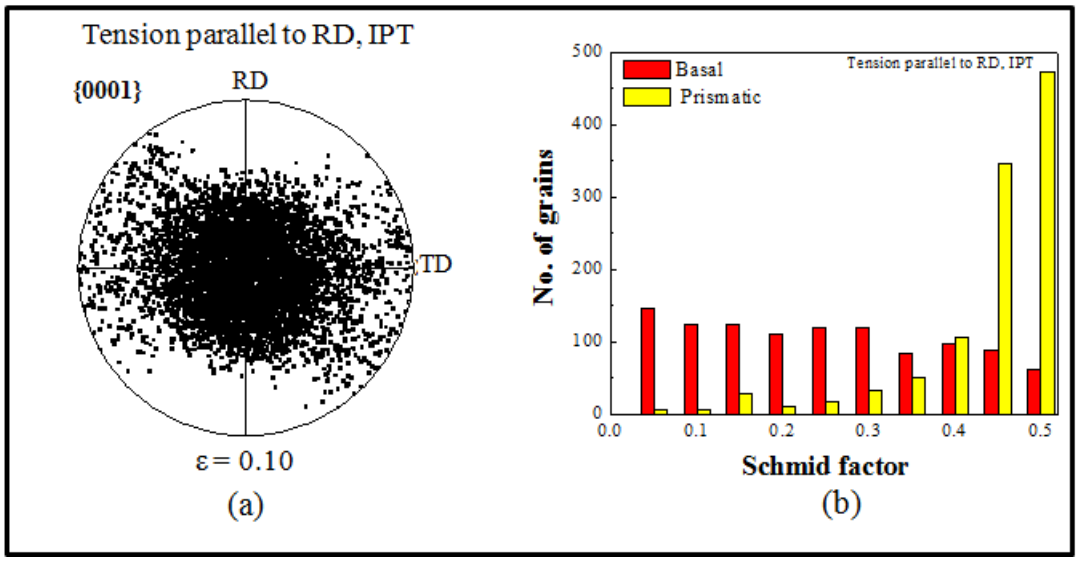

Figure 6.10: a) The {0001} pole figure illustrating the texture after IPT to a strain of 0.10 and **b)** a histogram generated from Schmid analyses on this texture for basal <a> (red bars) and prismatic <a> (yellow bars) slip.

6.3.1.3 In-plane compression (IPC)

In this case one would expect a large proportion of extension twinning. Figure 6.11a shows the simulated and experimental stress strain response for samples compressed in the RD direction (i.e. IPC) at 77K and 293K. The predicted relative slip and twin system activities for this case are presented in the Figure 6.11b and 6.11c, respectively. For the sake of clarity, the contribution from prism <a> slip is removed from this plot as it had a negligible contribution to the strain. The model predictions in this case are not in good agreement with the experiments, particularly at 77K. This is particularly true during the first 4-5% strain (4-5% strain correspond to $\sigma/\mu \sim 0.012$) where the majority of twinning takes place over this range of strains. The model over-predicts the hardening rate, while at higher strains it is significantly under predicted (Figure 6.11d).

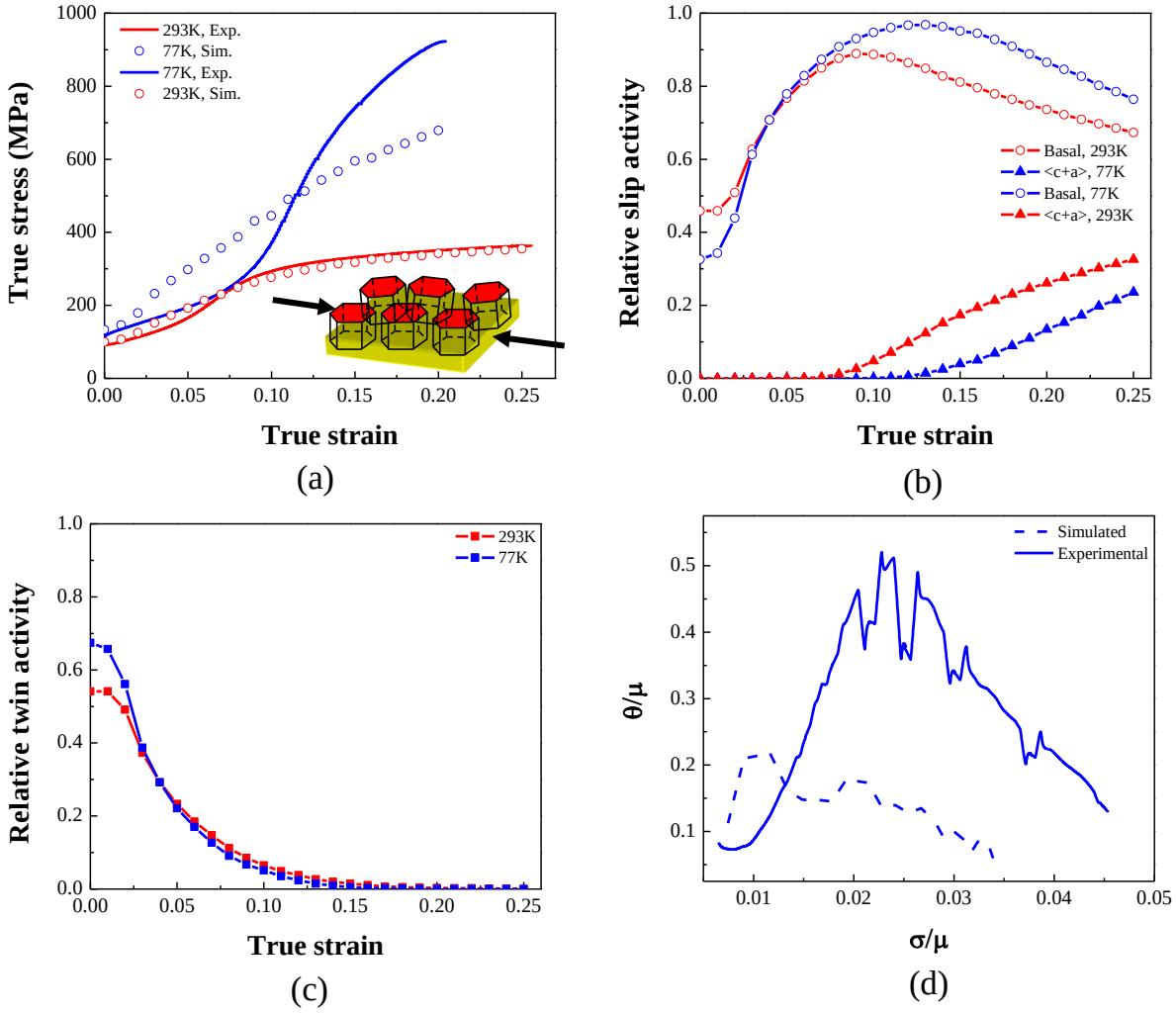

Figure 6.11: a) Experimental (–) and predicted (o) stress strain response (plastic region only) for strong textured solution-treated AZ80 alloy compressed along the IP direction at 77K (blue colour) and 293K (red colour) **b)** and **c)** respectively, show the relative slip system and twin system activities of each mode during straining and **d)** the normalised work hardening vs. stress plot derived from the data of 77K deformed sample. The inset drawing in a) illustrates the orientation and sense of loading axis with respect to the HCP <c> axis.

During IPC, once the majority of twinning finishes (i.e. around 10% strain) subsequent deformation behaviour might be expected to be similar to TTC. A comparison of experimental stress strain curves for TTC and IPC loadings (Figure 6.12a) shows some agreement with this idea (see the extended portion of the TTC curve in Figure 6.12a). A careful examination of mode activities after 10% strain suggests that deformation is still mostly basal dominated for the IPC case (Figure 6.12b). In contrast, the TTC case exhibits significant presence of hard pyramidal <c+a> slip. The reason for the different predicted flow stress in IPC and TTC is revealed in Figure 6.13a and 6.13b, which show the predicted textures for TTC and IPC samples at 10% strain. The textures are significantly different. For example, the IPC sample exhibits a texture with basal poles considerably

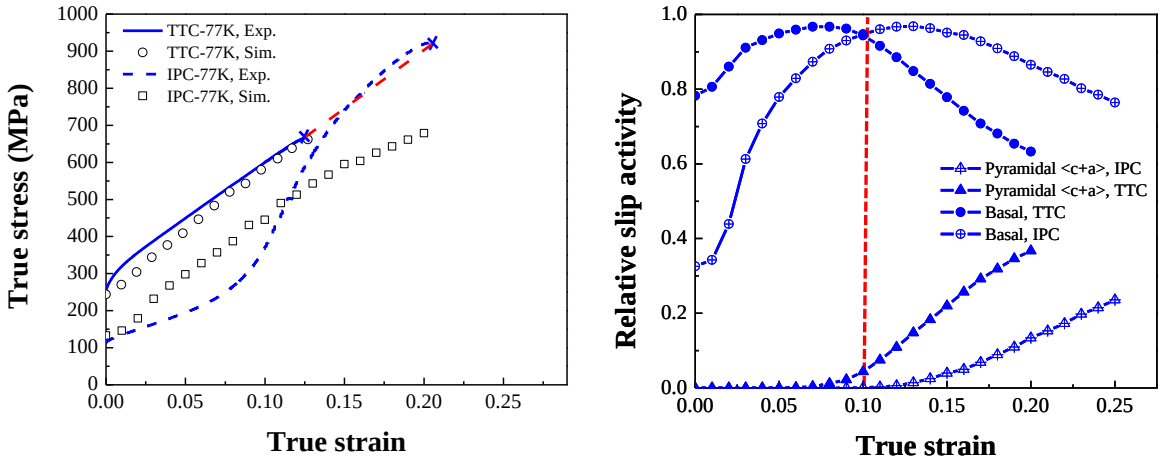

(a) (b)

Figure 6.12: a) Predicted and experimental stress strain response of AZ80 alloy tested in TTC and IPC at 77K and **b)** shows the corresponding predicted relative slip system activities. The broken red line in a) is the extended portion (drawn by hand) of TTC curve, while the symbol × indicates the fracture of the sample.

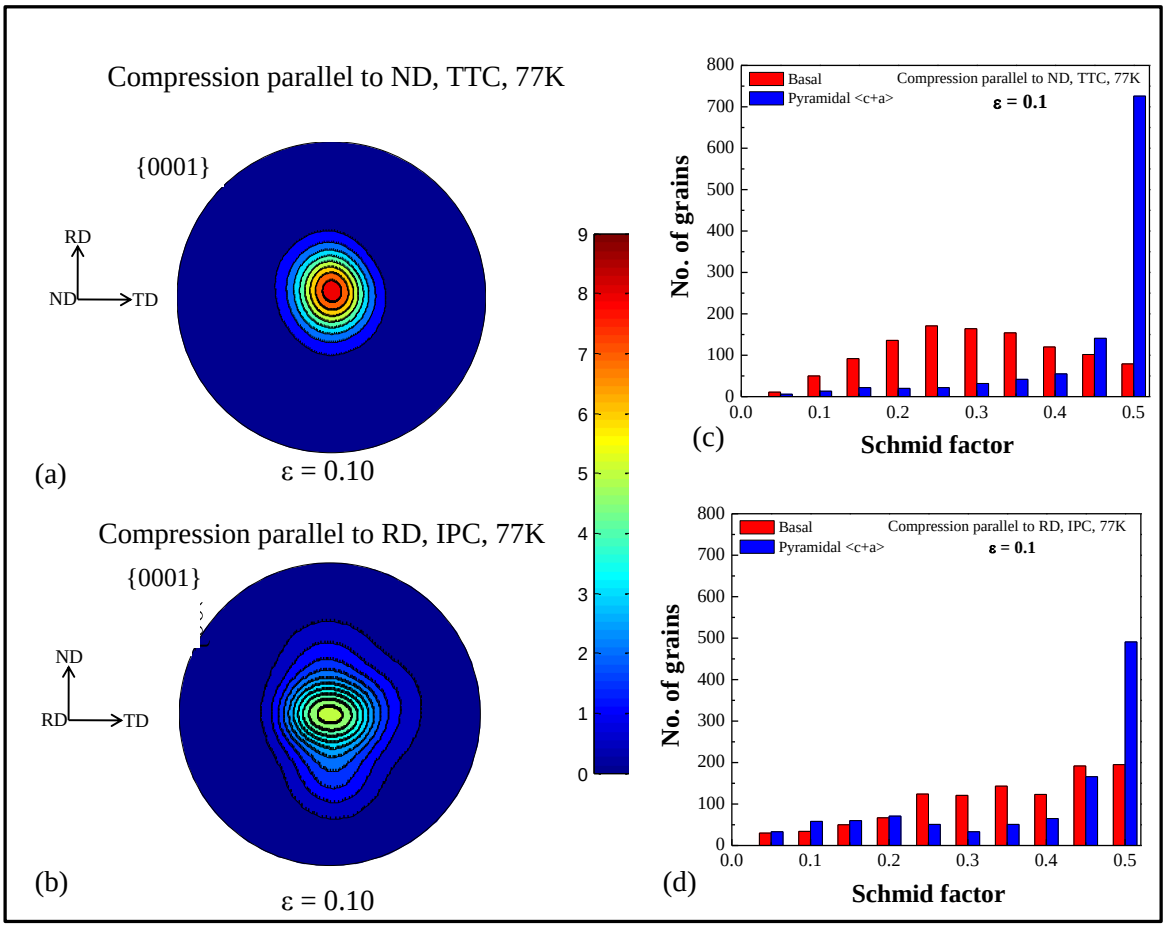

Figure 6.13: a) and **b)**, respectively show the predicted {0001} pole figures (recalculated from the ODF using Mtex [192]) for the samples compressed to a strain of 0.10 in TTC and IPC, while **c)** and **d)** show the corresponding histograms of Schmid factor calculations for basal and pyramidal <c+a> slip systems. The RD, TD and ND correspond to rolling, transverse and normal directions of the sample, respectively. The intensity colour scale is given in multiples of random distribution (m.r.d.).

scattered around the ND direction. In the TTC sample a strong basal texture component parallel to ND direction is observed. In addition, the predicted texture intensity is significantly higher for the TTC than the IPC. These differences in texture can cause significant changes to the activities of the available deformation modes as can be seen

through Schmid factor calculations presented in Figure 6.13c and 6.13d. For the TTC case, only 16% of total grains have Schmid factor > 0.4 for basal slip as opposed to 36% of grains during IPC.

The above results highlight the strong effect of texture on the activities of different deformation modes. One possible explanation for the poor prediction of the stress-strain response in IPC would therefore be that the model does not accurately capture the texture. The predominant twin reorientation (PTR) scheme (Appendix A2.4), is known to miss some aspects of twin prediction in magnesium. For example, it only considers one active twin system (the predominant one) per grain. However, the experimental results demonstrated that grains frequently contain more than one active variant per grain (see chapter 5, section 5.2.1.2.2). Furthermore, it reorients the entire grain simply based on threshold twinned fraction. Given the importance of twinning in this case, it is perhaps not surprising that this condition is most poorly captured by VPSC.

Despite the comments above, the model does predict that deformation is first dominated by extension twinning and basal <a> slip, then continues with the basal and pyramidal <c+a> slip at large strains, consistent with experiments (Figure 6.11b and 6.11c). Figure 6.11c shows that at low strains (2-3%) the relative contribution of $\{10\bar{1}2\}$ twinning is slightly higher at 77K than at 293K. This can be related to higher CRSS value of non-basal slip at low temperature [37, 38, 111]. Moreover, the model also predicts a higher activity of pyramidal <c+a> slip at 293K compared to 77K, qualitatively consistent with the slip trace analysis results (chapter 5, Table 5.3).

6.3.2 Mechanical behaviour of weak textured material

In this section, the results of simulations performed on weak textured material at 77K and 293K are presented. In this case, the ODF calculated from the measured neutron data was discretized into a weighted file of 10,500 orientations to use as an input for the simulations (Figure 6.14). Note that the parameters listed in Table 6.1 and Table 6.2 are used to simulate the response of this material.

Figure 6.15a shows the predicted (open circles) and experimental (solid lines) true stress strain response of weak textured samples compressed at 77K and 293K. For the 77K case, the model reasonably predicts the yielding and the hardening response of the alloy. Comparatively at 293K, it slightly under predicts the flow stress. The corresponding

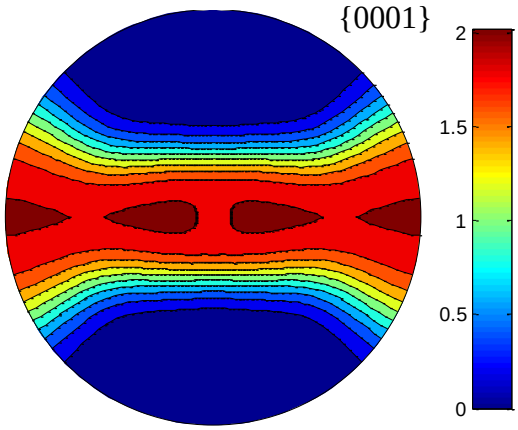

Figure 6.14: The {0001} pole figure (recalculated from the ODF using Mtex [192]) illustrating the input texture used for simulating the weak textured material response. Note that a discretized texture file containing 10,500 orientations (with weights) was used as an input for plotting in Mtex. The intensity colour scale is given in multiples of random distribution (m.r.d.).

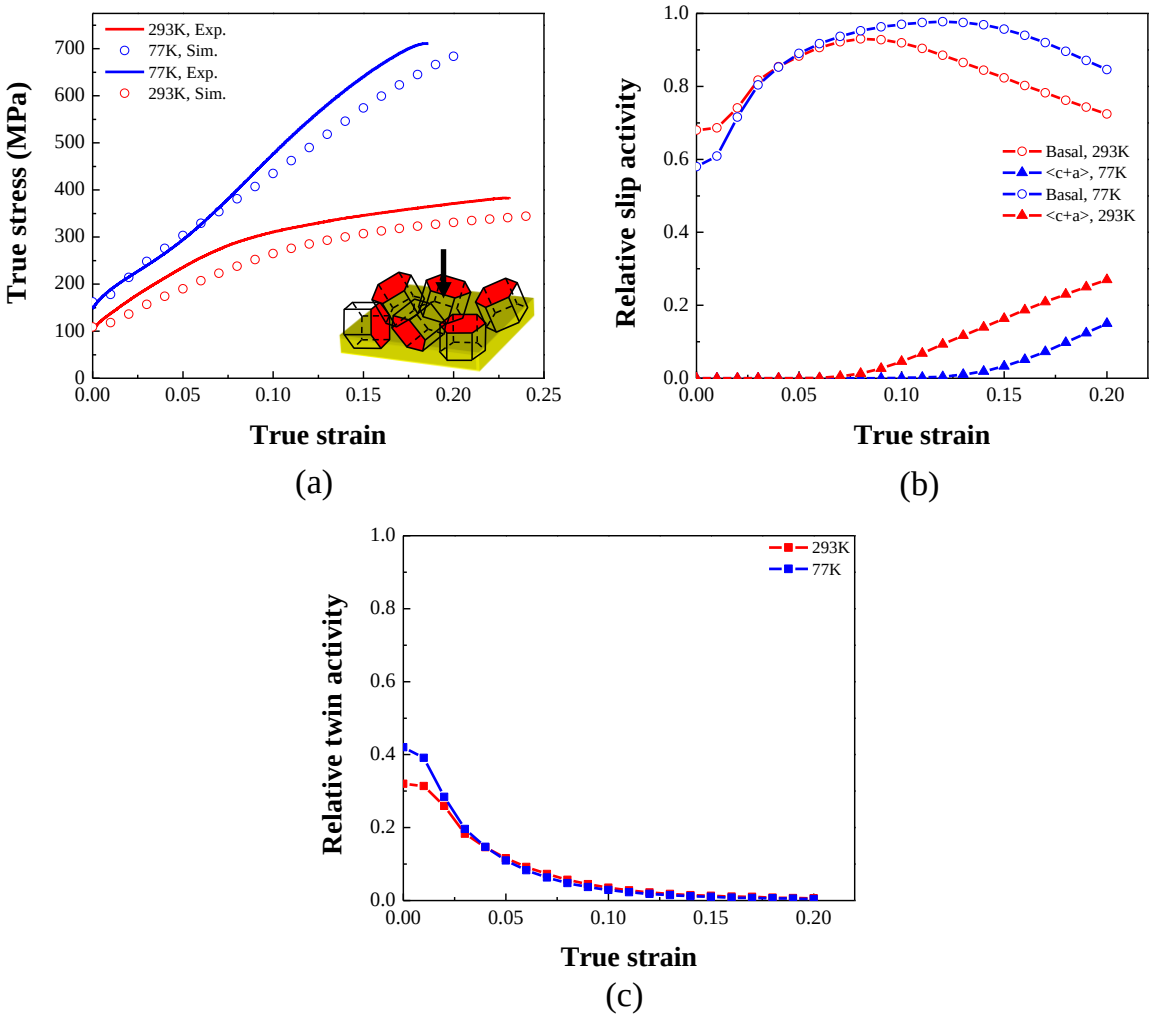

Figure 6.15: a) Experimental (--) and predicted (o) stress strain response (plastic portion only) for weak textured solution treated AZ80 alloy compressed at 77K (blue colour) and 293K (red colour) **b)** and **c)** show the corresponding predicted relative slip and twin system activities of each mode during straining, respectively. The inset drawing in a) illustrates the orientation and sense of loading axis with respect to the HCP <c> axis.

relative slip and twin system activities are presented independently in Figure 6.15b and 6.15c respectively. Note that the activity of prism <a> slip is not included in the plot because of its negligible contribution.

Compared to IPC, the model predictions of the weak textured case give a better agreement with the experimental curves. However, the prediction is slightly worse when compared with the TTC and IPT cases. As before, this indicates that when the twinning contribution increases the model predictions are less reliable.

The predicted relative mode activities at 293K suggest that deformation is first dominated by basal slip and extension twinning up to nearly 6-7% strain then it is accommodated by the combination of basal slip and 2nd order pyramidal <c+a> slip with a small amount of extension twinning. Alternatively, when loaded at 77K, deformation is accommodated by basal slip and extension twinning up to 10-11% strain then it is taken over by pyramidal <c+a> and basal slip. In this case the model correctly predicts a drop in <c+a> slip contribution with decreasing temperature, consistent with the slip trace analysis results (chapter 5, section 5.3.1.3.1). Interestingly, the model does not predict any strong effect of temperature on the propensity of deformation twinning (Figure 6.16), which is again in qualitative agreement with the experimental observations. Furthermore, it also predicts that the twinning activity for this case is higher than the TTC and IPT cases but, lower than the IPC case as expected. Overall, these predictions are largely in agreement with experimental findings except the absence of prismatic <a> slip. It is not clear at present why the prismatic <a> slip is absent in this case.

A further insight into the active deformation modes can be gained by examining the textures. Figure 6.17 shows the measured and predicted pole figures (basal and prismatic) corresponding to a strain of 18% for the samples compressed at 77K and 293K. At both temperatures, the measured and predicted textures look qualitatively similar, although the predicted intensity around the center of the {0001} pole figure is higher than

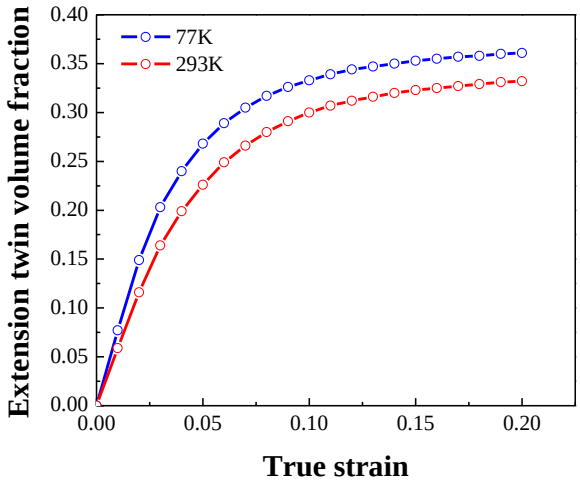

Figure 6.16: A comparison of VPSC predicted $\{10\bar{1}2\}$ twin volume fractions for the samples deformed at 77K and 293K.

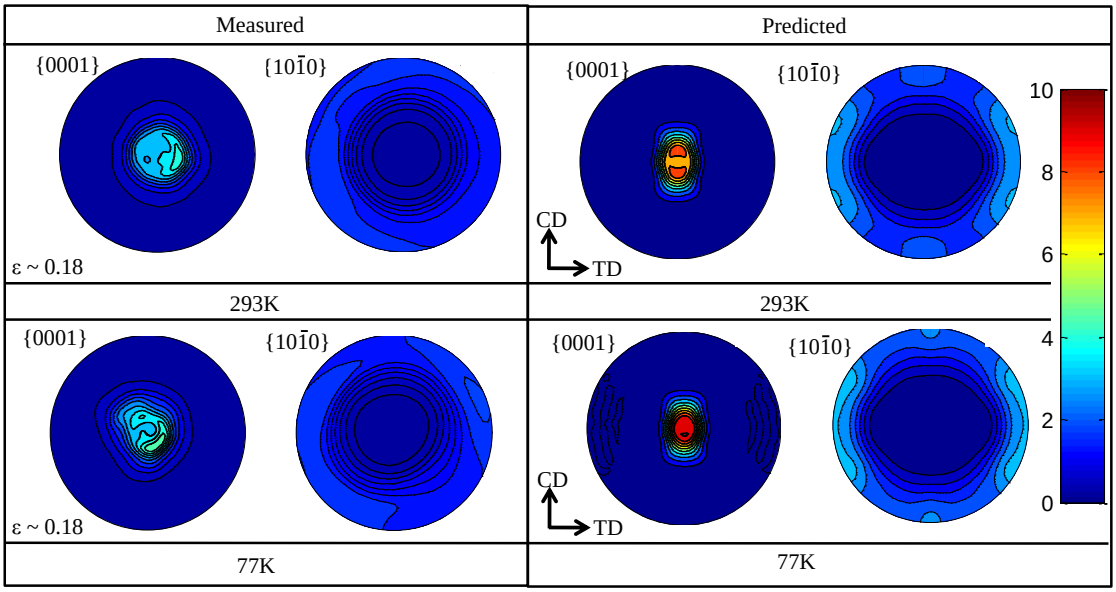

Figure 6.17: Comparison of measured and predicted $\{0001\}$ and $\{10\bar{1}0\}$ pole figures (recalculated from the ODF using Mtex [192]) for material with weak starting texture deformed in uniaxial compression at 77K and 293K. The measured pole figures were obtained from neutron diffraction. The intensity colour scale is given in multiples of random distribution (m.r.d.).

with the measured intensity (e.g. for 293K case the maximum measured intensity is 4 m.r.d., while the maximum calculated intensity is around 8 m.r.d.). The latter observation can be related to the fact that the model does not consider any local orientation change within the grain. It is likely that this would lower the overall intensity of the texture and result in greater spread of poles. Moreover, the PTR scheme flips the entire grain when the threshold twinned fraction is reached. This can have significant effects on the overall texture intensity. Further, the texture prediction shows a typical splitting in the basal fiber texture which is considered to be the signature of <c+a> slip system activity [48, 178]. It can be noticed that the strength of the calculated texture at 77K is higher than at 293K (e.g. at 0.18 strain the maximum calculated intensity is 10 m.r.d. for 77K, while 8 m.r.d. for 293K). This is related to the slightly higher contributions of extension twinning and basal slip at 77K as compared to 293K (Figure 6.15 and Figure 6.16).

As a final analysis, a comparison of twinning fractions evaluated from neutron diffraction experiments and VPSC predictions as a function of strain for the samples compressed at 293K and 77K are shown in Figure 6.18. For both cases, the model initially over predicts the twinning fractions. Beyond ~10% strain, the twinning fraction is under predicted. At large strains (> 10%), the model predicts a near saturation in the twinning fraction. Experiments show, in contrast, a continuous increase in twinning fraction at both temperatures. Here a simple CRSS law has been applied for twin activation. However, the recent [33] statistical analyses on deformation twinning suggest that twinning is highly sensitive to the factors such as microstructure (e.g. grain size, orientation, dislocation density, alloy content) and applied test conditions (e.g. strain rate, temperature, stress level). Further, the model only accounts for twinning fractions that obeys the Schmid law.

However, there are reports [33] in magnesium suggesting that the fraction of non-Schmid twins can be significant. It is clear that the existing twinning model requires further development.

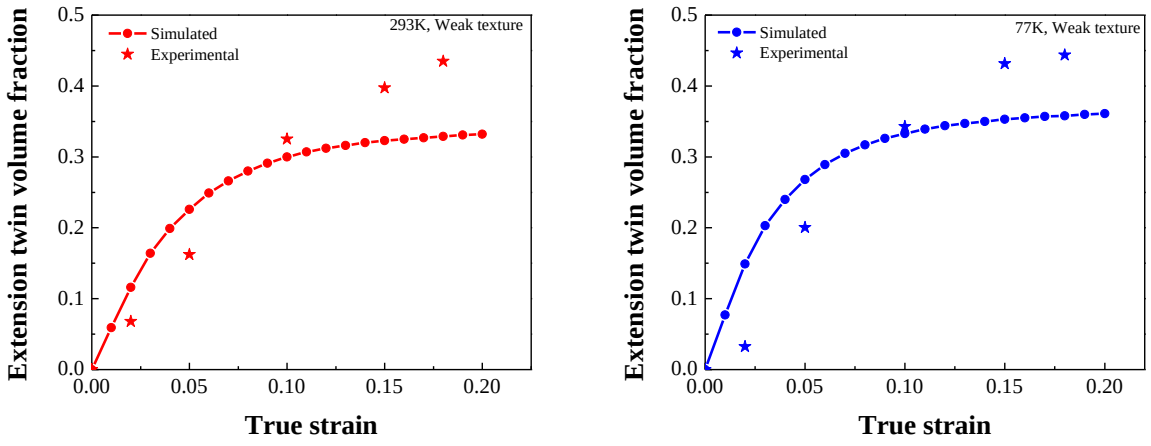

(a) (b)

Figure 6.18: $\{10\bar{1}2\}$ twin volume fractions determined from neutron diffraction (star symbols) and VPSC predictions (solid lines with closed circles) as a function of strain for **a)** 293K and **b)** 77K deformed samples.

6.4 Discussion

6.4.1 Discrepancy between single crystal parameters and their temperature dependence

It is well known from magnesium single crystal data that slip on non-basal slip systems is difficult [37, 38, 111]. This is reflected by the fact that the CRSS ratio of non-basal to basal slip lies in the range of 50-100. These values are roughly an order of magnitude larger than those determined from VPSC simulations (Table 6.1). The

noticeable difference between the single crystal and polycrystal behaviour can be accounted for with reference to i) solute content [189, 190], ii) grain boundaries which act as a potent source and sinks for dislocations [191, 193], and iii) type of grain-matrix interactions used for the calculations (i.e. the n_{eff} value) [191].

Most of the previous single crystal studies were carried out on pure magnesium or dilute magnesium alloys (solute concentrations < 0.5 at %). However, the commercial alloys of interest (e.g. AZ31, AZ80) contain significant amounts of solute elements. Thus one must be careful when making a direct comparison between different studies. Moreover, the solute elements have diverse effects on the strengthening and softening of slip systems. Recently, Hutchinson and Barnett [190] have calculated two bounds for the variation in CRSS ratio of prismatic to basal slip as a function of strengthening of the basal <a> slip due to the addition of common alloying elements (e.g. Al, Zn) (Figure 6.19). As can be seen in Figure 6.19, the CRSS ratio initially falls rapidly but then it almost saturates with increasing strength of the basal <a> slip. The CRSS ratios determined from the present simulation of AZ31 and AZ80 alloys are compared with these calculations (Figure 6.19). It can be noticed that the CRSS ratio of prismatic to basal slip determined for AZ31 and AZ80 alloy lie within the suggested bounds. This indicates that at higher solute concentrations the CRSS of basal slip increases such that the CRSS ratio of prismatic to basal <a> slip remains approximately same.

The dislocation density is another factor that can have significant effect on the CRSS ratios. The recent calculations of Hutchinson and Barnett [190] have suggested that an increase in dislocation density from 10^6 m^{-2} to 10^{12} m^{-2} results in a drop of CRSS ratio

of prismatic to basal slip from a value of 40:1 to ~7:1. Note that a soft annealed material has a dislocation density similar to this i.e. 10^{12} m^{-2}.

Recently, Raeisinia and Agnew [191] have pointed out the importance of the stiffness of the grain-matrix interaction (n_{eff}) on the CRSS ratios. According to this work, a stiffer grain-matrix interaction yields higher CRSS ratios, while more compliant grain-matrix interactions results in lower CRSS ratios. The CRSS ratios determined from the present work using n_{eff} = 10 are consistent with the ratios provided in ref. [191]. Moreover, these ratios follow the general trend that basal <a> slip and $\{10\bar{1}2\}$ twinning are the easiest modes, while the pyramidal <c+a> slip is the hardest mode.

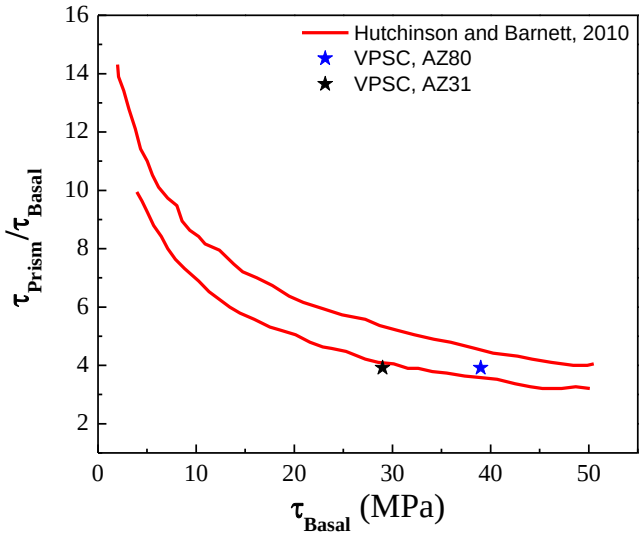

Figure 6.19: The upper and lower bound of variation in CRSS ratio of prismatic to basal slip as a function of CRSS of basal slip is replotted from the work of Hutchinson and Barnett [190]. The VPSC determined values for AZ31 (black star) and AZ80 (blue star) alloy from the present work are compared with these bounds.

Figure 6.20 shows the variation of CRSS values as a function of temperature for basal slip, prismatic slip, pyramidal <c+a> slip and $\{10\bar{1}2\}$ twinning. The plotted values were obtained from the present simulations. There are marked differences in the strength of deformation modes as a function of temperature. Extension twinning is predicted to be nearly athermal, while basal, prismatic and pyramidal <c+a> slip are predicted to be 1.7, 1.3 and 2 times stronger, respectively at 77K than at 293K (Table 6.4). The temperature dependence of these modes is similar to those previously determined from magnesium single crystals (Table 6.4).

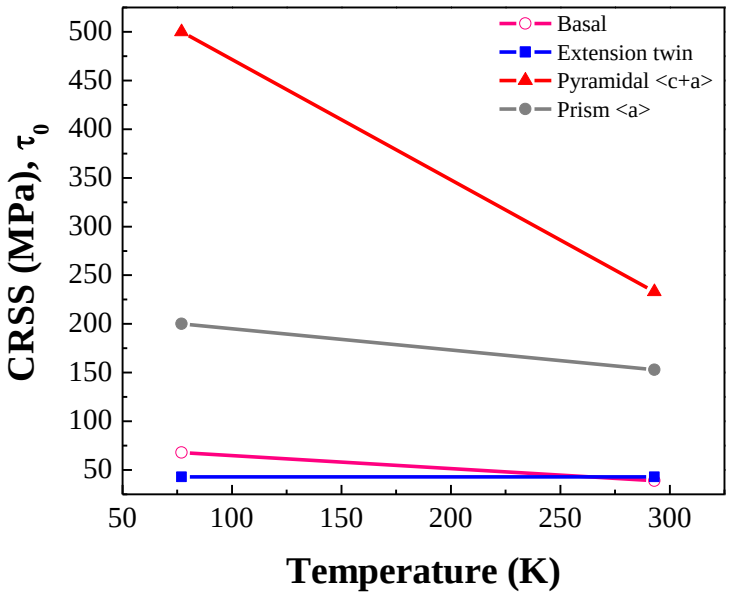

Figure 6.20: Variation of CRSS (τ_0) as a function of temperature (determined from VPSC simulation) for different deformation modes in an AZ80 magnesium alloy.

Table 6.4: Comparison of CRSS ratios of basal, prismatic and pyramidal <c+a> slip modes taken at 77K and 293K with the literature values

CRSS ratios	*Present study (VPSC determined)*	*Literature (single crystal experiments)*	*References*
$\tau_{Basal}^{77K} / \tau_{Basal}^{293K}$	1.7	1.5	[37]
$\tau_{Prism}^{77K} / \tau_{Prism}^{293K}$	1.3	2.1	[38]
$\tau_{Pyramidal<c+a>}^{77K} / \tau_{Pyramidal<c+a>}^{293K}$	2.2	2.4, 3.6	[43, 111]

6.4.2 Applicability of CRSS criterion for twinning

Similar to slip, twinning in a grain is considered to be active when a resolved shear stress on twinning plane (K_1) along twinning shear direction (η_1) reaches to some critical value. The available literature provides conflicting views on the applicability of such a criterion for the activation of twinning. For instance, Gharghouri and co-workers [157] have reported that a CRSS criterion is applicable for the activation $\{10\bar{1}2\}$ twinning in Mg-7.7at%Al alloy. On the other hand, there are reports that extension twins frequently violate the CRSS criterion, with twins having low Schmid factors being active [33]. In some cases the variants with the lowest Schmid factor have been found to be active [57]. The recently published work on AZ80 alloy [173] supports the latter observation.

6.4.3 Hardening models for twinning

As mentioned earlier, a modified Voce law has been used here to describe the hardening behaviour of both slip and twin systems. This hardening law seems appropriate for the hardening associated with slip systems. Consistent with this the results of the

predictions of the stress-strain response of TTC and IPT cases (presented in section 6.3.1.1 and 6.3.1.2), were found to be in good agreement with the experiments. However, the appropriateness of this model for twinning is questionable. This is evident from the fact that twinning dominated IPC cases gave predictions far from the experiments (section 6.3.1.3). Indeed, it was found that it was not possible to adjust the Voce parameters for twinning (equation 6.1) to give a good prediction of experimental hardening behaviour observed during IPC.

The experimental results presented earlier in chapter 5, section 5.2.1.2 and section 5.3.1.3 indicate that the microstructure which originates from twinning deformation is extremely complex, particularly for the 77K case. One observes cases where many twins subdivide the parent grain, different variants of same twinning system impinging on each other, secondary twins forming within the primary twin. These factors could have non-negligible role in the hardening behaviour, but are not considered in the simulations.

There was no separate consideration given to the phenomenon of twin nucleation and its subsequent growth. Previous studies [194-196] have suggested that very high stresses are needed to nucleate the twin embryos. Therefore, it is generally believed that slip must precede twin nucleation. Dislocation structures such as pile-ups provide stress concentrations required for the twin nucleation. There are reports for magnesium [162, 197, 198] that suggest that twinning starts only when some dislocations are introduced in the material. Moreover, the twin nucleation stress should evolve distinctly depending on the type of dislocations. As indicated by Agnew and colleagues [72, 162], the basal <a> and prism <a> dislocations have a negative effect on the twin CRSS value (basal dislocations

have stronger effect than prism dislocations) whereas the pyramidal <c+a> slip has a positive effect.

Moreover, the present model accounts for slip-twin and twin-twin interactions only empirically via the latent hardening coefficients. In an attempt to discern the effect of dislocations on subsequent twinning activity, Proust and co-workers [162] have tested AZ31 samples by changing the strain-paths. The samples were first loaded in TTC up to strains of 5% and 10%, and then reloaded in IPC. During TTC, the material primarily deforms by basal <a> and pyramidal <c+a> slip, though there is some possibility of compression twinning as indicated from experiments (chapter 5, section 5.2). Both the reload IPC curves exhibit higher yield strength (the yield strength was increased by 40 and 60 MPa for 5% and 10% prestrained samples, respectively) and a more prolonged transition from easy to hard deformation than the monotonic IPC curve. According to Proust et al. [162] this can be related to the effect of <a> and <c+a> dislocations introduced during the preloading stage that could potentially acts as a barrier for twin nucleation or/and twin propagation.

Overall, in the present VPSC model twinning is treated in a very simplistic manner. Certainly, a more sophisticated description of twinning is required. Since the start of this work there have been some efforts towards improving the twinning model. Recently, Proust et al. [162] have improved the treatment of twinning in VPSC by discriminating each twinned grain as a composite grain consisting of layers of twin and matrix. This new approach accounts for the barrier effect that a specific twin poses to specific dislocation via a Hall-Petch like effect. Most recently, Beyerlein and Tomé [168] have developed a new probabilistic theory for twin nucleation in HCP metals and then

implemented this into a multi-scale constitutive model. The model was validated for pure zirconium deformed at 76 and 300K. Their reported results seem to suggest that the model correctly captures the observed statistical nature of deformation twinning.

6.5 Summary

In this work, the VPSC model has been utilized to simulate the mechanical behaviour of strong and weak textured solution-treated AZ80 alloy deformed at 77K and 293K. A single set of hardening parameters were established to predict the response of alloy in different deformation paths (TTC, IPT and IPC) with different initial textures for 77K and 293K. To the author's knowledge, no such attempt was made to do this in the past for the AZ80 alloy. Moreover, the present study examines the strengths and weaknesses of the VPSC model. At both temperatures, the model predictions of TTC and IPT cases were in good agreement with the experiments. During TTC and IPT, the deformation was mainly dominated by slip. However, the disagreement with the experiments grows with increasing twinning contributions as evident from the weak textured and the IPC cases that were examined. The analysis indicates that the present criterion for the twin activation and its subsequent hardening is not sufficient. It points towards a need of improved representation of twinning. Nonetheless, the model interpretations of experiments can be summarised as follows:

i) During TTC, deformation was mainly accommodated by basal slip and pyramidal <c+a> slip. The importance of latter was found to increase with increasing temperature and the plastic strain.

ii) During IPT, deformation was dominated by basal and prismatic slip at both temperatures. However, the results indicated a drop in contribution of prismatic <a> slip at 293K as compared to 77K.

iii) During IPC, deformation was largely accommodated by basal slip and $\{10\bar{1}2\}$ twinning. The pyramidal <c+a> slip only participates at large strains i.e. when significant fraction of grains had already been twinned. The propensity of $\{10\bar{1}2\}$ twinning was found to be weakly temperature dependant.

iv) Deformation of weak textured material was initially dominated by the basal slip and $\{10\bar{1}2\}$ twinning then at higher strain levels the pyramidal <c+a> slip became important. The temperature appears to have a small effect on the propensity for $\{10\bar{1}2\}$ twinning. The importance of pyramidal <c+a> slip was however, found to increase with increasing temperature. The model seems to capture well the important features of deformation textures, although the twinning fractions evaluated from the model were not in good agreement with experiments.

CHAPTER 7 - Effect of Precipitates on the Deformation Behaviour of AZ80

7.1 Introduction

In the previous two chapters, the effects of initial texture and temperature on the mechanical behaviour of solution-treated AZ80 alloy have been examined using combined experimental and modelling methodologies. In this chapter, the effect of microstructure i.e. a homogenous distribution of precipitates (aged) on deformation behaviour of weakly textured AZ80 alloy will be studied. Modelling the plastic deformation of two-phase polycrystals requires a more complex approach compared to the one utilised in the last chapter. The VPSC model is a so-called one-site model meaning that each crystal (grain or precipitate) is considered as though it is surrounded by an "effective medium". There is no way to capture the reality of one phase (precipitate) within the grains of the second phase (matrix). The heterogeneity arising from the fact that precipitates with different symmetry and properties are embedded within the matrix (each with its own slip systems and associated activation stresses) is impossible to replicate accurately in this sort of model. Given these reasons, no attempt was made to model the two-phase behaviour of the AZ80 alloy.

While most of the experimental results presented in this chapter come from the work on weakly textured material, some observations on strong textured material will also be presented. The chapter is organised as follows. Section 7.2 contains experimental results which include uniaxial tension and compression, neutron diffraction, Nomarski microscopy and high resolution EBSD characterization. The discussion of experimental results will be

presented in section 7.3, where the influence of precipitates on the mechanical properties, texture evolution and deformation mechanisms of the alloy will be discussed. A summary of results will be presented in section 7.4.

7.2 Experimental results

In this section, the experimental results obtained on weakly textured solution-treated and aged material will be presented. For this purpose, the loading axis IPF maps illustrating the initial microstructures of solution-treated and aged samples prior to deformation are presented in Figure 7.1a and 7.1b, respectively. The average initial grain size for both solution-treated and aged samples was similar (i.e. ~32 µm). As can be

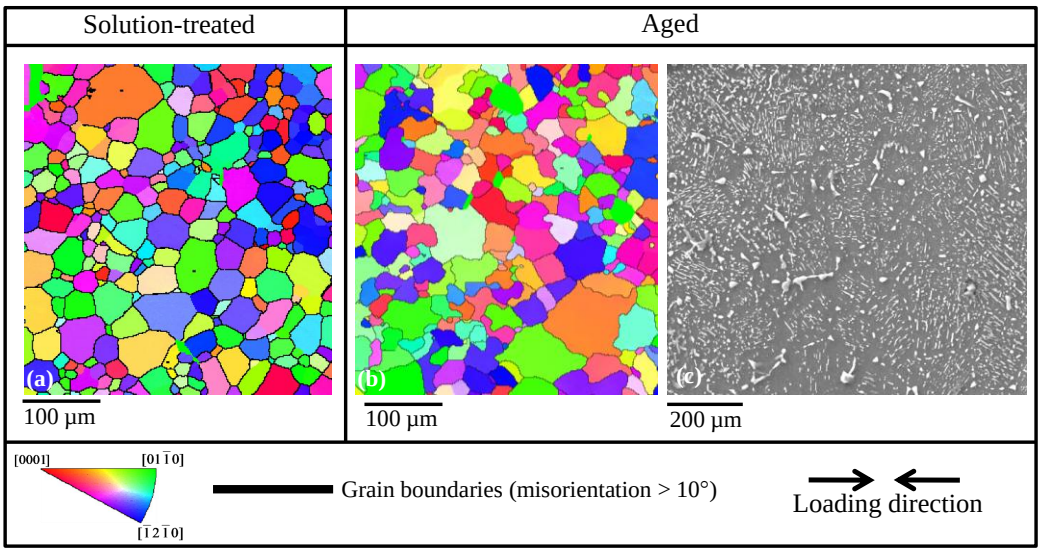

Figure 7.1: a) and **b)** respectively, show the loading axis inverse pole figure maps of solution-treated and aged samples, while **c)** shows the SEM image of an aged sample prior to deformation. The colouring in the IPF map indicates the orientation of loading axis with respect to the HCP reference frame.

inferred from the colour of the grains, the initial texture of the material is weak (see chapter 4, section 4.4.1 for more details on the initial texture). A SEM micrograph illustrating the distribution of precipitates (both intergranular and intragranular) in an aged sample is shown in Figure 7.1c. Note that a high volume fraction of precipitates (~ 9-10 vol% of $Mg_{17}Al_{12}$ phase) exists in this condition. Also, the precipitates are relatively large (several μm in dimensions) and homogenously distributed (Figure 7.1c).

7.2.1 Macroscopic stress-strain behaviour

Figure 7.2a illustrates the compressive and tensile true stress-true strain curves of weak textured alloy in the solution-treated condition (red curves). Both the yield strength and the work hardening rate show asymmetry. The ratio of the yield strength in compression to the yield strength in tension (denoted here as the asymmetry ratio) is 1.15. The work hardening rate in tension is also significantly lower than that in compression throughout the entire stress-strain curve as can be seen independently in Figure 7.2b.

The tensile and compressive stress-strain curves of the weak textured alloy in the aged condition (black curves) is also shown in Figure 7.2a. In this state, the stress-strain curves show identical yield and work hardening response up until fracture (giving an asymmetry ratio of 1.0). The only significant difference in the tensile and compressive stress strain curves is the uniform elongation, which is lower in tension than in compression (i.e. 5% vs. 11%).

A further comparison of yield stress data (Table 7.1) indicates that the aged material has a yield stress in tension that is nearly 2 times higher than that of the solutionized material. In compression the yield stress of the aged material is approximately 1.75 times higher that of the solutionized material. On the other hand, the fracture stress in

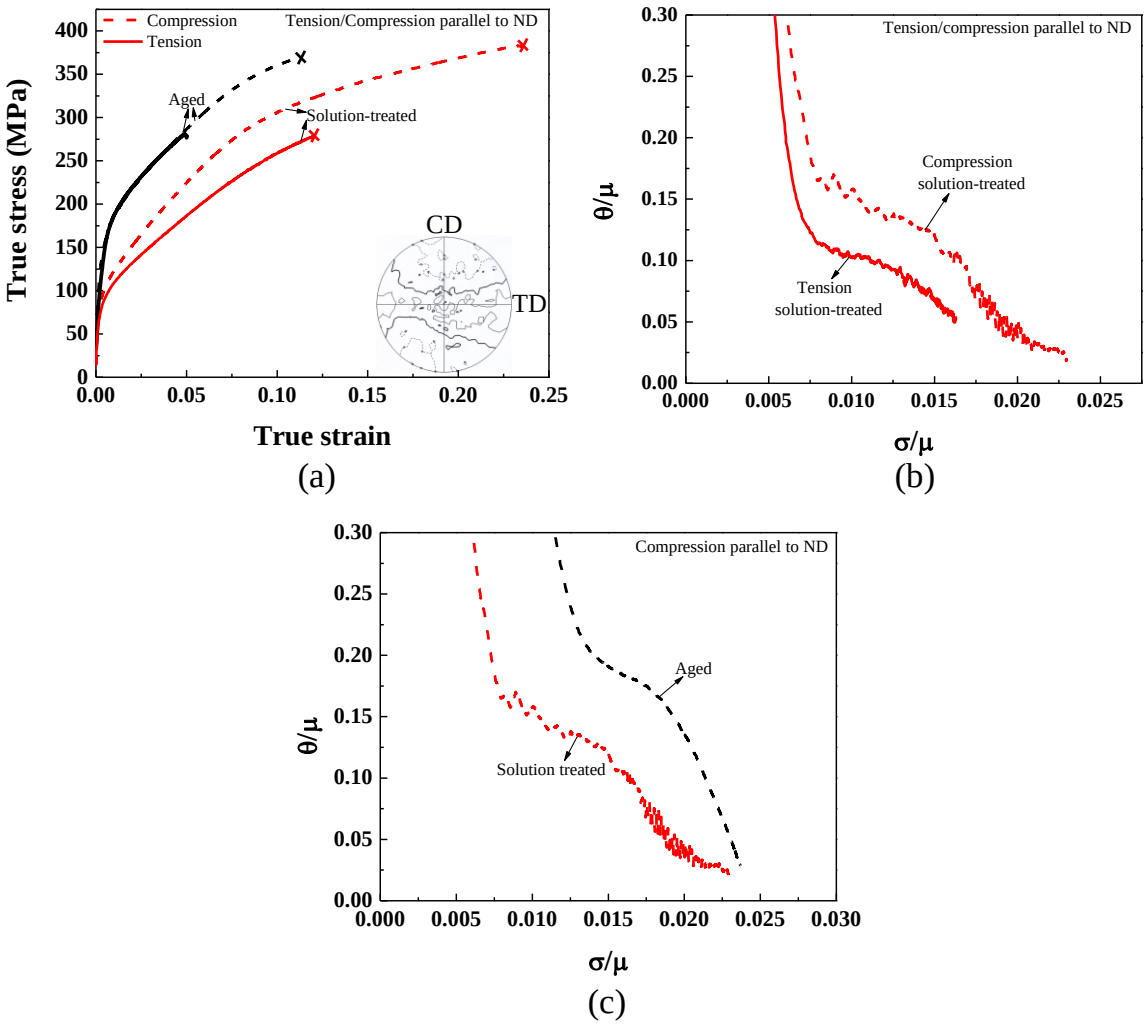

Figure 7.2: a) True stress-true strain response of weak textured solution-treated (red curves) and aged (black curves) AZ80 alloy tested in compression (dashed lines) and tension (solid lines) at 293K **b)** and **c)** show the normalised work hardening rate (θ/μ) vs. normalised stress (σ/μ) plots for solution-treated and aged samples obtained from their compression and tension tests data. The {0001} pole figure in a) (inset) illustrates the texture prior to tension/compression, where the CD and TD correspond to casting direction and transverse direction of the sample, respectively. Notice that the symbol × indicates the fracture of the sample, while the compression/tension direction is at the center of the pole figure (i.e. along ND direction).

Table 7.1: Comparison of measured macroscopic yield (0.2% plastic strain) and fracture stress of aged and solution-treated samples tested in uniaxial tension and compression at 293K. Each reported value is an average of three measurements. The variation between these three measurements was within ± 4%

Condition			*0.2% Offset yield stress (MPa)*	*Fracture stress (MPa)*
Weak textured	Tension	Solution-treated	82	279
		Aged	167	280
	Compression	Solution-treated	95	382
		Aged	167	395

the solution-treated and aged states is almost the same for both tension and compression (see Table 7.1).

Figure 7.2c shows the work hardening ($d\sigma/d\varepsilon$) behaviour (plotted against stress) of aged and solution-treated samples obtained in compression. The normalized values of $d\sigma/d\varepsilon$ (θ) and stresses (σ) have been plotted in Figure 7.2c. For both cases, the work hardening rate decreases with increasing flow stress, the work hardening rate for the aged sample being higher than that of the solution-treated sample (e.g. at $\sigma/\mu \approx 0.015$ the $(\theta/\mu)_{\text{Aged}} \approx 0.19$ vs. $(\theta/\mu)_{\text{Solution-treated}} \approx 0.12$).

7.2.2 Bulk texture evolution

Figure 7.3 show the neutron diffraction measured {0001} and $\{10\bar{1}0\}$ pole figures obtained from solution-treated and aged samples compressed to various strain levels. The

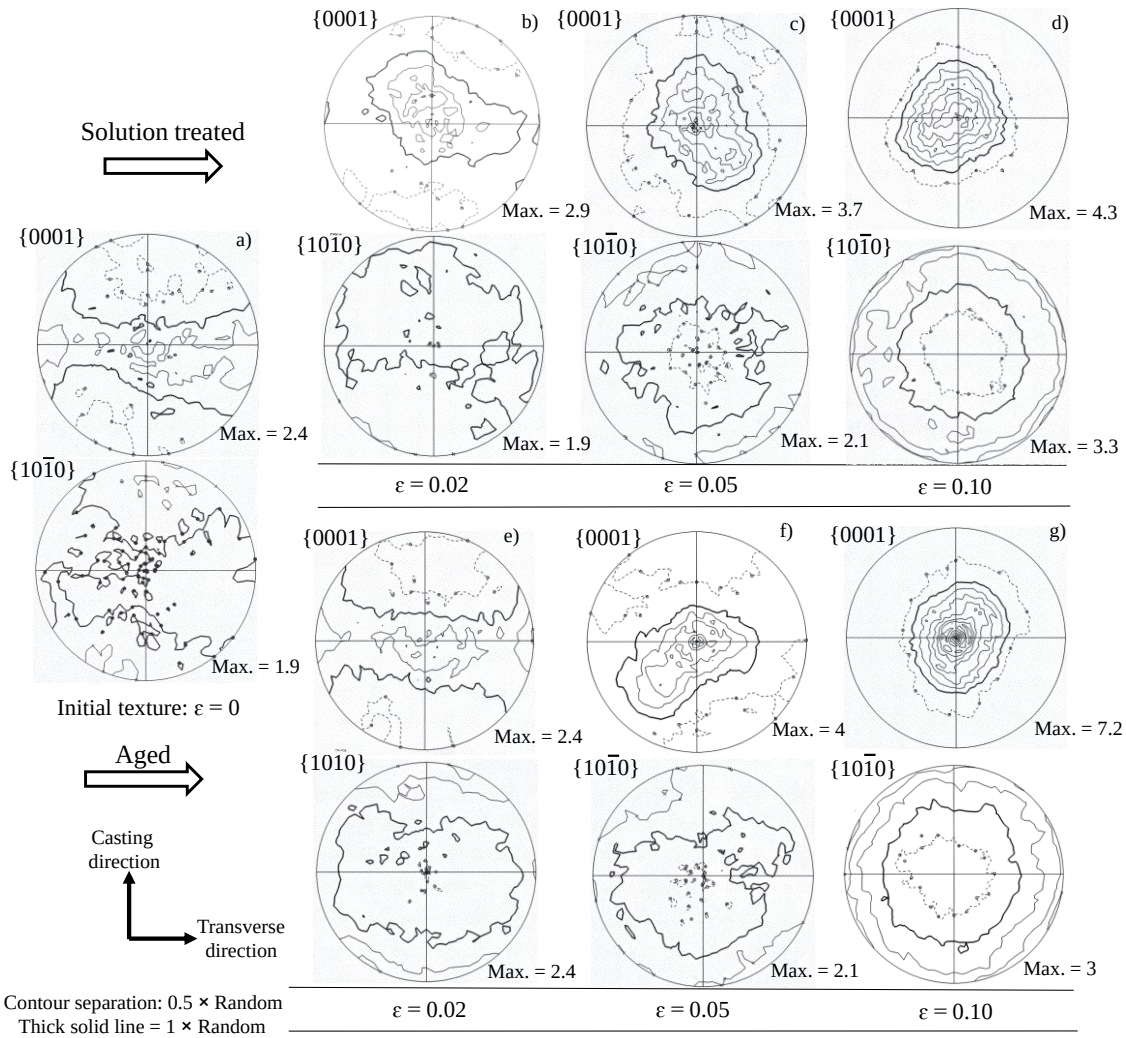

Figure 7.3: {0001} and {10$\bar{1}$0} pole figures (stereographic) representing the textures of solution-treated samples at a strain of **a)** 0 **b)** 0.02 **c)** 0.05 and **d)** 0.10 and aged samples at a strain of **e)** 0.02 **f)** 0.05 **g)** 0.10. Note, the compression direction is at the center of the pole figure (i.e. along the ND direction). The pole figures are contoured in multiples of random distribution (m.r.d.) with the thick solid black line corresponds to 1 m.r.d.. The contour levels above and below 1 m.r.d. are given by solid and dotted lines, respectively, in 0.5 m.r.d. steps.

texture prior to compression (labelled as $\varepsilon = 0$) and the texture after true strain of 0.02, 0.05 and 0.10 for solution treated samples are shown in Figure 7.3a, 7.3b, 7.3c and 7.3d, respectively. Similarly, the textures after true strain of 0.02, 0.05 and 0.10 for aged samples are presented in Figure 7.3e, 7.3f and 7.3g, respectively.

There are noticeable differences between the measured pole figures of solution-treated and aged samples. For instance, after 0.02 strain, the re-orientation due to extension twinning ($\approx$ 86°) causes the basal poles originally close to the transverse direction to switch to new orientations close to the compression direction (the centre of the pole figure) for the solution treated case (Figure 7.3b). Conversely, the texture in the aged and deformed material (Figure 7.3e) is similar to the initial undeformed texture (Figure 7.3a) after 0.02 strain. Further straining to a strain of 0.05 resulted in a qualitatively similar texture for both conditions (see Figure 7.3c and 7.3f). In each case, the texture can be described as a basal texture with the <c> axes inclined around the compression direction, while the $<10\bar{1}0>$ direction resides approximately normal to the compression axis. The strength of this basal texture is further increased with increasing strain to 0.10 as indicated in Figure 7.3d and 7.3g (e.g. the maximum intensity of basal poles increases from 3.7 m.r.d. to 4.3 m.r.d. with increasing strain from 0.05 to 0.1 for the solution-treated case).

These results can be further interpreted in a more quantitative manner by determining the volume fraction of $\{10\bar{1}2\}$ extension twins from the experimentally measured {0001} pole figures. Texture analysis on undeformed material and on samples deformed in compression suggests that the grains present within the outer rim of the {0001} pole figure, corresponding to tilt angles between 50° and 90°, should undergo

$\{10\bar{1}2\}$ extension twinning (see Appendix A3 for more details). The volume fraction of grains where twinning is expected can thus be calculated by integrating the normalized intensity from the outer 40° rim of the {0001} pole figure. As deformation proceeded it was observed that the volume fraction of grains in this rim decreased as the grains reoriented due to twinning. Therefore, the decrease in volume fraction of grains in this rim was used as a measure of the twinned volume fraction.

Figure 7.4 shows the $\{10\bar{1}2\}$ extension twin volume fractions for solution treated (red line with closed circles) and aged (black line with closed circles) samples at several strain levels. It can be noticed that the extension twin fraction increases with increasing strain for both cases. The solution treated samples, however, exhibit a higher volume fraction of $\{10\bar{1}2\}$ twins at 2 and 5% strain compared to the aged samples. At 2% strain,

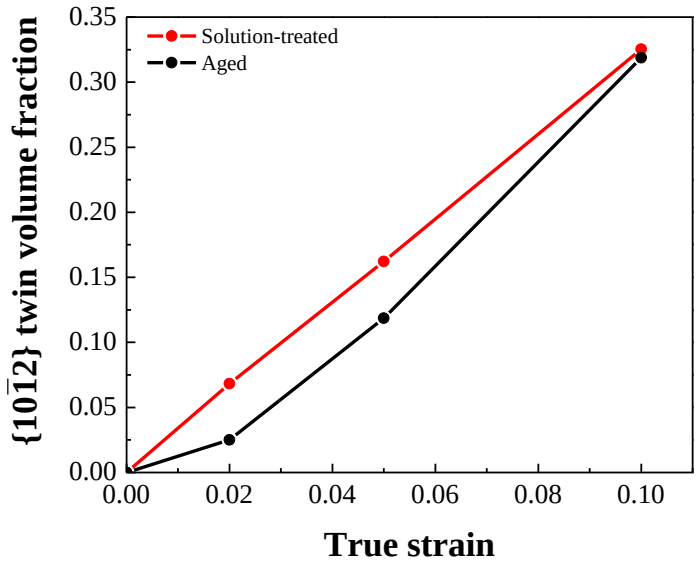

Figure 7.4: $\{10\bar{1}2\}$ twin volume fractions as a function of true strain for solution-treated (red line with closed circles) and aged (black line with closed circles) samples deformed in uni-axial compression at 293K.

the ratio of the twinned volume fraction in the solution-treated sample to that in the aged sample is approximately 3, i.e. volume fractions of 6.9% and 2.5%, respectively. At 5% strain the ratio has decreased to approximately 1.5. While, both samples exhibit similar twinning fractions at 10% strain.

7.2.3 Microstructural observations

7.2.3.1 Nomarski optical microscopy

Figure 7.5 shows optical Nomarski micrographs from the pre-polished surface of a solution-treated and an aged samples that were deformed to 5% strain in uniaxial compression at 293K (see chapter 4, section 4.6.1 for more details on slip trace analysis).

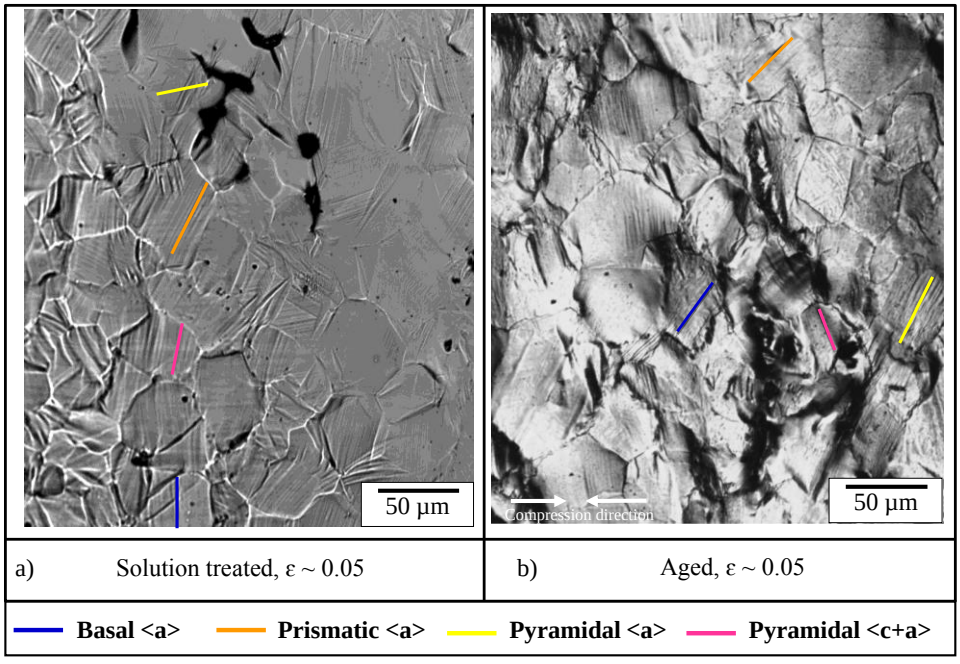

Figure 7.5: Optical Nomarski micrographs illustrating the slip markings on pre-polished surface of **a)** solution-treated and **b)** aged sample deformed to ε ~ 0.05. The colour code of slip lines are provided at the bottom of the maps.

The slip traces were analyzed in several grains, though the slip markings in many grains are not very clear, particularly for the aged case (Figure 7.5b). The present analysis neglects the ambiguous traces. A few examples of the observed slip modes are shown in Figure 7.5a and 7.5b. The traces in this figure correspond to basal <a>, prism <a>, pyramidal <a> and pyramidal <c+a> type slip modes. The results indicate that the active slip modes are of both <a> (basal and non-basal) and <c+a> type. Following this, a Schmid analysis has been carried out on slip traces with the purpose of checking whether the observed trace corresponds to the one with highest Schmid factor or not. The magnitude of Schmid factors for all the slip systems identified above have been calculated from the orientation of the grain and results were plotted as a histogram between the observed slip traces and the corresponding Schmid factor (see Figure 7.6). It is important to note that the non-basal (both <a> and <c+a> type) slip occurs only at high Schmid factor values (Schmid factor > 0.45); whereas the basal slip can be found at lower Schmid factors. This is consistent with the fact that the CRSS for nonbasal slip is higher than the basal slip at low-temperature.

Table 7.2 provides a comparison of slip traces observed from solution-treated and aged samples compressed to a strain of 0.05 at 293K. This comparison has been made from a limited number of grains (50-100 grains). Compared to the solution-treated sample, the aged sample has a higher fraction of grains with basal <a> slip traces and lower fraction of grains with non-basal (pyramidal <a> and pyramidal <c+a> type) slip traces.

7.2.3.2 High resolution EBSD observations

High resolution EBSD was employed to discern the nature of twinning in deformed samples. The inverse pole figure maps and corresponding band contrast maps

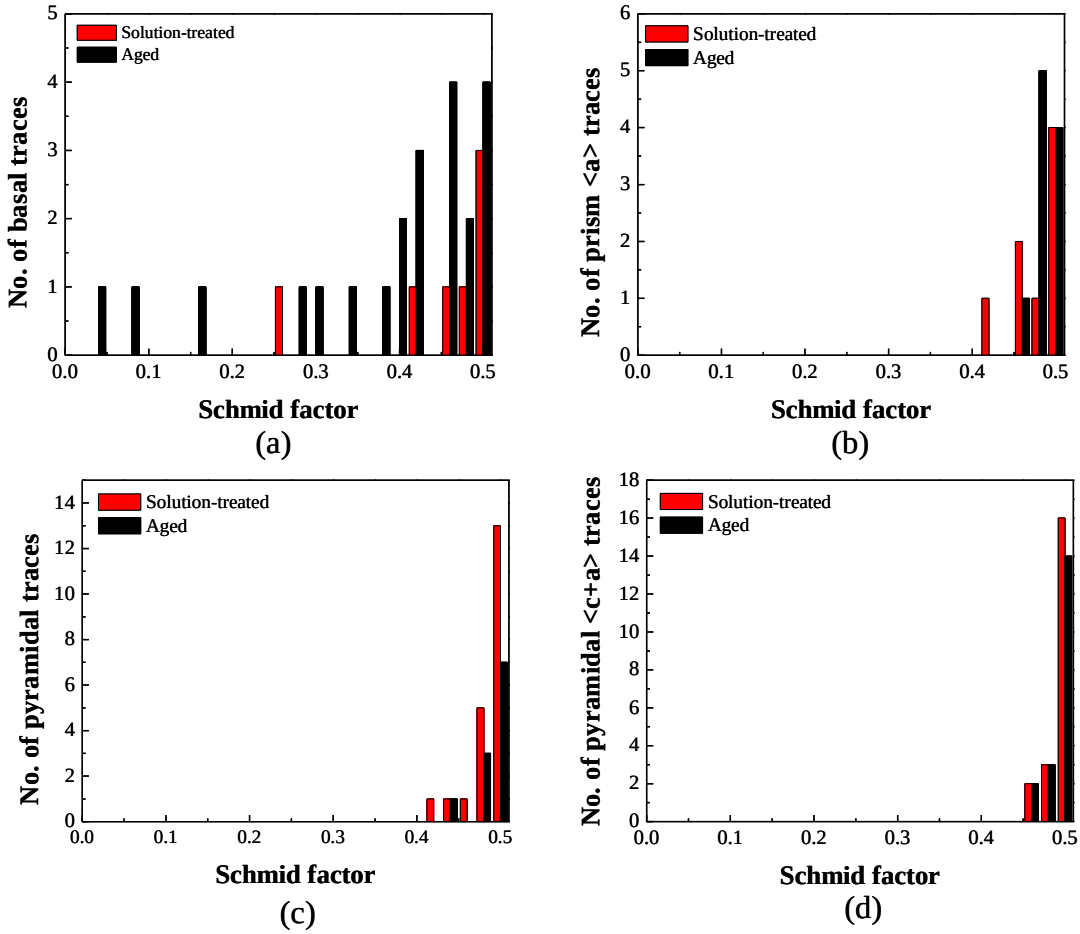

Figure 7.6: A histogram of observed slip traces versus Schmid factor for **a)** basal <a> type **b)** prism <a> type **c)** pyramidal <a> type and **d)** pyramidal <c+a> type. The black and red bars indicate traces observed for the aged and solution-treated condition, respectively.

Table 7.2: Comparison of observed slip traces for solution-treated and aged samples deformed to a strain of 0.05 at 293K

Condition	*Total grains analysed*	*% Basal <a>*	*% Prism <a>*	*% Pyramidal <a>*	*% 2nd Pyramidal <c+a>*
Solution-treated	100	11	17	28	44
Aged	58	37	17	17	29

showing the evolution of microstructure with strain for the solution-treated and aged samples are shown in Figure 7.7a-7.7k. The white boundaries in these maps correspond to extension-twin boundaries based on 86° $<11\bar{2}0>$ misorientation angle/axis pair. While the red colour and blue colour boundaries equivalent to $(10\bar{1}2)-(\bar{1}012)$ and $(10\bar{1}2)-(0\bar{1}12)$ twin impingement boundaries, respectively.

The $\{10\bar{1}2\}$ extension twin is the most commonly observed twin mode in these maps. No evidence of either contraction or contraction-extension double twinning was found at the observed strain levels. At a strain of 0.02, several grains with c axes oriented nearly 90° to the compression axis contain $\{10\bar{1}2\}$ extension twins (see the colour of the grains that exhibit extension twins). For the solution-treated case, the size of these twins increases with increasing plastic strain from 0.02 to 0.08, as can be seen in Figure 7.7d. This figure highlights a specific case where two variants of extension twins in a grain had grown to an extent where they impinge on each other, resulting in a boundary of 60° (± 5º) misorientation about $<10\bar{1}0>$ (see the expanded view of a grain in Figure 7.7i). This is to be contrasted with the aged case where no such impingement was observed. Moreover, there is evidence of twin precipitate interactions. Compared to the solution-treated material, the twins appear significantly finer at a strain of 0.08 for the aged case. Moreover, the twin boundaries appear curved (Figure 7.7g and 7.7h). The fine scale of these twins is also reflected by the fact that even the high resolution EBSD maps contain many unidentified features (see the expanded view of a grain in Figure 7.7j) which are likely twins. Qualitatively, it can be observed that the fraction of extension twins in the aged material is lower than in the solution treated case, in agreement with the analysis of the bulk texture.

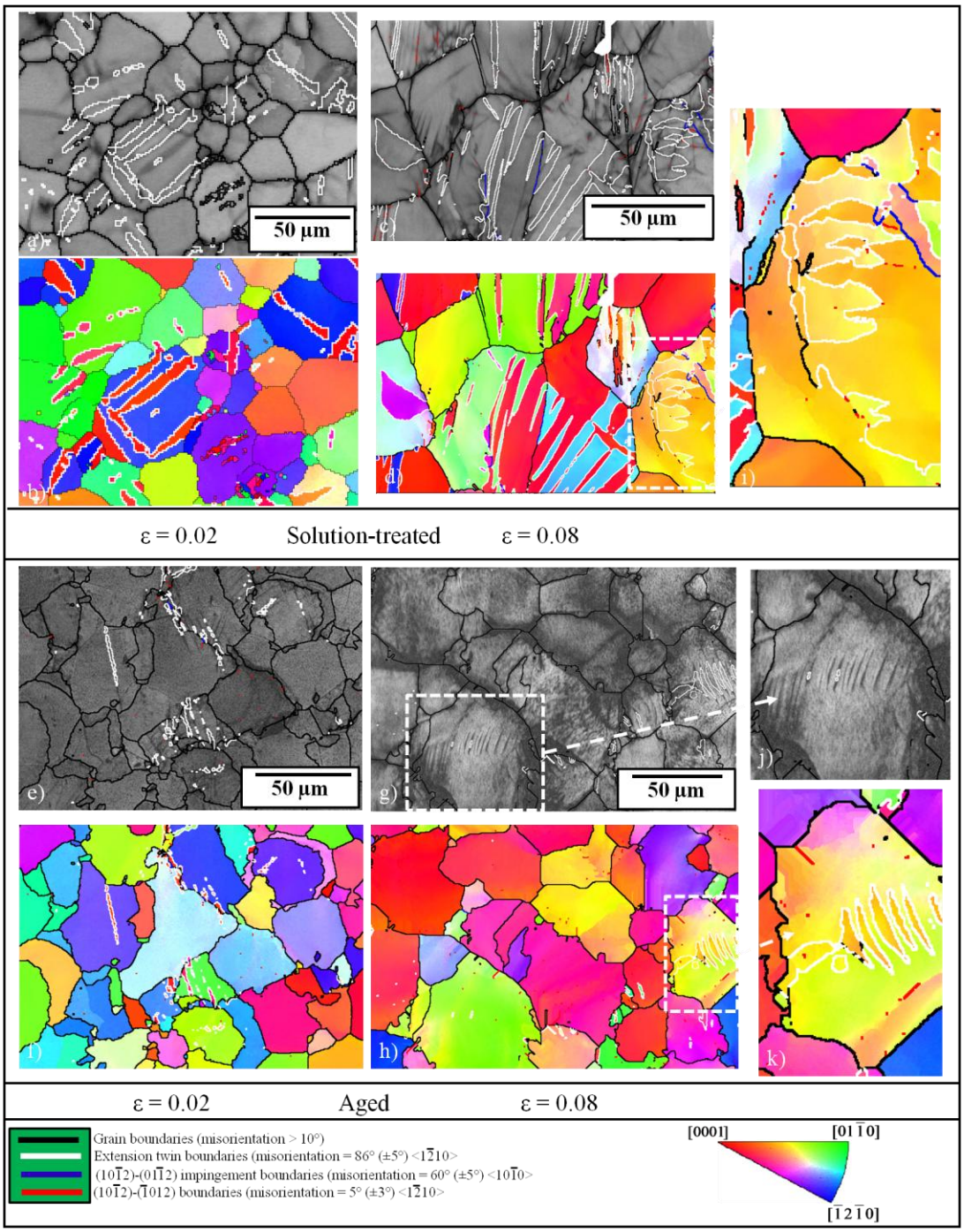

Figure 7.7: Show the compression axis inverse pole figure (IPF) maps and the corresponding pattern quality EBSD maps of solution-treated and aged samples after compression to a strain of 0.02 and 0.08. The colour code of IPF map is provided at the bottom right of the maps measurements.

7.3 Discussion

7.3.1 Effect of precipitates on the stress-strain behaviour

7.3.1.1 Yield strength

The aged samples tested in tension and compression exhibit a yield strength that is about a factor of 2 times and 1.75 times higher respectively, than the yield strength for the solution-treated case (Figure 7.8). An upper bound estimate for the increase in yield stress ($\Delta\sigma_Y$) can be made by considering the Orowon stress due to non-shearable precipitates [55, 122],

$$\Delta\sigma_{Orowan} = \frac{2\mu b}{L} \tag{7.1}$$

This equation assumes $\sigma = 2\tau$, where τ is the resolved shear stress on the slip plane, with μ = 17 GPa the shear modulus, and b = 0.32 nm the Burgers vector. The $Mg_{17}Al_{12}$ interparticle spacing, L, is taken to be of the order of 0.2 μm, as has been previously used by Cáceres et al. [122]. The $\Delta\sigma_Y$ due to the Orowan stress is found to be $\approx$55 MPa, which is very close to the increase in yield stress observed for the aged case (Figure 7.8). The other factor that could contribute to the yield stress is the solid solution strengthening. It has been suggested by Gharghouri et al. [55] that the strengthening due to alloying additions (primarily Al) in these alloys is very little. This can be ascribed to the small difference between the atomic diameters of magnesium and aluminum (about 3%).

7.3.1.2 Tension/compression yield asymmetry

In contrast to cubic metals, the yield strength of most magnesium alloys differs significantly in tension and compression [199, 200]. This effect complicates the

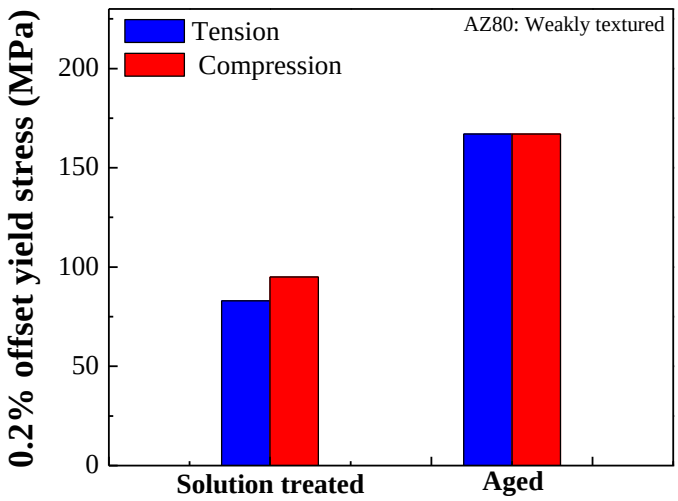

Figure 7.8: Comparison of 0.2% offset yield stresses for solution-treated and aged samples tested in uniaxial tension (blue bars) and compression (red bars) at 293K.

deformation and forming of magnesium alloys and the ability to develop mathematical models to describe this behaviour. The yield asymmetry has been attributed to the polar nature of extension twinning on the $\{10\bar{1}2\}$ plane. For HCP magnesium with a c/a ratio of approximately 1.622 extension twinning is activated by a compressive stress parallel to the basal plane or a tensile stress perpendicular to the basal plane [12]. In polycrystalline samples the orientation of the applied stress relative to the basal plane is dependent on the crystallographic texture of the material and, as a result, the yield asymmetry is sensitive to texture. For example, the yield asymmetry is lower in cast alloys [201], which tend to have weak textures compared with wrought alloys [91].

It is well known that pure magnesium exhibits a lower yield strength and rate of work hardening (until twinning is exhausted) when plastic deformation is dominated by

twinning rather than slip [15]. The behaviour observed in Figure 7.9a can thus be interpreted as a manifestation of this tendency, attenuated by the relatively weak texture. For a random texture there will be more twinning in compression than in tension, however, the initial texture of the material used in this study was not random. Indeed the texture prior to compression is such that it exhibits preferred alignment of basal poles normal to the casting direction (see the {0001} pole figure shown in the inset of Figure 7.9a). The lower yield strength and rate of work hardening exhibited by the solution-treated material in tension relative to compression are consistent with the larger fraction of grains oriented favourably for $\{10\bar{1}2\}$ twinning in tension compared to compression.

The differences in the tensile and compressive response of a solution treated AZ80 alloy can be eliminated when the sample is aged to contain a high density of $Mg_{17}Al_{12}$ precipitates (Figure 7.9b). The more symmetric behaviour of aged samples compared to the solution treated samples can be attributed to the differences in the twinning behaviour (more elaborately discussed later in section 7.3.3.2). The analysis of the neutron data (Figure 7.4) and the microstructural observations (Figure 7.7) confirms that the fraction of extension twins in the aged material is lower than in the solution treated case.

It should be mentioned that the work presented above concerns material having a relatively weak starting texture (arising from casting). The effect of precipitates on the tension/compression asymmetry can be even more striking in a highly textured material. Here one expects significant $\{10\bar{1}2\}$ twinning in compression and little $\{10\bar{1}2\}$ twinning in tension. A pronounced yield asymmetry (asymmetry ratio of 0.59) was found in the solution treated sample (see Figure 7.10a). However, aging reduced the asymmetry drastically to an asymmetry ratio of 0.87 (Figure 7.10b). The current results are

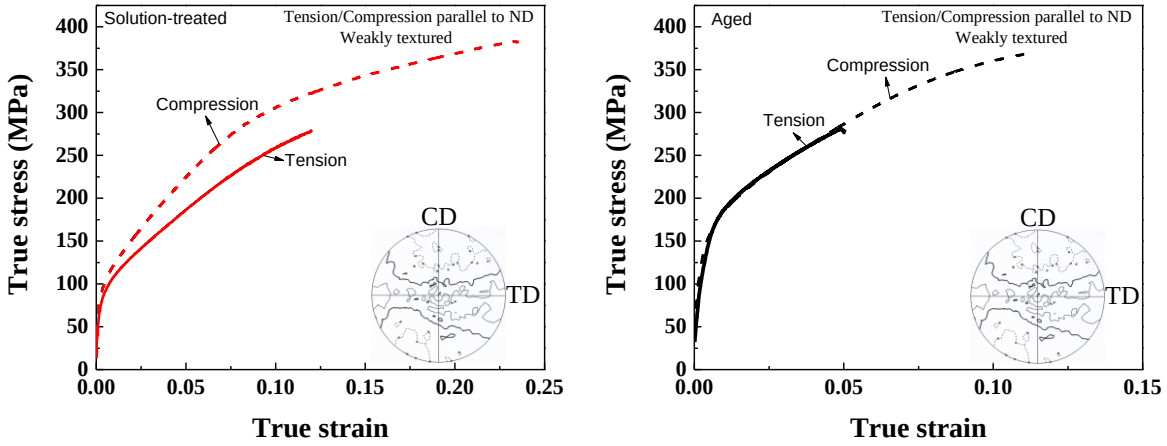

Figure 7.9: a) and **b)** respectively, show the true stress strain responses of weakly textured solution-treated and aged samples deformed in uniaxial tension and compression. The {0001} pole figure shown in the inset of a) and b) illustrate the texture prior to tension/compression.

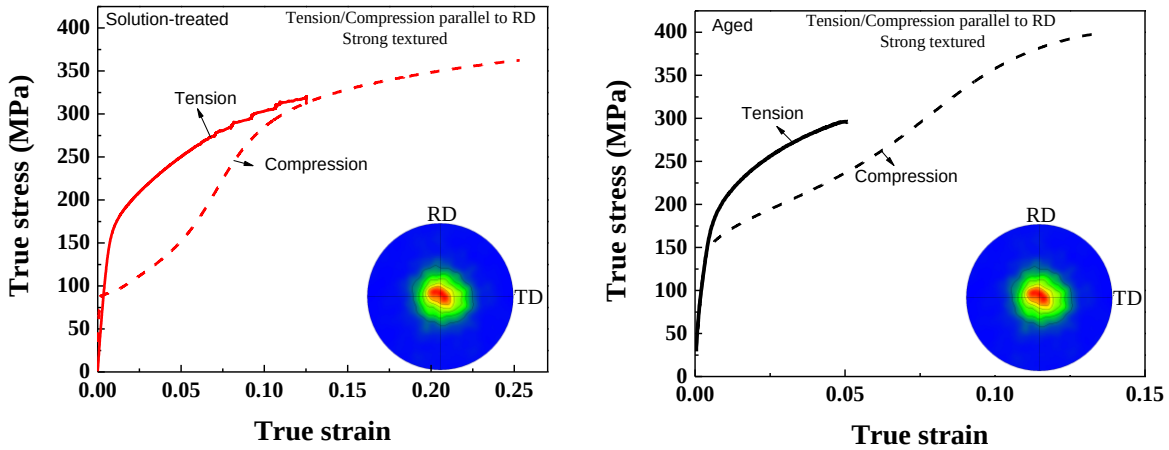

Figure 7.10: a) and **b)** respectively, show the true stress strain responses of strong textured solution-treated and aged samples deformed in uniaxial tension and compression along RD direction. The {0001} pole figure shown in the inset of a) and b) illustrate the texture prior to tension/compression.

qualitatively similar to those previously reported by Kleiner and Uggowitzer [202] in an extruded AZ80 alloy (0.52 in solution treated to 0.76 in aged). The small differences between their work and the current study were presumably related to the less intense initial texture (maximum intensity of 4 m.r.d) and different heat treatment conditions, which produced a different state of precipitation.

7.3.1.3 Work hardening behaviour

The work hardening rate for the aged sample is higher than the solution-treated sample (Figure 7.11). The increase in work hardening rate caused by particles can be estimated through the simplified approach suggested earlier by Brown and Clarke [134] and later applied to magnesium alloys by Gharghouri et al. [55] and Cáceres et al.[122]. The contribution of mean back stress to the slope of the stress strain curve can be deduced by assuming that there is no plastic relaxation around particles. Gharghouri et al. [55] reported that the stress due to particles reaches maximum at plastic strains of about 0.007 in similar alloys. The mean back stress in matrix due to the particles is given by (assuming disc shaped particles and elastic isotropy for both matrix and particle):

$$\sigma = 4\mu f\varepsilon \qquad (7.2)$$

where μ is the shear modulus of the matrix, f is the volume fraction of dispersed phase and ε is the strain. Differentiating equation (7.2) gives $\theta/\mu \approx 4f$. The volume fraction of particles for AZ80 alloy is roughly 9-10%, so that $\theta/\mu \approx 0.36$-0.40. Comparing this with the work hardening plot shown in Figure 7.11 at low strains reveals that the increase in θ/μ is in the range of 0.07-0.09, which is significantly lower than the theoretical value. Thus, it would appear that the role of precipitates on work hardening behavior cannot be

simply understood by an approach suggested by Brown and Clarke. This may be due to the complex slip and twinning behavior associated with the aged material.

It is further interesting to examine the work hardening plots of the twinning dominated IPC case in the solution-treated (ST) and the aged conditions (Figure 7.11b). As can be seen in Figure 7.11b, after initial yield, the work hardening rate for both cases increases with increasing stress, it reaches a maximum and then starts to decline again. This is a typical hardening curve obtained from the twinning dominated deformation of magnesium. The important points here to notice are: i) the lower rate of increase in work hardening rate for aged-IPC as compared to ST-IPC and ii) the maximum hardening rate attained by aged-IPC sample is lower by ≈ 0.057 (i.e. $(\theta/\mu)_{max.}$) than the ST-IPC sample. These effects can be related to the influence of precipitation on the twinning behaviour.

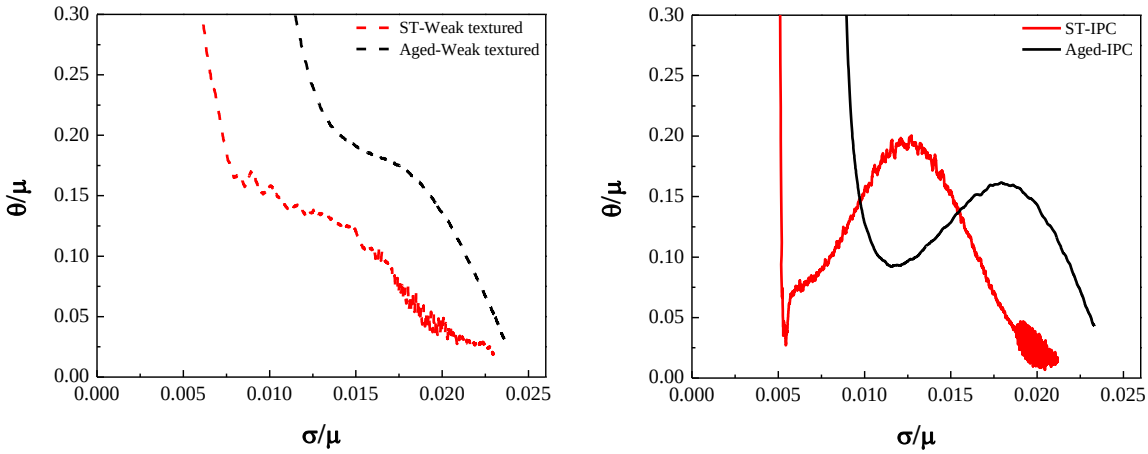

Figure 7.11: Normalised work hardening rate (θ/μ) vs. normalised stress (σ/μ) plots **a)** for weakly textured solution-treated (ST) and aged samples and **b)** for strong textured ST and aged samples deformed in compression. Note that for a) the compression direction was along ND direction, while for b) the compression axis was parallel to the RD direction (i.e. IPC).

7.3.2 Effect of precipitates on texture evolution

In the present study, the effect of precipitates on the texture evolution of AZ80 alloy has been systematically investigated. The potential for using precipitation to control texture is interesting. Precipitation can be used to strengthen materials directly but also to modify mechanical response by changing twinning and slip behaviour. Quantitative analyses of pole figures suggest that precipitates delay the formation of basal texture in the weakly textured aged samples (Figure 7.12). This can be observed in Figure 7.12 where the volume fraction of grains having their <0001> oriented within 40° of the compression axis is plotted as a function of strain for solution-treated and aged samples. Notice that the strength of <0001> basal texture increases with increasing strain for both the cases, albeit initially at a slower rate for the aged case than the solution-treated case. Further, the final

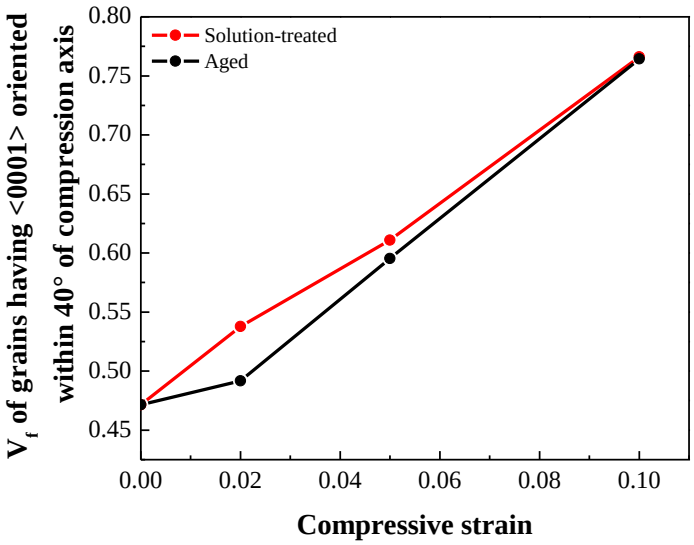

Figure 7.12: Volume fraction of grains having c-axes oriented within 40° of compression axis determined from the {0001} pole figures.

textures (i.e. at around 10% strain) are very similar for both cases i.e. a strong basal texture component parallel to ND direction. The initial differences in textures can be primarily ascribed to the delay in $\{10\bar{1}2\}$ twinning for the aged case compared to the solution-treated case. Though not done in this study, it would be interesting to carry out a similar analysis on the strong textured solution-treated and aged samples deformed under IPC (i.e. in twinning dominated orientation).

7.3.3 Effect of precipitates on deformation mechanisms

7.3.3.1 Slip modes

The results of slip trace analysis indicates that the basal and the non-basal (both <a> and <c+a> type) slip modes both contribute to the strain accommodation of aged and solution-treated samples (Figure 7.13). Although there is very limited information in the literature regarding the deformation mechanisms of aged materials. Slip with <a> type Burgers vectors on basal and non-basal planes have been previously reported by Clark [117] and Gharghouri et al. [55] in precipitate containing magnesium alloys tested at ambient-temperature. Gharghouri and colleagues [55] attributed the non-basal slip of <a> type to the presence of stress concentrations near particle-matrix boundaries.

Preliminary comparison of the data obtained from trace analysis of an aged sample compared to the solution-treated sample suggests that basal slip is more common in the aged sample (Figure 7.13). This can be understood based on consideration of the alloying elements. The alloy investigated here contains significant amounts of Al (about 8 wt %) and Zn (about 0.5 wt %). The work of Akhtar and Teghtsoonian [37, 38] on dilute Mg-Al and Mg-Zn alloy single crystals (i.e. at concentrations less than 0.5 at %) revealed that Zn

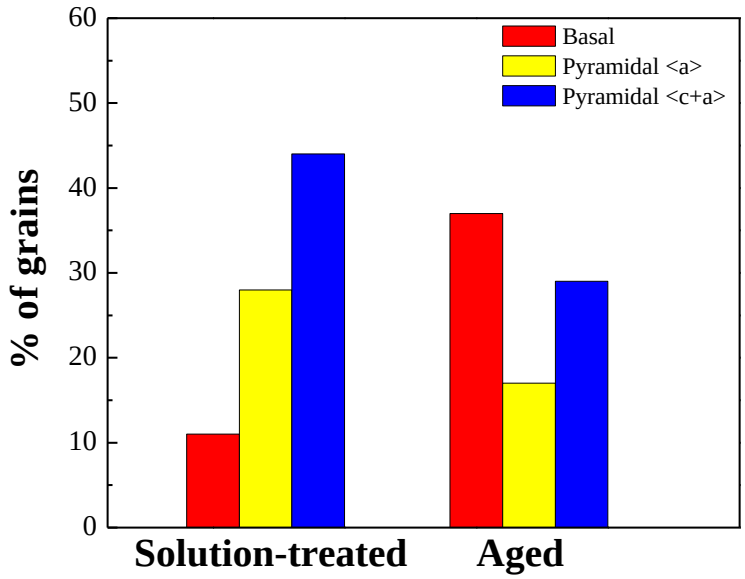

Figure 7.13: Shows a comparison of grains exhibiting basal <a> (red bars), pyramidal <a> (yellow bars) and pyramidal <c+a> (blue bars) slip traces for solution-treated and aged AZ80 samples.

and Al additions reduce the CRSS for non-basal prismatic slip while increasing the CRSS of basal slip. Although, there is no experimental study available on concentrated magnesium alloy single crystals, the recent work of Raeisinia and Agnew [165] suggests that the addition of Zn to pure magnesium (up to 2.3 wt% Zn) increases the CRSS for the basal slip. Most recently, Hutchinson and Barnett [190] have reported similar results. The VPSC simulation results presented here is consistent with the trend that the addition of Al to 8 wt% increases the CRSS value of basal <a> slip (e.g. $(\tau_{CRSS}^{Basal})_{AZ31} \approx$ 29 MPa while $(\tau_{CRSS}^{Basal})_{AZ80} \approx$ 39 MPa). The higher level of basal slip in aged samples would be consistent with the reduced amount of solute following ageing.

It has been suggested earlier by Clark [117] and later by Gharghouri et al. [55] that the presence of non-deformable particles (e.g. $Mg_{17}Al_{12}$) in magnesium alloys eases the

non-basal <a> type slip. Quantitative comparisons of results do not show this at least in a simple manner (Figure 7.13). One might argue that the presence of residual solute in the matrix could also be important in determining the non-basal activity. At present, however, there is no systematic study available on the effect of solute elements on the activity of pyramidal <a> and pyramidal <c+a> slip systems. Therefore, it would be difficult to understand the present results from that perspective. Further work focussing on the effect of alloying elements on the activity of non-basal slip systems would be required to better understand these results.

7.3.3.2 Twin modes

Precipitates have a pronounced effect on the twinning behaviour of the AZ80 alloy. The β-phase ($Mg_{17}Al_{12}$) in the aged alloy affects the twinning kinetics by delaying twinning to larger strains. A comparison of twinning fractions at low strain levels (Figure 7.14) illustrates this. It is worth pointing out that the case examined here had experienced overall less twinning compared with the strong textured case loaded under IPC. It is possible that the differences in twinning fractions of solution-treated and aged samples could be larger when deformation is exclusively dominated by twinning.

It is important to understand whether twin nucleation, twin growth or both processes are modified in the aged samples compared with the solution treated samples. Grain boundaries are generally considered to be the most common sites for twin nucleation in these alloys [10, 168, 203, 204] and thus anything that acts to modify the structure or the chemistry of these boundaries could also influence twin nucleation. In aged materials discontinuous and continuous precipitates at grain boundaries could modify twin nucleation

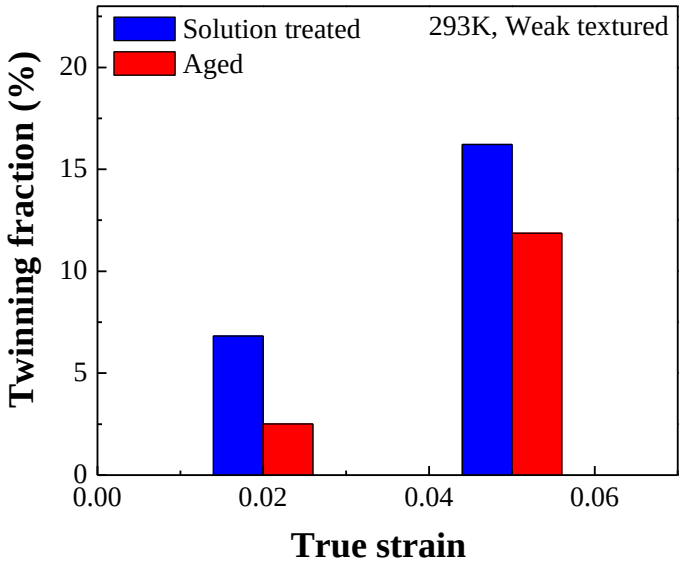

Figure 7.14: A comparison of $\{10\bar{1}2\}$ twinning fractions as a function of strain for solution-treated and aged samples.

sites. Moreover, precipitation will alter the local boundary chemistry and could, therefore, affect the rate of twin formation. Once nucleated, the lengthening and widening of twins has been described in terms of various dislocation glide based mechanisms. The presence of obstacles in the path of a migrating twin boundary can markedly influence the twinning behaviour of an alloy. For example, the early work of Partridge [205] on pure magnesium illustrated the pinning of twin boundaries due to oxide particles. More recently, Serra et al. [206] studied the interaction of a moving $\{10\bar{1}2\}$ twin boundary with clusters of self-interstitial atoms and vacancies in zirconium using atomistic simulations. These results indicate that obstacles such as these cause strengthening by pinning the twinning dislocations and restricting boundary motion. Finally, the detailed work of Gharghouri et al. [130] on a binary Mg–Al alloy containing $Mg_{17}Al_{12}$ precipitates showed many examples

of twin boundary–precipitate interactions, including cases of twins bowing around and bypassing precipitates.

The present EBSD observations on samples deformed to large strains showed that the twin boundaries became curved in the presence of precipitates, similar to the observations of Gharghouri et al. [130]. To illustrate this further the IPF maps of aged samples deformed to 5% and 8% strain are presented in Figure 7.15a and 7.15b, respectively. Notice the arrowed regions of the maps which indicate the curved nature of extension twins present in the aged microstructure. In addition, it is significant to point out the local misorientations that exist within the grains (e.g. see the line scan 1 and 2 in Figure 7.15c). This is presumably related to the heterogeneity of the slip activity.

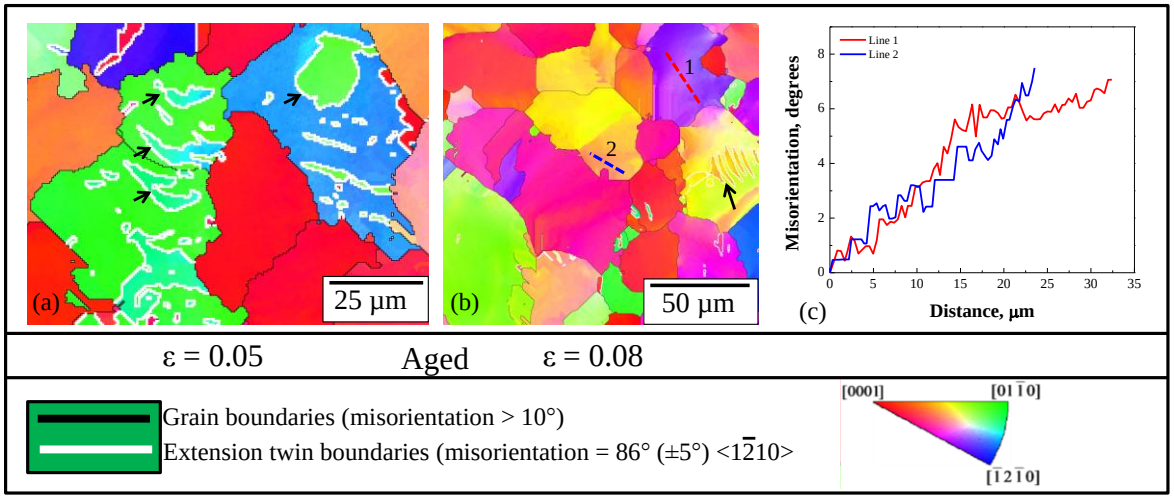

Figure 7.15: The compression axis inverse pole figure maps of aged samples compressed to a strain of **a)** 0.05 and **b)** 0.08. The line misorientation profile of lines drawn in b) (i.e. line 1 and 2) is shown in **c)**. The black and white boundaries correspond to grain and extension twin boundaries identified using the same procedure outlined before. The arrow indicates the curved nature of extension twins present in the aged samples.

It is clear that the interaction between migrating twin boundaries and precipitates hinders the rate of twin propagation, but it is unclear how strong the effect of the precipitates is on the nucleation of twinning. Determining whether the number density of twins (i.e. the number of twins nucleated) is significantly different for the solution treated and aged samples is much more difficult, given that the thickness of the twins observed in the aged material was at the limit of resolution of the EBSD technique. Nevertheless, the observations made here and the argument of less twinning in aged sample is very similar to what had been reported by Clark [117] in Mg-9wt% Al alloy and Gharghouri et al. [130] in Mg-7.7at % Al alloy.

7.4 Summary

The effect of precipitates on the mechanical behaviour of weakly textured AZ80 alloy has been systematically investigated. In this study, the influence of precipitation on the mechanical properties, work hardening characteristics, texture evolution and deformation mechanisms of the AZ80 alloy has been evaluated and compared with the solution-treated case. Precipitation of the β-phase ($Mg_{17}Al_{12}$) had significant effects on the yielding and the work hardening characteristics of the alloy. The increase in yield stress due to precipitation can be explained by precipitate-dislocation interactions (Orowan looping), however, the role of precipitates on the work hardening behaviour cannot be simply understood by the continuum approach suggested by Brown and Clarke. One of the outcomes of this study is that the controlled precipitation can be effectively used to reduce the well known tension/compression asymmetry exhibited by magnesium and its alloys.

This was ascribed to reduced amounts of $\{10\bar{1}2\}$ twinning in aged samples compared to the solution-treated samples.

In the present study, the effects of precipitates on deformation mechanisms and the resulting texture development have been quantitatively analysed. Precipitation of β-phase in an AZ80 alloy can be used to manipulate the twinning behaviour. The microscopic analysis on aged samples indicates that the $Mg_{17}Al_{12}$ precipitates affect twin growths, though their influence on twin nucleation is unclear. Overall, the effect of precipitation on slip behaviour is complex and related to the amount of solute in the matrix as well as to the precipitate distribution.

CHAPTER 8 – Conclusions and Future Work

8.1 Conclusions

Four main conclusions arising from this work can be summarised as follows.

This study has contributed to an improved understanding of the work hardening rates in magnesium alloys. The significance of texture in hardening and the temperature of deformation on the rate of dynamic recovery has been shown to be sufficient to explain the high hardening rates in the alloy studied. The results suggest that the hardening effect arising from dynamic Hall-Petch effects and the Basinski mechanism is less significant.

A quantitative understanding of the effect of temperature on the deformation mode activities has been developed. The results show that $\{10\bar{1}2\}$ twinning is weakly temperature dependant, whereas the $\{10\bar{1}1\}$ contraction twinning activity decreases with decreasing temperature between 293K and 77K. Further, with decreasing temperature the activation of pyramidal <c+a> slip is reduced, while prismatic <a> slip increases in activity. This was conclusively shown to agree with both experiments and micromechanical simulations.

This work also presents the first systematic attempt at applying a physically based approach to setting the adjustable parameters of the VPSC model for predicting the deformation of magnesium alloys. The strengths and weaknesses of the VPSC model for predicting the behaviour of this alloy were analysed. The model was successfully applied to infer the effects of temperature in the TTC and IPT sample orientations. During TTC and IPT testing, deformation was mainly dominated by slip. Alternatively, for IPC samples

whose deformation is the twinning dominated, the model predictions showed disagreement with the experiments. It has been argued here that this behaviour is attributed to limitations of the twinning model.

It was shown that precipitates can significantly improve the mechanical behaviour of the AZ80 magnesium alloy. The difference in the tensile and compressive yield strengths of a solution treated AZ80 magnesium alloy can be reduced, and in some cases eliminated, when the sample is aged to contain a high density of $Mg_{17}Al_{12}$ precipitates. This is ascribed to reduced amounts of $\{10\bar{1}2\}$ twinning in aged samples compared to the solution-treated samples.

Precipitation of the β-phase has proven the great potential in varying the balance of deformation mechanisms and texture development of the alloy. Texture analysis indicates that precipitates delay the basal texture formation in the aged samples. Microstructural analysis reveals that precipitates significantly affect the $\{10\bar{1}2\}$ twin morphology and its growth. In addition, surface observations indicate that basal slip is more common in the aged sample than the solution treated sample.

In summary, the deformation behaviour of the AZ80 alloy is strongly influenced by varying the initial texture, temperature, stress state and microstructure. The knowledge that has been gained here will be crucial for improving the behaviour of existing magnesium alloys and developing new ones. Efforts similar to present will further be required to develop the magnesium technology.

8.2 Future work

There are a number of areas indentified for which further studies could enhance the present understanding. Some of these areas include:

i) The behaviour of strong textured material in twinning dominated orientation (i.e. IPC) needs to be further characterized in more detail. It is shown that both temperature and precipitates have strong effect on deformation response of alloy during IPC. The current interpretation of this is however limited due to lack of knowledge on twinning related aspects. It is essential to determine the effect of temperature and precipitates on twinning behaviour of the alloy.

ii) In the present study, the temperature dependence of $\{10\bar{1}2\}$ twinning in a weak textured AZ80 alloy has been determined. Similarly, it is necessary to understand the temperature dependence of other twin modes such as $\{10\bar{1}1\}$ contraction twinning. Qualitative observations on samples compressed in through thickness direction (i.e. TTC) suggest a drop in contraction twinning levels with decreasing temperature from 293K to 77K. Further studies are required to understand this result in more detail.

iii) Modelling twinning is crucial for predicting the plastic deformation and texture evolution of HCP metals. It is shown that the existing twinning model (i.e. PTR model) is not sufficient to capture the twinning behaviour of the AZ80 magnesium alloy. More sophisticated twinning models are required to better predict the twinning related effects.

iv) Efforts are needed to evaluate the significance of latent hardening in magnesium alloys. The present work has shown that high values of latent hardening parameter from twinning (h^{TT}) are essential to model the experimental behaviour. In the present

case, h^{TT} of 4 was used for twin related interactions. This is very high if one compares with the FCC case where the maximum value was reported to be 1.4 (resulted from slip-slip interactions) [174]. In addition, it is not clear as how this will change with temperature.

v) For the present simulations, it was assumed that solute elements have same effect on all slip and twin systems. This was due to the lack of data available in the literature. Fundamental studies focussing on analysing the effects of solute elements (e.g. Al, Zn) on the non-basal and twinning activities are required. Currently, there is no study that deals with the effect of solute elements on the behaviour of pyramidal <c+a> slip and $\{10\bar{1}2\}$ extension twinning.

vi) The present work demonstrates that $Mg_{17}Al_{12}$ precipitates are effective in blocking $\{10\bar{1}2\}$ twin growth. The effect, however on $\{10\bar{1}1\}$ contraction twinning is not known. It is known that these twins readily form double twins (contraction-extension type) which then subsequently affect the fracture and recrystallisation behaviour of the magnesium alloys. Thus, any significant influence of precipitates on contraction twinning could be utilised to tailor these processes.

References

[1] P. G. Partridge, *Met. Rev.*, Institute of Metals, **118** (1967) 169.

[2] D. Hull, D. J. Bacon, *Introductions to dislocations*, 2001, Butterworth and Heinemann (Publishers).

[3] R. von. Mises, Z. Agnew, *Math. Mech.*, **6** (1928) 85.

[4] B. Legrand, *Phil. Mag. B*, **49** (1984) 171.

[5] A. Couret, D. Caillard, *Acta Metall.*, **33** (1985) 1447.

[6] A. Couret, D. Caillard, *Acta Metall.*, **33** (1985) 1455.

[7] J. Koike, T. Kobayashi, T. Mukai, H. Watanabe, M. Suzuki, K. Maruyama, K. Higashi, *Acta Mater.*, **51** (2003) 2055.

[8] S. R. Agnew, Ö. Duygulu, *Int. J. Plast.*, **21** (2005) 1161.

[9] R. Clark, G. B. Craig, *Prog. Met. Phy.*, **3** (1952) 115.

[10] J. W. Christian, S. Mahajan, *Prog. Mater. Sci.*, **39** (1995) 1.

[11] C. N. Reid, *Deformation Geometry for Materials Scientist*, Pergamon Press, 1st Edition, 1973.

[12] W. F. Hosford, *The Mechanics of Crystals and Textured Polycrytals*, Oxford University Press, 1993.

[13] B. A. Bilby, A. G. Crocker, *Proc. Roy. Soc. A*, **288** (1965) 240.

[14] E. Schmid, W. Boas, *Plasticity of Crystals with Special Reference to Metals*, Chapman and Hall, 1st Ed., London, 1968.

[15] R. E. Reed-Hill, *The Inhomogeneity of Plastic Deformation*, 1972, ASM Metals Park, Ohio.

[16] E. Orowan, Dislocations in Metals, M. Cohen (Ed.), *Transactions AIME* (1954) 116.

[17] N. Thompson, D. J. Millard, *Phil. Mag.*, **43** (1952) 422.

[18] S. Vaidya, S. Mahajan, *Acta Metall.*, **28** (1980) 1123.

[19] S. Mahajan, G. Y. Chin, *Acta Metall.*, **21** (1973) 1353.

[20] L. Capolungo, I. J. Beyerlein, *Phy. Rev.*, **78** (2008) 711.

[21] A. H. Cottrell, B. A. Bilby, *Phil. Mag.*, **42** (1951) 573.

[22] J. A. Venables, *J. Phys. Chem. Solids*, **25** (1964) 693.

[23] M. H. Yoo, *Metall. Trans.*, **12A** (1981) 401.

[24] P. B. Price, *Proc. Roy. Soc. Lond.*, Mathematical and Physical Sciences, **260** (1961) 251.

[25] A. Serra, D. J. Bacon, *Phil Mag.*, **73** (1996) 333.

[26] J. Wang, R. G. Hoagland, J. P. Hirth, L. Capolungo, I. J. Beyerlein, C. N. Tomé, *Scripta Mater.*, **61** (2009) 903.

[27] J. Wang, J. P. Hirth, C. N. Tomé, *Acta Mater.*, **57** (2009) 5521.

[28] L. Capolungo, I. J. Beyerlein, C. N. Tomé, *Scripta Mater.*, **60** (2009) 32.

[29] I. J. Beyerlein, C. N. Tomé, *Proc. R. Soc. A*, doi:10.1098/rspa.2009.0661.

[30] M. R. Barnett, *Scripta Mater.*, **59** (2008) 696.

[31] L. Capolungo, P. E. Marshall, R. J. McCabe, I. J. Beyerlein, C. N. Tomé, *Acta Mater.*, **57** (2009) 6047.

[32] N. Stanford, M. R. Barnett, *Mater. Sci. & Eng. A*, **516** (2009) 226.

[33] I. J. Beyerlein, L. Capolungo, P. E. Marshall, R. J. McCabe, C. N. Tomé, *Phil. Mag.*, **90** (2010) 2161.

[34] J. H. Brunton, M. P. W. Wilson, *Proc. Roy. Soc. Lond. A.*, **309** (1969) 345.

[35] S. H. Park, S. G. Hong, C. S. Lee, *Scripta Mater.*, **62** (2010) 202.

[36] W. F. Sheely, R. R. Nash, *Trans. Metall. Soc. AIME*, **218** (1960) 416.

[37] A. Akhtar, E. Teghtsoonian, *Acta Metall.*, **17** (1969) 1339.

[38] A. Akhtar, E. Teghtsoonian, *Acta Metall.*, **17** (1969) 1351.

[39] R. E. Reed-Hill, W. D. Robertson, *Trans. TMS-AIME* **220** (1957) 496.

[40] R. E. Reed-Hill, W. D. Robertson, *Trans. TMS-AIME* **221** (1958) 256.

[41] T. Obara, H. Yoshinga, S. Morozumi , *Acta Metall.*, **21** (1973) 845.

[42] S. Ando, K. Namamura, K. Takashima, H. Tonda, *J. Jpn. Inst. Light Met.*, **42** (1992) 765.

[43] B. Bhattacharya, PhD Thesis, McMaster University, 2006, Hamilton, Ontario, Canada.

[44] F. E. Hauser, P. R. Landon, J. E. Dorn, *Trans. ASM* , **48** (1956) 986.

[45] Z. Keshavarz, M. R. Barnett, *Scripta Mater.*, **55** (2006) 915.

[46] J. Koike, T. Kobayashi, T. Mukai, H. Watanabe, M. Suzuki, K. Maruyama, K. Higashi, *Acta Mater.*, **51** (2003) 2055.

[47] J. Koike, *Metall. & Mater. Trans. A*, **36A** (2005) 1689.

[48] S. R. Agnew, M. H. Yoo, C. N. Tomé, *Acta Mater.*, **49** (2001) 4277.

[49] M. R. Barnett, *Metall. Mater. Trans A*, **34** (2003) 1799.

[50] A. Staroselsky, L. Anand, *Int. J. Plast.*, **19** (2003) 1843.

[51] M. H. Yoo, *Metall. Trans. A*, **12** (1981) 409.

[52] B. C. Wonsiewicz, W. A. Backofen, *Trans. Metall. Soc. AIME*, **239** (1967) 1422.

[53] P. Van Houtte, *Acta Metall.*. **26** (1978) 591.

[54] C. N. Tomé, P. J. Maudlin, R. A. Lebensohn, G. C. Kaschner, *Acta Mater.,* **49** (2001) 2863.

[55] M. A. Gharghouri, G. C. Weatherly, J. D. Embury, J. Root, *Phil. Mag. A,* **79** (1999) 1671.

[56] S. Godet, L. Jiang, A. A. Luo, J. J. Jonas, *Scripta Mater.,* **55** (2006) 1055.

[57] J. Jonas, S. Mu, T. Al-Samman, G. Gottstein, L. Jiang, Ė. Martin, *Acta Mater.,* Submitted.

[58] J. Jiang, A. Godfrey, W. Liu, Q. Liu, *Scripta Mater.,* **58** (2008) 122.

[59] J. Koike, Y. Sato, D. Ando, *Mater. Trans.,* **48** (2008) 2792.

[60] H. Yoshinaga, R. Horiuchi, *Trans. JIM,* **4** (1963) 1.

[61] M. R. Barnett, *Mater. Sci. & Engg A,* **464** (2007) 1.

[62] M. R. Barnett, *Mater. Sci. & Engg A,* **464** (2007) 8.

[63] R. E. Reed-Hill, W. D. Robertson, *Acta Metall.,* **5** (1957) 717.

[64] R. E. Reed-Hill, *Trans. of Met. Soc. AIME,* **218** (1960) 554.

[65] W. H. Hartt, R. E. Reed-Hill, *Trans. of Met. Soc. AIME,* **239** (1967) 1511.

[66] S. L. Couling, J. F. Pashak, L. Sturkey, *Trans. ASM,* **51** (1959) 94.

[67] É. Martin, L. Capolungo, L. Jiang, J. J. Jonas, *Acta Mater.,* **58** (2010) 3970.

[68] M. R. Barnett, Z. Keshavarz, A. G. Beer, X. Ma, *Acta Mater.,* **56** (2008) 5.

[69] P. G. Partridge, *Phil. Mag.,* **12** (1965) 1043.

[70] C. H. Cáceres, T. Sumitomo, M. Veidt, *Acta Mater.,* **51** (2003) 6211.

[71] Z. Keshavarz, M. R. Barnett, In: N. R. Neelameggham, H. I. Kaplan, B. R. Powell (Eds.), *Mag. Tech. 2005,* TMS, San Francisco, CA, USA, 171.

[72] X. Y. Lou, M. Li, R. K. Boger, S. R. Agnew, R. H. Wagoner, *Int. J. Plast.,* **23** (2007) 44.

[73] H. Mecking, *The encyclopaedia of materials: science and technology*. Oxford; Elsevier Science, Amsterdam, (2001) 9785.

[74] U. F. Kocks, H. Mecking, *Prog. Mater. Sci.*, **48** (2003) 171.

[75] Z. S. Basinski, *Aust. J. Phy.,* **13** (1960) 284.

[76] X. Y. Lou, M. Li, R. K. Boger, S. R. Agnew, R. H. Wagoner, *Int. J. Plast.*, **23** (2007) 44.

[77] J. Jain, W. J. Poole, C. W. Sinclair, In: M. O. Pekguleryuz, N. R. Neelameggham, R. S. Beals, R. S. Nyberg (eds.), TMS, *Mag. Tech. 2008,* New Orleans, LA, USA, 171.

[78] S. R. Agnew, C. N. Tomé, D. W. Brown, T. M. Holden, S. C. Vogel, *Scripta Mater*. **48** (2003) 1003.

[79] C. H. Cáceres, D. M. Rovera, *J. Light Met.*, **1** (2001) 151.

[80] C. H. Cáceres, A. H. Blake, *Mater. Sci. & Engg.* A, **462** (2007) 193.

[81] C. H. Cáceres, P. Lukác, A. H. Blake, *Phil. Mag.*, **88** (2008) 991.

[82] A. Jain, S. R. Agnew, *Mater. Sci. & Engg. A,* **462** (2007) 29.

[83] A. A. Salem, S. R. Kalidindi, R. D. Doherty, *Acta Mater. ,* **51** (2003) 4225.

[84] R. W. K. Honeycombe, *The plastic deformation of metals,* 1968, Edward Arnold (Publishers) Ltd.

[85] M. H. Yoo, *Trans. Metall. Soc. AIME,* **245** (1969) 2051.

[86] M. H. Yoo, *Met. Trans. A,* **12** (1981) 409.

[87] Z. S. Basinski, M. S. Szczerba, M. Niewczas, J. D. Embury, S. J. Basinski, *Metall. Rev.,* **94** (1197) 1037.

[88] I. Karaman, H. Sehitoglu, A. J. Beaudoin, Y. I. Chumlyakov, H. J. Maier, C. N. Tomé, *Acta Mater.,* **48** (2000) 2031.

[89] A. A. Salem, S. R. Kalidindi, S. L. Seminatin, *Acta Mater. ,* **53** (2005) 3495.

[90] M. R. Barnett, Z. Keshavarz, A. G. Beer, D. Atwell, *Acta Mater.,* **52** (2004) 5093.

[91] M. R. Barnett, C. H. J. Davies, X. Ma, *Scripta Mater.,* **52** (2005) 627.

[92] E. Schmid, W. Boas, *Plasticity of crystals,* Published by F. A. Hughes and Co., 1950.

[93] R. W. K. Honeycombe, *The plastic deformation of metals,* 1968, Edward Arnold (Publishers) Ltd.

[94] M. R. Barnett, Z. Keshavarz, X. Ma, *Metall. Mater. Trans. A,* **37** (2006) 2283.

[95] E. C. Burke, W. R. Hibbard, *Trans. Metall. Soc. AIME,* **194** (1952) 295.

[96] E. W. Kelley, W. F. Hosford, *Trans. Metall. Soc. AIME,* **242** (1968) 5.

[97] M. J. Philippe, *Mater. Sci. Forum,* **157-162** (1994) 1337.

[98] E. W. Kelley, W. F. Hosford, *Trans. Metall. Soc. AIME,* **242** (1968) 654.

[99] M. D. Nave, M. R. Barnett, *Scripta Mater.,* **51** (2004) 881.

[100] R. Gehrmann, M. Frommert, G. Gottstein, *Mater. Sci. & Engg. A,* **395** (2005) 338.

[101] P. Yang, *J. Mater. Sci. & Tech.,* **21** (2005) 331.

[102] C. N. Tomé, P. J. Maudlin, R. A. Lebensohn, G. C. Kaschner, *Acta Mater.,* **49** (2001) 2863.

[103] P. Rangaswamy, M. A. M. Bourke, D. W. Brown, G. C. Kaschner, R. B. Rogge, M. G. Stout, C. N. Tomé, *Metall. Mater. Trans. A,* **33** (2002) 757.

[104] D. W. Brown, M. A. M. Bourke, B. Clausen, T. M. Holden, C. N. Tomé, R. Varma, *Metall. Mater. Trans. A,* **34** (2003) 1439.

[105] L. Addessio, E. K. Cerreta, G. T. Gray, *Metall. Mater. Trans. A,* **36** (2005) 2893.

[106] G. C. Kaschner, C. N. Tomé, I. J. Beyerlein, S. C. Vogel, D. W. Brown, R. J. McCabe, *Acta Mater.,* **54** (2006) 2887.

[107] R. J. McCabe, E. K. Cerreta, A. Misra, G. C. Kaschner, C. N. Tomé, *Phil. Mag.,* **86** (2006) 3595.

[108] G. C. Kaschner, C. N. Tomé, R. J. McCabe, A. Misra, S. C. Vogel, D. W. Brown, *Mater. Sci. & Engg A,* **463** (2007) 122.

[109] I. J. Beyerlein, C. N. Tomé, *Int. J. Plast.,* **24** (2008) 867.

[110] L. Capolungo, I. J. Beyerlein, G. C. Kaschner, C. N. Tomé, *Mater. Sci. & Engg A,* **513** (2009) 42.

[111] J. F. Stohr, J. P. Poirier, *Phil. Mag.,* **25** (1972) 1313.

[112] F. E. Hauser, P. R. Landon, I. E. Dorn, *Trans. ASM,* **51** (1959) 51.

[113] S. Ando, H. Tonda, *Mater. Trans. JIM,* **41** (2000) 1191.

[114] FactSage, Version 6.1, User defined thermodynamic database.

[115] S. Celotto, *Acta Mater.,* **48** (2000) 1775.

[116] S. Celotto, T. J. Bastow, *Acta Mater.,* **49** (2001) 41.

[117] J. B. Clark, *Acta Metall.,* **16** (1968) 141.

[118] D. Duly, J. P. Simon, Y. Bréchet, *Acta Metall. Mater.,* **43** (1995) 101.

[119] A. F. Crawley, K. S. Milliken, *Acta Metall.,* **22** (1974) 557.

[120] A. F. Crawley, B. Lagowski, *Met. Trans.*, **5** (1974) 949.

[121] D. A. Porter, J. W. Edington, *Proc. Roy. Soc. Lond. A.*, **358** (1977) 335.

[122] C.H. Cáceres, C. J. Davidson, J. R. Griffiths, C. L. Newton, *Mater. Sci. Eng. A*, **A325** (2002), 344.

[123] C. R. Hutchinson, J. F. Nie, S. Gorsse, *Metall. Mater. Trans. A*, **36** (2005) 2093.

[124] J. G. Byrne, *Acta Metall.*, **11** (1963) 1023.

[125] J. S. Chun, J. G. Byrne, *J. Mater. Sci.*, **4** (1969) 861.

[126] J. S. Chun, J. G. Byrne, *Phil. Mag. A*, **20** (1969) 291.

[127] K. Eckelmeyer, R. W. Hertzberg, *Metall. Trans.*, **1** (1970) 3411.

[128] J. B. Clark, *Acta Metall.*, **13** (1965) 1281.

[129] N. Stanford, M. R. Barnett, *Mater. Sci. & Eng. A*, **516** (2009) 226.

[130] M. A. Gharghouri, G. C. Weatherly, J. D. Embury, *Phil. Mag. A*, **78** (1998) 1137.

[131] L. M. Brown, W. M. Stobbs, *Phil. Mag.*, **23** (1971) 1185.

[132] L. M. Brown, W. M. Stobbs, *Phil. Mag.*, **23** (1971) 1201.

[133] L. M. Brown, *Acta Metall.*, **21** (1973) 879.

[134] L. M. Brown, D. R. Clarke, *Acta Metall.*, **23** (1975) 821.

[135] D. Uko, J. D. Embury, R. Sowerby, *Met. Tech., Parts I and II*, 1979.

[136] D. V. Wilson, *Acta Metall.*, **13** (1965) 807.

[137] D. J. Lloyd, *Acta Metall.*, **25** (1977) 459.

[138] C. H. Cáceres, C. J. Davidson, J. R. Griffiths, C. L. Newton, *Mater. Sci. & Eng. A*, **325** (2002) 344.

[139] G. Sachs, *Zur ableitung einer filebendingung. Zeitschrift des Vereines Deutscher Ingenieure*, **72** (1928) 734.

[140] G. I. Taylor, *J. Inst. Metals*, **62** (1938) 307.

[141] G. I. Taylor, *Strains in crystalline aggregates*, In: R. Grammel (ed.), *Deformation and flow of solids*, Springer, Berlin, (1956) 3.

[142] J. F. Bishop, R. Hill, *Phil. Mag.*, **42** (1951) 1298.

[143] U. F. Kocks, H. Chandra, *Acta Metall.*, **30** (1982) 695.

[144] P. Van Houtte, *Mat. Sci. Eng.*, **55** (1982) 69.

[145] S. R. Kalidindi, C. A. Bronkhorst, L. Anand, *J. Mech. Phys. Solids*, **40** (1992) 537.

[146] P. Bate, *Phil. Trans. R. Soc. A*, **357** (1991) 1589.

[147] D. P. Mika, P. R. Dawson, *Acta Mater.*, **47** (1999) 1355.

[148] A. Molinari, G. R. Canova, S. Ahzi, *Acta Metall.*, **35** (1987) 2983.

[149] R. A. Lebensohn, C. N. Tomé, *Acta Mater.*, **41** (1993) 2611.

[150] C. N. Tomé, P. J. Maudlin, R. A. Lebensohn, G. C. Kaschner, *Acta Mater.*, **49** (2001) 3085.

[151] C. N. Tomé, R. A. Lebensohn, U. F. Kocks, *Acta Metall. Mater.*, **39** (1991) 2667.

[152] J. D. Eshelby, *Proc. Roy. Soc. Lond. A*, **241** (1957) 376.

[153] S. R. Kalidindi, *J. Mech. Phys. Sol.*, **46** (1998) 267.

[154] S. R. Kalidindi, *Int. J Plast.*, **17** (2001) 837.

[155] S. B. Yi, C. H. J. Davies , H. G. Brokmeier, R. E. Bolmaro, K. U. Kainer, J. Homeyer, *Acta Mater.*, **54** (2006) 549.

[156] Annual book of ASTM standards (1988) ASTM Designation E-112-88, ASTM, Philadelphia, PA.

[157] M. A. Gharghouri, G. C. Weatherly, J. D. Embury, J. Root, *Phil. Mag. A*, **79** (1999) 1671.

[158] ASTM D 3379-82, Annual Book of ASTM Standards. 15.03. 181 (1987).

[159] C. N. Tomé, *ODFVF3,* Version 14th Feb. 2008, Los Alamos National Lab, USA.

[160] C. N. Tomé, R. A. Lebensohn, U. F. Kocks, *Acta Metall. Mater.,* **39** (1991) 2667.

[161] R. A. Lebensohn , C. N. Tomé, *Acta Mater.,* **41** (1993) 2611.

[162] R. A. Lebensohn , P. A. Turner, J. W. Signorelli, G. R. Canova, C. N. Tomé, *Modelling Simul. Mater. Sci. Eng.,* **6** (1998) 447.

[163] G. Proust, C. N. Tomé, A. Jain, S. R. Agnew, *Int. J. Plast.,* **25** (2009) 861.

[164] G. E. Mann, T. Sumitomo, C. H. Cáceres, J. R. Griffiths, *Mater. Sci. Eng. A,* **456** (2007) 138.

[165] B. Raeisinia, S. R. Agnew, *Scripta Mater.,* **63** (2010) 731.

[166] C. Corby, C. H. Cáceres, P. Lukác, *Mater. Sci. & Engg. A,* **387-389** (2004) 22.

[167] A. A. Salem, S. R. Kalidindi, R. D. Doherty, *Acta Mater. ,* **51** (2003) 4225.

[168] I. J. Beyerlein, L. Capolungo, P. E. Marshall, R. J. McCabe, C. N. Tomé, *Proc. R. Soc. A,* **466** (2010) 2517.

[169] M. A. Meyers, O. Vohringer, V. A. Lubarda, *Acta Mater.,* **49** (2001) 4025.

[170] P. W. Flynn, J. Mote, J. E. Dorn, *Trans. Am. Inst. Min. (Metall.) Engg,* **221** (1961) 1148.

[171] H. Yoshinaga, R. Horiuchi, *Trans. Japan Inst. Metals,* **5** (1964) 14.

[172] A. Urakami, M. Meshii, M. E. Fine, *Acta Met.*, **18** (1970) 87.

[173] J. Jain, J. Zou, C. W. Sinclair, W. J. Poole, *J. of Microscopy, doi: 10.1111/j.1365-2818.2010.03434.x* (2010).

[174] U. F. Kocks, *Reprinted from Unified constitutive equations for creep and plasticity*, A. K. Miller, ed. (Elsevier 1987).

[175] C. H. Cáceres, P. Lukác, *Phil. Mag.,* **88** (2008) 977.

[176] M. M. Niewczas, Z. S. Basinski, S. J. Basinski, J. D. Embury, *Phil. Mag. A,* **81** (2001) 1121.

[177] C. H. Cáceres, P. Lukác, *Phil. Mag.,* **88** (2008) 991.

[178] J. Bohlen, M. R. Nürnberg, J. W. Senn, D. Letzig, S. R. Agnew, *Acta Mater.*, **55** (2007) 2101.

[179] F. E. Hauser, P. R. Landon, J. E. Dorn, *Trans. ASM* , **48** (1956) 986.

[180] S. Ando, H. Tonda, *Mat. Sci. forum*, **350** (2000) 43.

[181] Z. Keshavarz, M. R. Barnett, *Scripta Mater.*, **55** (2006) 915.

[182] T. A. Mason, J. F. Bingert, G. C. Kaschner, G. C. Wright, S. I. Larsen, R. J. Larsen, *Metall. Mater. Trans. A.*, **33** (2002) 949.

[183] B. L. Henrie, T. A. Mason, J. F. Bingert, *Mater. Sci. Forum*, **495-497** (2005) 191.

[184] P. Rangaswamy, M. A. M. Bourke, D. W. Brown, G. C. Kaschner, R. B. Rogge, M. G. Stout, C. N. Tomé, *Metall. Mater. Trans. A,* **33** (2002) 757.

[185] J. Jain, W. J. Poole, C. W. Sinclair, M. A. Gharghouri, *Scripta Mater.*, **62** (2010) 301.

[186] D. A. Porter, K. E. Easterling, *Phase transformations in metals and alloys*, Chapman & Hall, Second edition.

[187] R. A. Lebensohn, C. N. Tomé, *Mater. Sci. & Eng. A,* **175** (1994) 71.

[188] H. R. Wenk, C. N. Tomé, *J. Geophys. Res.,* **104** (1999) 513.

[189] A. H. Blake, C. H. Cáceres, *Mater. Sci. & Engg. A,* **483-484** (2008) 161.

[190] W. B. Hutchinson, M .R. Barnett, *Scripta Mater.,* **63** (2010) 737.

[191] B. Raeisinia, S. R. Agnew, *Metall. & Mater. Trans. A,* Submitted.

[192] R. Hielscher, H. Schaeben, *J. App. Crystall.,* **41** (2008) 1024.

[193] F. E. Hauser, P. R. Landon, J. E. Dorn, *Trans. ASM,* 50 (1958) 856.

[194] D. G. Westlake, *Acta Metall.,* **9** (1961) 327.

[195] M. H. Yoo, J. K. Lee, *Phil. Mag. A,* **63** (1991) 987.

[196] C. K. Chyung, C. T. Wei, *Phil. Mag.,* **15** (1967) 161.

[197] D. W. Brown, A. Jain, S. R. Agnew, B. Clausen, *Mat. Sci. Forum,* **539–543** (2007) 3407.

[198] B. Clausen, C. N. Tomé, D. W. Brown, S. R. Agnew, *Acta Mater.,* **56** (2008) 2456.

[199] C. S. Roberts, *Magnesium and its Alloys*, John Wiley & Sons, New York, 1960.

[200] E. A. Ball, P. B. Prangnell, *Scripta Met. Mater.,* **31** (1994) 111.

[201] M. Avedesian, H. Baker (Eds.), ASM Metals Handbook, Magnesium and Magnesium Alloys, ASM International, Metals Park, OH, 1999.

[202] S. Kleiner, P. J. Uggowitzer, in: Proceedings of the 1st International Light Metal Technology Conference, 2003, 327.

[203] L. Capolungo, I. J. Beyerlein, *Phys. Rev.,* **78** (2008) 711.

[204] J. Wang, R. G. Hoagland, J. P. Hirth, L. Capolungo, I. J. Beyerlein, C. N. Tomé, *Scripta Mater.,* **61** (2009) 903.

[205] P. G. Partridge, *Acta Metall.,* **13** (1965) 1329.

[206] A. Serra, D. J. Bacon, Yu. N. Osetsky, *Phil. Mag. Lett.,* **87** (2007) 451.

APPENDIX: A1 - Crystallographic Formulae for HCP Crystal

Conversions	*Crystallographic formulae*	*References*
Normal to a plane (hkil)	$[hki\frac{3}{2}(\frac{a}{c})^2 l]$	[1]
Miller-Bravais indices of a plane (hkil) to miller indices of a plane (HKL)	$H = (h - k/2 - i/3)$ $K = \left(\sqrt{3}/2(k - i)\right)$ $L = (3/2(a/c)l)$	[2]
Miller-Bravais indices of a direction [uvtw] to miller indices of a direction [UVW]	$U = (u - v/2 - t/3)$ $V = \left(\sqrt{3}/2(v - t)\right)$ $W = ((c/a)w)$	[2]

References

[1] P. G. Partridge, *Met. Rev.*, Institute of Metals, **118** (1967) 169.

[2] W. F. Hosford, *The Mechanics of Crystals and Textured Polycrytals,* Oxford University Press, 1993.

APPENDIX: A2 - Viscoplastic Self-Consistent (VPSC) Model

This section is concerned with the details of the VPSC model. The single crystal constitutive relationship utilised in the model is described in section A2.1. The linking of single crystal response to the aggregate behaviour is described in section A2.2. Section A2.3 introduces the hardening model utilised for slip and twin system hardening. Section A2.4 contains the description of predominant twin reorientation (PTR) scheme employed in VPSC for accounting the texture development resulting from twinning.

A2.1. Grain level constitutive response

A rate sensitive constitutive law has been applied to relate the plastic strain rate ($\dot{\varepsilon}_{ij}$) with the applied stress (σ_{kl}) on the grain [1] (also known as viscoplastic equation), i.e.

$$\dot{\varepsilon}_{ij} = \dot{\gamma}_0 \sum_s m_{ij}^s \left(\frac{m_{kl}^s \sigma_{kl}}{\tau_0^s}\right)^n \qquad \text{(A2.1)}$$

$\dot{\gamma}_0$ is a reference strain rate (1 s^{-1}), m_{ij}^s is the Schmid tensor of slip and twin system, which is given by normal, n_i^s, and Burgers vector, b_i^s, of the system as, $m_{ij}^s = \frac{1}{2}(n_i^s b_j^s + n_j^s b_i^s)$, τ_0^s is the CRSS of the system, n is the rate sensitivity exponent.

A2.2. VPSC formulation

The VPSC model deals with the plastic deformation of aggregates, it ignores the elastic effects. In addition, the entire model is formulated in terms of deviatoric stress tensors, since the plastic deformation is independent of hydrostatic stress. Within VPSC the grain level heterogeneity of plastic deformation is incorporated using the Eshelby [2]

inclusion solution. Accordingly, it is necessary to linearize the non-linear behaviour of both the grains and the HEM. The grain level constitutive relationship can be written as,

$$\dot{\varepsilon}_{ij} = M_{ijkl}\sigma'_{kl} \tag{A2.2}$$

Where M_{ijkl} is the grain compliance and σ'_{kl} is the grain deviatoric stress.

According to [1, 3], the equation A2.1 can be rewritten in a pseudo-linear form as,

$$\dot{\varepsilon}_i = \left\{ \dot{\gamma}_0 \sum_S \frac{m^S_{ij} m^S_{kl}}{\tau^S_0} \left(\frac{m^S_{pq}\sigma'_{pq}}{\tau^S_0} \right)^{n-1} \right\} \sigma'_{kl} \tag{A2.3}$$

where

$$M_{ijkl} = \dot{\gamma}_0 \sum_S \frac{m^S_{ij} m^S_{kl}}{\tau^S_0} \left(\frac{m^S_{pq}\sigma'_{pq}}{\tau^S_0} \right)^{n-1} \tag{A2.4}$$

Similar to above the constitutive relationship for the HEM can be given as,

$$\bar{\dot{\varepsilon}}_{ij} = \overline{M}_{ijkl}\bar{\sigma}'_{kl} \tag{A2.5}$$

Here $\bar{\dot{\varepsilon}}_{ij}$, $\overline{M}_{ijkl}$ and $\bar{\sigma}'_{kl}$ now corresponds to the HEM. After linearising the response of the grain and the aggregate, the Eshelby [2] solution is adopted to relate the stress and strain rate in the grain to the overall stress and strain rate in the aggregate [1, 3], as,

$$(\dot{\varepsilon}_{ij} - \bar{\dot{\varepsilon}}_{ij}) = -\tilde{M}_{ijkl}(\sigma'_{kl} - \bar{\sigma}'_{kl}) \tag{A2.6}$$

The above equation is termed as the interaction equation, where $\tilde{M}_{ijkl}$ is the interaction tensor and can be given as [4, 5],

$$\tilde{M}_{ijkl} = n^{eff} (I_{ijmn} - S_{ijmn})^{-1} S_{mnpq} \overline{M}_{pqkl} \qquad \text{(A2.7)}$$

where n^{eff} is the interaction strength parameter, I_{ijkl} is the identity tensor, S_{ijkl} is the Eshelby tensor.

In the following, we explained how the iterative procedure of the self-consistent theory can be utilised to predict the response of the aggregate (i.e. how to obtain $\overline{\sigma}_{ij}^{'}$ when $\overline{\dot{\varepsilon}}_{ij}$ is imposed on the aggregate). A schematic representation of the steps involved in the self consistent algorithm is shown in Figure A2.1. Central to this is the need to determine the aggregate compliance ($\overline{M}_{ijkl}$) using the self consistent criterion (i.e. the volume average of the strain rate and stress over aggregate coincides with the macroscopic strain rate and stress) and the interaction equation. If $\overline{M}_{ijkl}$ is too large then solution will be close of Sachs, while if it is too small then it will be close to Taylor. There are other intermediate cases like secant, affine and tangent.

A2.3. Slip and twin systems hardening

In this section, a brief overview of the hardening model utilised in the VPSC code is provided. The hardening of individual slip and twin systems is described by the Voce-type hardening law:

$$\tau = \tau_0 + (\tau_1 + \theta_1 \Gamma)(1 - \exp(-\frac{\theta_0 \Gamma}{\tau_1})) \qquad \text{(A2.8)}$$

where, τ is the threshold stress which describes the resistance for the activation of particular deformation mode and it usually evolves with deformation due to strain

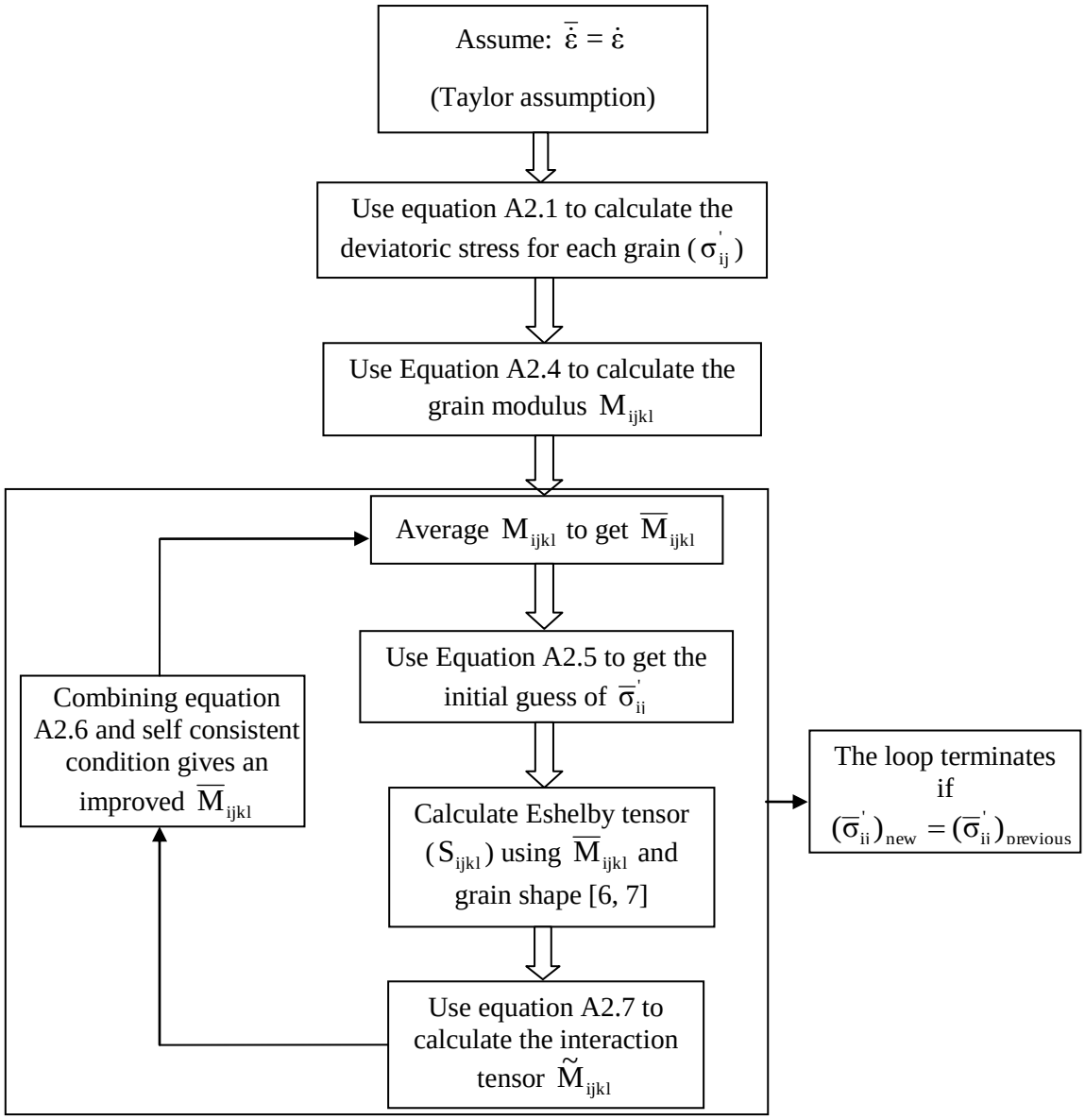

Figure A2.1: A schematic representation of the steps involved in the self-consistent algorithm of the VPSC model.

hardening and Γ is the accumulated shear strain in the grain; both are plotted schematically in Figure A2.2. τ_0 and τ_1 are the initial and back-extrapolated increase in the threshold

stress, while θ_0 and θ_1 are the initial and final slope of the hardening curve, respectively, as indicated in Figure A2.2.

Empirically, the model allows for both "self" and "latent" hardening of systems by defining the coupling coefficient 'h^{st}' in a hardening matrix which accounts for the effect of *s*th mode on the hardening of *t*th mode (i.e. it describes the slip-slip, slip-twin and twin-twin interactions). Finally, the increase in threshold stress of a system due to shear activity in the grain can be given by:

$$\Delta\tau = \frac{d\tau}{d\Gamma}\sum_t h^{st}\Delta\gamma^t \qquad \text{(A2.9)}$$

where $\Delta\gamma^t$ is the shear accommodated by "t" deformation mode.

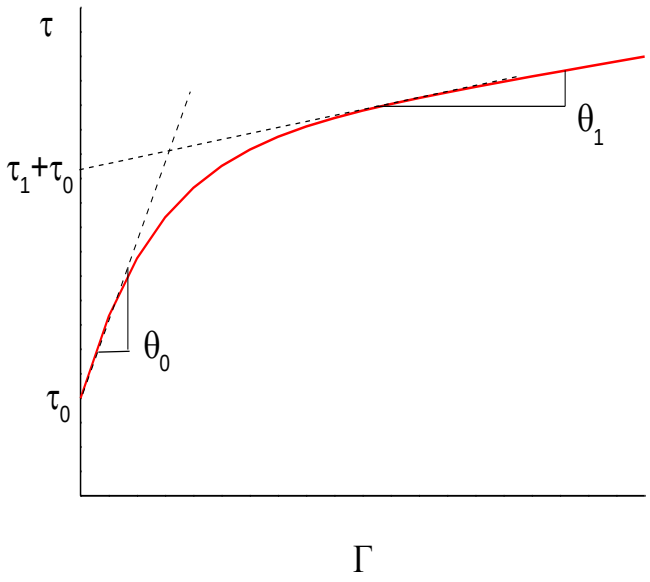

Figure A2.2: Schematically illustrating the parameters of equation (A2.8).

A2.4. Twinning model

In the VPSC model, the twin systems are considered to be active like slip i.e. according to CRSS criteria (albeit only in one direction). The contribution of twinning to the texture evolution was considered based on predominant twin reorientation (PTR) scheme which was originally proposed by Tomé et al. [8] and works as follows: the amount of twinning shear $\gamma^{t,g}$ by each twinning system, t, is monitored within each grain, g, and of the associated volume fraction $V^{t,g} = \gamma^{t,g} / S^t$ as well (S^t is the characteristic twin shear of the twinning mode, t). The accumulated twin fraction (sum of twinned volume) is made over all grains as,

$$V^{acc,mode} = \sum_g \sum_t \gamma^{t,g} / S^t \qquad \text{(A2.10)}$$

After each deformation step, grains are randomly checked whether or not the volume fraction of predominant twin system exceeds a threshold value. If so, the entire grain is reoriented to a new orientation which will be reflective of that twinning system. The twinned volume fraction of newly oriented grain is then add to a quantity named as "effective twinned volume fraction", $V^{eff,mode}$. This check will continue until all the grains are checked or the value of $V^{eff,mode}$ exceeds the total accumulated twinned volume fraction, $V^{acc,mode}$. The above mentioned threshold volume fraction is defined as follows:

$$V^{th,mode} = A^{th1} + A^{th2} \frac{V^{eff,mode}}{V^{acc,mode}} \qquad \text{(A2.11)}$$

The threshold volume fraction starts typically at 10% (A^{th1}, imposes the delay in reorientation due to twinning until the grain exhibits a defined trend) and increases rapidly,

saturating at 50% (A^{th2}). The above procedure is self-controlling in a sense that both, $V^{eff,mode}$ and $V^{acc,mode}$, tend to remain approximately same throughout the deformation.

There are several disadvantages of this scheme: i) it imposes the reorientation to the whole grain based on the threshold value, ii) it only accounts for the most active twinning system in each grain and iii) it does not consider any multiple twinning.

References

[1] R. A. Lebensohn, C. N. Tomé, *Acta Mater.*, **41** (1993) 2611.

[2] J. D. Eshelby, *Proc. Roy. Soc. Lond. A*, **241** (1957) 376.

[3] A. Molinari, G. R. Canova, S. Ahzi, *Acta Metall.*, **35** (1987) 2983.

[4] A. Molinari, L. S. Tóth, *Acta Metall. Mater.*, **42** (1994) 2453.

[5] C. N. Tomé, *Modelling Simul. Mater. Sci. Eng.*, **7** (1999) 723.

[6] R. A. Lebensohn, P. A. Turner, J. W. Signorelli, G. R. Canova, C. N. Tomé, *Modelling Simul. Mater. Sci. Eng.*, **6** (1998) 447.

[7] C. N. Tomé, R. A. Lebensohn, In: D. Raabe, F. Roters, F. Barlat. L-Q Chen, Editors, Continuum Scale Simulation of Engineering Materials, Weinheim, Wiley-VCH, 2004, 473.

[8] C. N. Tomé, R. A. Lebensohn, U. F. Kocks, *Acta. Metall.*, **39** (1991), 2667.

APPENDIX: A3 - Quantitative Analysis of Twinning Using Neutron Diffraction Data

Conventional metallographic ways (e.g. optical microscopy, EBSD) for analysing the twinning fractions are generally considered to be inadequate due to limited quantitative statistical information. The other common practice is to track systematically the crystallographic texture development during deformation at several strain levels via diffraction techniques (e.g. neutron diffraction). It is known that as both slip and twinning contribute to texture evolution, the large re-orientation associated with twinning results in very significant and rapid texture evolution. The distinct characteristic of twinning can be utilised in estimating twinning fractions from an experimentally measured {0001} pole figures. Although some efforts have been made in this direction [1, 2], there is up to now no well-defined practice to extract the twinning fractions from texture measurements. The intent of this Appendix is to illustrate a procedure of estimating the twin volume fractions from texture data. The procedure outlined here was applied to texture measurements collected from neutron diffraction experiments on the AZ80 magnesium samples deformed in compression. The present Appendix also addresses the challenges and limitations associated with the proposed analysis.

The two things need to be identified before assessing the twinning fractions from {0001} pole figures. Firstly, the re-orientation associated with a particular twinning mode should be known a priori (e.g. $\{10\bar{1}2\}$ twinning rotates the <c> axis by ~86°). Secondly, the fraction of grains that is initially favourably oriented for twinning. In other words, the range of orientation space where grains would prefer to undergo twinning have to be

recognized beforehand (an explanation to identify this is given later in the text). For an example, Figure A3.1a depicts two outer rims of {0001} pole figure namely, 20° and 40°, where grains could potentially exhibit $\{10\bar{1}2\}$ twinning during compression parallel to ND (i.e. along the center of the pole figure).

The numerical integration of {0001} pole figure distribution over a given range of orientations gives the volume fraction of grains within that range. Mathematically, the volume fraction of grains within a ring of radius χ around the center of the pole figure can be given as (refer Figure A3.1a):

$$(V_f)_\chi = \frac{V_\chi}{V_{tot}} \tag{A3.1}$$

Where, $V_\chi = \int_0^{360}\int_0^{\chi} I(\eta,\chi)\sin(\chi)d\eta d\chi$ and $V_{tot} = \int_0^{360}\int_0^{90} I(\eta,\chi)\sin(\chi)d\eta d\chi$

Here, the normalised intensity (I) is a function of χ (tilt angle, 0-90°) and η (azimuthal angle, 0-360°) angle. As deformation proceeds, the reorientation due to twinning causes the change in intensity within a ring. The evolution of twinned volume fraction can thus be calculated by recording the change in intensity from its undeformed state to its deformed state.

Figure A3.1b shows an example where the $\{10\bar{1}2\}$ extension twin volume fractions were determined from the {0001} pole figures using an outer rim of size 20° and 40°. Clearly, the difference in calculations using two different rim sizes is little up to 5% strain, but it becomes sufficiently large after 5% strain. This pointed out the importance of

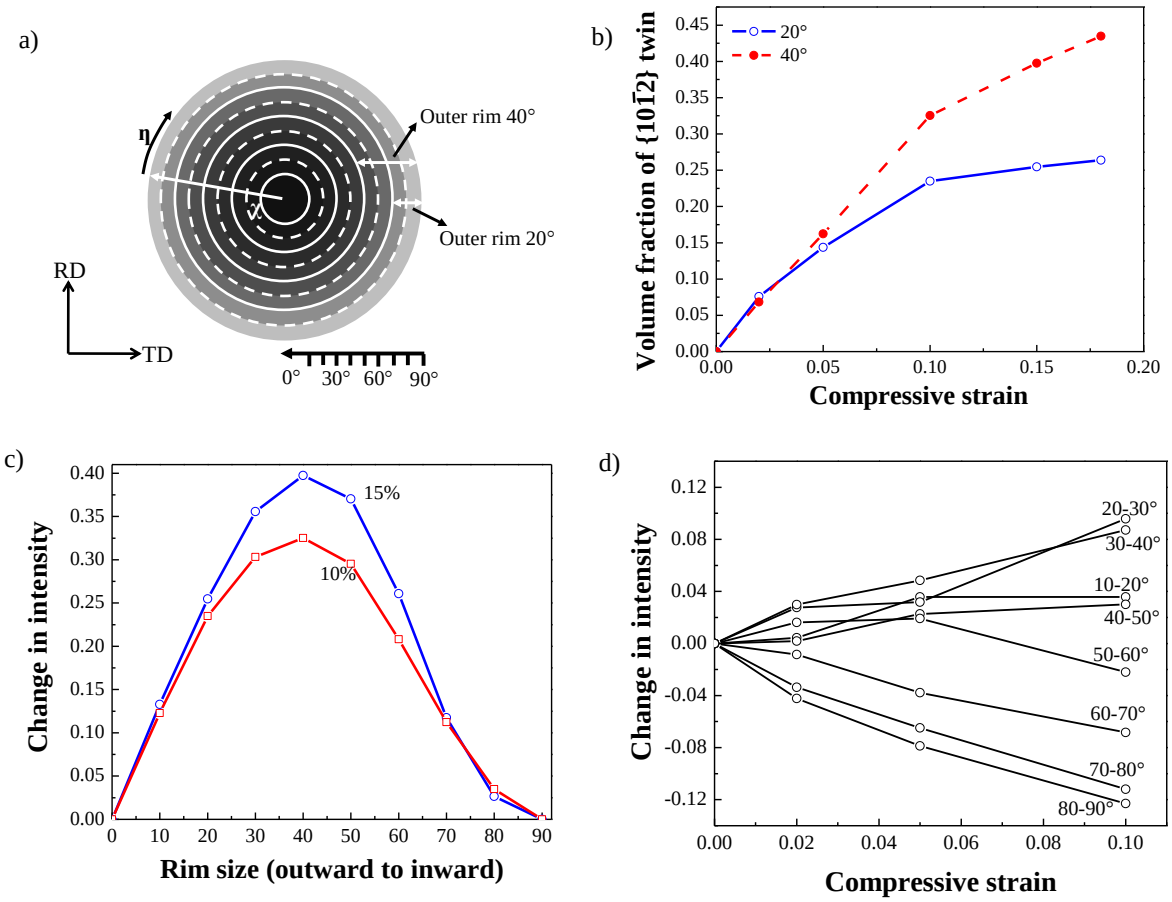

Figure A3.1: a) A schematic drawing of pole figure (orientation space), where η is the azimuthal angle (0-360 degrees) and χ is the tilt angle (0-90 degrees), illustrating the various regions of the pole figure (e.g. outer rim 20° and 40°) by drawing the concentric circles in radial increments of 10° ranging from 0-90° **b)** the {10$\bar{1}$2} twin volume fractions estimated from the grains lying in the outer rim of 20° (dashed lines and closed circles) and 40° (solid lines with open circles) of the {0001} pole figure **c)** change in intensity as a function of rim size for samples deformed in compression at 10% and 15% strain and **d)** the plot of change in intensity as a function of true compressive strain in an individual rim going from outward to inward of the {0001} pole figure in increment of 10°.

correct rim size selection. The following approach can be used in selecting an optimal rim size. Figure A3.1c shows a typical plot of change in intensity as a function of rim size at 10% and 15% strain. As can be noticed, the difference in intensity reaches to a maximum at some intermediate rim size before it gets down. The increase in change in intensity is indicative of the fraction of grains that were already twinned. Therefore, the rim size which corresponds to a maxima in the plot (here at ~40°) can be used as a cut-off angle in determining the volume fraction of grains favourably oriented for twinning.

Figure A3.1d shows the variation of change in intensity as a function of compressive strain within individual rim. Plotting data in this manner provides additional information about the rate of twinning. For instance, if the change in intensity is substantial then higher fraction of grains were twinned and vice versa.

In the end, it is meaningful to compare the results of twin fractions estimated from neutron data with other techniques. Table A3.1 provides a comparison of $\{10\bar{1}2\}$ twin fractions estimated from EBSD measurements and neutron data analysis. The method used in approximating twinned area fractions from EBSD maps is outlined chapter 4, section 4.6.2. As can be seen, the neutron results are in reasonable agreement with the EBSD results.

The above analysis becomes little complicated when twin modes other than the primary twin modes (e.g. double twinning) contribute significantly to the texture evolution. In such a situation, it turns out to be difficult in isolating the effect of individual modes (cf. [2]).

The procedure outlined in this Appendix can be used explicitly in treating the texture data for quantitative analysis of twinning fractions in HCP metals. Additional information regarding the twinning kinetics can also be gathered with such examination. However, the analysis is limited to a situation where no overlapping of primary and secondary twinning modes occurs.

Table A3.1: Comparison of $\{10\bar{1}2\}$ twin fractions estimated from EBSD measurements and neutron analysis for weak textured sample deformed in compression at 293K

Compressive strain	*0.02*	*0.05*	*0.1*
EBSD measurements	6%	13%	37%
Neutron analysis (Outer 40° rim)	7%	16%	33%

References:

[1] P. Rangaswamy, M. A. M. Bourke, D. W. Brown, G. C. Kaschner, R. B. Rogge, M. G. Stout, C. N. Tomé, *Metall. & Mater. Trans. A,* **33** (2002) 757.

[2] R. J. McCabe G. Proust, E. Cerreta, A. Misra, *Int. J. Plast.,* **25** (2009) 454.

APPENDIX: A4 - Double Extension Twinning in a Mg-8Al-0.5Zn Alloy

This section is concerned with the details of observation of double extension twinning in an AZ80 alloy. The analysis presented here is largely published recently in the reference [1]. In the following, the results of microstructure and micro-texture observations on AZ80 tested in compression at 77K are presented. In this case, the formation of double extension twins, i.e. extension twins formed within extension twins was unambiguously observed. This is to be contrasted with observations at room temperature where no such double twinning has been observed. Herein, two examples of double extension twins are presented. In the first example, the double extension twins appear to reduce the local plastic anisotropy while in the second example the double extension twinning appears to come from the impingement of two primary extension twins. In addition, the morphology of these newly observed double twins is compared with the previously reported contraction-extension double twins.

A4.1. The deformed state: double extension twins

An illustration of the deformed microstructure is presented in Figure A4.1. Figure A4.1a shows a band contrast map representative of the microstructures produced via deformation to a strain of 0.08 at 77K. Several types of boundaries (high angle, extension twin, extension twin impingement) are illustrated within this map. The boundary misorientation axis-angle pair analysis on these maps reveals many extension twins (86.3° disorientation about $<1\bar{2}10>$). Also observed are a few low angle boundaries with disorientations of between 7° and 8° about $<1\bar{2}10>$. Such boundaries are the results of the

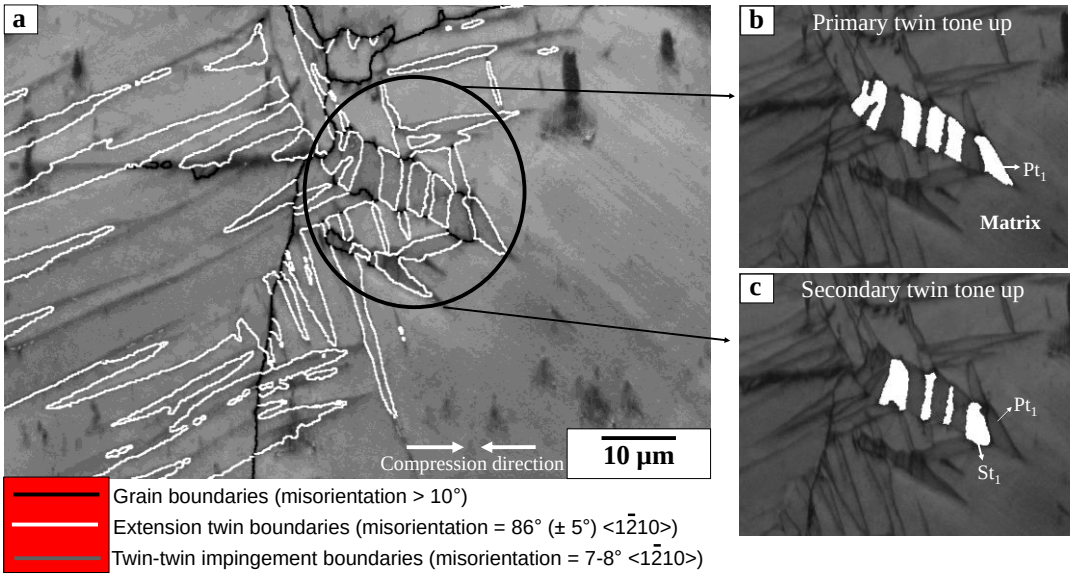

Figure A4.1: a) EBSD band contrast map of solution-treated sample after deformation to true strain of 0.08 at 77K. The extension twin boundaries are plotted as white boundaries (boundaries of misorientation = 86° (± 5° $<1\bar{2}10>$)). Notice that the grey boundaries correspond to low angle boundaries (misorientation = 7-8° $<1\bar{2}10>$) resulting from the impingement of two extension twin variants [2]. The regions of primary extension twins (Pt_1) and secondary extension twins (St_1) are highlighted in white in **b)** and **c)**.

variant specific twin-twin impingements. For instance, in this case the impingement of $(10\bar{1}2)$ $[\bar{1}011]$ and $(\bar{1}012)$ $[10\bar{1}1]$ twin variants in a grain leads to a boundary of 7-8° misorientation about $<1\bar{2}10>$ axis. A detailed explanation on the formation of such boundaries was given by Nave and Barnett [2]. Notice that a second boundary consistent with the impingement of extension twins has a 60^o misorientation about $<10\bar{1}0>$ [2] but was not observed in these samples. No evidence of either compression twinning ($\{10\bar{1}1\}$) nor double compression-tension twinning ($\{10\bar{1}1\}-\{10\bar{1}2\}$) could be found in these samples as expected from the starting texture relative to the imposed deformation.

In approximately 10% of extension twins (10 observations in 110 primary extension twins), complex morphologies were observed. The circled region in Figure A4.1a, shown in higher magnification in Figure A4.1b and Figure A4.1c, illustrates an example of one of these regions in more detail. Analysis of the boundary misorientation within this region reveals an interesting morphology with the apparent superposition of two extension twins highlighted as Pt_1 and St_1 in Figure A4.1b and A4.1c. Extracting the specific orientations from within these two twinned regions (Figure A4.2) one can readily see that St_1 has a extension twin relationship with respect to Pt_1 but not with respect to the surrounding matrix (Figure A4.2). The basal pole figure in Figure A4.2a illustrates that the sequence of twinning can be traced from matrix to Pt_1 ($\approx 86^o$) and subsequently from Pt_1 to St_1 ($\approx 86^o$). It is also important to note that the rotation axis associated with the

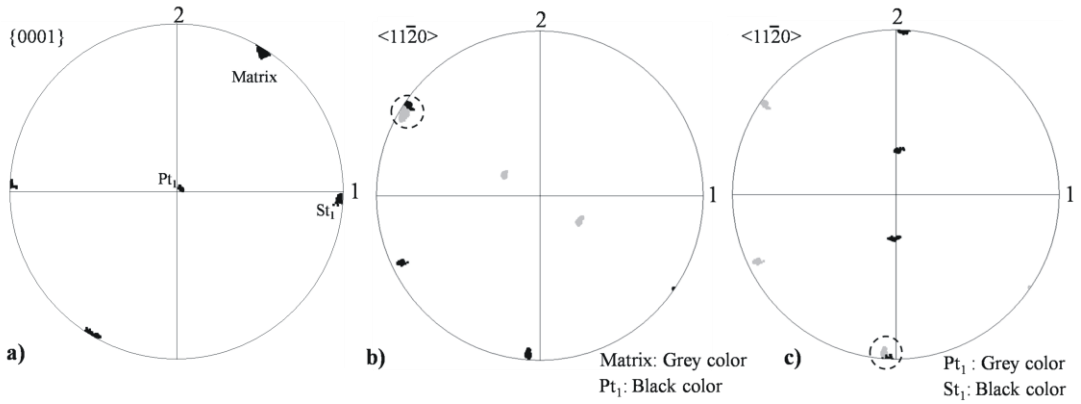

Figure A4.2: a) The {0001} pole figure illustrates the corresponding orientation of matrix, primary twin (Pt_1) and secondary twin (St_1) (map in Figure A4.1). The $<11\bar{2}0>$ pole figure in **b)** and **c)** describes the shared poles between the matrix and the primary extension twin and between the primary and secondary extension twins (see the dotted delineated circles over the common poles), respectively. Notice that the misorientation relationship between matrix and Pt_1 is ~86° about $<1\bar{2}10>$ and Pt_1 and St_1 is ~86° about $<1\bar{2}10>$. The macroscopic compression direction is oriented parallel to the direction 1.

crystallographic reorientation is common between the matrix and Pt_1 (e.g. $<11\bar{2}0>$) and Pt_1 and St_1 (e.g. $<11\bar{2}0>$) but that these reorientation axes are different between the matrix and St_1. In addition, the mean misorientation relationship between the matrix and the secondary extension twin (St_1) was determined to be $50° <\bar{2}021>$.

A second example of this double extension twinning is shown in Figure A4.3.

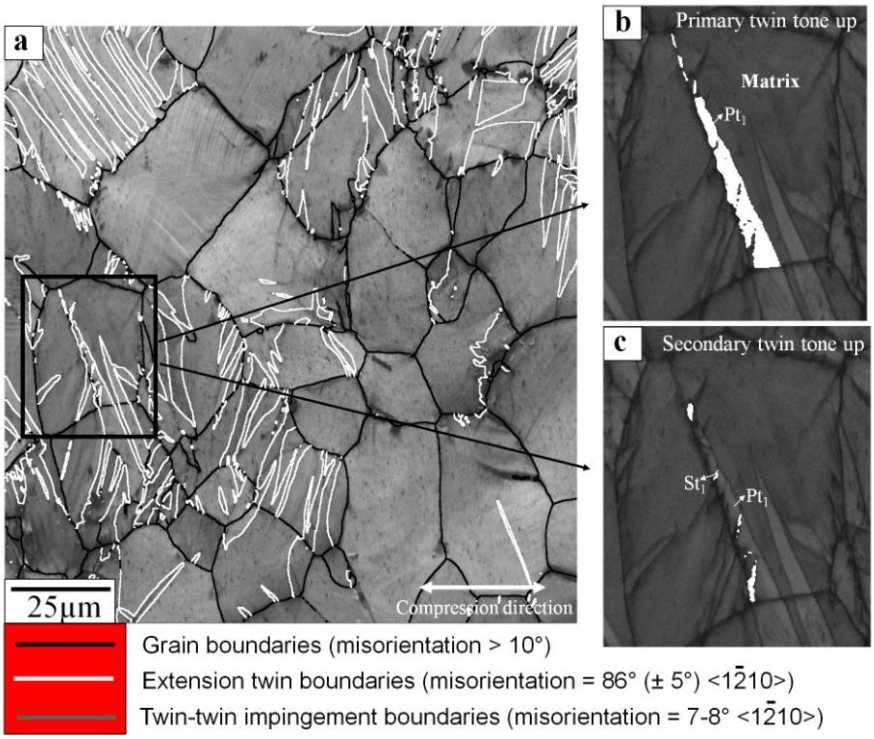

Figure A4.3: A second region mapped in EBSD using the same scheme as in Figure A4.1. This map illustrates a second case of double extension twinning in a grain. **a)** EBSD pattern quality map after deformation to true strain of 0.08. Grain boundaries (misorientation > 10°) are drawn in black and extension twin boundaries (misorientation = 86° (± $5°<11\bar{2}0>$) are plotted as white. The grey color boundaries correspond to the low angle boundaries (misorientation = 7-8°$<1\bar{2}10>$) resulting from the impingement of two extension twin variants [2]. **b)** An enlarged view of the region marked in (a) showing characteristics within primary extension twins (white regions denoted as Pt_1). Similarly, the features of secondary extension twins (St_1) can be seen in **c)**.

Focusing on the indicated grain in Figure A4.3a, one can see two particular extension twin variants (Pt_1 and St_1) within the grain. These two are highlighted in Figure A4.3b and Figure A4.3c. Within the twin variant Pt_1 one can observe fine features that are highlighted in Figure A4.3c. As before, it can be observed that these fine features have an 86^o misorientation with respect to Pt_1, consistent with them being extension twins (Figure A4.4). Moreover, examining the basal pole figure (Figure A4.4a) one can clearly see the sequence of 86^o rotations first from matrix → Pt_1 then Pt_1 → St_2. As above, the $<11\bar{2}0>$ rotation axis is different for the matrix → Pt_1 reorientation and the Pt_1 → St_1 reorientation.

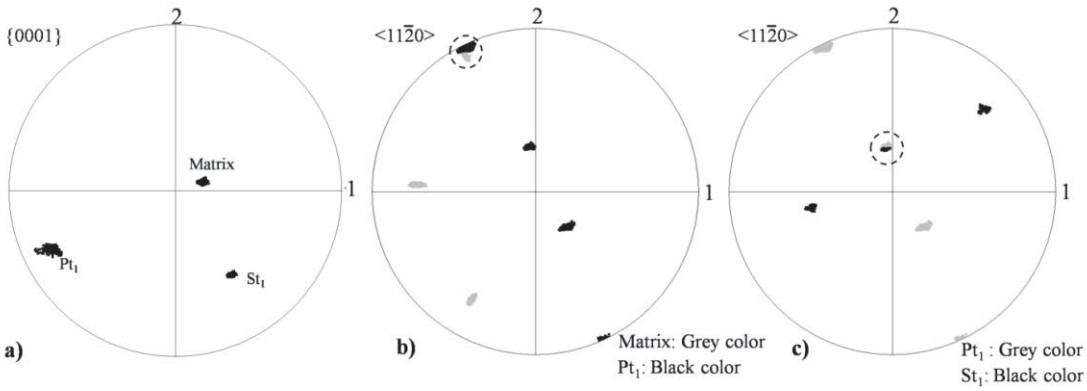

Figure A4.4: a) The {0001} pole figure illustrates the corresponding orientation of matrix, primary twin (Pt_1) and secondary twin (St_1) (map in Figure A4.3). The $<11\bar{2}0>$ pole figure in **b)** and **c)** describes the shared poles between the matrix and the primary extension twin and between the primary and secondary extension twins (see the dotted delineated circles over the common poles), respectively. Notice that the misorientation relationship between matrix and Pt_1 is ~86° about $<1\bar{2}10>$ and Pt_1 and St_1 is ~86° about $<1\bar{2}10>$**.** The macroscopic compression direction is oriented parallel to the direction 1.

As a final confirmation of the morphology and crystallography of these double extension twins, TEM analysis was performed on the same material as described above. Figure A4.5a shows a dark field image of a extension twin containing fine secondary extension twins using the $[1\bar{1}00]$ reflection from the primary twin. A selected area diffraction pattern taken at the triple junction between matrix, primary and secondary extension twins (Figure A4.5c-A4.5e) confirms the crystallographic analysis of the EBSD

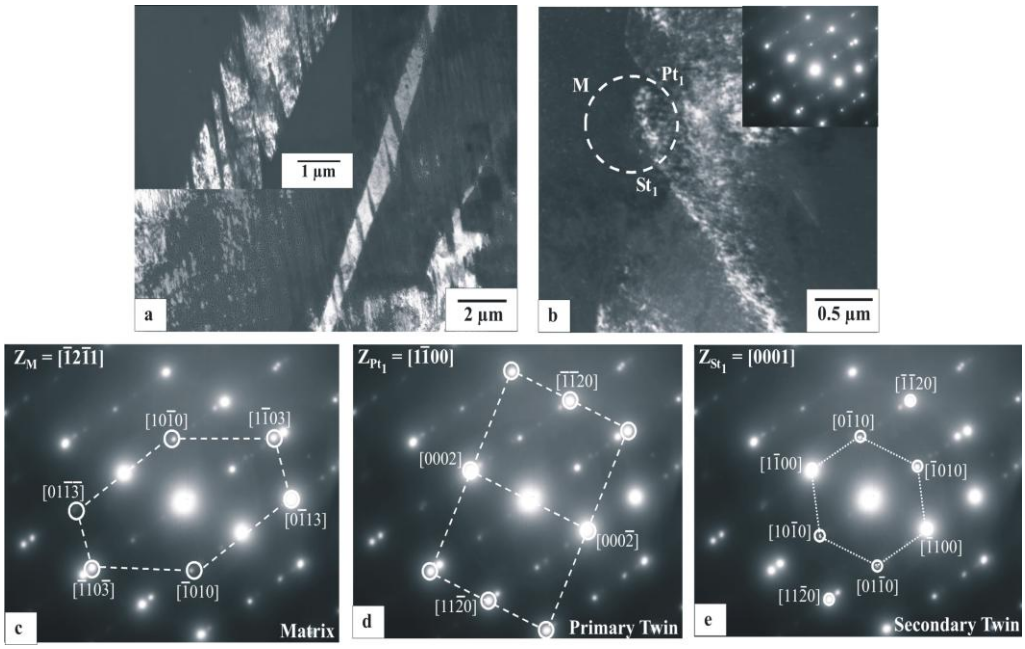

Figure A4.5: a) TEM dark field micrograph showing double extension twin after deformation to a true strain of 0.08 at 77K. The inset shows a higher magnification of the twins. **b)** Higher magnification on a twin-twin-matrix triple junction and the corresponding composite diffraction pattern. The diffraction spots are indexed in **c)**, **d)** and **e)** as $[\bar{1}2\bar{1}1]$, $[1\bar{1}00]$ and [0001], zone axes respectively. The rotation axis in going from matrix (M) to primary extension twin (Pt_1) is $[\bar{1}2\bar{1}0]$ while, primary to secondary extension twin (St_1) is $[11\bar{2}0]$. Extra spots in the SAD arise from double diffraction.

results described above. Whereas our observations on samples compressed at room temperature to similar levels of strain never revealed double extension twinning in EBSD or TEM observation, many of the extension twins observed in the TEM from samples compressed at 77K exhibited such an internal structure. It is notable that, while our statistics in the TEM are poor, it appeared that in the TEM a higher fraction of primary extension twins contained secondary extension twins compared to the results obtained from EBSD. It may be that this point to the limitation of spatial resolution of the EBSD compared to the fine scale of the extension twins (e.g. Figure A4.5). The fine lenticular morphology of the secondary extension twins observed in the TEM should be contrasted with the extension twins observed in double compression-tension twins, where a single extension twin can grow to fill an entire compression twin.

A4.2. The potential role of secondary extension twinning as a mechanism of plastic accommodation

The double extension twins observed above are relatively rare events, yet it is essential to understand them owing to the following reasons. These twins could potentially affect the subsequent recrystallisation behaviour of the alloy. They could play a significant role in the process of damage initiation and ensuing fracture in the material. It is also important to understand these observations in order to better understand the local conditions which can lead to their appearance. Moreover, it is significant, as noted above, that in this same alloy tested and observed under the same conditions but deformed at room temperature we have been unable to observe any double extension twins in EBSD or TEM.

The detailed crystallography and knowledge of the macroscopic loading conditions allows us to check whether the occurrence of the double twinning observed in Figures A4.1-A4.5 can be rationalized based on macroscopic arguments or whether local effects have to be considered as has been argued in the case of anomalous twinning observations in other cases [2-4].

A4.2.1. Double extension twinning and plastic anisotropy (case: I)

Starting with the case of the double extension twinning observed in Figure A4.1 (identified here as case: I), a simple qualitative argument suggests that double twinning is possible in this case since the first twinning leaves the <c>-axis within Pt_1 oriented approximately 90° from the compression axis. Thus, the observed secondary twinning also allows for a compressive strain parallel to the macroscopic compression direction. One could also argue this by considering the Schmid factor analysis based on the macroscopic loading direction. Table A4.1 summarizes the Schmid factor calculations performed on all the six possible primary and secondary twin variants (see case: I). As it can be seen that the activation of both primary and secondary twin variants are governed by the Schmid factor criterion i.e. the twin variants with the highest Schmid factor values are found as active. The present case can further be analysed in a more quantitative manner by means of enquiring the strain induced by the primary and the double twinning sequences. To see this, we start from the knowledge that extension twinning, written in terms of twin coordinate system (comprises of a direction normal to the twinning plane (K_1) and a shear direction (η_1)), can be described as a deformation gradient tensor as (refer Table A4.2),

Table A4.1: Schmid factors of primary and secondary twin variants for the cases reported in Figure A4.1 and Figure A4.3. The experimentally observed variants are highlighted with the red boxes

	Extension twin variants	*Schmid factor of primary variant*	*Schmid factor of secondary variant*
Case I: (Figure A4.1)	$(10\bar{1}2)[\bar{1}011]$	0.05	0.003
	$(01\bar{1}2)[0\bar{1}11]$	0.03	0.40
	$(\bar{1}102)[1\bar{1}01]$	0.29	0.34
	$(\bar{1}012)[10\bar{1}1]$	0.03	0.003
	$(0\bar{1}12)[01\bar{1}1]$	0.006	0.40
	$(1\bar{1}02)[\bar{1}101]$	0.24	0.34
Case II: (Figure A4.3)	$(10\bar{1}2)[\bar{1}011]$	0.057	-0.106
	$(01\bar{1}2)[0\bar{1}11]$	0.14	-0.23
	$(\bar{1}102)[1\bar{1}01]$	0.46	-0.087
	$(\bar{1}012)[10\bar{1}1]$	0.06	-0.118
	$(0\bar{1}12)[01\bar{1}1]$	0.13	-0.18
	$(1\bar{1}02)[\bar{1}101]$	0.44	-0.05

Table A4.2: Illustrates the Euler angles (of both matrix and primary twin), primary twin system and secondary twin system utilised in strain calculations associated with Figure A4.1 and Figure A4.3

Strain calculations		*Euler angles*			*Primary twin system*	*Secondary twin system*
		ϕ_1	ϕ	ϕ_2		
Case I: (Figure A4.1)	Matrix	146.01	93.05	28.16	$(\bar{1}102)[1\bar{1}01]$	$(01\bar{1}2)[0\bar{1}11]$
	Primary twin	111.97	4.5	3.71		
Case II: (Figure A4.3)	Matrix	109.12	19.8	37.31	$(10\bar{1}2)[\bar{1}011]$	$(1\bar{1}02)[\bar{1}101]$
	Primary twin	114.74	102.34	31.54		

$$F_{Pt_1} = \begin{bmatrix} 1 & 0 & 0 \\ 0 & 1 & 0 \\ 0.13 & 0 & 1 \end{bmatrix}$$

It can then transformed to the external coordinate system (see ref. [5] for more details) aligned with the compression axis and the two perpendicular transverse directions (2, 3), knowing from the EBSD measurements the orientation (Table A4.2) of the twin (written as the transformation matrix $T_{Pt_1}^{External}$),

$$F_{Pt_1}^{External} = (T_{Pt_1}^{External})^T F_{Twin} T_{Pt_1}^{External}$$

This gives a deformation gradient,

$$F_{Pt_1}^{External} = \begin{bmatrix} 0.972 & 0.1234 & -0.00758 \\ -0.006 & 1.0279 & -0.00171 \\ 0.0005 & -0.0021 & 1.00013 \end{bmatrix}$$

For small deformations of a continuum body, Lagrangian strain closely approximates to engineering strain and can be give as [6],

$$E = \frac{1}{2}(F^T + F) - I$$

Where I is the identity matrix. Thus, the above deformation gradient tensor ($F_{Pt_1}^{External}$) can be expressed as Lagrangian strain,

$$E_{Pt_1} = \begin{bmatrix} -0.0280 & 0.0587 & -0.0035 \\ 0.0587 & 0.0279 & -0.0019 \\ -0.0035 & -0.0019 & 0.0001 \end{bmatrix} \quad \text{(A4.1)}$$

Equation A4.1 is consistent with the fact that the twinning involves an invariant plane strain deformation. It should be noticed that the orientation of the twinning plane is 43^o from the compression axis, resulting in the external co-ordinate system being nearly the principal axes for E_{Pt_1}. Moreover, one can see that the extension twinning leads to a compressive strain along the macroscopic compression direction and a extension strain along one perpendicular axes. However, along macroscopic direction '3' the strain induced by this extension twin is nearly zero and yet macroscopically the sample is observed to deform (at least at small strains) with nearly isotropic expansion perpendicular to the compression axis.

Now, considering the secondary twin one can write its deformation gradient as,

$$F_{St_1}^{External} = (T_{St_1}^{External})^T F_{Twin} T_{St_1}^{External}$$

$$F_{St_1}^{External} = \begin{bmatrix} 0.9485 & -0.025 & -0.0458 \\ -0.025 & 0.988 & -0.0224 \\ 0.0713 & 0.0339 & 1.0635 \end{bmatrix}$$

Superimposing this with the deformation gradient from the primary twin gives the total deformation gradient within the doubly twinned region as,

$$F_{St_1}^{Net} = (F_{St_1}^{External} F_{Pt_1}^{External})$$

$$F_{St_1}^{Net} = \begin{bmatrix} 0.922 & 0.092 & -0.0530 \\ -0.031 & 1.0125 & -0.0239 \\ 0.0696 & 0.0414 & 1.0630 \end{bmatrix}$$

Or, written in terms of the Lagrangian strain,

$$E_{St_1}^{Net} = \begin{bmatrix} -0.078 & 0.0305 & 0.0083 \\ 0.0305 & 0.0125 & 0.0087 \\ 0.0083 & 0.0087 & 0.0630 \end{bmatrix} \quad \text{(A4.2)}$$

One can note that the strains within the double extension twinning and within the primary twin are similar in the sense that they both lead to contraction along the macroscopic compression direction and expansion in the other two perpendicular directions. The important difference, however, is that the region that undergoes double twinning achieves expansion parallel to the macroscopic '3' direction with a much smaller strain along the '2' direction. Thus, it ends up with a composite twinned region that provides a more isotropic response in the plane perpendicular to the compression axis (the '2-3' plane) then had either of the twins individually formed. While at higher temperatures

slip might be able to more easily accomplish this task (more uniformly) under the present testing conditions where non-basal slip is suppressed, double extension twinning may provide an opportunity to improve the local strain compatibility.

A4.2.2. Double extension twinning and twin impingement (case: II)

The example illustrated in Figure A4.3 and A4.4 (identified here as case: II) is more difficult to explain based on the macroscopic deformation conditions. In this case, if we invoke a simple Schmid analysis then it is found that the primary active twin variant exhibits a considerable divergence from the maximum Schmid factor criterion (see Table A4.1). The observed twin variant corresponds to the one with the lowest Schmid factor value. Moreover, it can be noticed that the primary twinning re-orients the <c>-axis to be oriented close to the macroscopic compression direction (Figure A4.4a). In this orientation one would not expect secondary extension twinning, as indicated from the negative values of Schmid factors in Table A4.1, implying that all of the possible secondary extension twins would give rise to an extension along the macroscopic axis of compression.

The apparent anomalous behaviour of extension twins has been previously described in magnesium and its alloys. In order to explain extension twinning in pure magnesium with its <c>-axis under macroscopically imposed compression, Nave and Barnett [2] argued for consideration of deviations in the local stress state due to plastic anisotropy. It was also noted that internal stresses acting in the opposite sense to the applied stress could also give rise to twinning during the unloading of the sample [7]. Koike et al. [3] have proposed a different explanation, suggesting that the in-homogeneity of basal slip in a grain could induce extension twinning. In this case, Koike et al. [3] referred to the twins as accommodation twins to emphasize the fact that they act so as to

reduce the plastic anisotropy. Most recently, Wu and colleagues [8] have studied the internal strains (stresses) in the parent grains and in the twinned grains separately in the magnesium alloy via neutron diffraction. They found that a large internal residual extension stress generated in the material during twinning drives the detwinning event during the compressive unloading (i.e. no extension loading is required).

In the present case we have not sought to provide an explanation for the appearance of the apparently (macroscopically) unfavourable primary extension twins in figures A4.3 and A4.4. However, it would appear that the appearance of the secondary twins may be explainable as an accommodation mechanism to help maintain strain compatibility due to twinning in other parts of the grain under investigation. In Figure A4.6

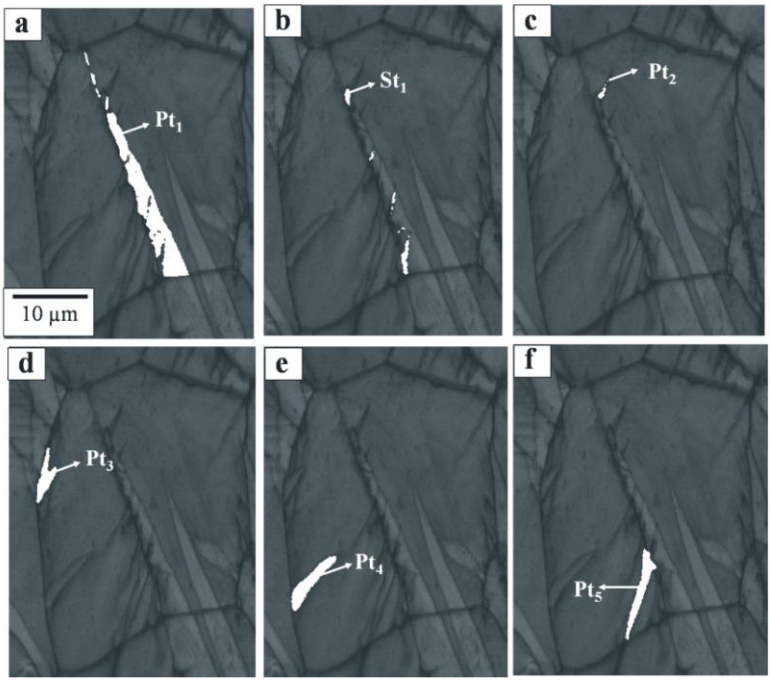

Figure A4.6: Shows the pattern quality map of the grain presented in figure 5. Noted that the extension twins identified from Pt_1- Pt_5 and St_1 are shown in white in **a)** to **f)**. All the twins are recognised as extension twins.

we identify 6 different twins in the grain presented earlier in Figure A4.3. In this case Pt_1 and St_1 are the primary and secondary extension twins, respectively which were identified in Figure A4.3. Twins Pt2 – Pt_5 are also all extension twins, but of a different variant compared to Pt_1 (Figure A4.7). It is important to note an apparent spatial relationship in the maps of Figure A4.6 between the twins Pt_1 and St_1 and the twins Pt_2— Pt_5. Notably, it appears that the position of the twins St_1 corresponds to the extended line of intersection between the twins Pt_2— Pt_5 and Pt_1. In this instance, one might question whether the

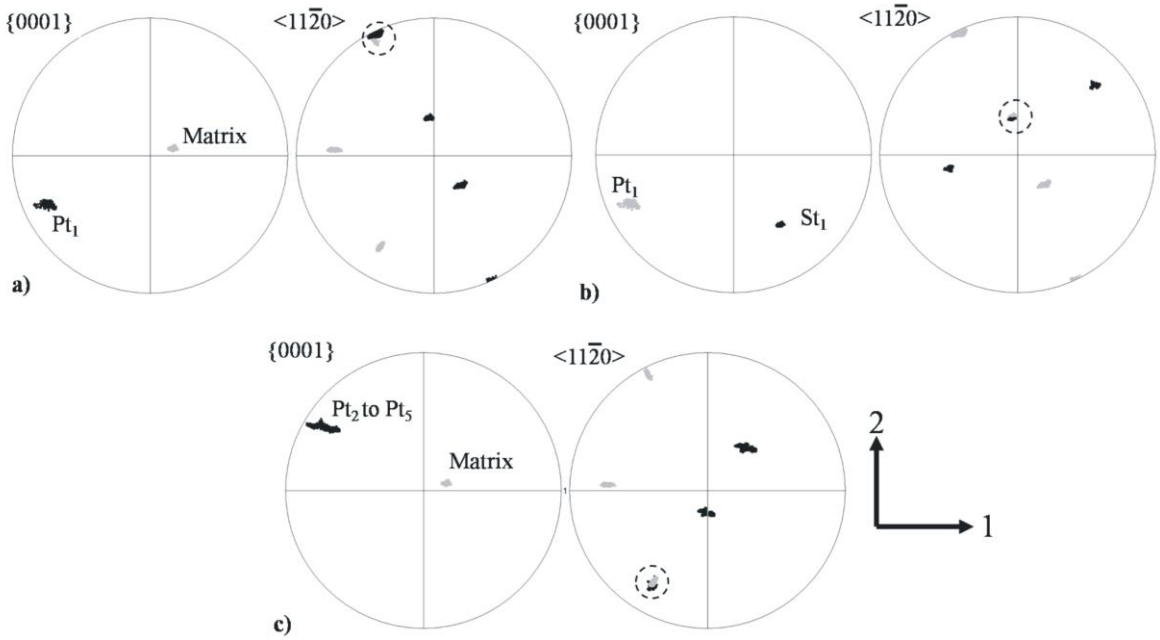

Figure A4.7: The {0001} pole figures in **a)** to **c)** illustrates the orientation of matrix and primary extension twin (Pt_1), orientation of primary and secondary extension twin (St_1) and orientation of matrix and Pt_2-Pt_5 extension twins, respectively. Additionally, the $<11\bar{2}0>$ pole figures in a) to c) describe the shared poles between the matrix and primary extension twin, between the primary and secondary extension twins and between the matrix and Pt_2-Pt_5 extension twins (see the dotted delineated circles over the common poles), respectively. Note that the macroscopic compression direction is parallel to the direction 1.

secondary extension twins St_1 form in response to the local stress field associated with the twins Pt_2— Pt_5. In this case, one might expect that the strains associated with the doubly twinned regions should be similar to that arising from the twins Pt_2— Pt_5.

The strain arising from the twins Pt_2— Pt_5 can be calculated (as performed above) to be

$$F_{Pt_2-Pt_5} = \begin{bmatrix} 0.9911 & -0.0101 & -0.0067 \\ -0.037 & 0.9581 & -0.0280 \\ 0.0667 & 0.0759 & 1.0508 \end{bmatrix}$$

$$E_{Pt_2-Pt_5} = \begin{bmatrix} -0.0089 & -0.0235 & 0.030 \\ -0.0235 & -0.0419 & 0.0239 \\ 0.030 & 0.0239 & 0.0508 \end{bmatrix}$$

Relative to the macroscopic axes. The strain arising from twin Pt_1 is,

$$F_{Pt_1} = \begin{bmatrix} 0.9508 & -0.001 & -0.0226 \\ 0.016 & 1.0003 & 0.00737 \\ 0.1062 & 0.0021 & 1.04884 \end{bmatrix}$$

$$E_{Pt_1} = \begin{bmatrix} -0.0492 & 0.0075 & 0.0418 \\ 0.0075 & 0.0003 & 0.0047 \\ 0.0418 & 0.0047 & 0.0488 \end{bmatrix} \qquad \text{(A4.3)}$$

And from twin St_1 is,

$$F_{St_1} = \begin{bmatrix} 1.0428 & -0.018 & -0.0078 \\ 0.109 & 0.9542 & -0.0198 \\ -0.016 & 0.0068 & 1.0029 \end{bmatrix}$$

$$E_{St_1} = \begin{bmatrix} 0.0428 & 0.0455 & -0.0119 \\ 0.0455 & -0.0458 & -0.0065 \\ -0.0119 & -0.0065 & 0.0029 \end{bmatrix}$$

Combining the strains from Pt_1 and St_1 we obtain,

$$F_{St_1}^{Net} = \begin{bmatrix} 0.9905 & -0.019 & -0.0318 \\ 0.1168 & 0.9544 & -0.0162 \\ 0.0911 & 0.0089 & 1.0523 \end{bmatrix}$$

$$E_{St_1}^{Net} = \begin{bmatrix} -0.0095 & 0.0489 & 0.0296 \\ 0.0489 & -0.0456 & -0.0036 \\ 0.0296 & -0.0036 & 0.0523 \end{bmatrix} \quad \text{(A4.4)}$$

Which is very similar to the strains associated with the twins Pt_2— Pt_5. Thus, in this case, the presence of the double twinning appears to occur so as to assist with maintaining strain compatibility between local regions within an individual grain where two twin variants impinge. In this case we would envision that twins Pt_2— Pt_5 impinge on twin Pt_1. Since the twins Pt_2— Pt_5 cannot directly cross the boundary associated with Pt_1, new secondary extension twins are nucleated within Pt_1. These secondary extension twins produce similar twinning strains to Pt_2— Pt_5. Under other conditions of twin impingement it is possible that slip, rather than secondary twinning, could accomplish the maintenance of strain compatibility.

A4.3. Morphology of double extension twins

Barnett et al. [9] have argued in the case of double contraction-extension twinning that the lateral growth of secondary extension twins inside the primary contraction twins

depends on the angle between the habit plane of the primary twin and the secondary twin. The larger the angular difference between these planes the higher the additional compatibility strain required and therefore the higher the barrier for a secondary twin to grow. The evidence for such an assertion includes the fact that the secondary extension twin variant characterised by a 38° $<11\bar{2}0>$ misorientation with respect to the primary contraction twin is the most common of $\{10\bar{1}1\}-\{10\bar{1}2\}$ double twins. This variant selection is consistent with the above argument since it gives the smallest possible angle between the primary and secondary twinning plane (18.8°). Most recently, Martin et al. [4] have further confirmed this notion by presenting their strain calculations which suggest that this particular variant has a very low associated accommodation strains.

In the case of double extension twinning the morphology of the secondary extension twins tends to be very fine, the growth of the secondary extension twins appearing to be limited. The angles between the primary and secondary habit planes, for the three possible double extension twin variants all result in very high values (as listed in Table A4.3). On the basis of the argument by Barnett, we therefore expect the growth of secondary twins inside primary twin to be difficult, consistent with the fine nature of the observed twins.

Table A4.3: Lists the possible combinations of primary and secondary twinning systems and their corresponding angle between the habit planes

Primary twinning plane (K_1)	*Primary shear direction (η_1)*	*Secondary twinning plane (K_1)*	*Secondary shear direction (η_1)*	*Combination primary-secondary*	*Angle between the primary and secondary habit planes (K_1 planes)*
$(10\bar{1}2)$	$[\bar{1}011]$	$(\bar{1}012)$	$[10\bar{1}1]$	$(10\bar{1}2)$-$(\bar{1}012)$	86.2°
$(10\bar{1}2)$	$[\bar{1}011]$	$(1\bar{1}02)$	$[\bar{1}101]$	$(10\bar{1}2)$-$(1\bar{1}02)$	39.9°
$(10\bar{1}2)$	$[\bar{1}011]$	$(0\bar{1}12)$	$[01\bar{1}1]$	$(10\bar{1}2)$-$(0\bar{1}12)$	72.5°

References

[1] J. Jain, J. Zou, C. W. Sinclair, W. J. Poole, *J. of Microscopy, doi: 10.1111/j.1365-2818.2010.03434.x* (2010).

[2] M. D. Nave, M. R. Barnett, *Scripta Mater.,* **51** (2004) 881.

[3] J. Koike, Y. Sato, D. Ando, *Mater. Trans.,* **49** (2008) 2792.

[4] É. Martin, L. Capolungo, L. Jiang, J. J. Jonas, *Acta Mater.*, **58** (2010) 3970.

[5] V. Randle, O. Engler, *Introduction to Texture Analysis: Macrotexture, Microtexture and Orientation Mapping*, Gordon and Breach Science Publ., Amsterdam (2000) (now Taylor and Francis).

[6] J. Lubliner, *Plasticity Theory* (2006), University of California at Berkeley.

[7] M. R. Barnett, Z. Keshavarz, M. D. Nave, *Metall. Mater. Trans. A,* **36** (2005) 1697.

[8] L. Wu, S. R. Agnew, D. W. Brown, G. M. Stoica, B. Clausen, A. Jain, D. E. Fielden, P. K. Liaw, *Acta Mater.* , **56** (2008) 3699.

[9] M. R. Barnett, Z. Keshavarz, A. G. Beer, X. Ma, *Acta Mater.,* **56** (2008) 5.